UNIVERSITÀ
DEGLI STUDI
DI PADOVA

Sede Amministrativa: Università degli Studi di Padova

Dipartimento di Innovazione Meccanica e Gestionale

SCUOLA DI DOTTORATO DI RICERCA IN : INGEGNERIA INDUSTRIALE

INDIRIZZO: INGEGNERIA DELLA PRODUZIONE INDUSTRIALE

CICLO XXII

MODELING OF SINGLE POINT INCREMENTAL FORMING PROCESS FOR METAL AND POLYMERIC SHEET

Direttore della Scuola : Ch.mo Prof. Paolo F. Bariani

Coordinatore d'indirizzo: Ch.mo Prof. Enrico Savio

Supervisore :Ch.mo Prof. Paolo F. Bariani

Dottorando : LÊ VĂN SỸ

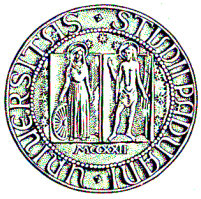

UNIVERSITY OF PADUA

DEPARTMENT OF INNOVATION IN MECHANICS AND MANAGEMENT

MODELING OF SINGLE POINT INCREMENTAL FORMING PROCESS FOR METAL AND POLYMERIC SHEET

A thesis submitted to the Doctoral School in Industrial Engineering in partial fulfillment of the requirements of the degree of Doctor of Philosophy, Cycle XXII

By

LE VAN SY

Director of School: Prof. Paolo F. Bariani

Supervisor: Prof. Paolo F. Bariani

PADOVA 2009

ACKNOWLEDGMENT

This work could not have been achieved without the financial support from ***Fondazione Cassa di Risparmio di Padova e Rovigo*** (CARIPARO) during the time in Italy. The author is grateful to all members of CARIPARO for this support.

First, I would like to express the deepest appreciation to Professor Paolo Bariani for his support, guidance and encouragement in the first days and during years of my stay at ***Department of Innovation in Mechanics and Management*** (DIMEG). He gave me a possibility as well as a direction of my PhD.

I am also very thankful to Dr. Andrea Ghiotti and Dr. Giovanni Lucchetta for valuable discussions, advices, and teachings.

I am grateful to Prof. Arturo N. Natali, Centre of Mechanics of Biological Materials, for giving me the opportunity to use the ABAQUS license and computer server in my simulations.

I am thankful to all my colleagues for their inestimable helps and friendly friendship at DIMEG. I would also like to express many thanks to the staff member of Administrative Office for their assistance in administrative problems. In addition, I am also thankful to my students for their helps in experiments and studies.

Finally, I would like to thank my wife, my son and my family who give me the zeal and encouragement to constitute my strength and complete this thesis.

Padova, 2009

Lê Văn Sỹ

ABSTRACT

Incremental Sheet Forming (ISF) is an innovative forming approach for sheet materials. This process has been promising a flexible, short time, and inexpensive way to form sheet products. The requiring equipments for SPIF process include a hemispherical forming tool and very simple frame to hold firmly a forming sheet. The forming tool is moved along a predefined toolpath which is a series of contour constructed a final shape of product by using numerical controlled technology. The sheet is deformed locally and finished in every layer in which is similar to the layered manufacturing principle of rapid prototype approach. Therefore, the process is relative slow and only suitable to small (or medium) production batch and rapid prototype production. Main advantages of SPIF technology are flexible, just-in time, short product development time, and inexpensive die/tooling. Additionally, it can form a product with an unlimited depth and allows high strain in comparison to conventional sheet forming technologies.

Realizing advantages of this process in industrial applications, the current study is performed the single point incremental forming process (SPIF) for both sheet metals and sheet polymers into main contents as following:

SPIF process is performed with magnesium alloy sheet and aluminum alloy sheet at an elevated temperature. Deforming sheet with SPIF process at a high temperature is to find a high formability in compared with previous researchers of aluminum sheet. Magnesium sheet has important industrial applications with a high ratio of weight/strength; however, it has low formability at room temperature. A heating system based on Joule effect is design to serve for experiments. It allows heating the sheet in very short time, which can avoid oxygenating phenomenon on sheet surfaces. This thesis also investigated FEM simulation to predict the mechanical failures in SPIF. A fully couple thermal analysis is performed with full cone-shaped model which is taken into account of material behaviors such as anisotropy and sensitivity of strain rate and temperature. The speeding up and adaptive meshing technologies for FEM simulation are also discussed in here.

The first effort to find an applicability of SPIF for polymeric materials was investigated in the current thesis. Preliminary experiments of SPIF performed on thermoplastic materials at room temperature. An experimental strategy based on DOE technique is designed to evaluate preliminarily the influence of processing parameters on the formability. Then, constitutive material model base on overstress theory (VBO) is developed to implement into FEM simulation for prediction of the thickness and geometric accuracy.

Keywords: SPIF, incremental sheet forming, DOE, FEM simulation, coupled thermal analysis.

Contents

List of Figures

List of Tables

Nomenclature

Acronyms

Adj MS	Adjusted means of square
Adj SS	Adjusted sums of squares
Alxxx	Aluminum Alloy
Axxx	Aluminum Alloy
ANOVA	Analysis of Variance
BCC	Body-centered cubic
CPU	Central Processing Unit
CAA	Computer Aided Analysis
CAD	Computer Aided Design
CAE	Computer Aided Engineering
CAM	Computer Aided Manufacturing
CAPP	Computer Aided Process Planning
CNC	Computer Numerical Control
CMM	Coordinate-measuring machine
DOE	Design Of Experiment
DRX	Dynamic recrystallization
FCC	Face-centered cubic
FE	Finite Element
FEM	Finite Element Method
FLD	Forming Limit Diagram
FFLD	Fracture Forming Limit Diagram
HCP	Hexaganal close packed structure
HVH	Hyper-Visco-Hysteresis constitutive law
IF	Incremental forming
ISF	Incremental sheet forming
LDR	Limiting drawing ratio
AZxx	Magnesium Alloy
MK	Marciniak-Kuczynski
NC	Numerical Control
PP	Polypropylene
Seq SS	Sequential sums of squares
SPIF	Single point incremental forming
SLS	Standard Linear Solid
TTS	Through Thickness Shear
TPIF	Two points incremental forming

UMAT	User-material
VBO	Viscoplasticity based on overstress

Symbols

A	Isotropic stress
A_0, A_c, A_f	Material constants of isotropic stress
A_G	Parameter in Gurson criteria
A_w, A_D	Parameters in Wilkins criteria
C	Critical value
C_1, C_2, C_3	Material constants of shape function
C^{NJ}	The lumped capacitance matrix
d, d_1-d_5, c	Material parameters
D, D_C	Overall damage variable, Critical damage value for ductile fracture
d_C	Material parameter in CrachFEM
$\Delta\tau$	Time increment
E, E_t	Young Modulus, Tangent Modulus
f, f^*, f_c, f_f, f_n	Void volume fraction (VVF), effective VVF, VVF at fracture, VVF at rupture, VVF of nucleating particles
f_k	Prager kinematic hardening
G	Shear modulus
$g[\ ]$,$k[\ ]$	Equivalent stress function, Viscosity function
h	The thickness of sheet after deformation
h_0	Initial thickness of sheet
$k1…k3$	Material constant in viscosity function
k_d	Material constant
l	Width of imperfection
$\mathcal{N}$	Normalization of the deviatoric overstress
P_i^J, F_i^J	The applied nodal source vector, the internal flux vector
q, p, k_s, f_s	Material parameters in shear criterion
R, r	Radius of a circle, Forming tool radius
$S1$-$S3$	The principal stress deviators
T	Temperature
t_0, t	Initial time, time
v	Spindle speed
x, y	x, y coordinates
x', y'	x', y' coordinates
X^{log}	Logarithmic rate of X
z_0	Height of cone

z_{M1}	Heigh of cone at M1
A_0^t, A_i^t, A_j^t	Data point
$R_{11}, R_{22,} R_{33}, R_{23}, R_{12}$	The factors in Hill's potential function
$r_0, r_{45,} r_{90}$	Normal anisotropy in direction of 0, 45, 90 degree

α	wall angle
β	Ductile fracture parameter
β_w, γ_w	Material constants in Wilkins criteria
γ, γ_c	Angle of local material orientation
σ_0	Material average plastic flow stress
$\bar{\varepsilon}$, $\bar{\sigma}$	Equivalent plastic strain, von Mises effective stress
$\bar{\varepsilon}_f$	Equivalent plastic strain to fracture
$\tau_{\max}$	Maximum shear stress
$\eta, \bar{\eta}$	Stress triaxiality, average stress triaxiality
η_d	Dashpot coefficient
$\varepsilon_1, \varepsilon_2$	Major principal strain, Minor principal strain
σ, ε	Total stress and strain
σ_m	Hydrostatic mean stress
$\tilde{\sigma}$	Ratio of $\sigma_1/\bar{\sigma}$
$\bar{\varepsilon}_S$, θ_S	Equivalent plastic strain for shear criteria, Shear stress ratio
$\theta_S^+ \theta_S^-$	Values of θ_S at $\eta+$ and $\eta-$
$\bar{\varepsilon}_f^d$, $\bar{\varepsilon}_f^S$	Equivalent plastic strain to fracture for ductile and shear criteria
μ	Elastic shear
σ_y	Yield stress
ε_d^+ , ε_s^+	Equivalent plastic strain for biaxial tensile of ductile and shear criterion
ε_d^- , ε_s^-	Equivalent plastic strain for biaxial compression of ductile and shear criteria
Φ	The modified yield function
$\varepsilon_N, \varepsilon_e$	Standard deviation, the mean strain in Gurson model
ω_f	Filtering high-frequency oscillation
ω	Angle velocity, feedrate
$\bar{\sigma}$	Equivalent stress
η_d	Dashpot coefficient
$\varepsilon^{el}, \varepsilon^{in}$	Elastic strain, Inelastic strain
ξ	Time ratio
Γ	Overstress
η_p, ν_p	Inelastic Poison's rate, Elastic Poison's rate
Ω^{log}	Logarithmic rat of any symmetric Eulerian
ψ	Shape function

θ_i^N	Temperature at node N with respect to ith increment of step
λ	Lamé's first parameter
δ	Kronecker tensor
τ_a, τ_b	Material coefficient of viscosity
ν	Viscosity coefficient
$\boldsymbol{\tau}^{log}$	Eulerian tensor
μ	Elastic shear
η_s, η_b	Shear and bilk coefficient of viscosity
θ	Wall angle of a point on circular generatrix

Chapter 1

Introduction

1.1 Background and motivation

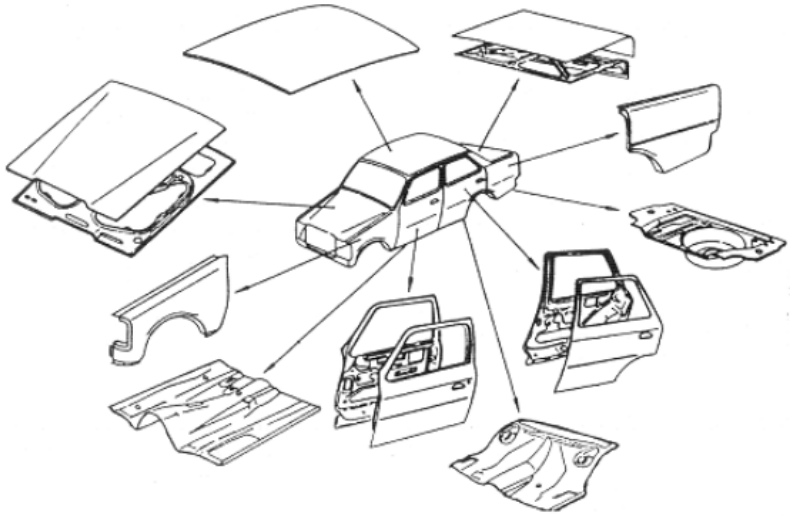

Fig. 1.1 Metal sheet parts in major panels of car body [1]

Sheet metal forming is a major manufacturing process in many civil and industrial sectors. Throughout the decades, technological advances have allowed manufacturing the extremely complex parts. The economical competitiveness of the process requires large production batches to amortize the costs of dies and tooling. Small, medium volume production of precision conventional process such as deep drawing and stamping process have still been a problem of the metalworking industry. The trend of customer is a demand for smaller volume production of diverse products, coupled with the highest product quality. Facing up to these requires, the manufacturing companies have to adapt to a new environment in which requires more flexible operations to satisfy different market segments. Thus, innovation of shorter production cycles is necessitated a significant reduction in development times.

In most manufacturing industries, prototype manufacturing is an important step in the development or improvement of a product before proceeding to the manufacture of production. It allows a preliminary evaluation of the product during the design stage, and a reduction in the product development time. For example, automotive industries need to produce about 40-50 critical panels per a car model (see Fig. 1.1) that require at least 150-200 dies for stamping process. Thus, a huge amount of work in the prototype manufacturing process for these dies is needed.

The tryout manufacturing of die and scaled model for testing progressed at a much slower rate, and they still depend heavily on trial-and-error method and the experience of skilled workers. Additionally, the investment cost and time consuming to produce dies, formed prototype and preproduction parts using conventional processes is too expensive. Successful production of these low-production batches with conventional processes demands an innovative thinking in relation to the cost of tools/dies and time consuming. In automotive industry, increasing competition demands the productivity improvements and reduction of manufacturing cost as well as product-cycle reduction. This trend gave rise to the reduction of product cost and development time, the need for faster turn-around times, more efficient mean of producing prototype, and short-run tooling for tryout manufacturing.

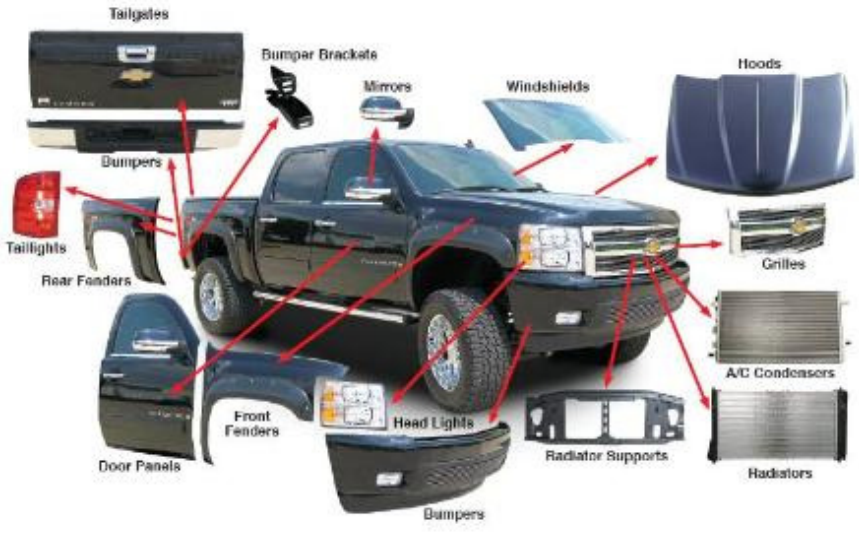

Fig. 1.2 Polymeric sheet parts in major panels of car body [1]

Similarly, injection-moulding technology has traditionally received extensive attention for the production of polymers parts. Although the high flexibility in the design of component shapes, the economical competitiveness of the process requires large production batches to amortize the costs of dies and tooling. Otherwise, flat components can be obtained by deforming sheet polymers in thermoforming processes as the combination of drawing and stretching mechanisms. However, these processes present strong limitations, particularly with respect to the forming of small to medium batch production. Thermoforming requires expensive and dedicated plants equipped with complex dies. Therefore, the improvement of the material forming limits and the manufacturing processes, especially for the small to medium production of complex shape components, is required.

As a result, incremental sheet forming technology (ISF) using CNC machine has made inroads into conventional technology with the aim of reducing the investment costs and lead-time of tooling development. Only several years ago, with the efforts of researchers and scientists, this technology has been investigated to become a pre-eminence process for low (or medium) production batches and rapid prototype manufacturing.

The major advantage of ISF technology is represented by the possibility to manufacture sheet parts (both metal and polymer sheet) which is difficult to form with traditional processes in a rapid and economic way without expensive dies and long set-up times. In IF, the tooling is usually a simple frame for the sheet metal clamping, while the deformation is realized by using a tool that is moved along a predefined path by a CNC machine or a robot. Although the process can be rather slow in comparison to the traditional processes, the IF process for sheet materials represents the best way to manufacture prototypes and complex components produced in small batches for aeronautical, automotive and medical applications.

1.2 Incremental forming technology

The ISF technology is a forming approach in which uses the numerically controlled (NC) technology to produce a part from the sheet materials. With this technology, the new product can be made in one day from CAD modeling to finished part. To response this

task, a fully digital integrated system for SPIF process has been developed in another project of this study. The system can recognize automatically the features of CAD model of SPIF product. Then, it generates toolpath based on machining data from the user or database of library (see Fig. 1.4). The key aspect of this system is a unique data flow used in the sub-module from CAD model to CNC code (see Fig. 1.5). The system is connected to CNC interface through RS-323B. All modules were integrated fully on commercial CAD/CAM software called CATIA (see Fig. 1.6). It is very suitable for prototype process of new part and low-quantities production. The basic elements of ISF system are illustrated in Fig. 1.4 included CAD system (**C**omputer **A**ided **D**esign), CAPP system (**C**omputer **A**ided **P**rocess **P**lanning), CAA system (**C**omputer **A**ided **A**nalysis) and CNC machine (**C**omputer **N**umerical **C**ontrol).

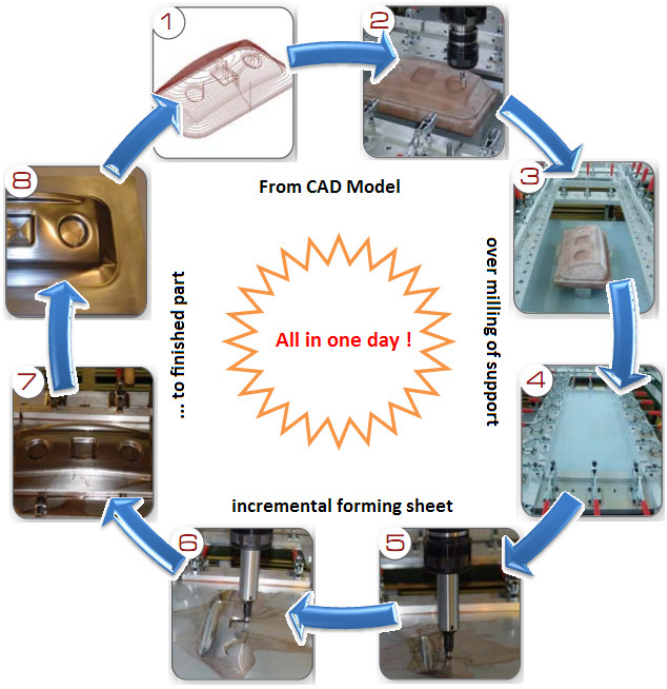

Fig.1.3 Steps of incremental forming process

However, the core aspect of this study is incremental forming technology for sheet materials. The ISF consists of a series of local forming operations leading to the final geometry of the part without the need for expensive tools or dies. The process involves the use of a single end-hemispherical tool to carry out progressively local deformation of sheet metal with three-axial CNC machine (or more axial CNC machine), or with an

industrial robot. The movement of forming tool based on NC technology is generated from normal CAM system. The product of this process can be made directly from a 3-D CAD model to finished product without any dedicated dies or special tools. Therefore, the ISF process offers the rapid prototyping advantages of short lead times, high flexibility and lower cost for small batch applications. For complex product, a simple support is required to reinforce the stability of the system.

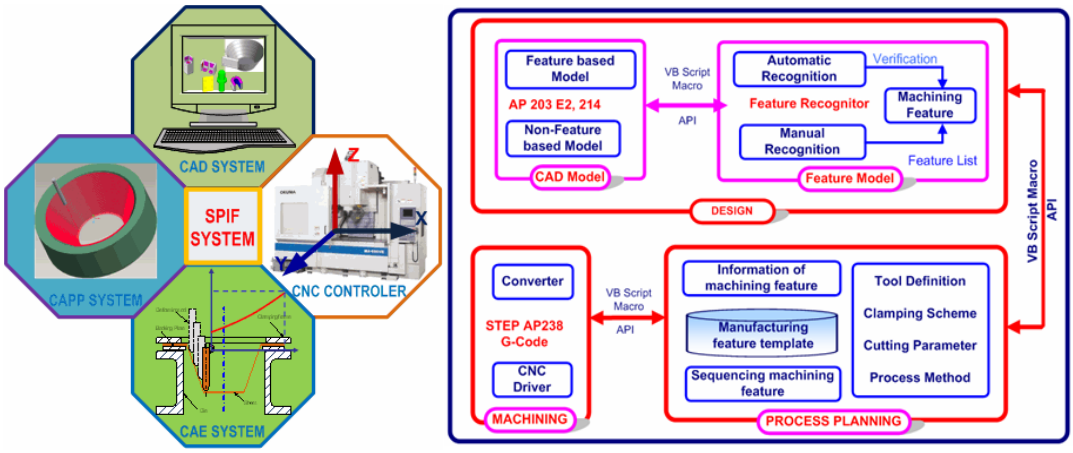

Fig. 1.4 The basic elements of Increment forming system

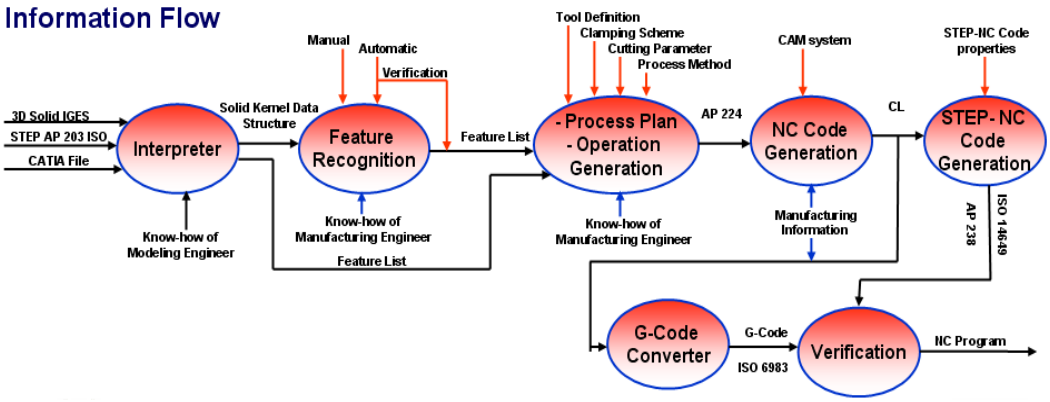

Fig. 1.5 Data flow used in fully integrated system for SPIF process

The incremental sheet forming techniques (ISF) can be divided into two categories: two points incremental forming (TPIF) and single point incremental forming (SPIF), also known as negative and positive forming, respectively [2,3]. The SPIF process is presented in the detail of section 1.5. In the TPIF process (see Fig.1.7 and Fig. 1.8), the sheet metal moves vertically on bearings, which move on sheet holder posts, along the z-axis, as the

forming tool pushes into the metal sheet. This process is called TPIF because it has two contacting points between forming tool and the sheet. The first point where forming tool presses down on the sheet metal to cause locally plastic deformation. The second point is a contacting point between a static post and the sheet creating when the tool pressed into the sheet. Although TPIF process used a partial die, it is often called as dieless forming [4,5].

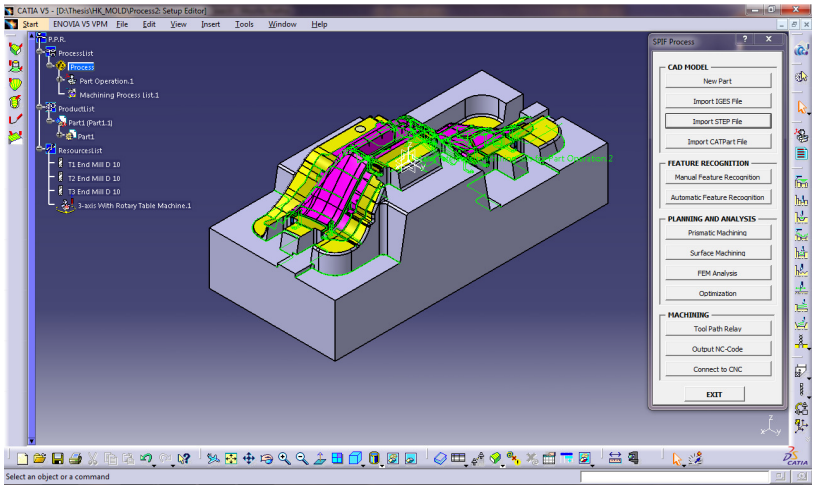

Fig. 1.6 Main interface of a digital integrated system of SPIF process

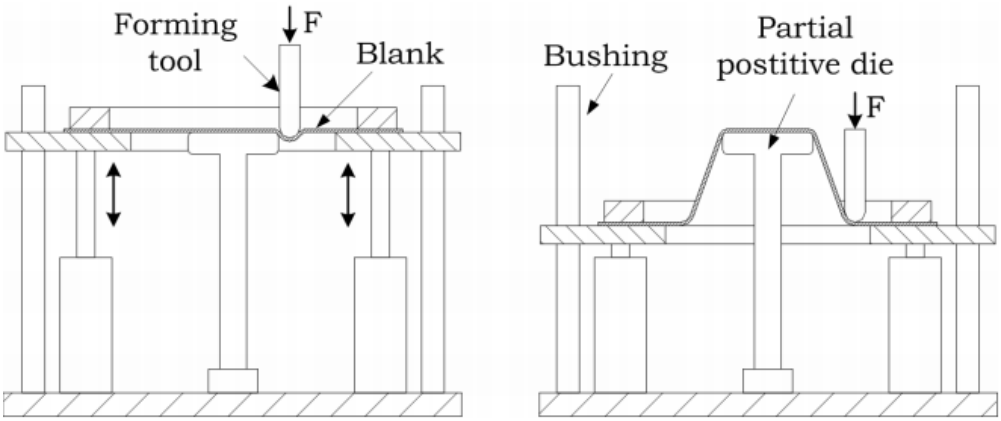

Fig.1.7 Two Points Incremental Forming [6]

The TPIF process can be classified into two types: TPIF with a static support and TPIF with a kinematic support. For TPIF with a static support (see Fig.1.7), the support is positioned firmly on the opposite face of the sheet metal (opposite with contacting surface between tool and sheet). The sheet metal is clamped firmly on a frame that can move up and down in the parallel direction to the tool. For TPIF with a kinematic

support, the support moves simultaneously with the forming tool. There are several configurations for this type in literature. Typically, Franzen et al. [7] designed a configuration as Fig. 1.8. In this configuration, the partial support is fixed on a rotating table which rotates simultaneously with forming tool. The rotating table holds a partial die that has a shape of final product. This system has the disadvantage to be only suitable for rotational symmetry products.

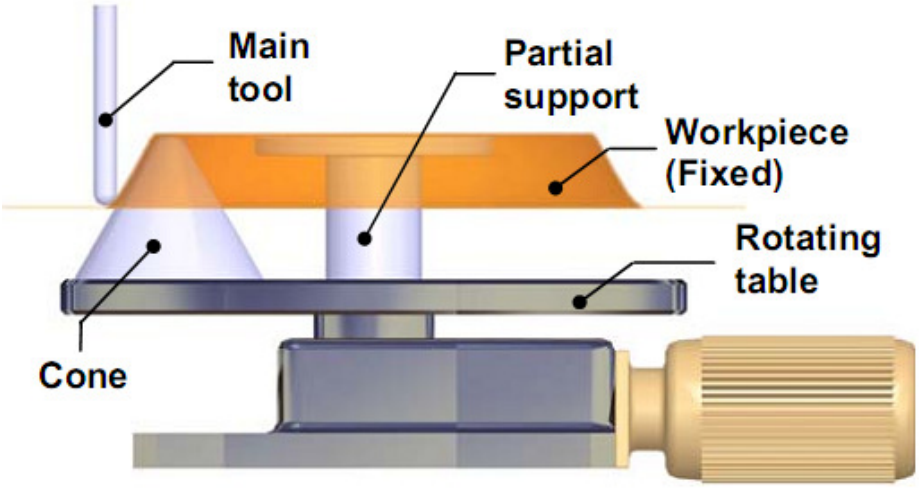

Fig. 1.8 TPIF with kinematic support (dyna-die) [7]

1.3 History

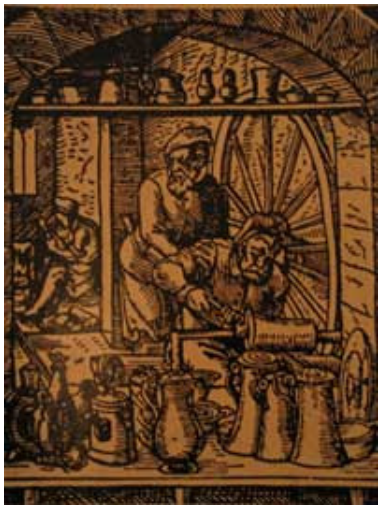

Fig.1.9 Wooden spinning with a manually operated flywheel [13]

The basic idea of ISF technology is patented in 1967 by Leszak, so-called dieless forming as in this patent [8]. Ever since the twenty-four years after, this idea started to be

interested and appeared in some scientific literatures. The main reason of this lateness is limitations of the CNC technology in milling and turning machines. In the late eighties, the CNC technology is mature and the production market becomes very complex. Manufacturing companies need to reduce the product development time and cost. The demand for faster turn-around times, more efficient means of producing prototype and short-run tooling has increased. They desiderated new technologies that can reduce product development time and variant products. The ISF technology using CNC machine for metal sheet forming and rapid prototype technology became one of the important topics in international conferences. Some researchers started to present the preliminary studies about ISF technology from the beginning of nineties [5,9,4,10].

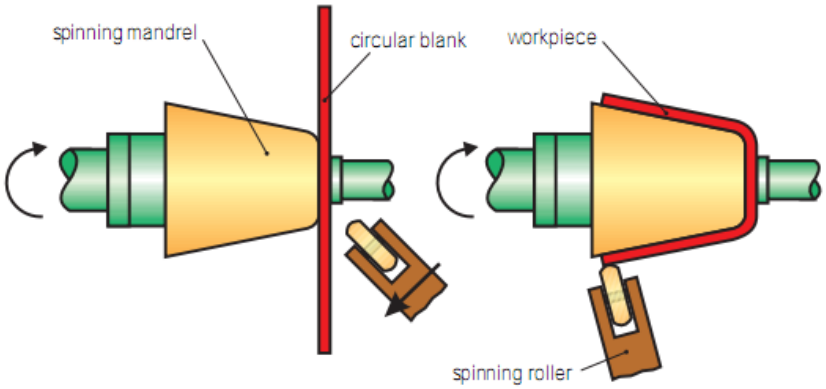

Fig.1.10 Spinning a hollow body with using roller [11]

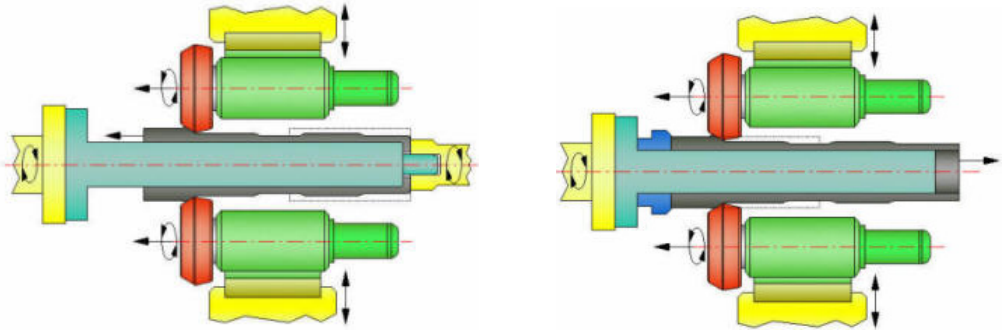

Fig.1.11 Forward and backward flow forming [11]

In the past, the ISF process used in the field metal forming such as conventional spinning, shear forming and flow forming. Spin forming belonged to the oldest shape changing techniques in history is considered as the forerunner of ISF for sheet materials [12]. This process is characterized by rotating a workpiece clamped rigidly against a

mandrel while the spinning tool approaches progressively and deform it to the required shape with respect to the profile of the mandrel. Belong to technology evolution; there are the changes in a rotational generator and spinning tool.

The spinning techniques used to form sheet metal started from the Middle Ages. Fig.1.9 described the use of spinning technique to form metal vessels. The first person uses a tool to force progressively the blank into a mandrel that has a shape of final product. The second person operating a large wheel connected to the mandrel spindle by belt provides the rotational power of the mandrel. In later years, there were the changes in rotational generators from manpower to water power, steam power and electric power. However, there was no change in the hand spinner which is still depended heavily on the skill of the first person.

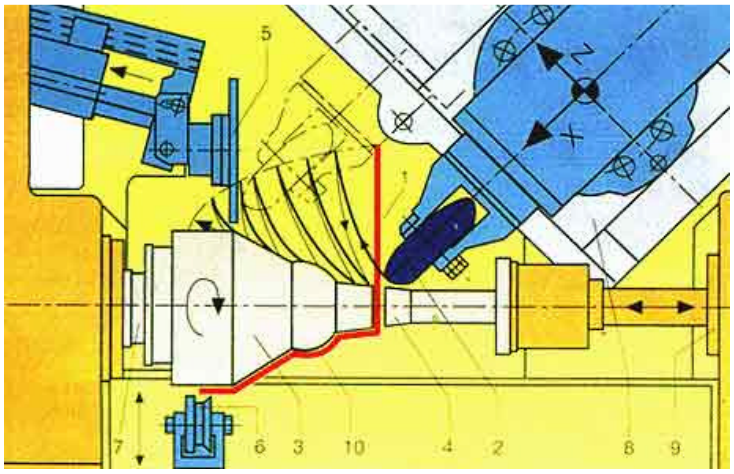

1 - Blank Sheet
2 - Spinning Roller
3 - Mandrel
4 - Clamping Plate
5 - Blank Support Unit
6 - Trimming Plate
7 - Spindle
8 - Cross Slide
9 - Tailstock

Fig.1.12 CNC Metal Spinning [13]

In the beginning of the 20th century, some forms of power assistance for the hand spinner are developed which brought a convenience for spinner in using the metal spinning techniques. In 1945, the hydraulic power lathes are introduced which provided a big force to be able to change the stick-type tool into a roller as showed in Fig.1.10. Thanks to big force from hydraulic power, the newer techniques allowed to deform harder materials called shear forming and flow forming as showed in Fig.1.11. In the early 1970s, metal spinning machines are integrated the numerical controlled technology as in Fig.1.12.

Flow forming is a process which formed the product from metal blank in hollow or tube types. It used one or more rollers to flow axially the material along the mandrel. The main difference between the spinning and flow forming is the thickness of the blank changed significantly in flow forming.

Shear forming process is a heritability of the previous spinning technology with the using the hydraulic equipment and CNC technology. The machine configuration for shear forming is very similar to one for the spinning forming. However, it is designed to able to stand a higher force during shear forming process. In deformation of conventional spinning, the thickness of blank is less changed than one in shear forming. The final thickness of a shear formed part can be calculated using the sine law:

$$h = h_0 \sin(\frac{\pi}{2} - \alpha) \tag{1.1}$$

where h_0 is the initial thickness, h is the final thickness, and α is the spinning angle.

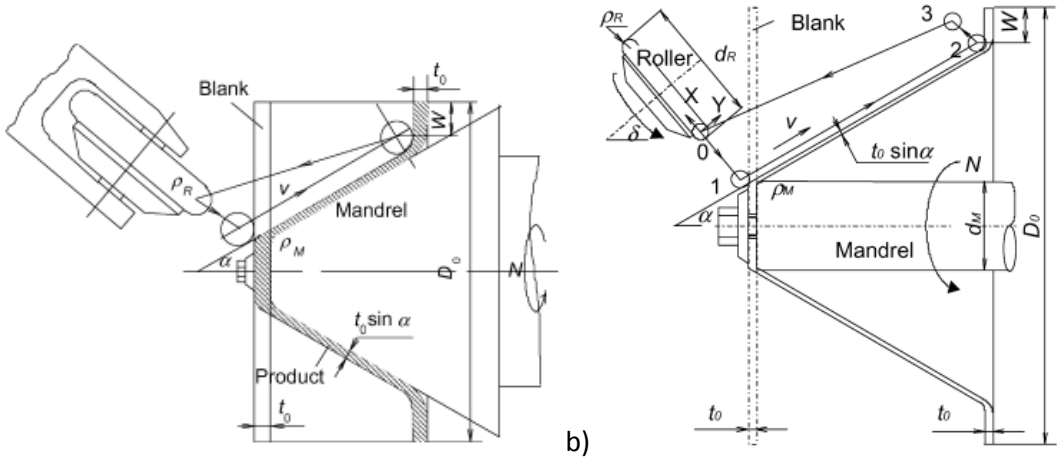

a) b)

Fig.1.13 Die-less shear forming [14]

a) Shear spinning with a mandrel b) Shear spinning with a cylindrical mandrel [15]

In the late eighties, die-less shear spinning forming is introduced [16,14,15]. There are two configurations of die-less shear spinning forming as showed in Fig.1.13. In Fig.1.13a, outer surface of the mandrel formed the inner surface of the product. This process does not require high stiffness of metal sheet. The failure of wall fractures and flange wrinkles usually occurs in this process [17]. In Fig.1.13b, the mandrel used in this configuration is

a cylindrical shape. The metal sheet is engaged on the end of the mandrel. The roller is moved along the generatrix of product shape while the mandrel is rotating together with a spindle of a spinning machine. This process is very flexible and consistent with forming of axis-symmetrical parts in small-batch production. However, the sheet is required high stiffness to maintain the shape of product during the spinning process. The problem of spring-back is relatively large and the accuracy of geometry is relatively low [18].

Nowadays, spinning and flow forming technology has developed into an important branch of trade in the metal forming industry. They are being applied for the most sector of manufacturing industry, especially for the automotive industry. However, the ISF process, truly dieless forming technology, enhanced as potential technology in recent years which to be more compatible with a small and medium volume batch and rapid prototype of sheet materials.

1.4 Principles

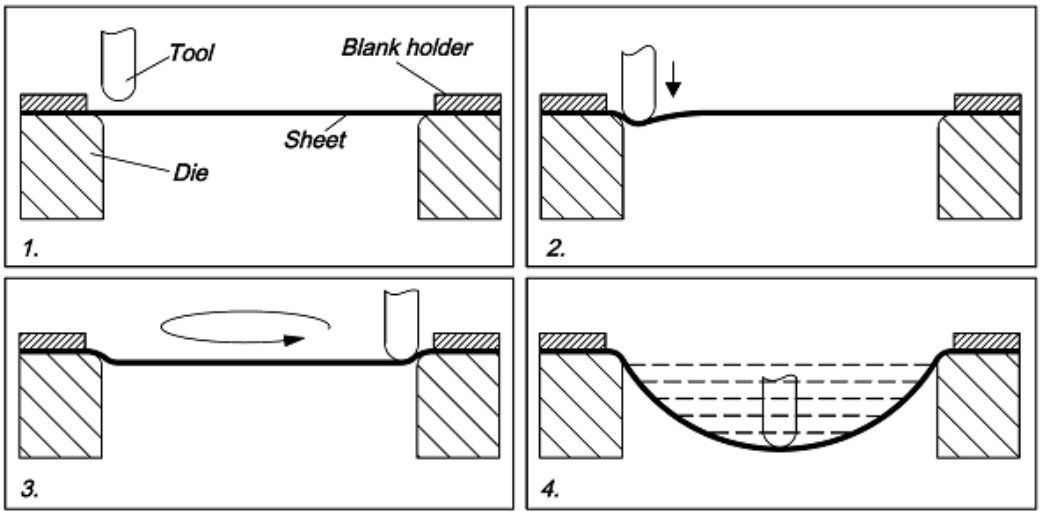

Fig. 1.14 Schematic diagram of the incremental sheet metal forming process [6]

ISF is a forming technique of sheet material based on layered manufacturing principles. The sheet part is locally deformed through horizontal slices. The moving locus of forming tool (called as toolpath) in these slices constructed to the finished part is performed by the NC technology. The toolpath is created directly from CAD model of final product by using CAPP techniques. The forming tool is a simple end-hemispherical tool, which is

moved along the toolpath while the edges of sheet material are clamped rigidly on simple frame. All of main steps in ISF process are presented on Fig. 1.14: i) sheet material is clamped firmly on the frame. ii) The forming tool goes down and contacts sheet. iii) The tool moves following the first round of toolpath that has the geometric shape of the final product. iv) So forth, the tool repeats these operations until it obtains the end of toolpath.

1.5 Single Point Forming Process

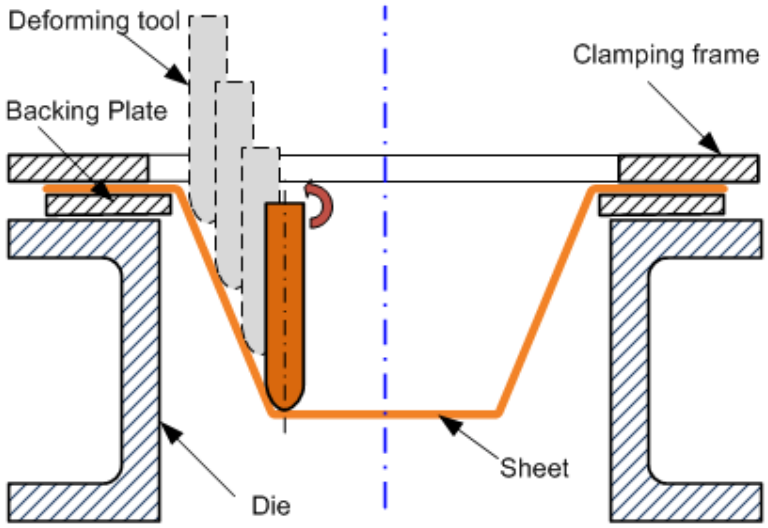

Fig.1.15 Single point incremental forming

The single point incremental forming (SPIF) process is performed on three-axis CNC machine without a partial die or a full die. It is truly dieless forming technology as envisioned by Leszak [8]. There is one major difference between SPIF and TPIF as shown in Fig.1.15 and Fig.1.7. In SPIF process, the lower surface of the sheet does not contact with any supporters. It creates different strain and stress patterns in the sheet when it is deformed. The configuration of Fig.1.15 shows that any CNC milling machine, used in conjunction with CAPP software, could be used to form sheet parts incrementally [19,20,21].

A backing plate is used to decrease spring-back problems in forming process. The spring-back problem is surmounted by using the compensative algorithm or the adaptive online-control.

A potential advantage of ISF is no need the dedicated die or expensive forming tools. A part can be performed in a day; therefore, it is very appropriate to small production batch or rapid prototype. Another advantage is a high deformation level in comparison with conventional forming. Several researchers reported that the classical forming limit diagram (FLD) is not able to predict the mechanical failures of deformed part since a much larger deformation can be reached in SPIF process. For this reason, new types of FLD need to be developed [22,23,24].

All experiments in the current thesis always use Single Point Incremental Forming (SPIF) due to potential advantages, in comparison with Two Points Incremental Forming (TPIF). Therefore, the term of "dieless forming" or "increment forming" is implied as SPIF.

1.6 Limitations of Incremental Forming

In the SPIF process, thickness of formed part is evaluated by formula (1.1) that is usually utilized for the shear forming process. The theoretical calculation shows that the thickness of vertical wall is zero. Therefore, the capacity of SPIF process only can deform the wall angle less than 90 degrees.

The parts having various steep walls are very difficult to apply this process. Because the thickness of deformed part is calculated uniformly by formula of (1.1) and the thickness of black is constant.

Researchers also claimed the geometric accuracy of deformed part and surface quality in SPIF process. The geometric accuracy is an important problem that is studied by many researchers [2,25,26,27]. They reported that the geometric accuracy seems to be lower than conventional forming. The surface quality is influenced mainly by the processing parameters such as depth step and feed-rate. These parameters have a close relationship with feasibility of SPIF process in industrial application.

However, the above limitations have been solved so that SPIF process becomes a potential in industrial applications. Researchers proposed a multistage forming strategy to overcome the limitation of wall angle. They could form a part with vertical wall (90^0) using TPIF [28].

The compensative algorithms in CNC programming technology were used to overcome the limitation of geometric accuracy. Geometric accuracy can overcome by approaches such as the iterative application of a correction algorithm to the tool path based on geometric error, the compensative techniques in CNC programming. In additional, using a backing-plate reduces the spring-back phenomenon in the formed part.

1.7 Objective

The objective of this thesis is the study of ISF technique for metal and polymeric materials. For metal material, magnesium alloy sheet (AZ31) and aluminum alloy sheet in series of 1010 were selected for this study. The main difference with previous studies is to apply SPIF process at an elevated temperature with expecting to obtain higher formability. For polymer material, some thermoplastics were selected to preliminarily evaluate the applicability of SPIF process at room temperature. Polypropylene was then used in all experiments to investigate the formability of SPIF process. To achieve the objective, a series of tasks is planned as following:

- Review on IF technique for sheet metal at room temperature
- Consider the applicability of SPIF process for polymer material at room temperature and for magnesium and aluminum sheet at an elevated temperature.
- Design cooling and heating system to serve for experiments of SPIF.
- Perform the experiments of SPIF on three types of material concerned in above.
- Review on deformation mechanisms on SPIF and common damage criteria for metal sheet.
- Perform FEM simulation to predict mechanical failures in SPIF process with metal sheet.
- Perform FEM simulation to evaluate the thickness of deformed sheet and geometric accuracy in SPIF process with polymer materials.

1.8 Structure of thesis

This thesis presents in six chapters with contents summarized as following:

The first chapter introduces the general information of IF technique, motivation of the study and objectives. It focuses on the SPIF process for both metal and polymeric material and its present limitations in industrial application.

Chapter 2 provides a concise state of the art in IF technique for metal and polymeric materials. In SPIF process with metal material, two materials investigated in this study is Magnesium alloy AZ31 and Aluminum alloy in series of 1010. Thermoplastic materials were investigated in SPIF with polymeric material. Novelties of this study compared to the state of the art are also presented in this chapter.

Chapter 3 presents equipments, procedures, and strategies of experiments for SPIF process with metals and polymers. The experimental equipments include forming tool, jig and fixture, CNC machine, heating and cooling system. To investigate the influence of processing parameters on formability of SPIF, two designs of experiment (DOEs) were established. For AZ31 and Al-1010 sheet, forming temperature, feed-rate, and depth step were considered in an experimental strategy. For polymers, the parameters (tool diameter, feed-rate, spindle speed, and depth step) are more than one of metal materials because SPIF process is applied the first time for polymeric materials at room temperature in the current thesis. Analysis of Variance (ANOVA) is performed to evaluate the influence of processing parameters on formability of material. Understanding of these influences is a fundament for selecting the optimal processing parameters using in FEM simulation in next chapter.

Chapter 4 presents a review of positive explanations about the mechanical fracture mode and deformation mechanism of SPIF process with metal sheet materials, and fracture criteria that used commonly for damage prediction of metal sheet. These criteria have been proposed in different spaces as plane strain, equivalent strain, stress triaxiality… etc. Therefore, they should be converted into a compatible space of equivalent strain-stress triaxiality in order to apply conveniently into a finite element simulation code (ABAQUS). Notes about material, temperature and strain rate dependent-data, and progressive damage for ductile metal in ABAQUS are presented in here.

Chapter 5 presents the experimental procedures and experimental analysis for both metal and polymeric material. The uniaxial and biaxial testing with different temperatures and strain rates performed on magnesium alloy. Then, their microstructure was investigated to understand more clearly about mechanical behaviors. For polymer, tensile, relaxation and creep testing with different strain rate is performed on sheet polypropylene at room temperature. A viscoplasticity constitutive equation based on the overstress model was considered to implement into ABAQUS under a user-material (UMAT) for numerical simulation of SPIF process.

Chapter 6 presents aspects of numerical simulation for predicting mechanical failure of SPIF process with magnesium alloy sheet and polypropylene sheet. The computational time consuming for FEM simulation of SPIF process is an important problem. Some methods that are able to reduce calculation time are also discussed. The simulated results were evaluated and compared and with actual experiment on formed thickness and geometric accuracy.

Final chapter gives summaries of obtained results of SPIF process with magnesium alloy ZA31 sheet, aluminum 1010 sheet and polymer material. The future studies also suggested in here.

Chapter 2

Literary review

2.1 State of the Art in Incremental Forming

2.1.1 Magnesium alloy

The applications of magnesium alloy have increased significantly in recent years due to good mechanical properties such as good tensile properties, high specific strength and stiffness, good damping characteristics, acceptable weldability, excellent machinability and castability, fatigue resistance, dimensional stability, dent resistance, and aesthetic appeal. Additionally, they also have excellent shielding capabilities against electromagnetic interference, high recyclability in a range of established foundry processes, environmental stability, and effective heat dissipation [29].

Magnesium alloy is usually used in automotive industry under two typical types such as cast magnesium (AZ91, AM50, AM60) and wrought magnesium (AZ80-T5, AZ31-H24). The first type has same yield strength and ductility as aluminum alloy A380. It can replace A380 aluminum with lighter weight in the non-structural applications of low-temperature components such as cases, brackets, covers, and housings. In structural applications, AM50 and AM60 showed high ductility and impact strength in comparison with A380 and A356 aluminum alloy.

The second type of magnesium alloy (AZ31, AZ80) is commercially produced in sheet form and is used the most commonly. AZ31 sheet offers a great potential to reduce weight by their low density (1.77g/m^3). It is lighter than aluminum and possesses high rigidity (about 35% lighter than aluminum alloys, 78% lighter than steel). In comparison with common 5xxx series of aluminum sheet, AZ31 offers a higher ductility and slight lower strength. Matching stiffness and strength requirements, it promises a significant

mass reduction in large surface area/thin walled applications (about 20% reduction compared with aluminum, and 50% compared with steel). Therefore, the AZ31 sheet is commonly utilized in various applications such as coverings of mobile telephones, notebook computers, portable mini-disks, load bearing and structural components, electronic housing and electromotor, outer body panels and components, bicycle components, automotive transmission and power steering components, light reflectors and components for defense, airplane components.

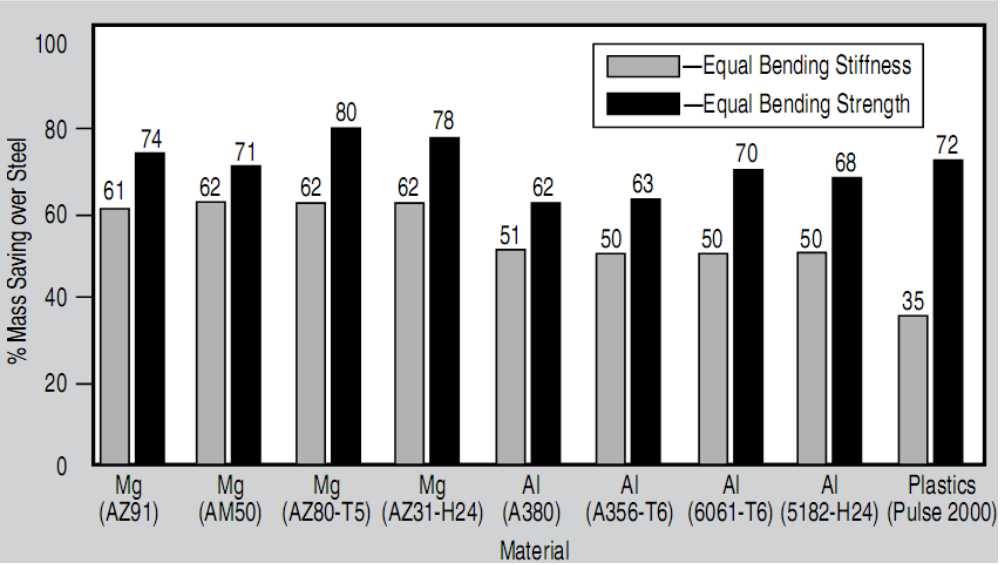

Fig. 2.1 The percentage mass savings of various materials vs. steel

The use of magnesium alloy to reduce weight of product predisposes much attention to environmental preservation. The Fig. 2.1 highlighted the resultant percentage mass savings of magnesium alloy and aluminum alloy when replacing a steel material. Reducing weight of components while maintaining their functional requirements drive to the decrease of materials, energy, and costs.

In automotive engineering, the reduction of fuel consumption and exhaust emissions is an important problem. They bring to the reduction of the perniciousness for environment which is one of the major goals of modern engineering design and manufacturing. There were many proposed ways to reduce them which included aerodynamics, friendly environmental fuels and mass reduction.

However, reduction of mass is the most influential and least costly. The results of some studies in automotive industry showed that more than 50% of fuel consumption is mass dependent and 6% drop in fuel consumption can be achieved by a 10% mass drop. The automotive companies are facing up to heavy pressure of a commitment postulated reduction of 25% fuel consumption in 15 years [30]. Therefore, the consideration of applying lightweight materials as magnesium alloy in design and manufacturing is a central challenge due to economical and ecological reasons as well as to improve product properties.

2.1.1.1 Low formability of AZ31 at room temperature

Although AZ31 sheet has excellent mechanical properties in comparison with other sheet metals as well as the high ratio between weight and strength, the deformation of AZ31 sheet at room temperature is so difficult. The poor formability of magnesium at room temperature is due to its hexagonal close-packed structure (HCP), which exhibits a lesser number of slip planes in comparison to BCC or FCC crystals [31].

The magnesium alloy products are mainly manufactured by die-casting, and the thixoforming. It showed excellent die-filling characteristic which allows large, thin-walled and complex products. The casting wall can obtain 1-1.5mm of a wall, thinner than wall of plastic or aluminum parts. A new processing technique for magnesium alloys is developed for magnesium alloy products, called thixomoulding injection moulding. It is a combination of substantial processing elements of the magnesium die-casting and the conventional plastics injection moulding [32].

Fig. 2.2 Fracture of cold deep drawing

a) Tearing b) Punch corner fracture c) Flange edge fracture [33]

The conventional sheet forming technologies (e.g. deep drawing, stamping, bending, isothermal gas forming, stretch forming and bulging) for sheet products of magnesium

and its alloys are still limited at room temperature. The fracture occurs suddenly without any obvious necking phenomenon prior to the forming limit [34]. It was reported that the limiting drawing ratio (LDR) for the cold deep drawing of commercial magnesium alloy sheets is considerably low, 1.2-1.4 [31,35]. However, there are efforts to improve formability of magnesium alloy sheet by optimizing the annealing temperature of the sheets (attained LDR=1.75 at 500°C) [33], by reduction of (0002) basal plane texture (LDR increase from 1.2 to 1.4) [36], by high temperature for improving the formability (LDR = 2.1) [37,38], by cooling and heating technique [39].

Although magnesium alloy has the poor formability at room temperature, it exhibited a good formability at an elevated temperature. It is explained that non-basal slip systems become active in addition to basal slip of HCP structure (pyramidal plane <1 1 0 1>) [40]. It is necessary to enhance the forming temperature in order to activate non-basal slip systems, e.g. improving effectively formability of magnesium alloys. Therefore, the forming techniques at the elevated temperature or warm forming become a dominant nowadays for magnesium alloy sheet. The processing temperature of magnesium alloy sheet is usually selected 150 and 500◦C. At a high temperature, however, magnesium alloys are easy to happen the oxidation phenomenon [41].

Other disadvantages of magnesium alloy are high galvanic corrosion and poor creep resistance at a temperature above 125°C. The level of galvanic corrosion is influenced significant by the compatibility of the second metal in contact with the magnesium parts. This problem can be prevented by proper design which usually uses non-conductive or compatible shims or washes. The poor creep strength in components made from magnesium alloys can result in clamping load reduction in bolted joints and poor bearing/housing contact leading to oil leakage and/or increased noise, vibration, and harshness in powertrains. New magnesium alloys improved creep resistance are being developed for powertrain applications at an elevated temperature.

2.1.1.2 SPIF process with magnesium alloy sheet

The ISF technique exhibited the high achievable strain and a flexible manufacturing approach. This process promises the potential applications for lightweight metals

according to increased work hardening and larger design possibilities. Presently, there are the efforts to carry out this process for magnesium AZ31 sheet.

Ambrogio et al. [42] performed the first study on SPIF process with AZ31 sheet. A forming chamber with a heating and insulation system is designed to achieve an effective thermal control on the sheet, avoiding thermal gradients. The research focused on the determination of the formability limits of AZ31 as well as the correlations between formability and process parameters by using a proper design of experiments (DOE). In temperature range of 200-300°C, the experiments were done to evaluate the effects of tool diameter, depth step and forming temperature. The results showed that a dramatic formability enhancement is possible working magnesium in warm conditions. The influences of temperature and tool depth step on formability are quite significant, while the influence of tool diameter is negligible. The maximum formability achieved at 250°C.

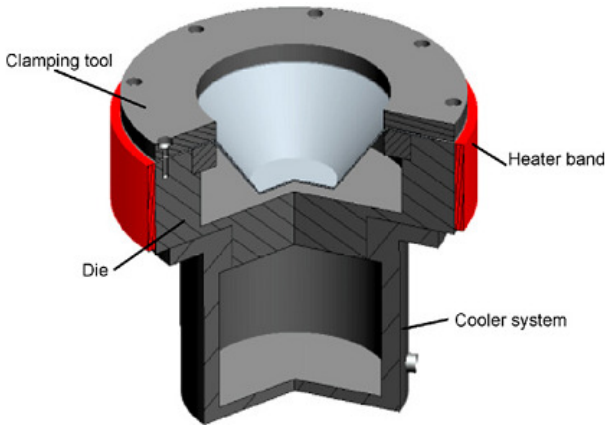

Fig. 2.3 A forming chamber used in Ambrogio's research

Ji et al. [43] investigated the SPIF process for AZ31 sheet with a large range of temperature (100-250°C). The preliminary stretching tests were performed to evaluate the influence of temperature to the forming limit in plane and axisymmetric strain at 20°C, 50°C, 100°C, 150°C, 200°C and 250°C. The results also showed that the formability of AZ31 sheet increases as temperature increases in ISF. The ISF experiments and FEM simulation of this process are then performed in a cone-shaped model with variant

temperatures. The authors suggested a concept of progressive forming which allowed exceeding the forming limit in deformation of a circular cup with a high inclination angle.

Zhang et al. [44] investigated the influences of manufacturing approaches on the mechanical anisotropy of magnesium sheets with ISF. This study focused on the four kinds of magnesium sheet which is fabricated by different methods. The fabricated methods include hot extrusion, slab + hot/cold rolling, strip-casting rolling and cross-rolling. The authors concluded that the casted slab-hot/cold rolled and cross-rolled sheet with the grain size of 5–15μm are not the remarkable anisotropy. The others are influenced significant on formability by anisotropic behavior, but it diminished the effect of anisotropy as increasing the forming temperature. The authors also suggested that cross-rolling sheet is much more suitable for warm SPIF process.

The surface quality of incremental formed parts is mainly depended on tool depth step and the lubricated conditions [2]. The lubrication methods to decrease the friction between forming tool and sheet surface were investigated in negative ISF with magnesium alloy sheet. The authors experimented SPIF process with AZ31 in different lubricating methods such as MoS_2, solid graphite, Nano-$K_2Ti_4O_9$. They are used under lubrication film and a pulsed anodic oxidation in SPIF process with AZ31. The result showed that the sheets treated with a pulsed anodic oxidation process have good surface quality. The Nano- $K_2Ti_4O_9$ whisker lubricating in the mixture with single solid graphite or MoS_2 has the coefficient about 0.07-0.1. It satisfied with the friction and lubrication conditions of IF of the sheet and given the best surface quality.

2.1.2 Aluminum alloys and other metal materials

Jeswiet et al. [2] has a complete summary of researches about the ISF technique until 2004. After that time, researchers have been investigated deeply to mature this process in industrial applications. Therefore, this section will list some obtained results on aspects of formability, numerical analysis, numerical simulation and failure prediction from 2004 up to now.

2.1.2.1 Influences of processing parameters

The processing parameters include depth step, feed-rate, spindle speed, tool diameter, thickness of sheet, type of material… etc. The influences of processing parameters are usually investigated by experimental strategies based on the design of experiment theory (DOE). The studies focused on the influences of those parameters on formability [45], forming force [46], online control [47], and geometric accuracy [48,25]. They included that the process parameters, which have main influence on the formability of SPIF, are feedrate, depth step, material, and tool diameter.

2.1.2.2 Thickness and geometric accuracy

Incremental forming known as a flexible, die-less technology that the sheet is deformed locally in a surface side and opposite side is freely. Thus, thickness and geometric accuracy are an important problem of this technology. The approaches to improve the thickness and geometric accuracy of product postulated to remain flexible and die-less characteristic of SPIF. There are researches for this topic and the results are reported in the recent year. Ambrogio et al. [48] obtained an accuracy of less than 1mm in their experiment to manufacture an ankle support. Leach et al. [20] reported that an accuracy of ±2mm achieved in deforming of asymmetric products. Duflou et al. [49] performed a scaled down model of a solar oven cavity with IF technique and reported the accuracy from -1.8 - 5.4mm.

The main approach to improve the geometric accuracy of product in ISF is the correction of toolpath. It is usually known as a compensative technique used in CNC-toolpath programming. Hirt et al. [50] developed an error compensation system based on using CMM and a geometry correction algorithm. Ambrogio et al. [48] also developed an evaluation and compensation system for geometric error based on DOE approach. Micari [51] suggested the different approaches to improve the geometric accuracy such as back-drawing ISF, flexible support, counter pressure, multipoint tools. However, these approaches compromised the flexibility of the process. Hence, correcting the tool path to compensate for this error to improve geometric accuracy is a better method without compromising the flexibility of the process.

2.1.2.3 Formability and failure prediction

The IF technique exhibited the deformation of the material is much higher than in conventional forming. Several authors reported that the conventional forming limit diagram (FLD) is not able to predict the failure in formed parts [2,45]. Instead, the fracture forming limit diagram (FFLD) is suggested for the failure prediction in this process. Several authors also published papers related to the development of FFLD based on an experimental investigation of the fracture occurring during the forming of various shapes. Each shape would produce a set of fracture points from which an empirical FFLD was derived [3,24,23,21].

There were authors suggested positive mechanisms to explain high formability in SPIF process. Eyckens et al. [52] suggested that this high formability was due to the non-monotonic serrated strain paths which the material is subjected during the SPIF process. The serrated strain path was constructed by taking the maximum principal strain as a function of the minimum principal strain at a solid brick element located in the region of the cone wall on the top layer. The evolution of thestrain path has the serrate style because the forming tool which has a small radius and a limited influence on its vicinity will approach and move away from the element in several times. Therefore, it triggered off the progressive increase of the level of plastic deformation.

Emmens et al. [53,54], Silva et al. [55], Martin et al. [56], Allwood et al. [57,58] have the possible explanation on deformation mechanism of SPIF as through-thickness shear, bending-under-tension (BUT), stress triaxiality… etc. The detail of explanations is presented in section 4.2.

2.1.2.4 Numerical analysis

Several authors have tried to develop analytical computations to predict various quantities related to the ISF process. Some of these predictions are summarized as following:

Iseki [59,60] developed an approximate deformation analysis of the bulging height for strain prediction in SPIF and multistage SPIF process. The author was used plane-strain deformation model and a FLD to propose the forming load and the strain distributions of

the shell. Then, FEM model applied this approximate deformation analysis was used for the calculation of the bulging height and the distributions of the strain and the stress. It also can predict the thickness profile in SPIF process.

Pohlak [61] investigate numerical analysis for forming force based on a simplified theoretical model to estimate the force components presented by Iseki. The author also took into account of effects on anisotropic behavior of material. The magnitudes of the forming load and its components, and their ratio, corresponding to theoretical and experimental models are found to be close.

Duflou et al. [49] investigated a relationship between forming force and the main processing parameters (depth step, tool diameter, wall angle, sheet thickness) by using Design of Experiment analysis technique (DOE). From this DOE, a regression equation of forming force and the processing parameters is extracted to predict the forming force for other complex shapes in SPIF process. Aerens et al. [62] continued this work and extended for five material types. They obtained a potential regression model which allowed computing the axial and tangential components of the forming force in a steady state with a good accuracy. In additional, they performed FEM simulation to evaluate again the analysis.

Filice et al. [47] developed an innovative monitoring and control approach to control in an online state of the most processing parameters during SPIF operation. To do so, the authors investigated a set of preliminary experiments in order to evaluate the effect of single processing parameters on the tangential force trend. Then, a statistical analysis carried out to obtain a relationship among the process parameters so-called “spy variable”. This relationship is very important to be able to perform the control strategies that permit to predict the force gradient.

Silva et al. [55] and Martins et al [56] used a membrane analysis to develop a theoretical model SPIF. The stress and strain state is divided into three types with respect to the three basic modes of deformation: i) flat surfaces under plane strain stretching conditions; ii) rotational symmetric surfaces under plane strain stretching conditions; iii)

corners under equal bi-axial stretching conditions. From this analysis, the authors can explain high formability, stress - strain state, mechanical fracture, hydrostatic stress... etc.

2.1.2.5 FEM Simulation for SPIF process

FEM simulation of SPIF process is a very complicate task in comparison with the conventional process due to large and complex model, and long motion of forming tool. Several nonlinearities (e.g. material, model, contact conditions) are involved in this simulation which triggered off a huge computational time consuming. It is difficult to optimize the simulation of SPIF process with a full model. Both implicit and explicit integration scheme of FEM simulation have been investigated for SPIF process. A biggest disadvantage of simulation of SPIF process is the computational time consuming. The researchers have been tried to find many solutions to solve this problem. The common ways to speed up simulation of SPIF process are time scaling, mass scaling in an explicit integration scheme. Most of the researchers claimed that the explicit solver is very faster than the implicit one. However, the accuracy of simulated results depended on aspects of simulating purpose and modeling properties. This section summarizes some studies about FEM simulation on ABAQUS and LS-Dyna which are used to perform FEM simulation for SPIF process.

IN ABAQUS

Bambach et al. [3] used both implicit and explicit solver to simulation SPIF process. They make a comparison among several element types available in the ABAQUS using the same cone-shaped model. The authors concluded that the computation time of SPIF simulation using an implicit solver is increased hugely by the nonlinear problems such as continuously alternating contact conditions. In their reports, the FEM simulation is simplified to save calculation time by using non-classic tool-path, large depth step. The tool-path does not follow final geometric product, it is started from the bottom of cone. The depth step is 5mm, too larger than the suggestion of a range from 0.1 to 1mm, which reduced large axial tool force and low surface quality.

Henrard et al. [63] performed a comparison between ABAQUS/Explicit and homemade code LAGAMINE for the influence of some crucial computational parameters on the simulation. The simulation only performed on a partial cone-shaped model with 50^0-degree in wall angle to evaluate the effects of mesh size, tool force on the geometric accuracy. The response of the process is given in terms of final geometry (which depends on the spring-back), strain history and distribution during the deformation, as well as reaction forces.

Robert et al. [64] used ABAQUS/Explicit for FEM simulation of SPIF process. The authors improved the movement of forming tool by using smooth path to avoid the dynamic effects. Therefore, they kept the dynamic energy under 10% of the total energy. The computational time is decreased by using a time-scaling method to speed the tool movement up to 25mm/s instead of mass scaling as other authors.

Eyckens et al. [65] used ABAQUS/Standard (implicit solver) for FEM simulation of SPIF process. The authors used a FE sub-modeling technique to improve the modeling of the plastic deformation zone in the SPIF process. The result showed that the distribution of the contact pressure between the sheet and forming tool is different. The comparison of the distribution of the contact pressure under different working conditions revealed that the contact could generally be split up into two parts. In their studies, 40° pie of a cone model is used for simulation to save the computational time consuming.

IN LS-DYNA

Yamashita [66] considered the travelling pattern of forming tool by a dynamic explicit finite element code DYNA3D. The simulation performed on a quadrangular pyramid with two variations in its height. Four kinds of the toolpath are evaluated on the effects of the deformation and the force acting on the traveling tool. The calculated deformation shapes are compared among tool paths and the distribution of thickness strain is also discussed. Effect of the density of the sheet material and the traveling speed of the forming tool are pre-examined to determine the computational condition for the practical applications in DYNA3D. The computational condition is optimized for reducing

the computational time without an inertial effect of the material on deformation behavior.

Qin et al. [67] used an explicit solver to simulate the forming of a pyramid part (100x150mm) with SPIF. They simulated with very large depth steps (2mm and 4mm) with pyramid height in 20mm and 450 slopes to analyze the influence of mass and time scaling on simulated results. To compare the mass scaling factors used in FEM simulation, they used three different factors of the mass scaling. The results showed that the computation time with mass scaling was reduced significantly, the deformation curves only was little different. On the case used a time-scaling factor up to 5000, only a small deviation of approximately 0.2mm was observed in the prediction of the geometry. The authors suggested that combination of mass scaling and time scaling method reduced significantly the computational time of FEM simulation for SPIF process.

Ambrogio et al. [25] also used an explicit solver with fully integrated shell elements to study the influence of some important parameters on the geometric accuracy with the time-scaling method to speed up the simulations. The tool velocity is increased by multiplying the feed-rate by a factor of 40 and used a velocity of 40m/s. They verified that the ratio of the kinetic energy and the total energy was always fewer than 10%. The simulated result has a good precision with the experimental ones.

Dejardin et al. [68] also used an explicit strategy with the reduced integration shell elements to form a cone model. The authors used an adaptive mesh refinement technique to improve the quality of meshing during the simulation. In particular, they performed an analysis of spring-back in SPIF process after the forming stage. The spring-back phenomenon is simulated by using an implicit solver. The authors concluded that implicit solver was more accurate than an explicit one.

Skjoedt et al. [28] also used an explicit solver to simulate SPIF process with fully integrated shell elements. The influence of forming direction (upwards or downwards) is investigated for the second stage comparing explicit FE analysis with experiments. They used a time-scaling factor between 1000 and 1500 times without additional mass scaling

to be able to reduce significantly the computation time. The authors reported that there was a good agreement between simulated and measured results in the geometric accuracy and the distribution of thickness.

2.1.3 Polymer and composite

The thermoplastic materials have been investigated in first time with SPIF process at room temperature in the current thesis. The preliminary results showed that ISF technology is completely able to apply on thermoplastic materials in room temperature promising a new approach to manufacture polymer sheet products with an unlimited depth. An experimental investigation used DOE technique was performed to evaluate the influence of processing parameters on the formability of polypropylene (PP). Sample models were also deformed to exhibit the capability of ISF for polymer materials. The results in detail will be presented in this thesis.

Up to the current time, other researchers have been investigated to the big amount of commonly industrial polymers with ISF technology. This section summarizes the obtained results of other researchers.

Franzen et al. [69] performed the experiments on polyvinylchloride (PVC) with ISF process. A cone-shaped part is used to evaluate the formability of PVC. The authors found three types of mechanical failure occurred in deformation process, which were similar to the failures found in the current thesis. The values of the maximum wall angle obtained in deformation of PVC vary between 67^0 and 72^0. The authors have efforts to overcome "'stress whitening" phenomenon which changed the color of deformed part. However, the obtained result seems to be unexpected.

Martins et al. [70] experimented on five polymers (PVC, PA, POM, PC, and PE) to focus on the determination of process limits and evaluation of product properties. The formability of SPIF with the polymer sheets was evaluated by means of bi-axial and tensile tests. Fracture forming limit diagram of PVC is established from those experiments. To evaluate the formability of polymers, a DOE planning is design with four parameters (type of polymer material, the thickness of the sheet, the tool radius, and

the initial drawing angle) in a full factorial approach. The aspects of material, variation of the color, and accuracy of deformed part were also mentioned in this research.

Jackson et al. [71] performed ISF on sandwich panels with three layers of metal-polymer-metal. To evaluate mechanical feasibility of ISF process with sandwich panels, four sandwich panels were investigated. They represented for a large range of properties of formable sandwich panels which were available in the industrial applications. The preliminary experiments used a simple straight path (100m) and short spiral path (step of 0.1mm) for considering the reduction in thickness, mechanical failures, and surface quality degradation after the deformation. The authors concluded that ISF process could apply well on sandwich panels with structure of Mild steel-Polypropylene-Mild steel and Aluminum- Polypropylene- Aluminum due to having high ductile and largely incompressible core and faceplates. The aspects of the through-thickness strains and the sine law described sheet thinning with wall angle are similar to sheet metal. The vertical tool force showed similar variations with tool radius and vertical pitch.

2.2 Novelties compared to the state of the art

Incremental forming is considered as a novel forming technology for the sheet materials in recent years. Many researchers and scientists have been concentrated on this topic to bring the feasibility of this technology to industrial applications. However, many aspects on both theoretical analysis and practical experiment still need to be investigated more. Those are also one of the main reasons to perform this study with ISF technology. In the current thesis, this technology is investigated on two groups of important materials in industrial applications such as lightweight sheet metals (magnesium alloy AZ31 and aluminum alloy in series 1010) and thermoplastic materials. The most important novelties in comparison to the state of the art are as following.

2.2.1 In sheet metals

This study is performed in scientific order from preliminary analysis by using the DOE technique, evaluation of material by experimental testing, FEM simulation to actual experiment. The results are compared between FEM simulation and actual experiment

to evaluate exactly the influences of processing parameters on the outputs of SPIF process.

SPIF process is applied for sheet metals at the elevated temperature to enhance the formability. DOE planning with three processing parameter (temperature, feedrate, depth step) is designed to investigate the formability at the elevated temperature.

A new heating system is designed which provided a uniform temperature in sheet metal during the deformation process. This system is based on Joule heating effect which can obtain a target temperature in very short time to ovoid an oxidizing phenomenon.

Fully coupled thermal analysis is applied for FEM simulation to predict the mechanical fracture during SPIF process. An explicit integration scheme is performed in 3D simulation with fully cone-shaped part instead of a piece of part as previous researches.

The approaches to speed up the computational time of FEM simulation such as time scale and mass scale are discussed in the case that the simulated material has a high sensitivity of strain rate and temperature. Adaptive meshing technology is also used to improve the accuracy of simulated results in this simulation.

The damage criterion, called CrachFEM, is implemented into ABAQUS software to predict the mechanical failures occurring on the deformed part during the deformation with SPIF process. This criterion is proposed specially to predict the mechanical failures which were caused by one or combination of the three mechanisms: i) void nucleation and coalescence; ii) shear band formation; iii) necking instability. Deeply, there is no definite answer as to which one causes the failures during SPIF process in the literature. Therefore, CrachFEM covered three mechanisms is a sole solution to predict the failures for this process.

2.2.2 In polymers

The first study is investigated to find an applicability of ISF technology for polymeric materials. The preliminary experiments are performed on thermoplastic materials at room temperature. It showed that ISF is a promising approach to manufacture polymer

sheet products with unlimited depth which can replace conventional technology in low and medium production batch.

To evaluate preliminarily the influence of processing parameters on the formability of ISF with polymeric materials, an experimental investigation is performed by using DOE technique. Four parameters such as the feedrate, spindle speed, depth step, and tool diameter are considered in this DOE planning.

A viscoplasticity constitutive model based on overstress theory is developed to implement into FEM simulation. The simulated result is evaluated on aspects of the accuracy of thickness and geometry.

Chapter 3

Experiments

3.1 Experimental equipment for metals and polymers

3.1.1 CAD and CAPP system

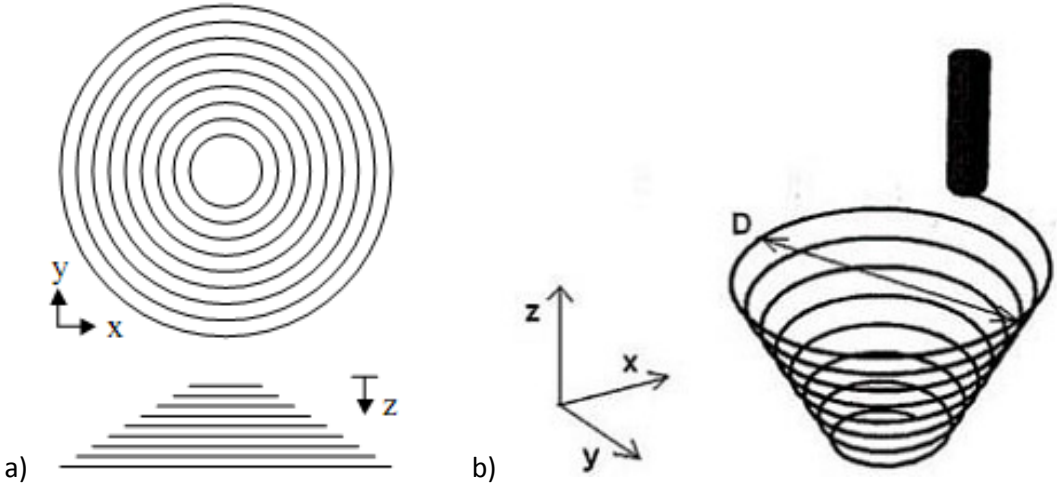

Fig. 3.1 a) Spiral tool-path, b) Helical tool-path

The exact CAD model of final product is built in normal CAD/CAM system such as CATIA, Pro Engineer. This model is used as an input object for CAPP system to generate toolpath. In normal commercial CAD/CAM system, there are two approaches for generating a tool-path that can be utilized for SIPF process, known as profile milling and contour milling. They are programmed to generate the spiral toolpath as showed on Fig. 3.1a. The characterization of this toolpath is only a continuous feedrate in X- and Y-direction of a deformed sheet plane. The feedrate in the Z-direction is done in the same angular position in the XY plane along a line down the side of the sheet. This causes the problems: i) a scarring occurs at the first contacting points between forming tool and sheet when the tool is moved down; ii) a peak occurs in the axial force as the tool steps

down. To eliminate these problems, the spiral toolpath should be converted into helical toolpath as Fig. 3.1b. The helical toolpath gives a continuous feed in all three directions [72].

3.1.2 Forming Tools

A forming tool for SPIF process with polymeric materials is a solid hemisphere head that made from hard steel material (BOHLER W300). This material is usually used to manufacture the press die and cutting tools. After manufacturing, the tool was treated temperature at a hemisphere top to increase hardness and wear resistant level (hardness about 52-56HRC) (see Fig. 3.2).

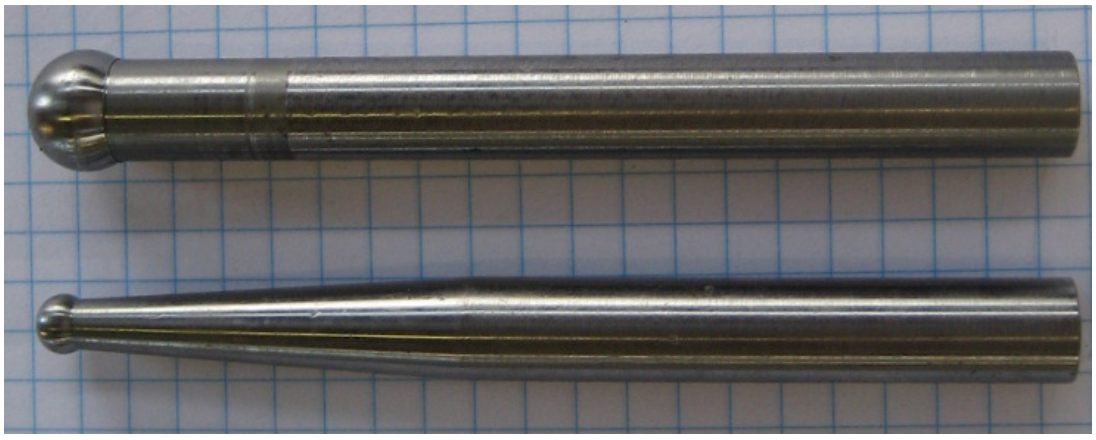

Fig. 3.2 Forming tools for SPIF process with polymeric materials

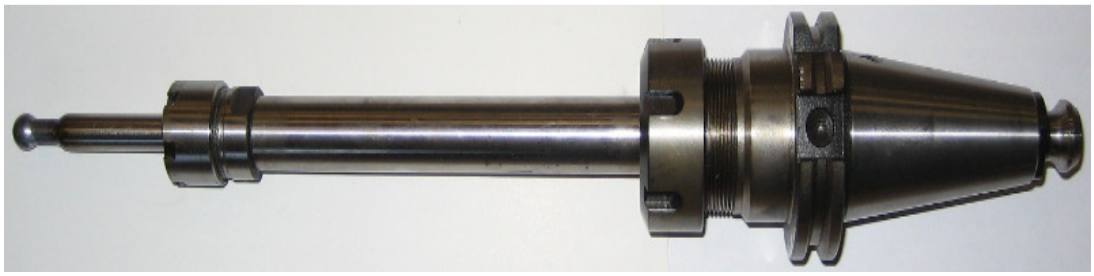

Fig. 3.3 Forming tools for SPIF process with metal materials

The diameter of a ball-head is selected in the large range of 5mm and 12mm. The previous researches pointed out that smaller diameter contributed into increasing formability of SPIF process [2]. However, the stability and stiffness of a tool does not allow too small diameter. It is suggested that the tool diameter is used in a wide range

from small diameters (about 6mm) to the large tool diameter (about 100mm) for manufacturing the large parts. The most commonly used diameters are 6mm and 12.5mm [2,3,5,73]. In this study, two different sizes of the forming tool were used in SPIF process.

A tool for SPIF process with metal materials is designed specially to avoid a magnetic effect from heating system to the spindle of CNC machine. It is made from tool steel (Tool Steel BOHLER K100) to assure a good hardness and wear resistance (see Fig. 3.3).

3.1.3 Forming Machines

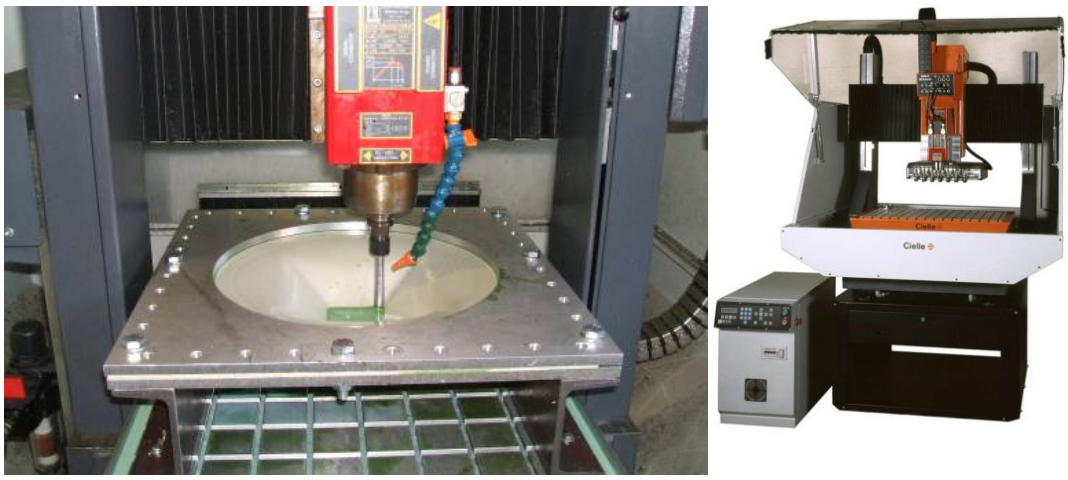

Fig. 3.4 CIELLE CNC machine using for SPIF process with polymeric materials

Fig. 3.5 MAZAK VTC-300C CNC machine using for SPIF process with metal sheet

SPIF process is performed by using general three-axis CNC machine. Nowadays, there are many types of three-axis CNC machine and some suggestions for selection of

machine are noted in [2]. A main disadvantage of common CNC machines is that they were designed for general-purpose milling, surface milling. The capacity of axial loading resistant in some machines is low, thus, it is limited in applications of SPIF process. The experiments of SPIF process in the current thesis were performed with two different CNC machines to deform two different groups of material. For polymeric sheet materials, CIELLE three-axis CNC machine is used as Fig. 3.4. MAZAK VTC-300C three-axis CNC machine is used for the experiments of metal sheet materials (see Fig. 3.5).

3.1.4 Fixture and jig system

a) 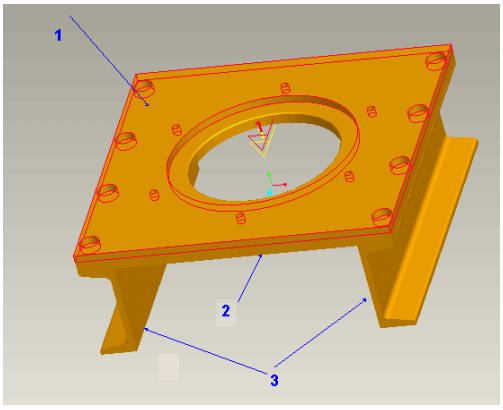

b) 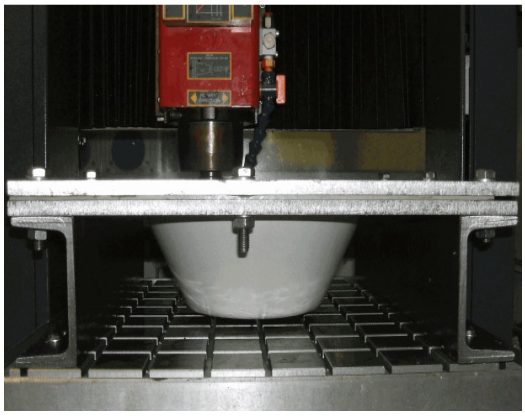

Fig. 3.6 Fixture and jig system for SPIF process with polymers

The fixture and jig used for SPIF process with polymeric materials is showed in Fig. 3.6a. It includes three parts: 1. upper plate, 2. backing plate, 3. two U-shape supports. A backing plate is used to decrease spring-back problems in deforming process. The spring-back problem is also surmounted by developing the compensative algorithms utilized in CNC programming technology. All components were connected together by bolts and are clamped firmly on the CNC machine table as shown in Fig. 3.6b.

The fixture and jig used for all experiments of sheet metal is designed specially to be able to operate at the elevated temperature. It is combined with heating and cooling system in special design for a purpose of electrical isolation and operating under high temperature. Two plates are made from fiber composite to isolate electricity and high temperature resistant. The lower plate is inserted a steel ring to serve as baking plate. The two plates are overlapped on the two copper electrodes that connected tightly

metal sheet. The whole system is placed on thick fiber composite plate to isolate completely the electricity with machine table. This plate is clamped firmly on the machine table by six bolts as showed on Fig. 3.7.

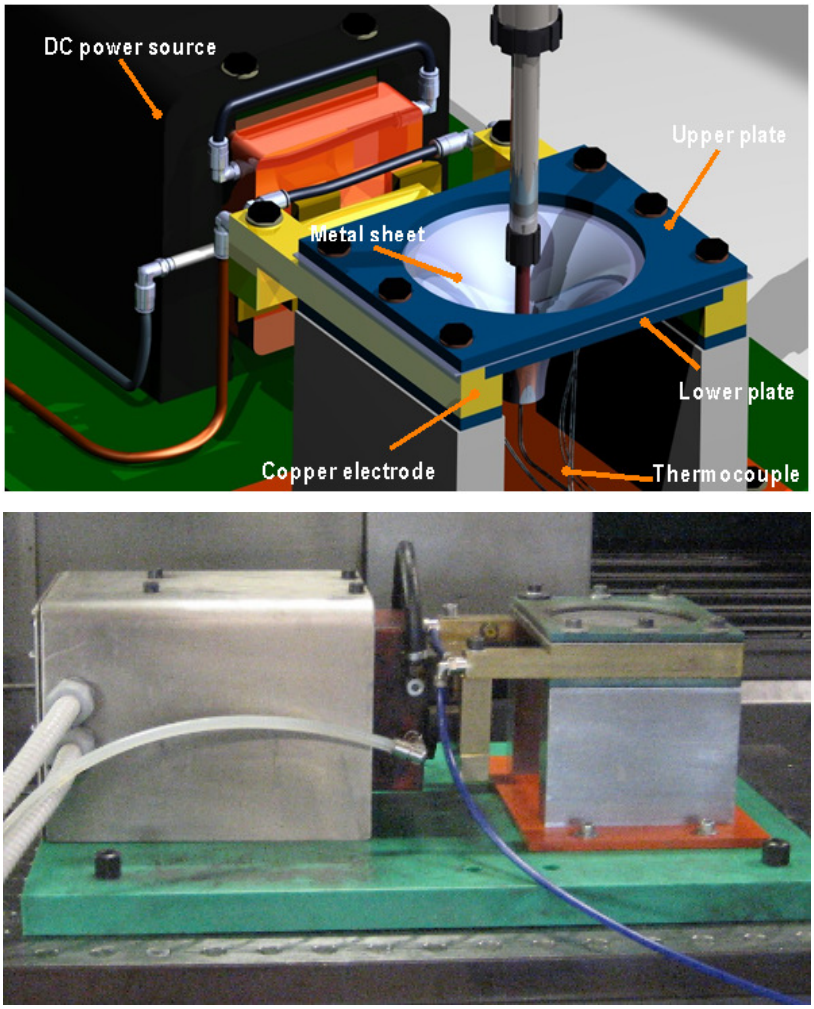

Fig. 3.7 Fixture and jig system for SPIF process with metal materials

3.1.5 Lubrication

The forming tool has the end-hemispherical shape, which is pressed into the metal sheet to cause the locally plastic deformation. The heat due to friction and wear of tool increases highly during the tool movement. Tool wearing and local heating influenced on the surface quality and the geometric accuracy. In order to decrease those effects, different lubrications need to be used for different types of deforming material. Zhang [74] have been investigated the suitable lubrications and lubricating methods. In this

study, solid graphite powder mixed special grease MoS_2 (for elevated temperature) is used for SPIF with metal materials.

For polymeric materials, the friction between the surface of sheet and the tool is relative high. The local heating can exceed the softening temperature of the thermoplastic polymer. In this case, the formability of SPIF process increases but the deformation of sheet is not stable. In order to avoid this effect, a cool water-miscible metalworking fluid should be used in the percentage of 25% (Blasocut™ 2000).

Additionally, to keep a minimal friction heat, the forming tool must roll over the surface of the workpiece when it is moving. This requires that the distance traveled along the workpiece be equal to the average circumference of the tool in contact with the material multiplied by the spindle speed. The following equation describes mathematically this problem. Spindle speed and feed rate are presented by ω and v respectively; the hemispherical tool radius and wall angle are r and α, respectively [73].

$$\omega = \frac{v}{\pi r \sqrt{\frac{1}{2}(1 - \cos 2\alpha)}} \tag{3.1}$$

3.1.6 Heating and cooling system

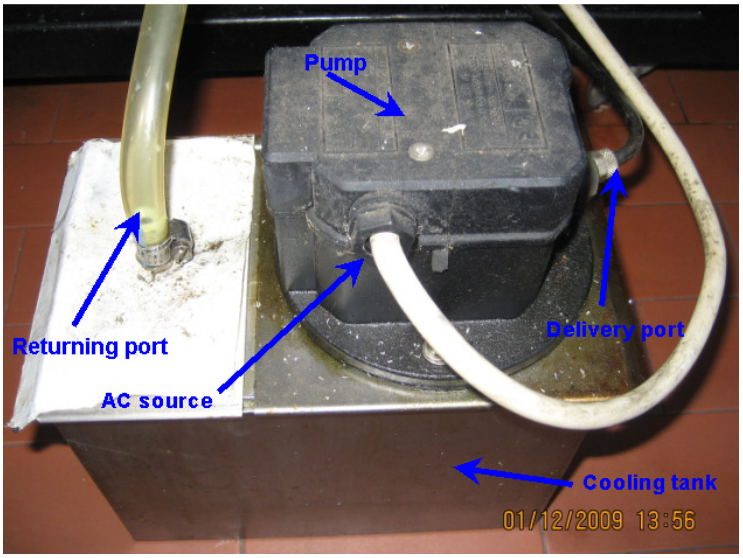

Fig. 3.8 Cooling system for SPIF process with polymeric sheet

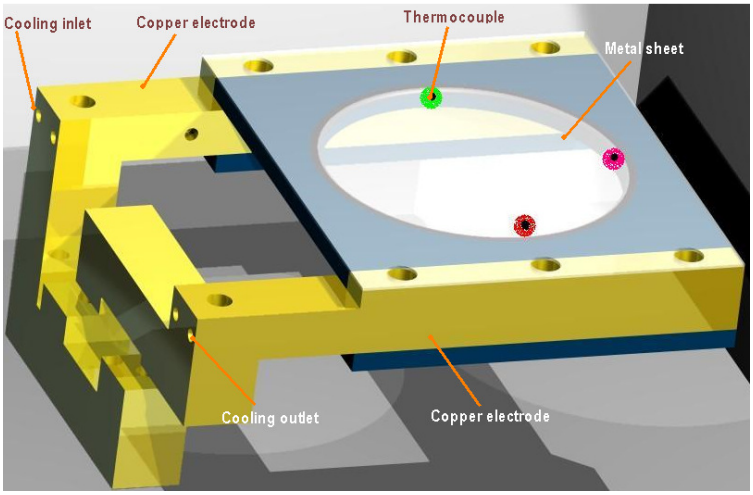

Fig. 3.9 Heating and cooling system for SPIF with metal sheet

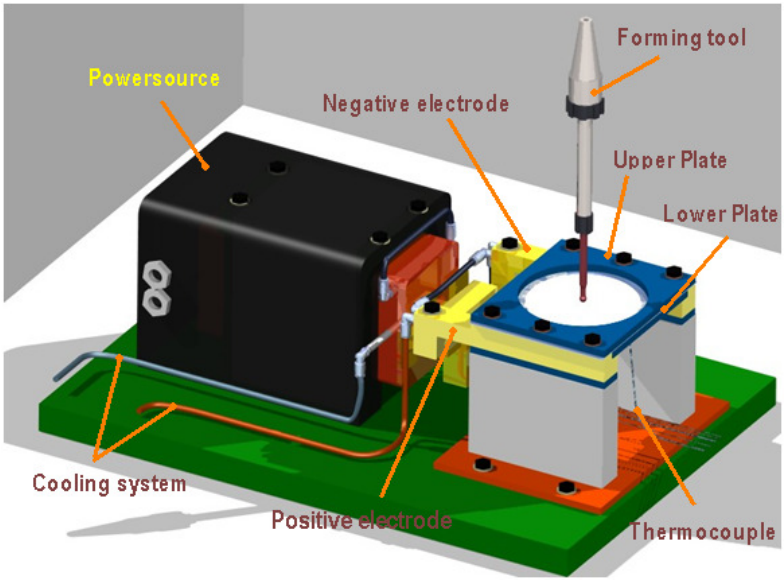

Fig. 3.10 Assembly of components for SPIF process with metal materials

For SPIF process with polymer materials, a cooling system is designed to keep the stable temperature of sheet at room temperature. A mixed lubrication-water is contained in a small cooling tank. A pump system supplies periodically this lubrication water during forming process with SPIF (Fig. 3.8). The polymer sheet and forming tool is always submerged in the lubrication water.

The heating system is designed for deforming the metal sheet with SPIF based on Joule heating effect. It included two electrodes that are provided by DC power source (1.25

volt, 15000 Amperes). They are cooled by the tube system inside of the electrodes. The forming temperature is adjusted by a feedback controller through four K-type thermocouples that welded firmly on a sheet. The heating system and whole system of SPIF are presented on Fig. 3.9 and Fig. 3.10, respectively.

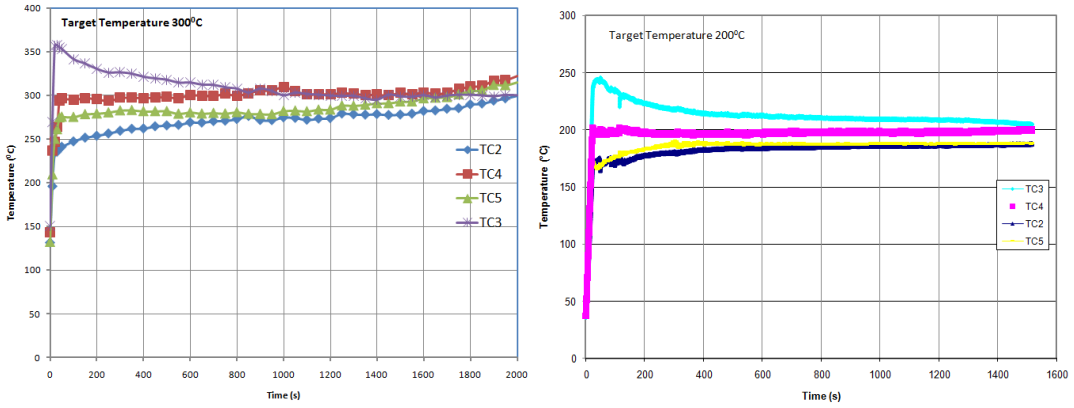

Fig. 3.11 History of temperature in forming process with target of 200 and 300°C

3.2 Design of Experiment (DOE)

3.2.1 Aluminum alloy and Magnesium Alloys

Experimental parameters	Level of Values	
	Low level	High level
Temperature (**°C**)	200	300
Depth step(mm)	0.2	1
Feedrate ($mm.s^{-1}$)	1000	6000

Table 3.1 The levels of factors for experiments with metal

To determine influences of the processing parameters to formability in SPIF process with magnesium alloy sheet AZ31 and aluminum alloy of 1010 series at an elevated temperature, a proper DOE is planned. The process parameters are chosen to be based on previous studies [2,45,75]. Three important parameters are temperature of sheet (T), tool depth step (Z), and federate (F) which have a significant influence on the formability of SPIF with metal sheet. The maximum wall angle obtained in SPIF process is considered as responding parameter of DOE. Two level factorial designs 2^k with two replicates was made in this experimental campaign to assure the high probability of experimented

results. The total number of experiment is 16 runs. The level value of experimental parameters presented in Table 3.1.

3.2.2 Polymer materials

Experimental parameters	Low level	High level
Step size (mm)	0.2	1
Tool size (mm)	6	12
Feed rate (mm/min)	1000	3000
Spindle speed (rpm)	200	700

Table 3.2 The levels of factors for experiments with polymers

This work is a preliminary investigation of SPIF process applied to thermoplastic materials. The most efficient way to investigate the influence of some variables on measurable outputs is by planning a DOE. The objective of this experimental strategy is to determine which forming parameters influence the formability of thermoplastic sheet and to understand the interacting effects.

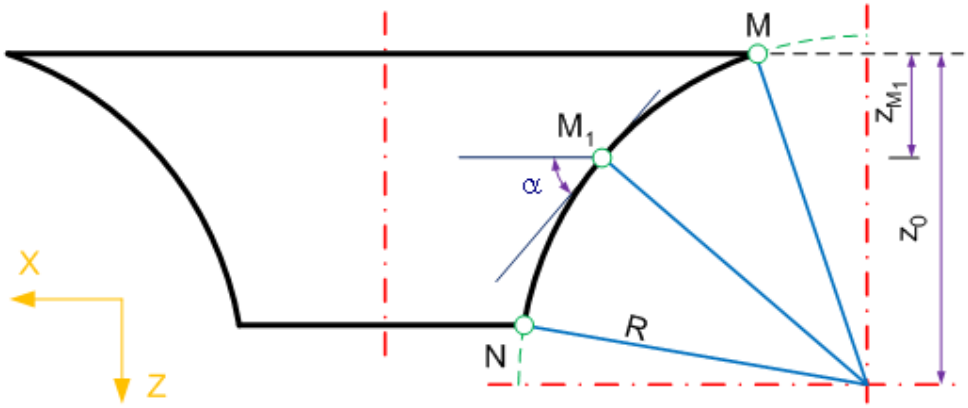

Fig. 3.12 Geometric illustration of part profile

Basing on the previous experimental fundament of the SPIF process with sheet metals, the main parameters mainly affected on this process is chosen for investigation of DOE. The four forming parameters (factors) were considered for the experiments with thermoplastic sheets: (i) step size; (ii) tool size; (iii) feed rate; (iv) spindle speed. Low level and high level of factors are shown on Table 3.2. The wall angle of deformed part

obtained period to any mechanical failure is defined as the maximum index of formability. It is also considered as the response of the DOE planning. A 24-1 factorial design of experiment was prepared in twenty-four runs, with three replications for each experiment (see Table 3.2).

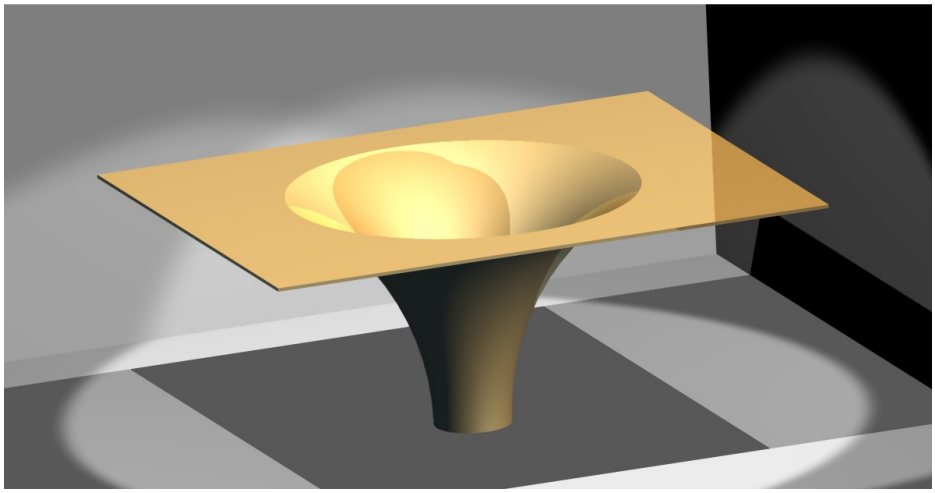

Fig. 3.13 CAD model for DOE of SPIF process with metal materials

The 2^{k-1}level fractional factorial design presents clear advantages in terms of reduction of costs, time, and resources needed to make the runs. The proposed plan did not consider effects of other parameters such as: type of material, thickness of polymer sheets, shape and local heating.

A cone-shaped part with a circular generatrix was selected to test the formability in the experiments. The part geometry was designed in order to enable investigating all the wall angles from zero to 90 degrees. Since the thickness of the part changes according to the sine law and the slope of part increases with its depth, the analyzed region is limited to an angle minor than 90 degrees (see Fig. 3.12).

Fig. 3.12 shows the generatrix of a part studied during in the experiments. The analyzed area is outlined by the arc of *MN*. The wall angle α of a generic point on the generatrix, defined by the tangent to the profile, can be calculated as follows:

$$\alpha = \arccos\left(\frac{x}{R}\right) \tag{3.2}$$

where the vertical coordinate given by:

$$x = z_0 - z_{M_1} \tag{3.3}$$

The value of z_0 is the maximum height of the cone and z_{M1} the vertical coordinate of the tool when the failure appears. This value is recorded from the CNC-controller interface and is verified by using a Coordinate Measuring Machine (CMM).

3.3 SPIF with metal materials at elevated temperatures

The current thesis investigated the formability of both magnesium alloy (AZ31) and aluminum alloy sheet (in series of 1010) with SPIF process at an elevated temperature. The range of forming temperature is listed on Table 3.2.

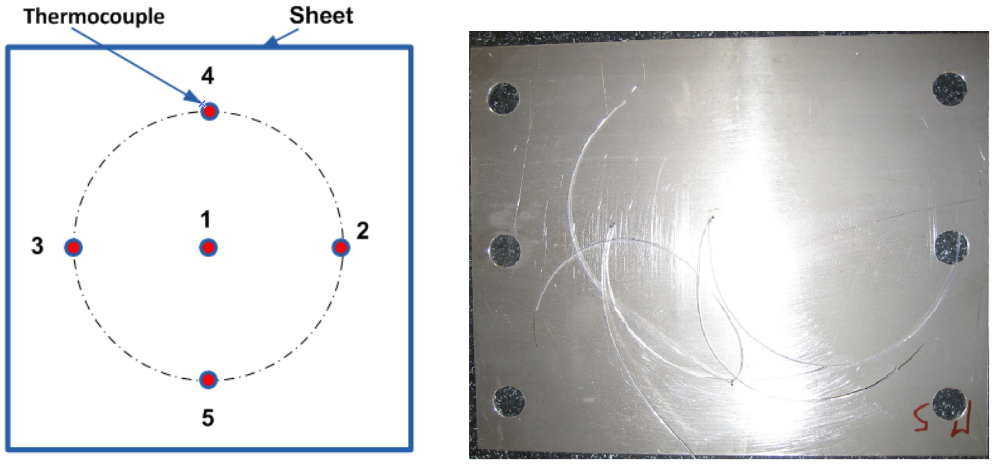

Fig. 3.14 Position of thermocouples on sheet

For aluminum alloy sheet, the previous researches investigated on series 1050, 3003, 5754, 5182, 6111, 6114… etc [2]. They deformed easily at room temperature with SPIF process. This study investigated the experiments of aluminum alloy sheet with SPIF at an elevated temperature to find a higher formability of SPIF.

For magnesium alloy sheet, the deformation of magnesium AZ31 at room temperature is very difficult. It exhibited low formability at room temperature. Therefore, the previous researches investigated the formability of magnesium with conventional forming process (e.g. deep drawing, stamping, stretching… etc) in the large range of processing temperature (20-500°C). Many forming limiting diagram is extracted from these experimental studies. It is evident that the forming limit increases drastically above

150^{o}C [76,42,74]. The deformation mechanics of the SPIF process are very complex. The previous studies provided some information about several aspects, but many problems were left unsolved. In this study, the experimental study to determine the influence of most important processing parameters to quality indicators was performed.

The processing temperature of magnesium AZ31 sheet with SPIF process is one of the important processing parameters. It is necessary to focus on the design of heating system to satisfy the temperature stability during the forming. The heating system is designed which is based on Joule effect as presented in Fig. 3.9.

For both magnesium alloy and aluminum alloy sheet, a CAD model used in the experiment is a cone-shaped model with curved generatrix. The profile and 3D illustration are showed on Fig. 3.12 and Fig. 3.13.

The metal sheets are cut in the rectangle of 200x200mm. The forming zone was a circle with the diameter of 150mm. They are welded with four thermocouples in a special position to monitor the temperature of sheet during a deformation process (see Fig. 3.14). The control of temperature sheet is governed by a feedback controller with four thermocouples placed at different radii on the sheet. The interface of the feedback controller is presented on Fig. 3.15.

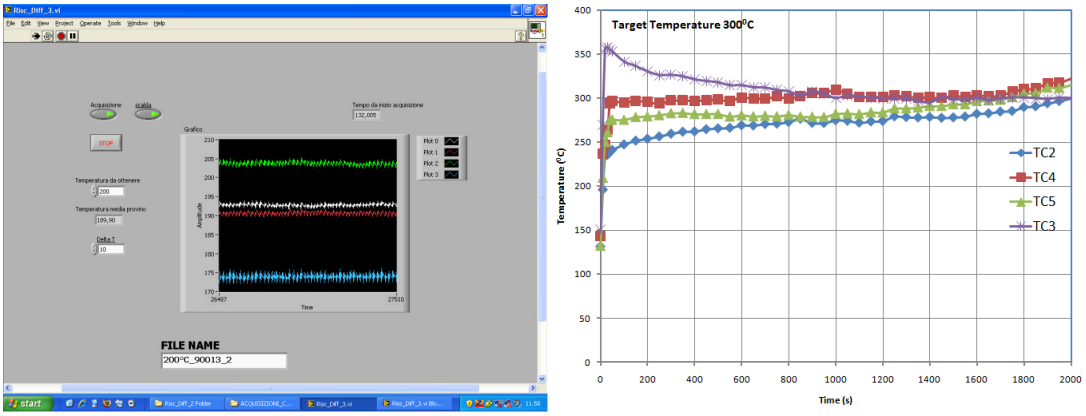

Fig. 3.15 Feedback controller for heating system

The SPIF with aluminum sheet at an elevated temperature exhibited two typical failures as Fig. 3.16. The first type of failure is similar to observation of previous researches called as “zigzag” failure propagation path. Silva et al. [55] concluded that the ‘zigzag’ failure propagation path was triggered by meridional tensile stresses but its morphology,

bouncing around the circumferential direction, was probably caused by friction towards the rotating forming tool. The second type of failure is an opening-V fracture which propagating mechanism is probably similar to the first failure type. It cannot propagate the next segment of the zigzag path because of high formability of aluminum sheet at an elevated temperature. Particularly, the step of "zigzag" failure propagation path of SPIF process with elevated temperature is larger that one of the room temperature. This is probably due to high ductile of aluminum sheet at an elevated temperature.

The observation of trace of material points on the formed cone with aluminum at an elevated temperature revealed that the plastic deformation flow of the material has bell-shapes propagated in rolling direction. The curvature of bell shape became narrower following the height of the cone obtained. The center of cracks occurred at a top of bell shape which has the narrowest curvature. The center of cracks is an axis-symmetry as presented on Fig. 3.18. It seems the bell-shape propagation path of material flow is trigged off tensile stress in an axial direction of forming tool. The material is always stretched in the deformation process.

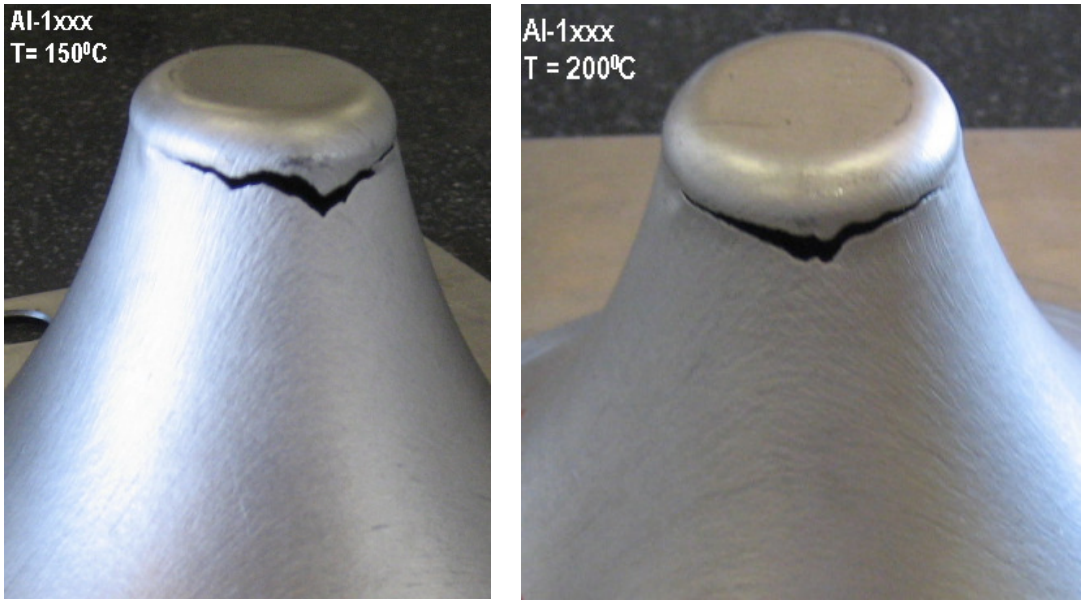

Fig. 3.16 Typical failure of SPIF process with Aluminum sheet at elevated temperature

For magnesium alloy sheet, it has low formability at room temperature. The mechanical fracture occurred after few rounds of toolpath with two types of fracture as presented

in Fig. 3.19. However, the AZ31 exhibited better formability at an elevated temperature. There are two types of failure in SPIF process at the elevated temperature. The first type is the fracture with the zigzag propagation path similar to one of the aluminum sheets. The second type appears under opercular shape before a crack occurs. The material was separated in layers of outer surface, propagates to an inner surface in incline direction of 45 degrees. The crack formed when the opercular layers developed and separated material into two surfaces (see Fig. 3.20).

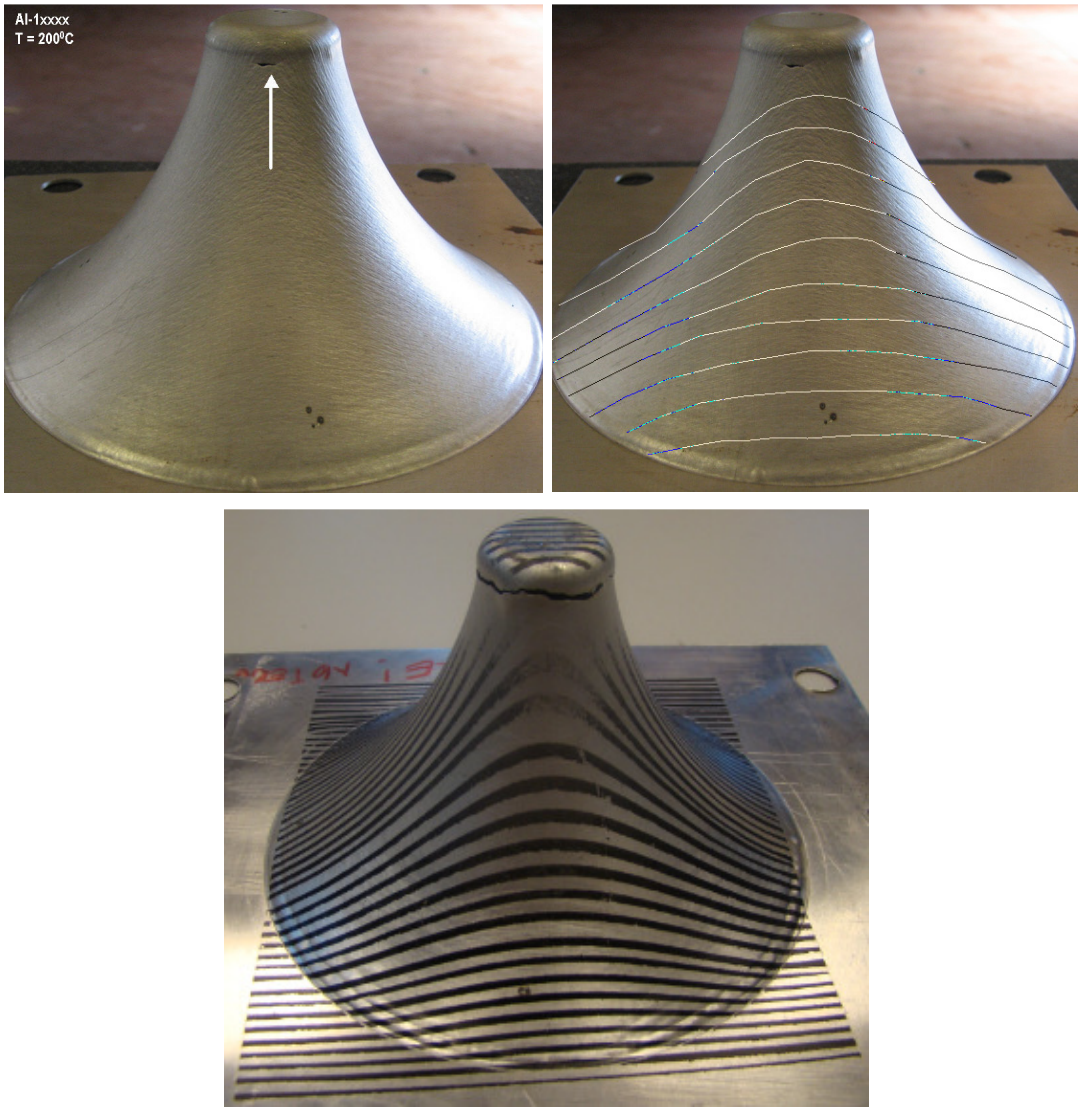

Fig. 3.17 The bell-shape propagation path of material flow

Fig. 3.18 Axis-symmetry of cracks in SPIF with aluminum at elevated temperature

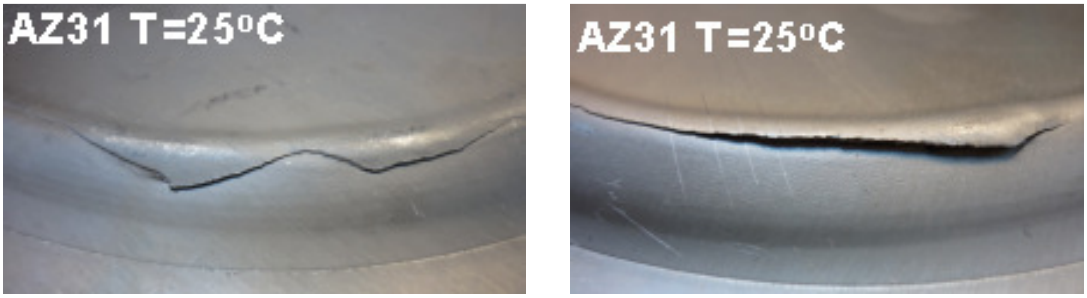

Fig. 3.19 Mechanical fractures in SPIF with AZ31 at room temperature

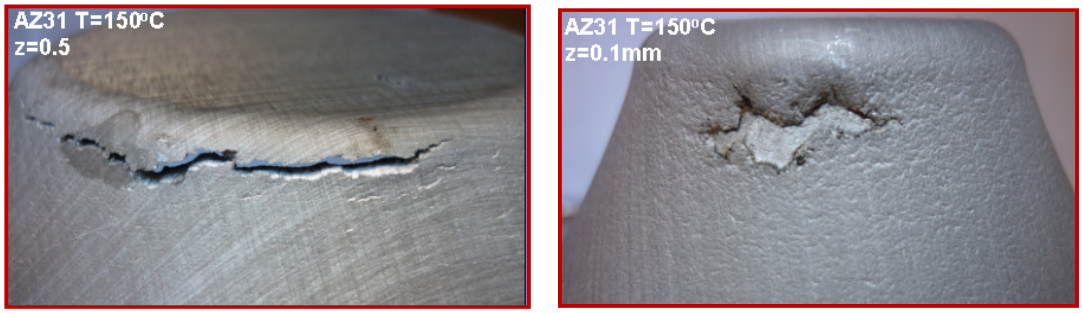

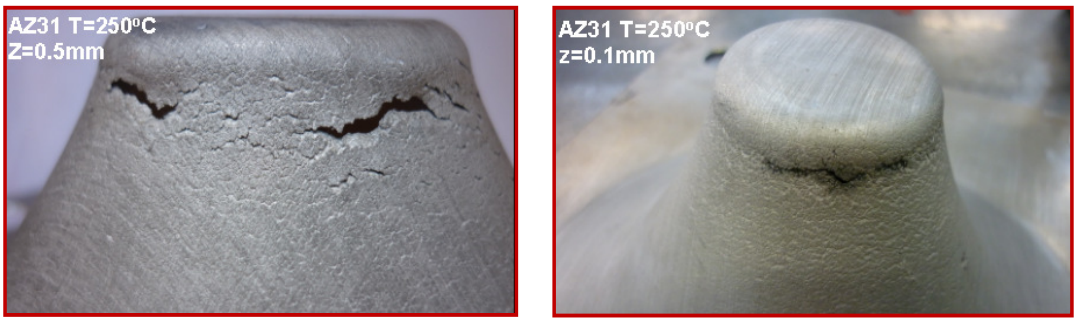

Fig. 3.20 Typical failure of SPIF process with AZ31 sheet at elevated temperature

3.4 SPIF with polymers at room temperature

3.4.1 Selection of polymers for SPIF process

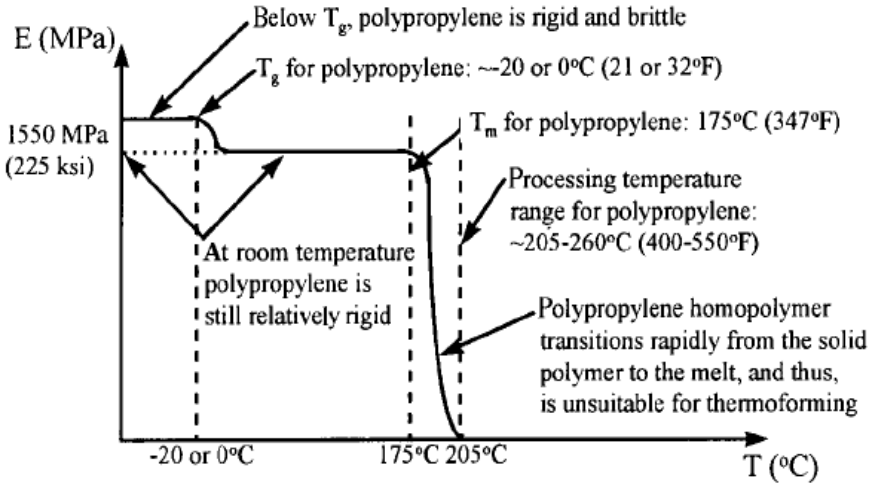

Fig. 3.21 Mechanical Properties of Polypropylene

Polymeric material used in the experiments of this study is a semi-crystalline, named polypropylene (PP). Choosing the PP as a representation for semi-crystalline group to apply SPIF process is due to semi-crystalline polymer constituted the largest group of commercially useful polymers. It is one of three important polymers in manufacturing industry (e.g. PVC, PP, and PE). Semi-crystalline materials have a highly ordered molecular structure with sharp melt points. They do not gradually soften with a temperature increase, instead, semi-crystalline materials remain solid until a given quantity of heat is absorbed and then rapidly change into a low viscosity liquid. This is an excellent behavior of the semi-crystalline group to be able to carry out SPIF process. In additional, the PP has a large processing temperature range from 20°C to 175°C. The elastic modulus is constant from room temperature to 175°C (Fig. 3.21).

3.4.2 Experiment

In experiments of SPIF process with polymeric material, square PP sheets (400x400x3mm) were used. The forming zone was a circle with the diameter of 300mm. The PP sheet was clamped firmly on the support frame and was engaged with machine table by bolts. A recurring lubrication is granted by a hydraulic system during the experiments. The sheets were deformed until either wrinkling or tearing occurred. The wall angle at where either wrinkling or tearing occurred was considered as the index of the maximum material formability. It was calculated by formula (3.2). Each experiment was performed three times to verify the repeatability.

Fig. 3.22 Three different failure modes in PP

In additional, other thermoplastics are also selected to carry out SPIF technique at room temperature. The preliminary experiments are performed same processing conditions with metal sheet on a commercial sheet blanks such as PP, PC and PE having a uniform thickness profile of 2mm and 3mm.

The experimentation of thermoplastic sheets revealed the existence of three different failure modes influenced on the formability of the SPIF process as Fig. 3.22.

- Wrinkling: (see Fig. 3.22 and Fig. 3.23) the forming part is twisted about the revolution axis in the rotating direction of the forming tool following the contour of deforming part. Wrinkle is usually initiated in the conterminous region between deformed part and undeformed part, and grew up following to the height of deformed parts. This failure is triggered by a thermal instability and high ratio of initial thickness and final thickness. When the processing temperature is over a viscoelastic regime (i.e. rubber plateau), elastic modulus is decreased quickly. The

deformed part is difficult to withstand twisting about a revolution axis of deforming part arising from the movement of the forming tool along the helical path. By using certain way that can keep thermal stability, the part still can be twisted due to the high ratio of t/t_0. This occurs in some of the slightly thin thermoplastic sheets. (less than 2mm in thickness).

- Cracking: (see Fig. 3.22 and Fig. 3.23) this failure is similar to failure usually found in SPIF with metal sheet. Cracking occurs at the transition zone between the inclined wall and the corner radius of the sheet. It is triggered by stretching mechanisms due to meridian tensile stresses. The morphology of the cracks and its propagation paths are along the circumferential direction.
- Tearing: (see Fig. 3.22 and Fig. 3.23) this failure is found in deformation of PVC or the polymer that has an amorphous structure [70]. It could also be experimentally observed when the initial drawing angle of the truncated hyperboloid shape was greater than 50°.

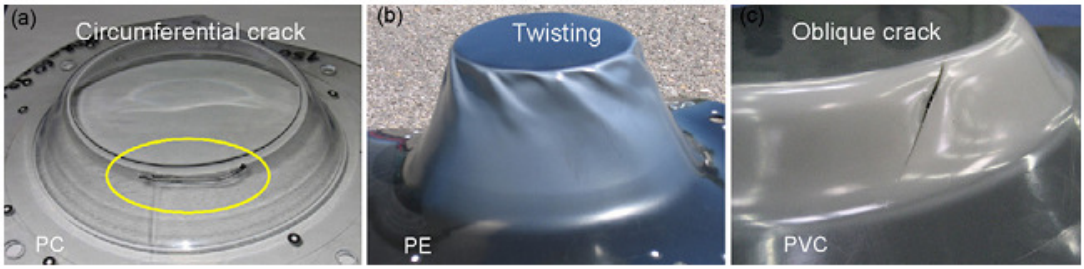

Fig. 3.23 Three different failure modes in PC, PE, and PVC [70]

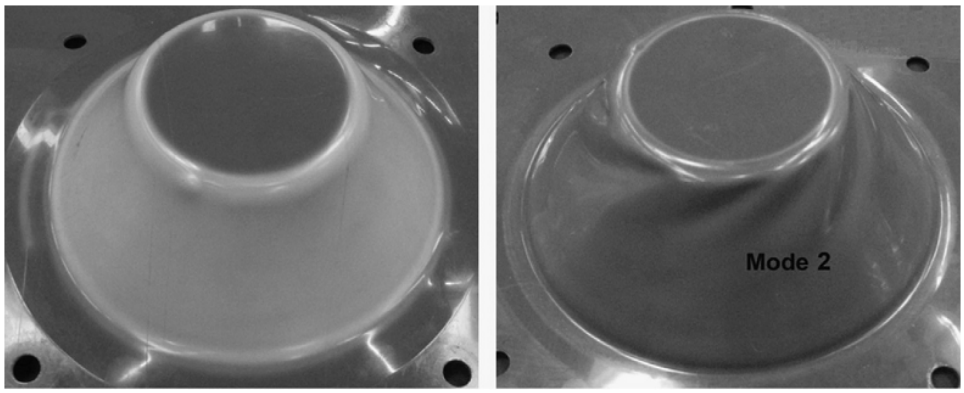

Fig. 3.24 Overcome the change of color in deformed part with PVC [69]

Besides the three failures depicted in Fig. 3.22 and Fig. 3.23, changing color in deformed part also found in the most colored polymer due to crazing mechanisms. Crazes are

known to take place when plastically deforming polymers below the glass transition temperature and its occurrence is linked to the overall level of tensile hydrostatic stresses. Franzen et al. [69] has first attempts to overcome this problem but result is unexpected as presented in Fig. 3.24.

3.5 Results and Discussions

3.5.1 Metal sheet

3.5.1.1 Magnesium Alloy sheet

Two responses used in this study are wall angle and surface roughness. The maximum wall angle obtained in the experiment without any mechanical failures is considered as maximum formability of SPIF for given materials. The surface roughness of deformed part measures both surfaces. However, the inner surface roughness is lower than outer ones due to the influences of contacting condition, lubrication, and processing parameters. Thus, the roughness values of inner surface are used in this regression analysis. The results of statistic analysis of variance for magnesium alloy sheet are summarized in Table 3.3.

	α	Ra		α	Ra
Std. Deviator	0.52	0.12	R-Squared	0.9983	0.9848
Mean	60.62	1.88	Adj. R-Squared	0.9974	0.9772
C.V.%	0.85	6.38	Pred. R-Squared	0.99956	0.9611
PRESS	6.87	0.37	Adeq. Precision	99.183	30.665

Table 3.3 The Analysis of Variance of Magnesium alloy

The value of R-Squared is a measure of the amount of variations around the mean of model response. Its adjusted and predicted value should be within 0.20 of each other. The analyzed result of this model showed that the predicted R-Squared value of 0.9956 for wall angle (or 0.9611 for surface roughness) is in reasonable agreement with the adjusted R-Squared of 0.9974 for wall angle (or 0.9772 for surface roughness). In addition, the adequate precision of the analyzed model is very high. The value of 99.183 for wall angle (or 30.665 for surface roughness) is a signal to noise ratio compared the

range of the predicted values at the design points to the average prediction error. Normally, it is required that ratios are greater than 4 indicating the adequate model discrimination.

Two regression models for most significant parameters on responses presenting a relationship among processing parameters and their interactions are shown below:

$$\alpha = 60.62 + 8.43A - 2.53B - 3.01C + 2.9BC - 1.39BC \quad (3.4)$$

$$Ra = 1.88 + 0.008A + 0.26B + 0.61C - 0.21AB + 0.31BC \quad (3.5)$$

The quality of deformed parts can obtain by controlling the important factors. To identify the most important factors and the combination of effects among the factors, it is recommended using the half-normal probability graph to choose an appropriate model of each response for 2-level factorials. The important factor is far from straight line in the right side (see Fig. 3.31a). The factors along this line are trivial which were eliminated in regression analysis. Although the half-normal graph of effects is strongly recommended to choose the statistically significant effects, it may be more complex in certain case. The Pareto Chart is an additional graphic used to display the t-values of the effects for selecting the significant effects (see Fig. 3.31b).

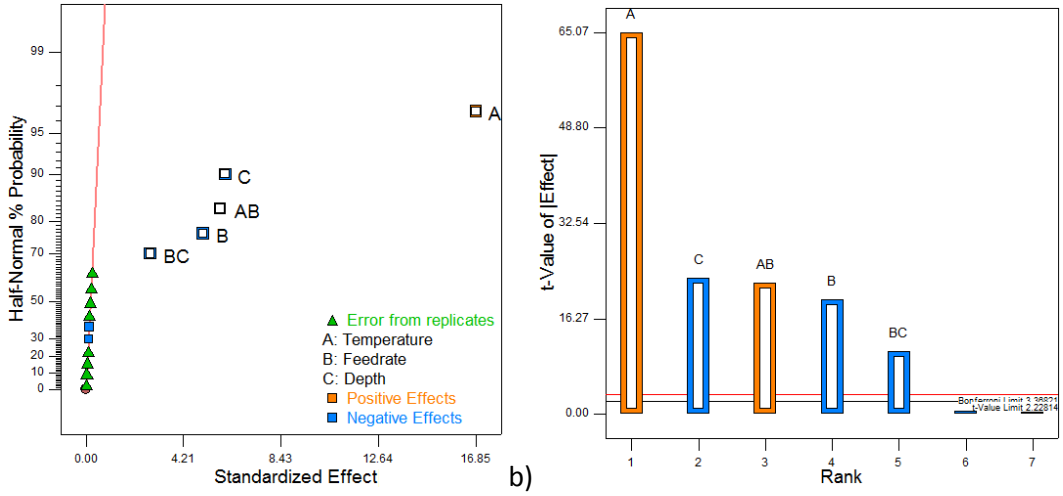

Fig. 3.25 Half normal Graph and Pareto Chart for wall angle

There are two different limits plotted on the graph based on the Bonferroni corrected t and a standard t. Effects that are above the t-value limit are possibly significant, approximations to the 5% risk level. Effects above Bonferroni limit are most likely

significant. Effects that are below the t-value limit are eliminated to regression analysis in next step. In this model, the significant effecting factors are consisted of temperature (A), feedrate (B), depth step (C), interaction between the temperature and depth step, and interaction between the feedrate and depth step (BC).

From the results of statistic analysis, the temperature factor is the most important effect on formability of magnesium alloy sheet. It contributes 73.22% into the effects on the formability. This is very consistent with the fact that magnesium sheet AZ31 is very poor formability when is deformed at an ambient temperature. Thus, deformation of AZ31 sheet at an elevated temperature should be considered as a main factor to deform successfully with SPIF process. The maximum wall angle obtained is relatively high in comparison with other researches for applying SPIF at an elevated temperature (maximum angle of 74.2 degrees).

Parameters	Aluminum alloy		Magnesium alloy	
	% Contr. into α	% Contr. into Ra	% Contr. into α	% Contr. into Ra
Temperature (A)	73.01	7.79	73.22	0.01
Feedrate (B)	18.43	4.21	6.6	11.18
Depth Step (C)	6.67	71.73	9.33	63.6
AB			8.67	7.6
BC	0.92	10.56	2	16.1

Table 3.4 % contribution of factors into response

The contribution of depth step and feedrate into the effect on formability of SPIF is relatively significant (9.33% and 6.6%, respectively). The result from mechanical testing showed that magnesium sheet has a high sensitivity to the deformation speed. The mechanical failures occur easily at a high feedrate. It restrained the industrial applications of SPIF in large production batch because SPIF is a slow process in comparison with the conventional process such as deep drawing and stamping process. The speed up the SPIF process by increasing feedrate is limited in the capability of machine. However, the interactive contribution of the feedrate and the depth step is relatively small (2%). It can is considered as a solution to speed up SPIF process in an

optimal way. The depth step effects mainly on axial deforming force and surface roughness. The capability of special machine for SPIF can provide an axial force up to 30kN [77]. Thus, increasing depth step and feedrate within respecting roughness is a good solution for SPIF process.

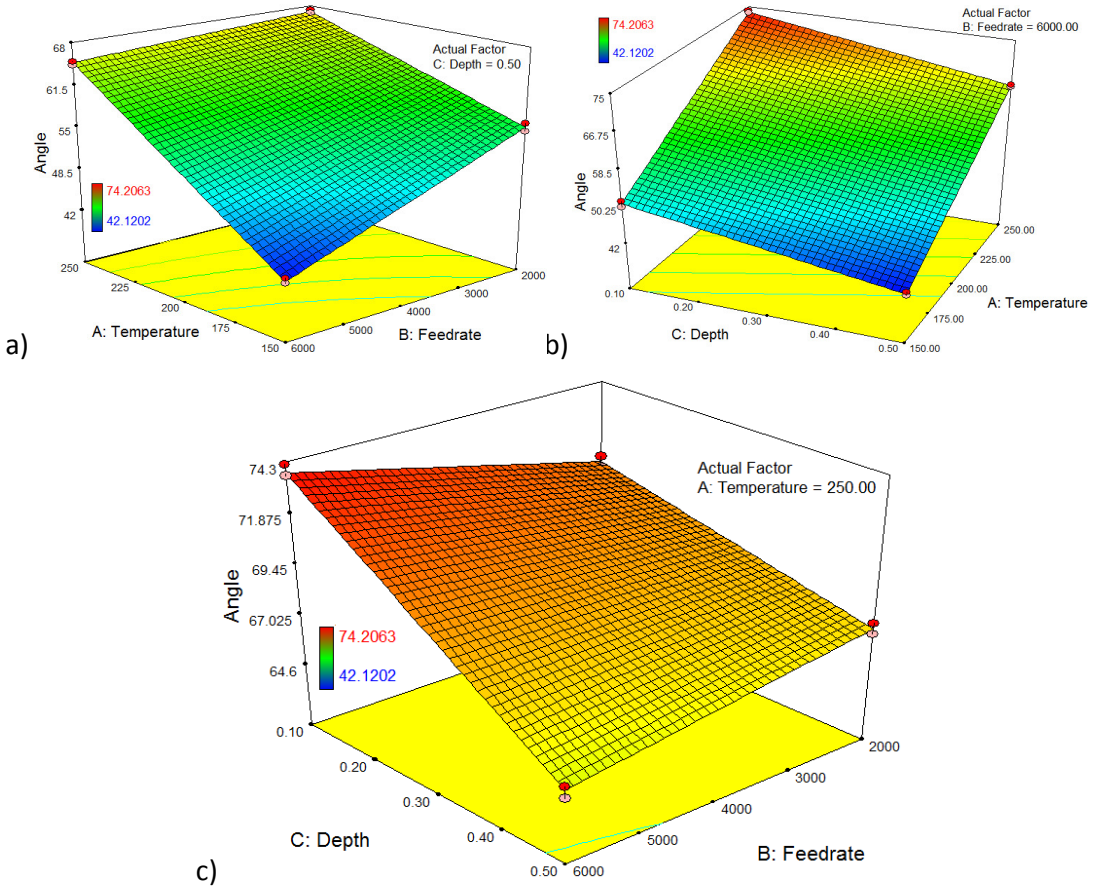

Fig. 3.26 Interaction effects of important factors on wall angle

The interaction of effect between temperature and feedrate is considerable. This can be explained by investigating to microstructure of AZ31 sheet. At high deformation speed, gains are elongated in the direction of deformation without the phenomenon of the dynamic recrystallization (see Fig. 5.6). At 300^{o}C and high deformation speed, it seems to start the appearance of the dynamic recrystallization but grain sizes are very large (see Fig. 5.6c). The large size of grain triggered off a hard deformation in sheet which influenced on the formability and the quality of sheet surface. Thus, the combination of high deformation speed and elevated temperate decreases the formability of SPIF with AZ31 sheet.

The interaction graph illustrated clearly the interactive effect of important factors on a maximum wall angle (see Fig. 3.26). They present the interaction of three factors in which a third factor is predefined at minimum (or maximum) value. The red points on ordinate axes are maximum achievable wall angle in the case of combination between two presented factors and minimum (or maximum) third factor. The interaction effect between depth step and feedrate in the case of maximum temperature induced a change of wall angle from 73.68° to 74.2° (see Fig. 3.26c). The combined effect of minimum feedrate and maximum depth step induced a change of wall angle in the range of (51.68°, 74.2°) for maximum and minimum temperature, respectively. Adjusting the value of depth step and feedrate in a consistent way improves significantly the formability of SPIF process with AZ31 sheet.

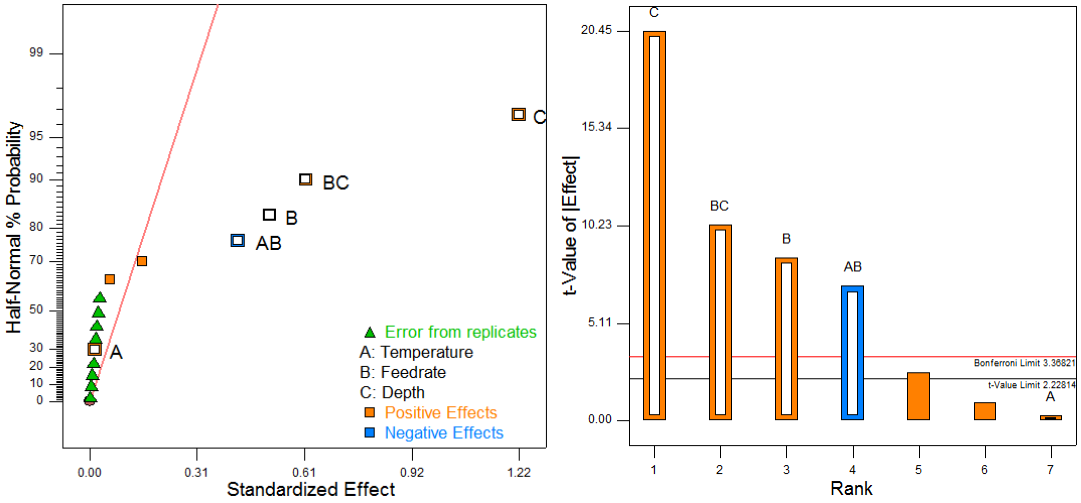

Fig. 3.27 Half normal Graph and Pareto Chart for surface roughness

Similar to conventional forming, the surface quality of deformed part is also an important aspect in SPIF process. It is the difficult tasks of a technician to decide which processing parameter take into account the quality of the surfaces. In milling process, to obtain higher quality an additional polishing operation may be required. The tool steps in a horizontal and down direction are important parameters affected to the quality of the surface. In SPIF process, it is easy to identify in first time that the contacting condition between forming tool and sheet induced an influence to the quality of surface. The influence of contacting condition can be decreased minimally by using different consistent lubrications (MoS_2 + Tribostart) in elevated temperature. The forming tool is

always checked before and after forming operation, thus, a tool wearing can be negligible.

The result from regression analysis showed that depth step is a most important parameter affected the quality of surface (contribution of 63.6%). The interactive effect between the feedrate and depth step is also relatively significant (16.1%). Similar to the response of wall angle, four significant effects are kept for regression analysis as showed on Fig. 3.27. However, the effect of temperature on the quality of surface is very small. It can be eliminated from regression analysis.

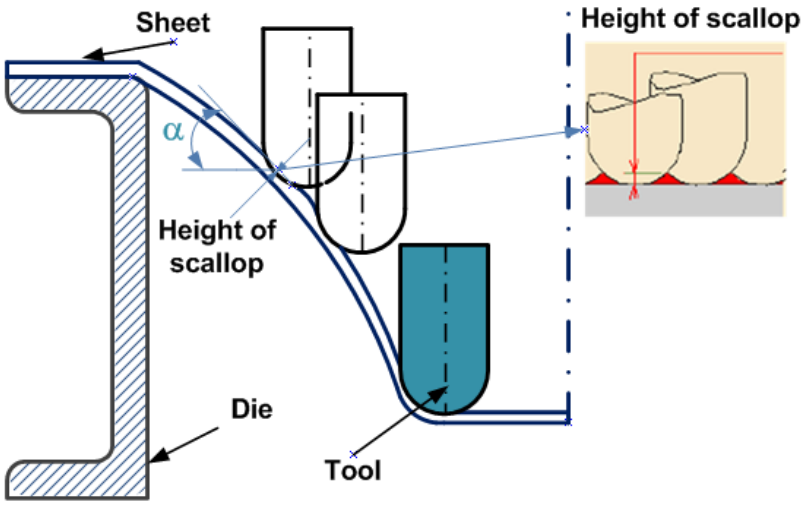

Fig. 3.28 Effect of depth step on surface quality

The effect of depth step in SPIF through the trace of forming tool left on the surface of deformed part is illustrated as Fig. 3.28. For milling operations, the height of scallop as a representation to the quality of surface is decided by tool radius and minimum distance between passes. A large radius induces a low height of scallop on a surface of a formed part due to a large superposition of milling tool. However, it is a fact that smaller radius of forming tool gives higher formability in SPIF process. This can be explained by an illustration of Fig. 3.28, a contacting zone between forming tool and sheet surface is relatively small. It seems to be depended on a wall angle of sheet. With same tool radius, smaller wall angle gives a larger superposition zone; higher surface quality is induced. Thus, the effect of tool radius on roughness can be negligible with small depth step and larger wall angle in SPIF. This effect is considerable at a higher depth step and smaller wall angle of sheet. This task will be investigated in the next study so that can

conclude that selecting of tool radius and depth step should be considered the wall angle of sheet.

It should be noted that all experiments of SPIF process in this thesis were used the helical toolpath. Using this path eliminated the effects of peak of downing force at beginning point of each layer in deformed part. Thus, the forming force does not depend on the size of the part and the quality of surface improved significantly.

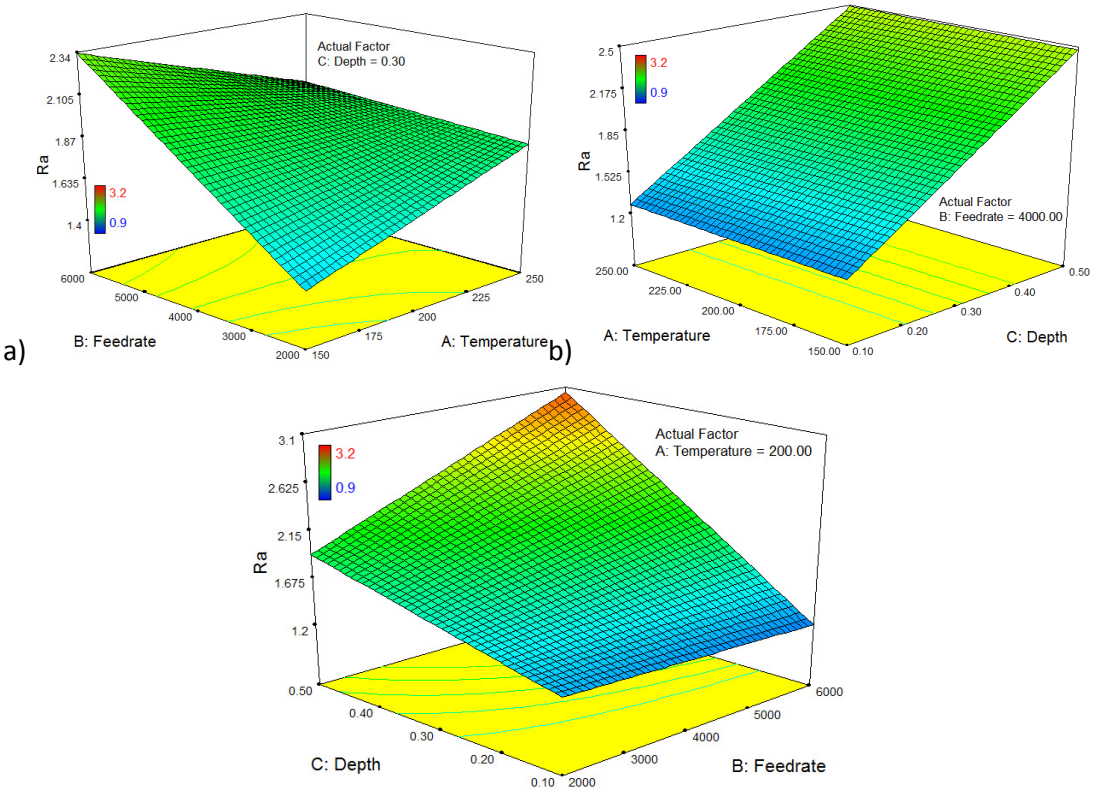

Fig. 3.29 Interaction effects of important factors on surface roughness

The influence of depth step on the surface quality is very significant at the elevated temperature as showed in Fig. 3.29b. The influence of feedrate is also considerable and the interaction between a feedrate and depth step is very significant (contribution of 16.1%, see Fig. 3.29c). Although the effect of temperature is very small, its combination with feedrate is relatively significant (7.6%) This can also be explained through investigation of microstructure and mechanical properties of the AZ31 sheet. At high deformation speed and over, the size of grains are very large and are elongated in the moving direction of forming tool without DRX process 200^{o}C (see Fig. 5.6b and c). The

deformation of sheet in case of large grain is difficult. Thus, the quality of surface is low because the failure in opercular style occurs on surface textile. This problem usually appears in most deformation of AZ31 sheet with SPIF at so high feedrate.

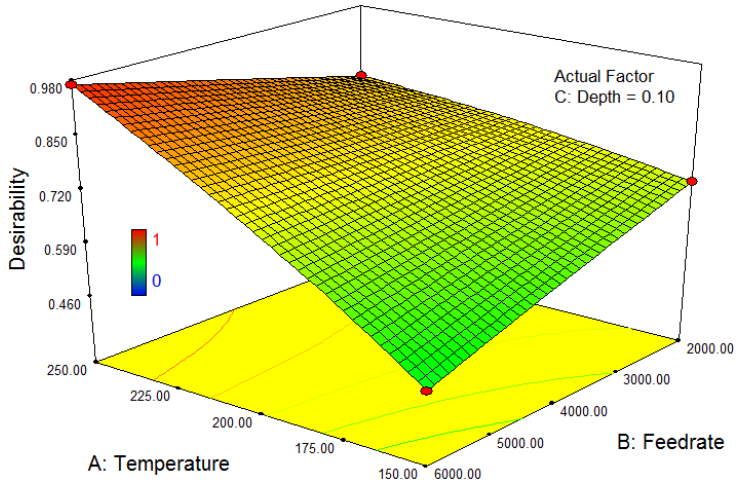

Fig. 3.30 Numerical optimization with multiple responses

The last step in the analysis of variances is to find an optimal setting for practice applications of SPIF. In fact, engineer designing a part with SPIF process desires a maximum achievable wall angle and a minimum surface roughness. This demand can be responded by using numerical optimization through an objective function for multiple responses, called the desirability function [78]. This function reflects the desirable ranges for each response in the desirable ranges from zero to one. The result of numerical optimization with maximum wall angle and minimum surface roughness is shown on Fig. 3.30.

3.5.1.2 Aluminum alloy

For aluminum sheet, a preliminary evaluation of factors and their interactions on response is presented in the half normal graph and Pareto chart, (see Fig. 3.31). Four effects used for regression analysis are temperature (A), feedrate (B), depth step (C) and interaction between the feedrate and depth step (BC). The formability of SPIF process is influenced mainly by main factors while interactive effects are very small (Fig. 3.31). The temperature has very significant influence on the formability of aluminum sheet (73.1%). The maximum wall angle obtained in SPIF process at elevated temperate is 89.5°. This value is very high in comparison with deformation at room temperature of

other researchers. Thus, deformation of aluminum sheet at the elevated temperature should be considered as a main factor to improve the formability of aluminum alloy sheet with SPIF process.

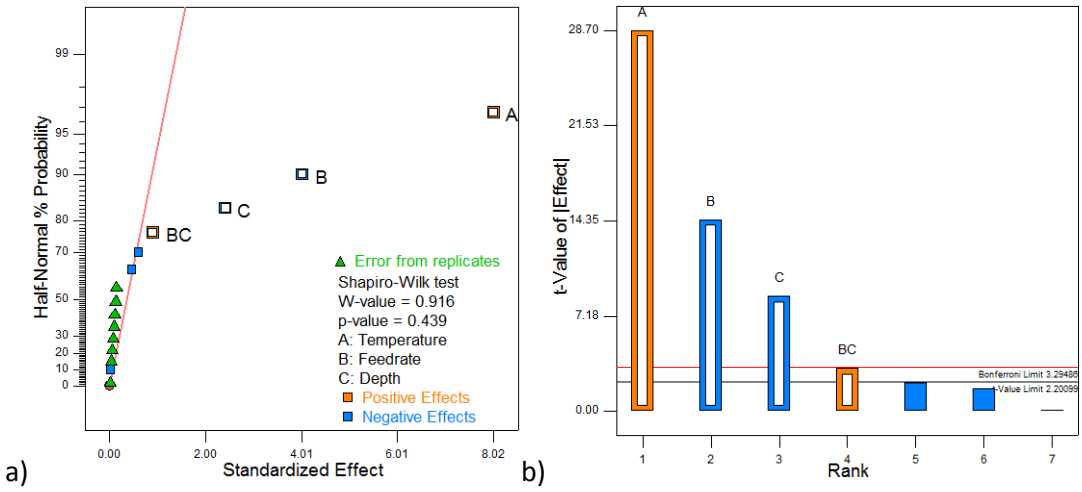

Fig. 3.31 Half normal Graph and Pareto Chart for wall angle

The effect of feedrate is higher than one of the depth step because of high ductile behavior of aluminum sheet at the elevated temperature. It can suffer a better axial deformation than the case of magnesium sheet when forming tool moves down. Other contributions are listed in Table 3.4.

	α	Ra		α	Ra
Std. Deviator	0.56	0.3	R-Squared	0.9903	0.9437
Mean	81.82	2.47	Adj. R-Squared	0.9867	0.9233
C.V.%	0.68	11.94	Pred. R-Squared	0.9794	0.8809
PRESS	7.26	2.03	Adeq. Precision	46.329	18.160

Table 3.5 The Analysis of Variance of Aluminum

The result of ANOVA for aluminum sheet has a reasonable agreement between the values of predicted R-Squared and adjusted R-Squared as showed on Table 3.5. Although the value of F-value implying the Lack of Fit is significant, this model can still be used to navigate the design space. Two equations of relationship among factors and their interactions are extracted from regression analysis as below:

$$\alpha = 81.82 + 4.01A - 2.01B - 1.21C + 0.45BC \quad (3.6)$$

$$Ra = 2.47 + 0.29A + 0.21B + 0.87C + 0.34BC \quad (3.7)$$

The interaction between the feedrate and the depth step on the formability of SPIF is presented in Fig. 3.32a. An optimal solution between best formability and saving deformation time can obtain by using this interaction because their interactive effect is very small (0.92%).

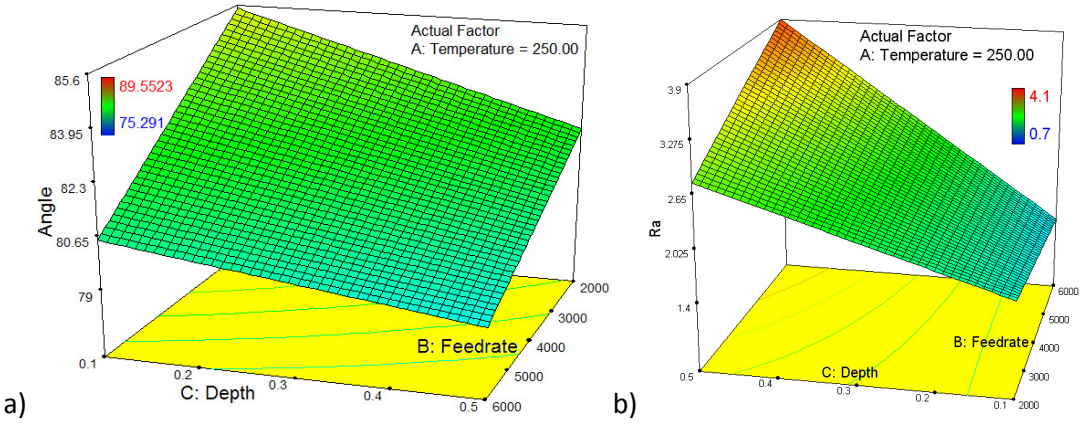

Fig. 3.32 Interaction of important factors on: a) wall angle, b) surface roughness

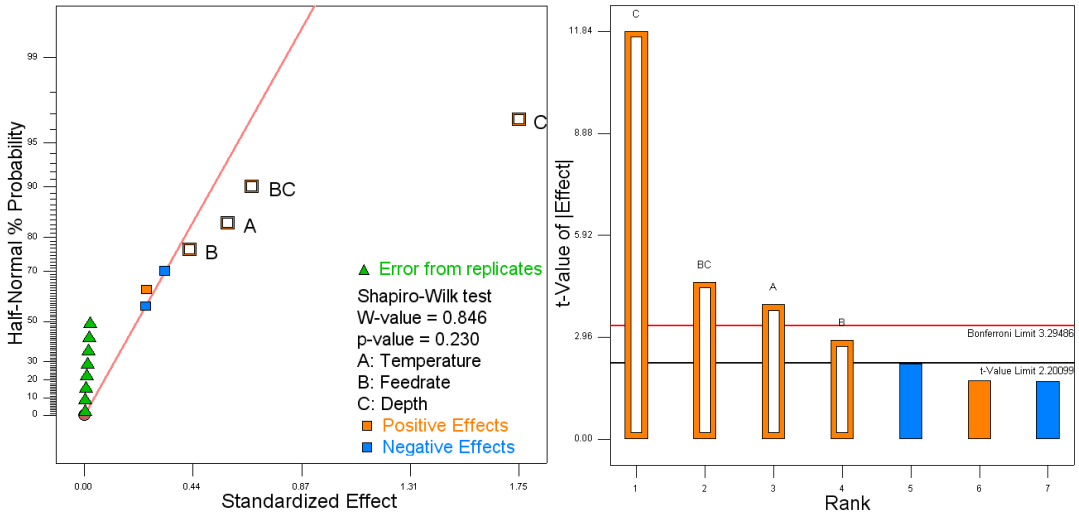

Fig. 3.33 Half normal Graph and Pareto Chart for surface roughness

The quality of surface in deformation of aluminum sheet is almost decided by level of depth step used in SPIF. The effect of others is not considerable as showed on Fig. 3.33. Similar to the case of magnesium sheet, the interaction between the feedrate and depth step is relatively considerable as showed on Fig. 3.32b. However, the forming

temperature of aluminum sheet has a more significant contribution into the quality of surface than one of the magnesium sheet. This phenomenon seems to be effected by large size of grain thanks to increasing the temperature.

The result of numerical optimization with maximum wall angle and minimum surface roughness is shown on Fig. 3.34.

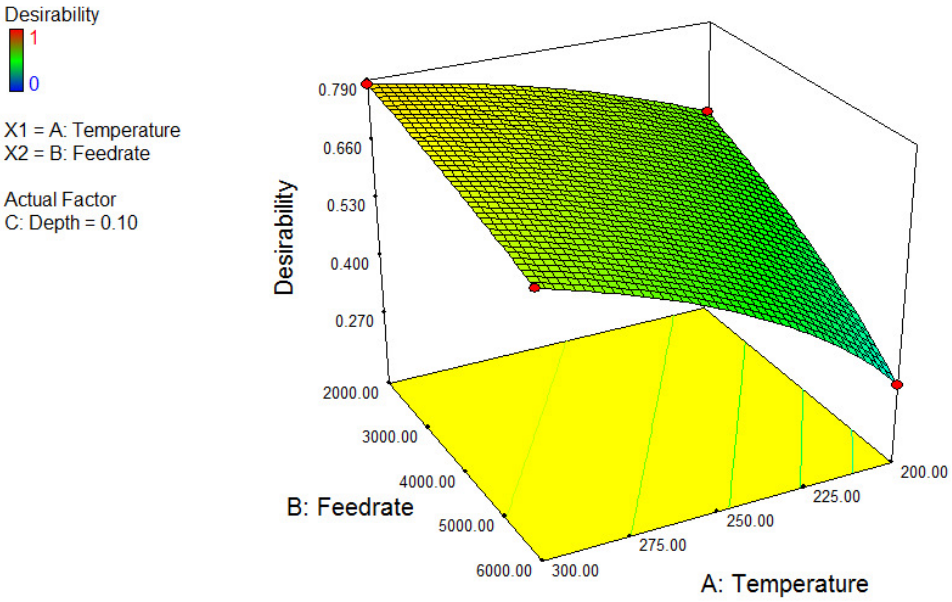

Fig. 3.34 Numerical optimization with multiple responses

3.5.2 Polymeric sheet

The Pareto chart and half-normal graph showed explicitly the level of effects and interactions of parameters on the formability of SPIF with thermoplastics. Four main factors and three interactions are over the Bonferroni limit and t-value limit. They are kept for regression analysis. The level of contribution of each effect is presented on Table 3.6. The formability of SPIF with thermoplastic is almost influenced by step size and tool radius. The influence of step size (36.68%) is similar to the case of the metal sheet. However, the influence of tool radius is a main difference with one of the metal sheet. This contributed significantly into the formability (31.38%).

The Analysis of Variance (ANOVA) is summarized in Table 3.7. It describes the effects of the input parameters and of their interactions on the output variable. It is shown that all

the analyzed parameters and their 2-way interactions are relevant to the process (very low P-values) and this model has a fairly good fit. Therefore, all the factors (forming parameters) have to be taken into account and used to model the response surface. Table 3.7 also indicates that the correlation coefficient R^2 and adjusted R^2_{adj} values (R^2 = 98,11% and R^2_{adj} = 97,29%) for accuracy of this model are very satisfactory. From analysis of variances, an equation presented a relationship among effects and interaction is extracted as below:

$$\alpha = 74.38A - 8.04A + 0.06B - 0.0012C + 0.003D + 0.5AB + 0.00093AC - 0.0024AD \quad (3.8)$$

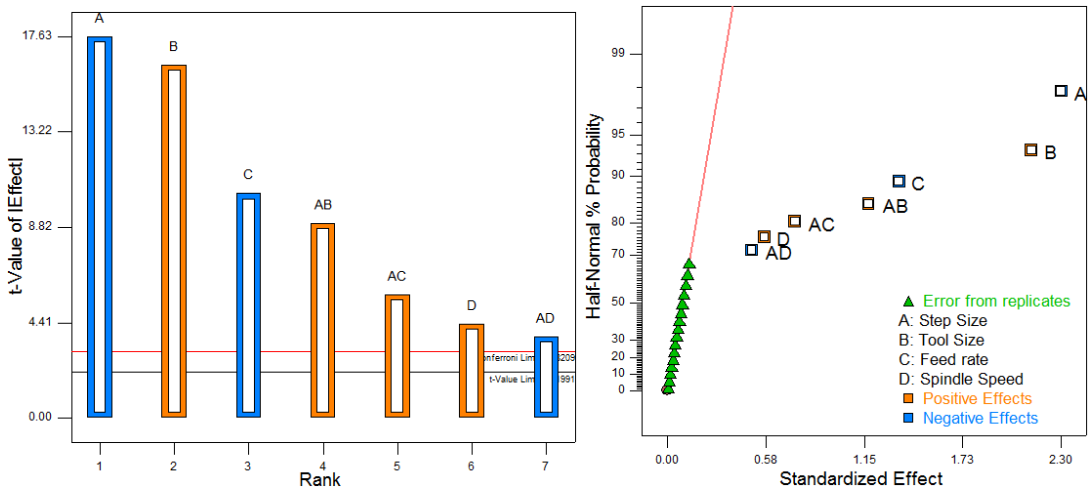

Fig. 3.35 Half normal Graph and Pareto Chart for wall angle of PP

Parameter	% contribution	Parameter	% contribution
Step size (A)	36.68	AB	9.58
Tool size (B)	31.38	AC	3.86
Feedrate (C)	12.7	AD	1.69
Spindle speed (D)	2.23		

Table 3.6 % contribution of effects into the formability of SPIF with thermoplastics

Information	Value	Information	value
Std. Deviator	0.32	R-Squared	0.9811
Mean	71.91	Adj. R-Squared	0.9729
C.V.%	0.44	Pred. R-Squared	0.9575
PRESS	3.68	Adeq. Precision	34.406

Table 3.7 The Analysis of Variance for PP

Main effects of forming parameters for maximum wall angle and their interactions are described on Fig. 3.36 and Fig. 3.37. The increase in step size and feed rate contributes to decrease α_{max}, that means a decrease in formability. In particular, the step size is particularly significant for the formability when its value is larger. These results are in accordance with previous researches carried out on SPIF of metal sheets [2]. Due to the excessive vertical movement of the tool and the high friction between the polymer sheet and the tool, the deformed part is wrinkled and is torn easily at larger step. The combination of smaller tool and larger step size contributes to significant decrease of formability as illustrated on Fig. 3.37.

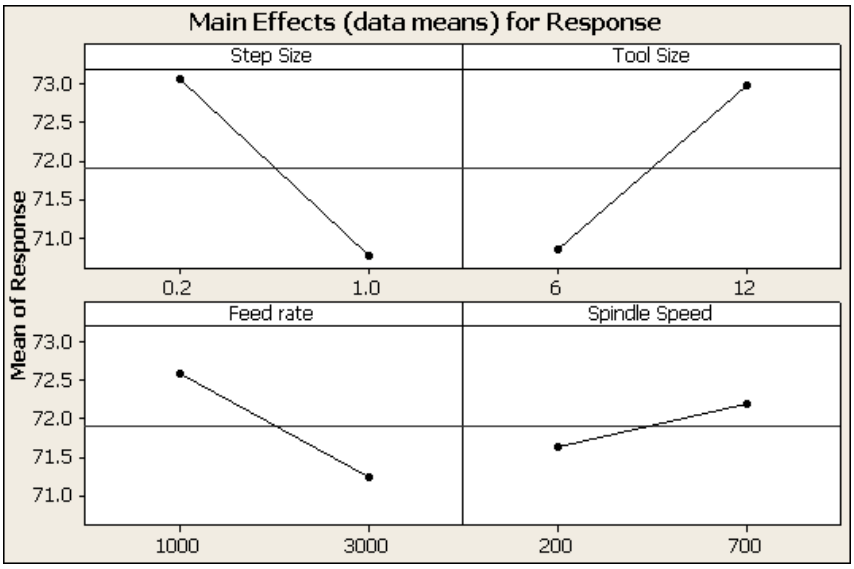

Fig. 3.36 Main effects for maximum wall angle

When using a small radius, the tool penetrated easily into the sheet and some pieces of chip are spited out. Thus, the formability decreases significantly if the radius of the forming tool is small. The interaction plot shows that smaller radius tool and larger step size (or feed rate) contribute to decrease significantly the formability. Results obtained in similar experiments carried out on metal sheets show a different behavior of polymers in comparison to metals.

In addition, the increase of spindle speed affects formability. In SPIF of metal sheet, previous researches indicated that decreasing in the spindle speed could result into a better formability. A reduction of the spindle speed can eliminate sliding friction and can

retain only rolling friction. In this experiment, the increase in spindle speed contributed to increase the formability of thermoplastic sheets only with either large tool size, small step size or large feed rate. The local heating originated by higher speed is reduced using coolant to proper temperature for plastic deformation. The combination between higher feed rate and higher spindle speed also improved the formability.

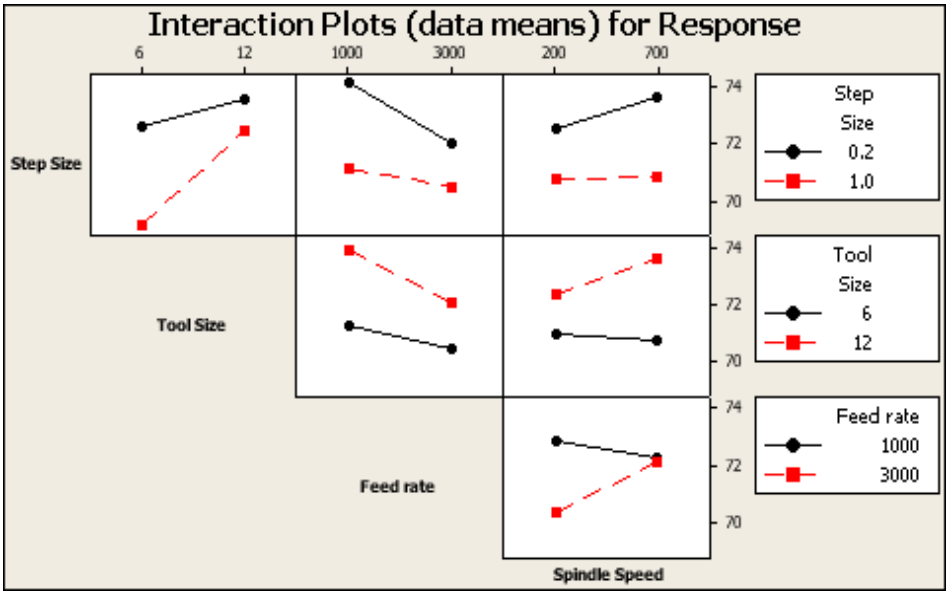

Fig. 3.37 Interaction among forming parameters for ϕ_{max}

The interaction effect between tool size (or step size) and spindle speed is relative significant for larger tool size (for smaller step size). Thus, the improvement of formability in thermoplastic sheets depends on the variation of four forming parameters.

Some sample parts are made in SPIF process with polymeric sheet materials.

Fig. 3.38 Pyramid and cone shape in PE

Fig. 3.39 Sample parts in PP

3.6 Conclusion of the chapter

This chapter described the experimental equipments for SPIF process with sheet metal and polymer. The heating system designed successfully which provided a uniform temperature on sheet metal in short time (about 2 minutes).

The maximum wall angle of aluminum is 89.30 at a temperature of 300^{o}C which is highest ever for traditional SPIF. The results of ANOVA showed that temperature is an important parameter to improve the formability of aluminum. The depth step is a main parameter that has a significant influence on the quality of surface.

The maximum wall angle of magnesium sheet is 74.2 degree at the temperature of 250°C. The temperature is also an important parameter influenced on the formability of SPIF. The depth step is also a main parameter influenced on the quality of surface. However, the effect of feedrate and depth step is considerable due to high sensitivity with deformation speed and the change of grain size following temperature and deformation speed. It is also revealed that an optimal selection of feedrate and depth step values brought a highest efficiency on formability and the quality of surface. Two mechanical failures are found in deformation of magnesium and aluminum sheet. The mechanism caused these failures is explained in next chapter.

The preliminary experiment of SPIF with thermoplastic showed a potential approach to deform sheet polymer at room temperature. The results of ANOVA showed that depth step, tool diameter, and feedrate have main influence on the formability of SPIF for thermoplastic. The maximum wall angle of SPIF with polypropylene is 75°.

Chapter 4

Fracture Criteria for sheet metal

4.1 Introduction

For ductile metal sheets, mechanical failure is often understood as initiation of necking in the formed part. Prediction of necking that limited their formability was proposed and has been developed over past several decades. The common approach used to predict the necking for metal sheet is Forming Limit Diagram (FLD). However, the failure mode in IF showed that there is no necking in deforming part before the fracture occurs. The prediction of fracture occurs in ISF process is one of the important problems.

In this chapter, it is necessary to review deformation and damage mechanics in ISF process. It will be fundamental to choose a suitable fracture criterion for prediction of failure in SPIF process. The damage criteria, which have been used commonly for ductile sheet metal, are focused. They were transformed into a unique space which was convenient to compare together and then to apply for numerical simulation. The key parameter greatly influenced on the amount of plastic deformations, which a material may undergo before ductile failure occurs, is stress triaxiality. The role of triaxiality for fracture criteria for metal sheet is also presented in this section.

The final, aspects relate to implementation of a progressive damage and failure model on numerical simulation for ductile metals in ABAQUS is mentioned. They are prepared for numerical simulated procedure in next chapter to predict the fracture in SPIF process.

4.2 Mechanical fracture in SPIF process

Incremental forming is known as a potential process which obtained the formability above the forming limit curve in comparison with conventional forming process. The

experimental evidence and analysis are concluded that the formability of ISF process is mainly influenced by four major parameters: tool depth step, speed of tool, tool diameter, sheet thickness [45,75]. The speed of tool means as both feed-rate and spindle speed. The feed-rate is displacement velocity of the tool which affected on efficiency forming process and also increased mechanical failure (e.g. formability) in the formed part. The spindle speed is known to influence the formability due to its influence on friction between tool and sheet surface. The influence of sheet thickness and depth steep were explained through sine law [2]. The last parameter, e.g. tool diameter, is usually explained due to a contacted area which concentrates the strain. The larger tool diameter intends the distribution of strain over extended zone.

Understanding of deformation and fracture mechanics in SPIF has a great importance for improving the formability and extending the applicability in manufacturing industry. The questions brought from experimental observation such as enhanced forming limit and cracking propagate along the circumferential direction. There are efforts to explain the deformation mechanism of SPIF process through theoretical analysis and experimental evident found in the literatures. In general, the deformation mechanism and fracture mechanism of SPIF process were explained on the view of localization of the deformation.

4.2.1 Membrane analysis and triaxiality

Silva et al. [55] used membrane analysis of a small plastic zone in the rotational symmetry components to explain aspects of formability and damage. The authors concluded that cracks triggered off in SPIF process due to meridional tensile stresses. The plane shearing stresses do not present in cracking. These conclusions brought from examination of a material failure at small-localized plastic zone (the transition area between the corner radius of the sheet and the inclined wall). The states of stress at this zone obtained from assuming of a rotational symmetric truncated cone under plane strain conditions. The additional assumptions include isotropic, rigid perfectly plastic material. The friction occurs between two in-plane components of meridian and circumference. The authors also explained the mechanism of crack propagation in the zigzag path.

Martins et al. [56] used the analysis presented by Silva which based on careful examination of geometry of the zone of localized deformation. The authors pointed out the evidence in which formability is limited by fracture without previous necking. It means that there is no evidence of an actual neck before the failure occurs in the part. Assumption of the small-localized plastic zone, which embedded in a surrounding area with lower stress, is very small to develop a neck. The crack cannot grow because forming tool always moves in the deformation process. When the crack is going to obtain the fracture limit, the tool is already moved in another place. This explanation is not satisfactory because the sheet still stands in deformation tension. Prediction of forming limit is suggested to use Fracture Forming Limit Diagram (FFLD) instead of conventional FLD. The FFLD in SPIF can be characterized by mean of the ductile damage mechanism based on void nucleation and growth models. It gives the slope line of FFLD in principal strain-space (see Fig. 4.1). The triaxiality ratio is used to explain the onset of fracture during SPIF process of pyramid shape part and influence of tool radius on formability.

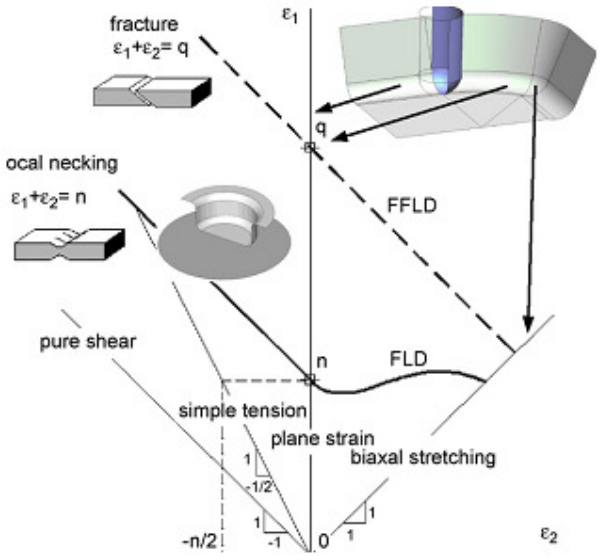

Fig. 4.1 The forming limits of SPIF against those of stamping and deep drawing

4.2.2 Bending under tension (BUT)

Emmens [53,54] investigated the continuous bending under tension (BUT) to study aspects of ISF. The tests have emphasized a crucial aspect of localized plastic

deformation. The author explained that the case of the bending radius is constant, the formability defined as the limit strain in a single operation should become proportional to the sheet thickness assuming the bending under a tension mechanism to operate. Based on the assumption of localized deformation a relation between strain and elongation was derived that was validated by the experiments. The pulling speed and depth setting in BUT experiments have a significant effect on the achieved results. The effect of the actual bending radius and a smaller radius is also significant in deformation.

4.2.3 Through-Thickness Shear

Allwood et al. [58] presented that through-thickness shear can affect the formability by modeling SPIF process with a finite element. The authors demonstrated a significant through-thickness shear (TTS) occurring in the direction parallel to tool motion. It is explained that the material on the top surface of the sheet metal tends to move in the direction of the tool displacement because of friction. However, in another publication of authors showed that shear perpendicular to the tool direction could not be explained directly by the aspects of friction due to the direction of the tool path. They suggested two alternative explanations: i) rotation of the tool and; ii) the tool pushed material downwards while it is moving in descending contours over the inclined wall. The effect of rotation of the tool in shear is eliminated by investigating of locking off the rotation of the indenter.

Jackson [57] continued this work by examining experimentally through forming of copper sheets with both TPIF and SPIF approach. The author presented that the deformation mechanisms are due to stretching and shear for both SPIF and TPIF process. The deformation due to stretching is in the plane perpendicular to the direction of a tool which was similarly observed in FE simulations of [3,58,79]. The deformation due to shear is parallel to the direction of forming tool and increases along the cross-section in the copper sheet which is similar to an experimental investigation of Allwood [58].

Eyckens et al. [80] used Marciniak–Kuczynski (MK) model to predict local necking in SPIF process. The authors revealed that TTS occurred in this process. The presence of TTS can influence significantly the limit strain in which depend on the strain mode. The increase

of the FLC is only the shear component in the plane perpendicular to the minor strain which is again in the moving direction of the tool has an effect on the FLD. The increase of formability because of TTS is explained by delaying a necking process. This delay is similar to the one in the onset of necking under a biaxial stretching mode in conventional forming process.

4.3 Fracture criteria in metal sheet

In the past decades, various fracture criteria to predict ductile fracture of sheet metal have been proposed and developed. They are based on different mechanical models with different assumptions. A number of simple fracture criteria used the limits of strains and stresses to characterize the fracture of a part have been proposed (e.g. Coulumb, Rankine, Tresca, von Mises). These criteria only consider solely the stress or strain and give relative accuracy in prediction of damage. Others are more complex models (e.g. Gruson, Wilkins, Cockcroft-Latham,) took into account of dependent on the loading history and give higher accuracy.

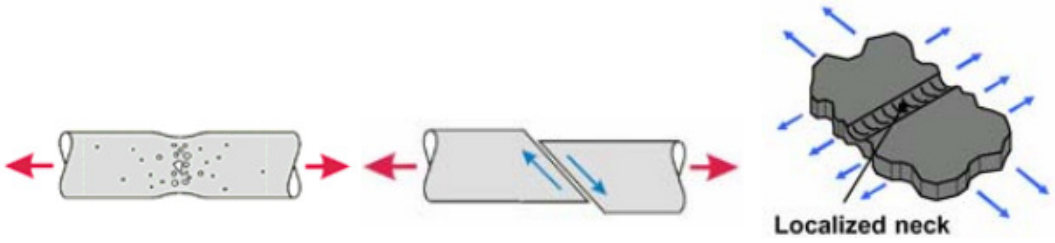

Fig. 4.2 Three main mechanisms of damage in ductile metal [81]

Three main mechanisms can cause the fracture in a ductile sheet metal: ductile fracture due to the nucleation, growth, and coalescence of voids; shear fracture due to shear band localization; and instability due to local necking (see Fig. 4.2). Based on phenomenological observations, these three mechanisms called for different forms of the criteria for the damage. In recent years, many theoretical studies have been developed for predicting the initiation and the growth stages of fracture in ductile metal. The damage criteria can be categorized into four groups: phenomenological model, Gurson-type model, Marciniak–Kuczynski (M-K) model, and the combination of the M-K theory with the Gurson-type models. Other ways, they can be roughly divided into two

groups: damage initiation criteria for fracture and damage initiation criteria for necking instability. This division is a convenience for using fracture criteria to predict mechanical failure in SPIF process (see Table 4.1).

The first group does not directly reflect the physical mechanism of ductile fracture, but it predicts the initiation of damage in deforming part. It is based on a macroscopic definition of a damage accumulation function. These criteria in this group include Johnson-Cook, Wilkins, Gurson, FFLD, shear criteria, CrashFEM, .etc. Particularly, Gurson model is based on nucleation and growth of voids in the metal. The yield function is modified to take into account of the presence and evolution of the voids. Modifications of Gurson model introduced by Tvergaard and Needleman made the model more complete [82,83].

Damage initiation criteria for fracture	Damage initiation criteria for necking instability
Ductile criteria	FLD criteria
Johnson-Cook criteria	FLSD criteria
Wilkins criteria	MSFLD criteria
Gurson criteria	Marciniak-Kuczynski criteria
FFLD criteria	
Shear criteria	

Table 4.1 Classification of damage initiation criteria

The second group is the damage initiation criteria for the necking instability of sheet metal. These criteria include types of forming limit diagrams (e.g. FLD, Forming Limit Stress Diagram - FLSD, and Müschenborn-Sonne forming limit diagram- MSFLD) and the Marciniak-Kuczynski (M-K). The types of forming limit diagram are the common approaches to predict the necking instability for metal sheet in a manner mimicking press floor methods to assess measured strains from circle grid measurements. Predicted in-plane principal strains are compared to measured forming limit curves. If the predicted strains lie below the forming limit curve, the part is predicted to be "safe". M-K criterion predicts necking instability in sheet metal taking into account the deformation history. It is based on the definition of a groove as an imperfection in

sheets. The thickness ratio of groove and sheet is monitored during the deformation process. The failure is assumed to occur when this ratio exceeds a critical value.

4.3.1 Role of Stress triaxiality on mechanical fracture

Theoretical and experimental studies showed that stress triaxiality is the important parameter significant influencing on the amount of plastic strain that a material may undergo before ductile failure occurs. The stress triaxiality describes the stress state and takes into account its influence during plastic loading of the material.

$$\eta = \frac{\sigma_h}{\bar{\sigma}} \tag{4.1}$$

$$\sigma_h = \frac{\sigma_1 + \sigma_2 + \sigma_3}{3} \tag{4.2}$$

where σ_h is the mean stress (hydrostatic stress), $\bar{\sigma}$ is the von Mises effective stress and σ_1, σ_2 and σ_3 are the principal stresses with $\sigma_1 \geq \sigma_2 \geq \sigma_3$.

The previous research showed that the range of stress triaxialities in general deformation is from -1/3 to 2/3. The low limit of -1/3 corresponds to the so-called cut-off value for negative triaxiality discovered by Bao et al. [84]. At the same time, the upper limit of 2/3 is the maximum value of stress triaxiality that can be obtained in plane stress. The diagram presented a large range of the stress triaxiality as Fig. 4.3 and is divided into three ranges.

To construct the locus of Fig. 4.3, Bao et al. [85] performed the experiments in many specimens with different geometry. High stress triaxiality range from 1/3 to 2/3 is taken from the experiments with different specimens. Intermediate stress triaxiality range is from 0 to 1/3. The first observation is that the range of intermediate stress triaxiality is seldom encountered in sheet metal forming problems because the corresponding stress state has one large compressive stress component, which may lead to winkling. The locus of this range is taken from the special geometric specimens based on the concept of a butterfly specimen. Negative stress triaxiality range from -1/3 to 0 is taken from

compression experiments of cylinder specimens with different heights. The locus of this range showed that there was a vertical asymptote at the value of or σ_h/σ_e = -1/3. The authors concluded that the value of -1/3 was a low limit of stress triaxiality [84].

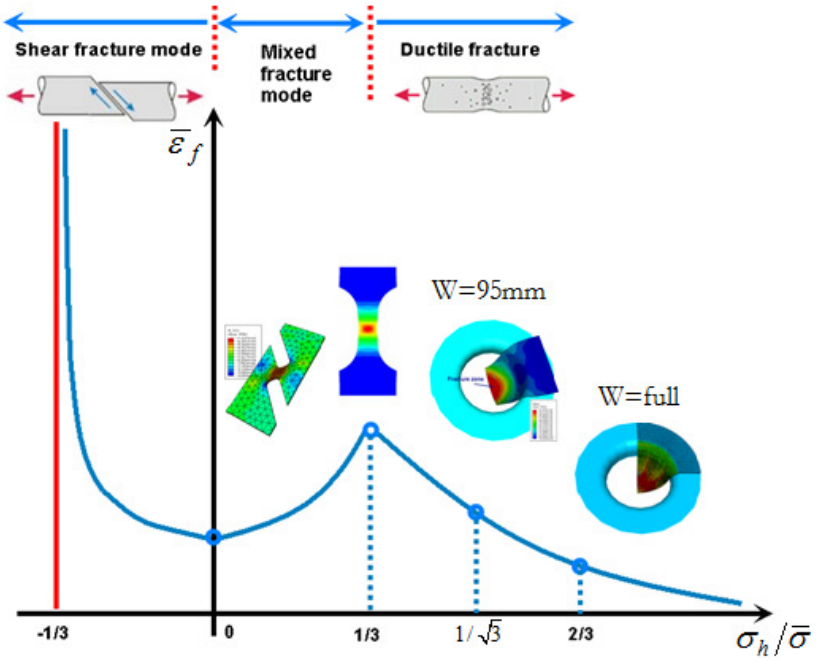

Fig. 4.3 Full range of stress triaxiality vs. equivalent strain

4.3.2 The fracture criteria for metal sheet

The objective of this section is to present some fracture criteria which were used widely in the prediction of damage initiation criteria for the metal sheet industry. The criteria were constructed in the different spaces such as principal strain, principal stress, and in the mixed space of the stress triaxiality and the equivalent strain. For comparison and using, it is necessary to transform into unique space. In this study, these criteria were transformed into the space of stress triaxiality and equivalent strain. This work is convenient to apply numerical simulation software (ABAQUS) that requires the damage criteria by providing the equivalent plastic strain at the onset of ductile damage as a function of stress triaxiality and strain rate [86].

Lee et al. [87,88,89,90] presented relations between stress and strain in three-dimension plasticity. These relations can use to convert fracture criteria into unique certain space. In this thesis, his transformations are used to convert the fracture criteria into a unique space of the stress triaxiality and the equivalent strain (see [87]).

4.3.2.1 Fracture criteria based on stress state, strain state.

The fracture criteria based on stress and strain state or combination of both stress and strain state are the phenomenological models which describe the failure in the material in limits of mechanical variables such as temperature , strain rate, stress, strain, etc (see Table 4.2). All models in this group presented the failure model is a function which depends of the variables and if the function reaches a critical value, failure is expected in the material. One of the simplest models to predict mechanical failure is only to consider the state of stress or strain. The failure occurs when the state of stress or strain reaches a critical value C.

$$\bar{\varepsilon} \text{ or } \bar{\sigma} = \mathrm{C} \tag{4.3}$$

$$\tau_{\max} = \mathrm{C} \tag{4.4}$$

Based on stress state	Based on strain state	Based on stress - strain state
Maximum principles tress	Maximum principle strain	Cockcroft-Latham
Tresca's and von Mises	Constant equivalent strains	
Mohr's failure criterion	Forming Limit Diagram	

Table 4.2 Fracture criteria based on stress state, strain state

4.3.2.2 Fracture forming limit diagram (FFLD)

The Forming Limit Diagram (FLD) describes a limitation of sheet forming operation in a space of principal strains. This limitation is a locus which the process of a localized neck is initiated. Lee [87] presented an approach which can transform the straight locus in the space of principal strains into the hyperbola locus in the $(\bar{\varepsilon},\eta)$space by analyzing the data points from fracture experiments. The author suggested that the fracture locus in the principal strain space could be approximated by the following relationship:

$$\varepsilon_1 + \varepsilon_2 = C \tag{4.5}$$

The above relationship showed that the FFLD is a straight made with horizontal direction in 45 degrees. It is easy to calibrate this criterion by one test. Nevertheless, it should be noted that this criterion applies only for metal sheets, which are in the state of plane stress. In $(\bar{\varepsilon},\eta)$ space, the formula of (4.5) can be written as following:

$$\bar{\varepsilon} = \frac{C}{\eta} \tag{4.6}$$

4.3.2.3 Cockcroft-Latham criteria

Cockcroft and Latham are damage criteria based on both stresses and strains. The total amount of plastic work done per unit volume, $(W_{cr})_f$, at the fracture point can be described in an integrate form of principal tensile test. This criterion is modified by Brozzo et al. [91], Clift et al. [92] and Oyane et al. [93] to become a criterion which depends on both stresses and plastic strains it means that only stress or strain can describe a ductile fracture. In this model, the fracture will not occur if all the principal stresses are a smaller or equal to zero. The fracture happens when integral of tensile stress reaches a critical value.

$$\int_0^{\bar{e}_f} \sigma_1 d\bar{\varepsilon} = (W_{cr})_f \tag{4.7}$$

4.3.2.4 Ductile criterion and Johnson-Cook

The ductile criterion is a phenomenological model for predicting the onset of damage due to nucleation, growth, and coalescence of voids. The model assumes that the equivalent plastic strain at the onset of damage, $\bar{\varepsilon}_f$, is a function of stress triaxiality and strain rate:

$$\bar{\varepsilon}_f(\eta, \dot{\bar{\varepsilon}}) \tag{4.8}$$

where η is the stress triaxiality, $\dot{\bar{\varepsilon}}$ is the equivalent plastic strain rate. The criterion for damage initiation is met when the following condition is satisfied:

$$\int \frac{d\bar{\varepsilon}}{\bar{\varepsilon}_f(\eta, \dot{\bar{\varepsilon}})} = 1 \tag{4.9}$$

The Johnson-Cook criterion is a special case of the ductile criterion in which the equivalent plastic strain at the onset of damage, $\bar{\varepsilon}_f$, is assumed to be the form of

$$\bar{\varepsilon}_f = \left[d_1 + d_2 e^{-d_3 \eta} \right] \left[1 + d_4 \ln\left(\frac{\dot{\bar{\varepsilon}}}{\dot{\varepsilon}_0} \right) \right] \left(1 + d_5 T \right) \tag{4.10}$$

where d_1 – d_5 are failure parameters and $\dot{\varepsilon}_0$ is the reference strain rate. T is the non-dimensional temperature. The constants d_1 – d_5 were determined from tests with high stress triaxiality. Therefore, the equation (4.10) may not describe correctly fracture behavior for zero or negative stress triaxialities. Furthermore, the Johnson-Cook fracture criterion does not tell how to deal with the situation when the stress triaxiality is not constant but changes in the loading process.

4.3.2.5 Shear criteria

The shear criterion is a phenomenological model for predicting the onset of damage due to shear band localization. The model assumes that the equivalent plastic strain at the onset of damage, $\bar{\varepsilon}_s$, is a function of the shear stress ratio and strain rate:

$$\bar{\varepsilon}_s \left(\theta_s, \dot{\bar{\varepsilon}} \right) \tag{4.11}$$

$$\theta_s = \frac{q + k_s p}{\tau_{\max}} \tag{4.12}$$

The θ_s is the shear stress ratio, $\tau_{\max}$ is the maximum shear stress, and k_s is a material parameter. The criterion for damage initiation is met when the following condition is satisfied:

$$\int \frac{d\bar{\varepsilon}}{\bar{\varepsilon}_s \left(\theta_s, \dot{\bar{\varepsilon}} \right)} = 1 \tag{4.13}$$

4.3.2.6 Wilkins criteria

Wilkins postulated that fracture occurs when the following integral exceeds a critical value D_C over a critical dimension R_C. This criterion is described in two factors: the hydrostatic stress and the asymmetric stress.

$$D_C = \int_0^{\bar{\varepsilon}_f} \frac{1}{\left(1 - \gamma_w \sigma_h \right)} \left(2 - A_w \right)^{\beta_w} d\bar{\varepsilon} \text{ in } \mathrm{R}_C \tag{4.14}$$

$$A_w = \max\left(\frac{S_2}{S_1}, \frac{S_2}{S_3}\right), S_1 > S_2 > S_3 \tag{4.15}$$

Where S_1,...S_3 is the principal stress deviators; β_w and γ_w are material constants. The parameter A_w ranges from 0 to 1 and when $A_w = 1$ the stress field is symmetric (and asymmetric when $A_D = 0$).

4.3.2.7 Gurson model

The Gurson model considers mechanical damage with the physical mechanism of ductile fracture and directly works with nucleation, growth, and coalescence of voids. The damage is described through a parameter, f, can vary from a value f = 0 for undamaged material, to f = 1 for a completely damaged material. The von Mises yield function is modified to account for the presence and evolution of voids. The modified yield function can be stated as following:

$$\Phi = \frac{\bar{\sigma}^2}{\sigma_m^2} + 2q_1 f^* \cosh\left(\frac{tr(\boldsymbol{\sigma})}{2\sigma_m}\right) - 1 - \left(q_1 f^*\right)^2 = 0 \tag{4.16}$$

where $\boldsymbol{\sigma}$, $\bar{\sigma}$, and σ_m are the macroscopic stress tensor, the effective Mises stress, hydrostatic pressure, and yield stress of the fully dense matrix material, respectively. q_1 is a constant that amplifies the hydrostatic stress effect for all strain levels. The f^* is the effective void volume fraction given by

$$f^*(f) = \begin{cases} f & if \quad \mathrm{f} \le \mathrm{f}_c \\ f_c + \dfrac{1/q_1 - f_c}{f_f - f_c}\left(f - f_c\right) & if \quad \mathrm{f} > f_c \end{cases} \tag{4.17}$$

where f is the void volume fraction, f_c the critical void volume fraction, and f_f is the void volume fraction at rupture. The evolution of the void volume fraction is due to two contributing phenomena, namely void growth and void nucleation. Therefore, the time derivative of the void volume fraction can be calculated as

$$\dot{f} = \dot{f}_{growth} + \dot{f}_{nucleation} \tag{4.18}$$

where subscripts 'growth' and 'nucleation' stand for void growth and void nucleation, respectively. Based on the mass conservation law, the change in the void volume fraction due to void growth can be described as follows

$$\dot{f}_{growth} = (1-f)\,tr(\dot{\varepsilon}) \tag{4.19}$$

The void nucleation dynamics is governed by the following relationship

$$\dot{f}_{nucleation} = A_G \dot{\varepsilon}_e \tag{4.20}$$

where $A_G = \frac{f_n}{s_N\sqrt{2\pi}} e^{-1/2\left(\frac{\varepsilon_e-\varepsilon_N}{s_N}\right)^2}$ (4.21)

where f_n is the void volume fraction of nucleating particles, ε_e is the mean strain for nucleation and s_N is the standard deviation. The Gurson model strongly depends on the density of element in FEM modeling [81].

4.3.2.8 CrachFEM model

This criterion is proposed by Gese and Hooputra [81] which is applicable to thin sheets and extrusions (plane stress). It distinguishes between three mechanisms responsible for ductile fracture, shear fracture and sheet instability in which are described by three different expressions. All three-failure modes are uncoupled from each other due to avoiding a localization of the strains due to softening of the material prior to fracture. CrachFEM is implemented into FEM codes coupled with the modular elasto-plastic material model under an explicit-dynamic integration scheme.

CrachFEM can be used to predict the damage driven to three main mechanisms for both shell and solid elements. The prediction of ductile and shear fracture can be applied consistently for shells and solids. However, the prediction of localized necking is only suited for shell elements. Thereby, there are two models for ductile fracture with the shell element and solid element.

Ductile fracture model

For plane stress condition, the equivalent strain to fracture is assumed to depend only on the stress triaxiality. Hooputra et al. [81] have given simplified analytical expressions, the equivalent plastic strain is given by the following function of the stress triaxiality and strain rate.

$$\bar{\varepsilon}_d(\eta,\dot{\bar{\varepsilon}}) = \frac{\varepsilon_T^+ \sinh\left[k_d\left(\eta^- - \eta\right)\right] + \varepsilon_T^- \sinh\left[k_d\left(\eta - \eta^+\right)\right]}{\sinh\left[k_d\left(\eta^- - \eta^+\right)\right]} \tag{4.22}$$

where ε_T^+ and ε_T^- correspond to the equivalent plastic strain at ductile damage initiation for equi-biaxial tensile and equi-biaxial compressive deformation, respectively. For isotropic yield rule, the stress triaxiality in equi-biaxial tensile deformation state, η^+, is 2/3, and in equi-biaxial compressive deformation state, η^-, is -2/3 (see more in [81]).

For 3D-stress condition, the stress triaxiality η is no longer unique. Additional parameter used to describe the stress state is the ratio $\tilde{\sigma} = \sigma_1/\bar{\sigma}$ of first principal stress and von Mises equivalent stress. Ductile fracture can occur only if the first principal stress σ_1 is positive. These two stress state parameters can be combined to a ductile fracture parameter β for an individual material:

$$\beta = \beta(\tilde{\sigma},\eta) = \frac{1 - s_d\eta}{\tilde{\sigma}} \tag{4.23}$$

or can be described by the analytical function following:

$$\bar{\varepsilon}_f^d = \varepsilon(\tilde{\sigma},\beta) = d\exp^{-3q\beta} \tag{4.24}$$

where s_d, q and d are a material dependent parameter. This equation assumes a monotonic decrease of the fracture strain with increasing stress triaxiality. A more general equation included the orthotropy of fracture is presented as following:

$$\bar{\varepsilon}_f^d = d_0 e^{-3c\eta} + d_1 e^{3c\eta} \tag{4.25}$$

Where d_0, d_1, c are material dependent parameters.

Shear fracture model

In the shear dominated zone, the fracture strain is postulated to depend both on the hydrostatic and deviatoric state.

$$\bar{\varepsilon}_f^s = d_2 e^{-f_S \theta_S} + d_3 e^{f_S \theta_S} \tag{4.26}$$

where c, $d_{0.}$- d_3, f_S and k_s are three material constants; new shear fracture parameter, θ_S, is defined by

$$\theta_S = \frac{\bar{\sigma}}{\tau_{\max}}(1 - 3k_s\eta) \quad ; \quad \tau_{\max} = \frac{\sigma_1 - \sigma_3}{2} \tag{4.27}$$

Since θ_S depends on the stress triaxiality and the ratio τ_{max}/σ_e, it can be used for both plane-stress and general 3D stress conditions. Similar, it has given simplified analytical expressions of the equivalent plastic strain for shear fracture with respect to θ_S is given in an analytical function for the plane stress condition:

$$\bar{\varepsilon}_s(\theta_s, \dot{\bar{\varepsilon}}) = \frac{\varepsilon_S^+ \sinh\left[f(\theta_s - \theta_S^-) \right] + \varepsilon_S^- \sinh\left[f(\theta_S^+ - \theta_S) \right]}{\sinh\left[f(\theta_S^+ - \theta_S^-) \right]} \tag{4.28}$$

where ε_S^+ and ε_S^- correspond to the equivalent plastic strain at shear damage initiation for equi-biaxial tensile and equi-biaxial compressive deformation, respectively. The parameters θ_S^+ and θ_S^- correspond to the values of θ_S at $\eta = \eta^+$ and $\eta = \eta^-$, respectively.

The equation (4.26) can be presented in the $(\bar{\varepsilon}, \eta)$ by converting θ_S. in different ranges as following:

$$\begin{cases} \theta_S = \dfrac{\sqrt{24}\,(3k_s\eta - 1)\left(2 - 3\eta - \sqrt{3}\eta\sqrt{4 - 9\eta^2}\right)}{9\eta - 2 - \sqrt{3}\eta\sqrt{4 - 9\eta^2}} & \text{with } 0 \le \eta \le 0.33 \\ \theta_S = \dfrac{\sqrt{24}\,(3k_s\eta - 1)\left(2 - 3\eta - \sqrt{3}\eta\sqrt{4 - 9\eta^2}\right)}{9\eta - 4 + \sqrt{3}\eta\sqrt{4 - 9\eta^2}} & \text{with } 0.33 \le \eta \le 0.67 \end{cases} \tag{4.29}$$

The model was clearly developed with a view of industrial application but involves totally in seven free parameters. The shear fracture model acknowledges the joint effect of stress triaxiality and the deviatory state through the definition of the parameter θ_S. Both fracture models are based on a fracture locus of the equivalent plastic strain and

stress triaxiality η (e.g. the equivalent plastic strain is given as a function of stress triaxiality $\bar{\varepsilon}^f(\eta)$). In the case of a linear strain path, this function can be used directly as a fracture criterion. However, in the case of nonlinear strain paths, it is necessary to use an integral fracture criterion as following [86].

$$\int_0^{\bar{\varepsilon}^f} \frac{d\bar{\varepsilon}}{\bar{\varepsilon}^f(\eta)} = 1 \tag{4.30}$$

Instability

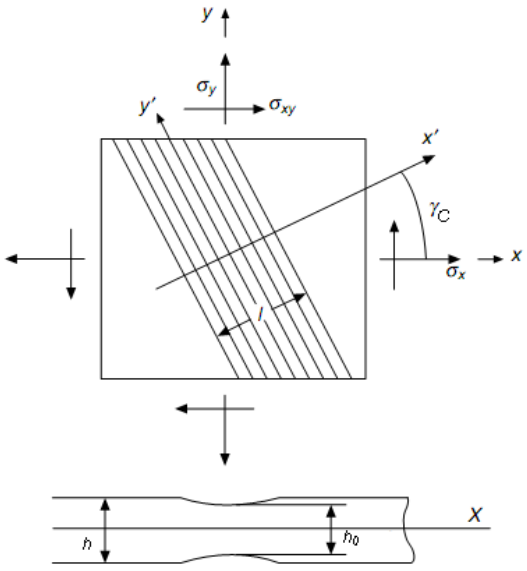

Fig. 4.4 The imperfection triggering a localised neck in the CRACH algorithm

The basic concept of sheet instability in CrachFEM algorithm is based on Marciniak–Kuczynski model (M-K). In CrachFEM model, the thickness ratio of imperfection and sheet is defined approximately at the neck cross section as following:

$$\frac{h}{h_0} = \left(1 - d_C \cos\left(\frac{\pi x'}{l}\right)\right) \tag{4.31}$$

where h and h_0 are the thickness of imperfection and initial sheet, respectively. The value of h_0 is set to 1 and it has no influence on the numerical problem. The parameter d_C is the inhomogeneity that its value increases with deformation in order to account for the roughening of the sheet during plastic deformation. Its initial value is calibrated from the limit strain measured in one tensile experiment of the individual sheet.

The changing level of necking is measure by a ratio x′/l in a coordinate of Ox'y', in which x′ direction is normal to the necking direction (see Fig. 4.4). This ratio will changes from 0 in the centre of the neck to 0.5 in the region of the sheet where deformation is homogeneous. The equation is used to calculate the strain inside imperfection. The strain outside of imperfection is calculated according to the strain history of a finite element.

Similar to MK model, CrachFEM model also allows the specification of an anisotropic distribution of thickness imperfections as a function of angle γ_C with respect to the local material orientation. The global strain in the vicinity of the neck is increased incrementally as long as the force equilibrium is fulfilled as (4.32) and the limit strain for one deformation path is derived through optimization of (4.33):

$$\frac{h_0}{h} = \frac{\sigma^{x'}}{\sigma_0^{x'}} \qquad \frac{h_0}{h} = \frac{\sigma^{x'y'}}{\sigma_0^{x'y'}} \tag{4.32}$$

$$\bar{\varepsilon}^f = \min_{\gamma_C} \left(\bar{\varepsilon}^f \left(\gamma_C \right) \right) \tag{4.33}$$

The onset of necking instability is assumed to occur if it may not be possible to find a solution that satisfies equilibrium and compatibility conditions once localization initiates at a particular zone; consequently, failure to find a converged solution is also an indicator of the onset of localized necking. Alternatively, the ratio of the rate of deformation inside a groove relative to the rate of deformation if no groove were present is greater than a critical value.

4.4 Comparison among damage criteria

Wierzbick et al. [94] has a full comparative study of the fracture criteria that is used commonly in industrial application (see Fig. 4.5). Enhancing in these criteria, CrachFEM criterion showed advantages that can be used to predict the fracture in SPIF process because of following reasons:

- ✓ It can predict the fracture due to three different mechanisms. Indeed, the mechanism of deformation and damage in SPIF process has still discussed on positive explanations in above. Thus, CrachFEM criteria are a first selection to predict the damage in SPIF. These failure modes are uncoupled from each other in CrachFEM criterion.
- ✓ The FEM simulation of SPIF process takes a huge computational time. In additional, the fracture criteria based on micromechanical approach (e.g. Gurson-type model and Wilkin model) have the predicted accuracy highly depended on mesh refinement as these models cause strain softening prior to fracture. Increasing in mesh refinement leads to increase in computational time.
- ✓ The damage criteria are limited to represent one of three mechanisms. For example, Gurson-type models only present ductile fracture and as such ignore the fracture mechanism based on shear.
- ✓ CrachFEM model can be used to predict the fracture for both solid element (3D stress state) and shell element (plane stress state). These two elements were used to model FEM simulation in SPIF process.
- ✓ The calibration of CrachFEM model only requires a narrow range of stress triaxiality through some experiments. Other ranges of stress triaxiality can be fitted by using the simplified analytical expressions.

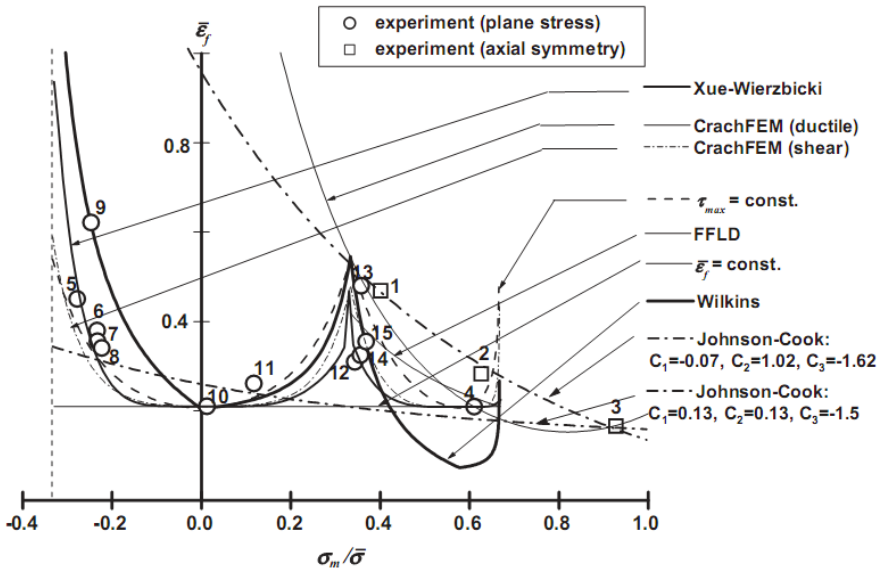

Fig. 4.5 Comparison of seven fracture criteria for 2024-T351 aluminums [94]

4.5 Progressive damage and failure for ductile metals in ABAQUS

ABAQUS is addressed as FEM simulation software for the failure prediction in SPIF process. Therefore, we need to clarify some computation concepts as well as the general framework for modeling damage and failure. For ductile metal, ABAQUS offers two options for prediction of damage initiation with distinct types of material failure criteria. They can be classified in the following categories: the damage initiation criteria for the fracture of metals and the damage initiation criteria for the necking instability of sheet metal. Most damage criteria are used under the explicit approach (ABAQUS/Explicit).

Particularly, ABAQUS offers many damage initiation criteria; more than one can be specified for a given material. In the case of multiple damage initiation criteria are specified for the same material, they are treated independently. Once a particular initiation criterion is satisfied, the material stiffness is degraded according to the specified damage evolution law for that criterion (see more in section 19.1 and 19.2 of [86]).

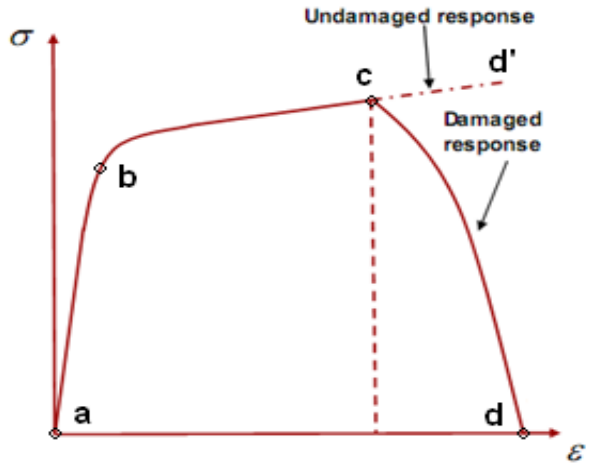

Fig. 4.6 General framework for modeling damage and failure

General framework for modeling damage and failure shows on Fig. 4.6. It is modeled in four distinct parts: (a-b-c-d`) evolution of material without failure modeling includes elastic part and plastic part; (point c) a damage initiation criterion; (c-d) a damage evolution law; (point d) material stiffness is fully degraded. Material failure is considered as the complete loss of load-carrying capacity that results from progressive degradation

of the material stiffness. The stiffness degradation process is modeled using damage mechanics.

4.5.1 Materials and temperature in ABAQUS

Data from tensile tests of metal materials showed high dependent on temperature and strain rate. They will be implemented in ABAQUS environment by using two options: strain rate-dependent data and temperature-dependent data. ABAQUS interpolates linearly for values between those given. The property is assumed to be constant outside the range of independent variables given. The data of tensile test (stress-strain) at two different temperatures is presented in ABAQUS as Fig. 4.7.

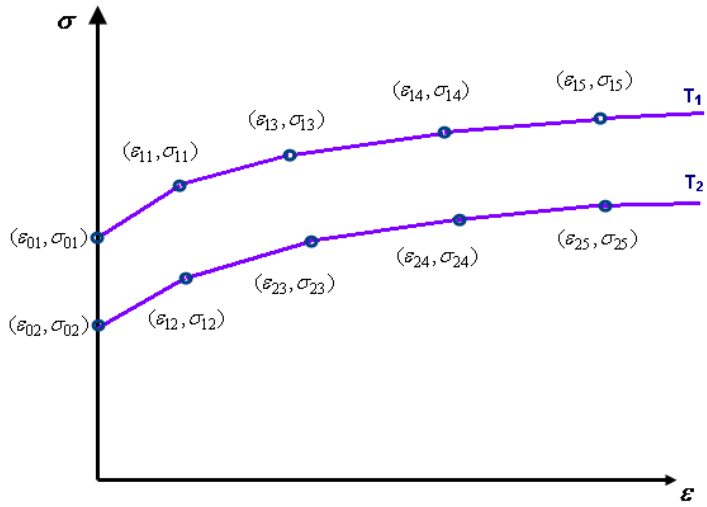

Fig. 4.7 Temperature-dependent data in ABAQUS

When material properties depend on several variables, the variation of the properties with respect to the first variable must be given at fixed values of the other variables, in ascending values of the second variable, then of the third variable, and so on. The data must always be ordered so that the independent variables are given increasing values. This process ensures that the value of the material property is completely and uniquely defined at any values of the independent variables upon which the property depends. Material data are often specified as functions of independent variables such as temperature. Material properties are made temperature dependent by specifying them at several different temperatures.

Rate-sensitive material constitutive behavior may introduce nonphysical high-frequency oscillations in an explicit dynamic analysis. To overcome this problem, ABAQUS/Explicit computes the equivalent plastic strain rate used for the evaluation of strain-rate-dependent data as:

$$\dot{\bar{\varepsilon}}\Big|_{t+\Delta t} = \omega\frac{\Delta\bar{\varepsilon}}{\Delta t} + (1-\omega)\dot{\bar{\varepsilon}}\Big|_{t} \tag{4.34}$$

Here $\Delta\bar{\varepsilon}$ is the incremental change in equivalent plastic strain during the time increment Δt, and $\dot{\bar{\varepsilon}}\Big|_{t}$ and $\dot{\bar{\varepsilon}}\Big|_{t+\Delta t}$ are the strain rates at the beginning and end of the increment, respectively. The factor $\omega(0<\omega\le 1)$ facilitates filtering high-frequency oscillations associated with strain-rate-dependent material behavior.

4.5.2 Damage evolution and fracture criteria

The damage evolution law describes the rate of degradation of the material stiffness once the corresponding initiation criterion has been reached. For damage in ductile metals ABAQUS/Explicit assumes that the degradation of the stiffness associated with each active failure mechanism can be modeled using a scalar damage variable, $d_i(i \in N_{act})$, where N_{act} represents the set of active mechanisms. At any given time during the analysis the stress tensor in the material is given by the scalar damage equation

$$\sigma = (1-D)\bar{\sigma} \tag{4.35}$$

where D is the overall damage variable and $\bar{\sigma}$ is the effective (or undamaged) stress tensor computed in the current increment. σ is the stresses that would exist in the material in the absence of damage.

As Fig. 4.8, the onset of damage is at D with respect to σ_y and $\bar{\varepsilon}$ (the yield stress and equivalent plastic strain, respectively). When the overall damage variable reaches the value D = 1 (at $\bar{\varepsilon}_f$, is the equivalent plastic strain at failure), the material has lost its load-carrying capacity. The value of the equivalent plastic strain at failure, $\bar{\varepsilon}_f$, depends on the characteristic length of the element and cannot be used as a material parameter for

the specification of the damage evolution law. Instead, the damage evolution law is specified in terms of equivalent plastic displacement, $\bar{u}^{pl}$, or in terms of fracture energy dissipation, G_f (see section 19.2 of [86]). By default, an element is removed from the mesh if all of the section points at any one integration location have lost their load-carrying capacity.

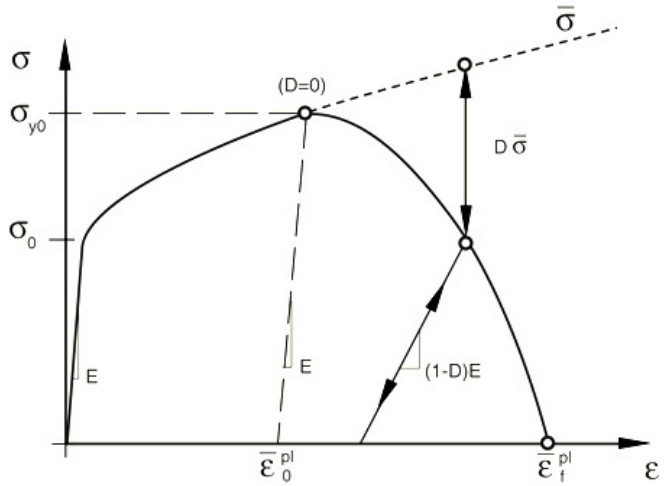

Fig. 4.8 Characteristic stress-strain behavior of a material undergoing damage

4.6 Summarizing the chapter

This chapter summarized the positive explanations about the deformation mechanism of SPIF process. There is no definitive answer which can explain all aspects of problems in deformation and fracture of material with SPIF process. It can to be a combination of all above explanations.

A comparison among the damage criteria used commonly in practical industry at recent years is also presented. The CrachFEM criterion is chosen to implement into ABAQUS for prediction of mechanical fracture in SPIF process with sheet metal.

The aspect of using ABAQUS for implementing material model with sensitivity of temperature and strain rate, and damage prediction is also mentioned in this chapter.

Chapter 5

Mechanical Testing

5.1 Mechanical testing for Magnesium alloy

The magnesium alloy sheet AZ31 used in all experiments has the chemical properties and mechanical properties as presented on Table 5.1 and Table 5.2.

Component Elements Properties	%
Aluminum, Al	2.50 - 3.50 %
Calcium, Ca	<= 0.040 %
Copper, Cu	<= 0.050 %
Iron, Fe	<= 0.0050 %
Magnesium, Mg	97.0 %
Manganese, Mn	>= 0.20 %
Nickel, Ni	<= 0.0050 %
Silicon, Si	<= 0.10
Zinc, Zn	0.60 - 1.40 %

Table 5.1 Component Elements Properties of AZ31

Mechanical Properties	SI Unit
Density	1770 kg/m^3
Elastic Modulus	45.10^9 N/m^2
Poisson Ratio	0.35
Shear Modulus	17.10^9 N/m^2
CTE	26.10^{-6}m/m-°C (0-100°C), 27.10^{-6}m/m-°C (20-200°C)
Specific Heat Capacity	1000 J/kg-°C
Thermal Conductivity	96.0 J/s-m-K

Table 5.2 Mechanical Properties of AZ31

5.1.1 Uniaxial Testing

To investigate the mechanical properties of magnesium AZ31 at both room temperature and elevated temperature. The experiments were performed on standard dog-bone specimens that were cut from the magnesium sheet (1.5mm) in three orientations of 0°,

45°, and 90° with respect to the rolling direction RD. The experiments were considered with four levels of temperature and three level of strain, as showed on Table 5.3. They were used to check anisotropic properties of AZ31 as well as the sensitivity to temperature and deformation speed. The experimental setup for uniaxial tensile testing to be performed at elevated temperatures was arranged as shown in Fig. 5.1.

Temperature (°C)	Rate	
	Speed of cross-head (mm/s)	Average strain rate (s^{-1})
Ambient	0.02, 0.2, 2	0.1, 0.01, 0.001
200	0.02, 0.2, 2	0.1, 0.01, 0.001
250	0.02, 0.2, 2	0.1, 0.01, 0.001
300	0.02, 0.2, 2	0.1, 0.01, 0.001

Table 5.3 Experimental parameters for tensile testing

The servo-hydraulic computer-controlled MTS 322 was used to perform a displacement controlled zero to tension uniaxial tests. Change in specimen strain can be measured using an ARAMIS™ vision system. It operates based on recording the images of a specimen surface in gauge length at a predefined frequency. The front surface of a specimen in gauge length postulated to make a clear pattern. The images are then analyzed through a matrix of points linked to the painted pattern, enabling the measurements of strains and displacements of each point and their evolution in the test timeframe.

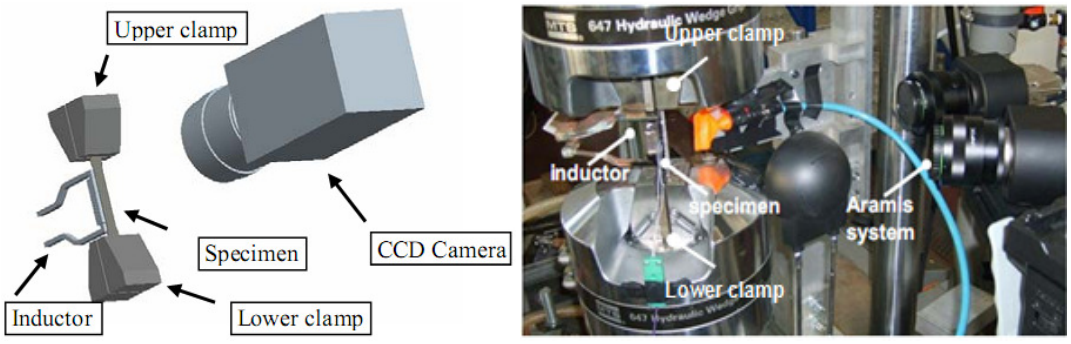

Fig. 5.1 Experimental apparatus for uniaxial tensile tests at elevated temperatures

An induction head places in parallel to back surface of a specimen. The shape of the inductor is optimized to provide uniform and highly controllable temperature profiles

[95].Temperature of a specimen was controlled through a K-type thermocouple, spot-welded in the middle of the specimen gauge length. The position of the induction head is adjusted during heating process by means of a brushless motor to get uniform thermal profile at the middle of specimen. The experimental system is presented in Fig. 5.1.

The adopted tensile test procedure consists of four major subsequent phases: i) the specimen is heated till the deformation temperature in 120 second; ii) it maintained deformation temperature in the next 120 second to insure a uniform thermal zone at the middle of the specimen; iii) the specimen is deformed according to testing parameters; iv) the specimen is cooled in calm air. The speed of the cross-head is kept at constant as showed on Table 5.3. The test is stopped when a fracture appears. The segments of a specimen are removed and then the observation of their microstructures is investigated.

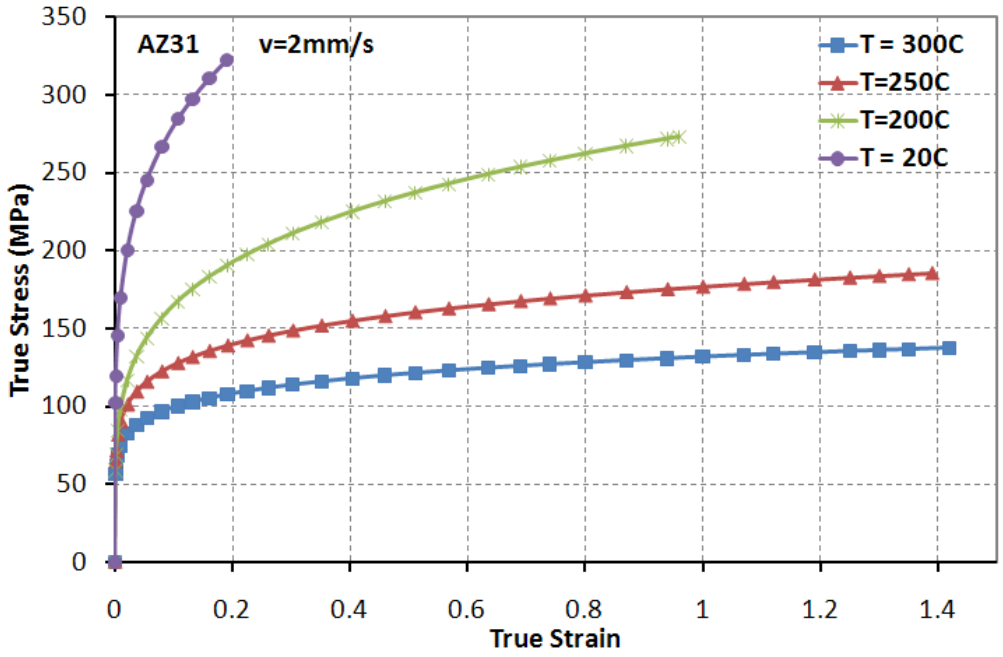

Fig. 5.2 The sensitivity to temperature at failure for a speed of 2mm/s.

The relationships between stress and strain are the crucial information for the study of formability of a sheet metal. The stress-strain curves are extracted from analyzing the images recorded from the ARAMIS system. In the section where the fracture appears, the five points will be chosen in equal spaces to calculate major and minor strain values.

The average calculated values of these points are used in subsequent analyses. The procedure is performed automatically until the system is able to recognize the five points in the necked region. The values of stress are calculated from the force recordings by applying the volume constancy for instant area determination [96].

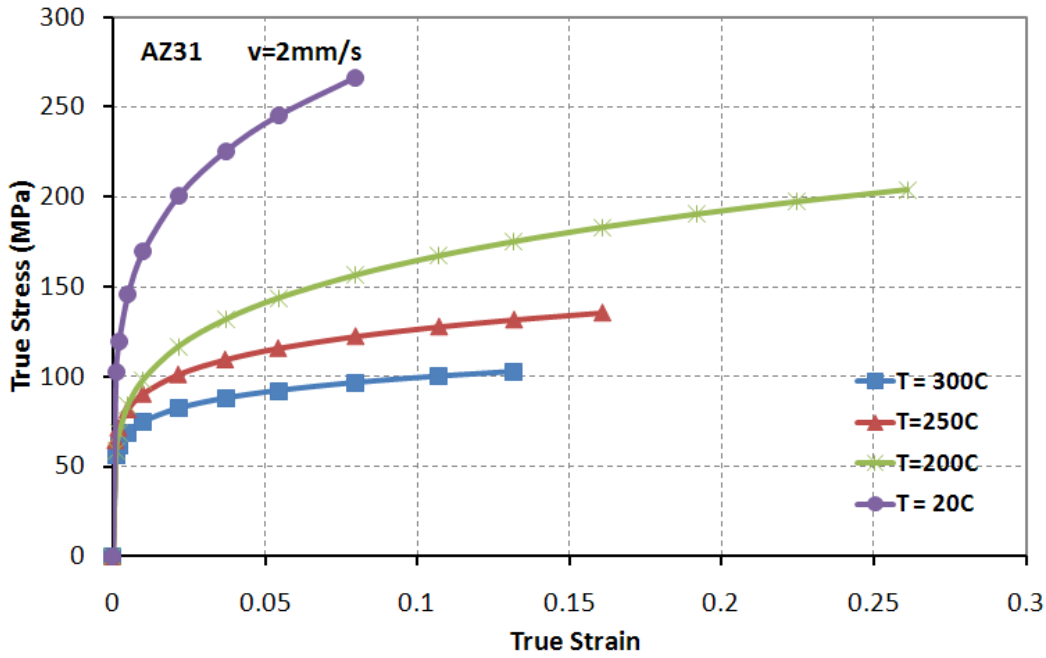

Fig. 5.3 The sensitivity to temperature at necking for a deformation speed of 2mm/s

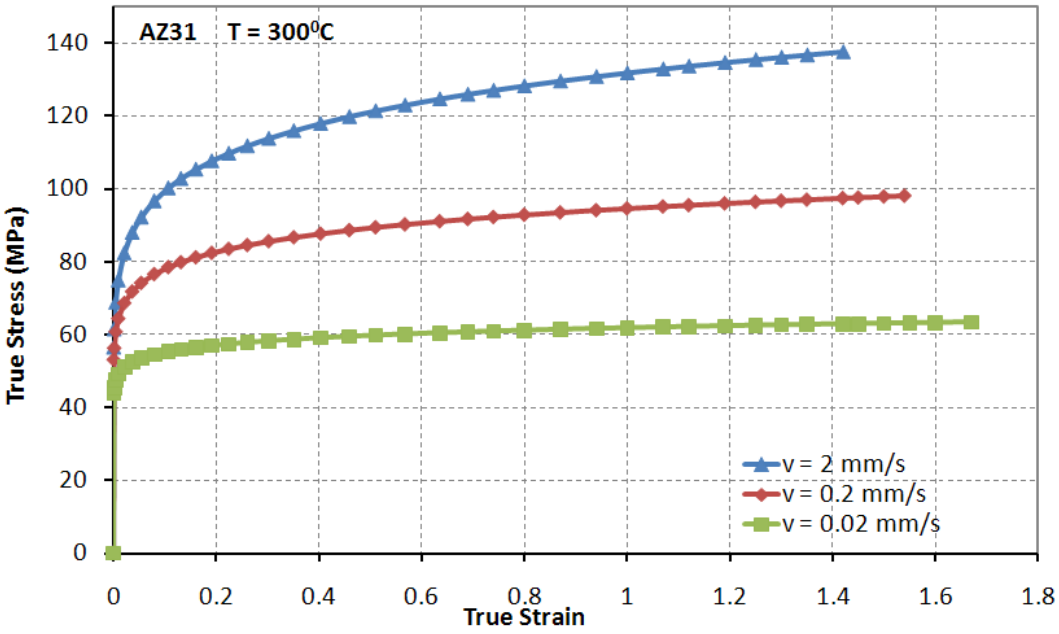

Fig. 5.4 The sensitivity to deformation speed at failure for temperature 300°C

The magnesium alloy AZ31 exhibits poor formability at the ambient temperature (T = 20°C). The formability increases following increase of processing temperature. Fig. 5.2 showed the material sensitivity to temperature at failure, for a constant cross-head speed of 2mm/s. It is noted that the considerable decrease in the flow strength together with a significant increase in the material strain to failure thanks to the increase of processing temperature. The strain at fracture also increases with increasing of temperature. Fig. 5.3 refers to the same process conditions of Fig. 5.2, but the curves were cut when the necking was reached. It becomes evident that the post-necking deformation is much more pronounced; showing that at necking the material presents at room temperature a strain at failure even higher than at the elevated temperature.

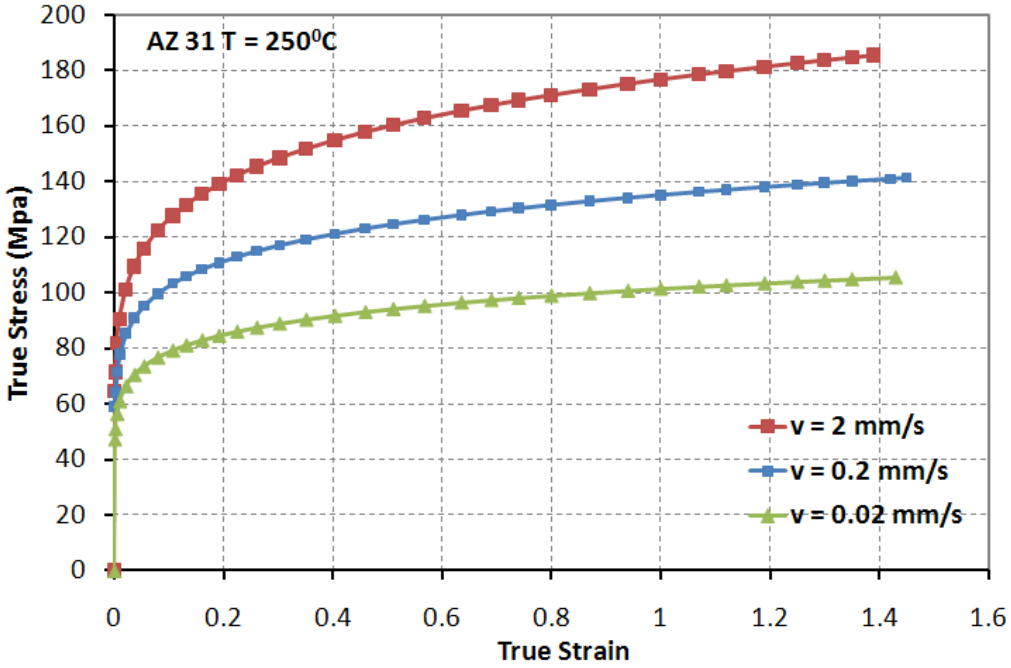

Fig. 5.5 The sensitivity to deformation speed at failure for temperature 250°C

Fig. 5.4 and Fig. 5.5 shows the significant material sensitivity to deformation speed in terms of the increase of flow stress and strain at failure at T=250°C and T=300°C. Similar results were found for T=200°C. The increase of fracture strain thanks to the decrease of deformation speed at T = 300°C. However, the fracture strain at T = 250°C showed that a slight decrease is in the strain for v=0.02mm/s. This phenomenon can be due to grain growth at low deformation speed (see Fig. 5.7b).

5.1.2 Micro-structural characterization

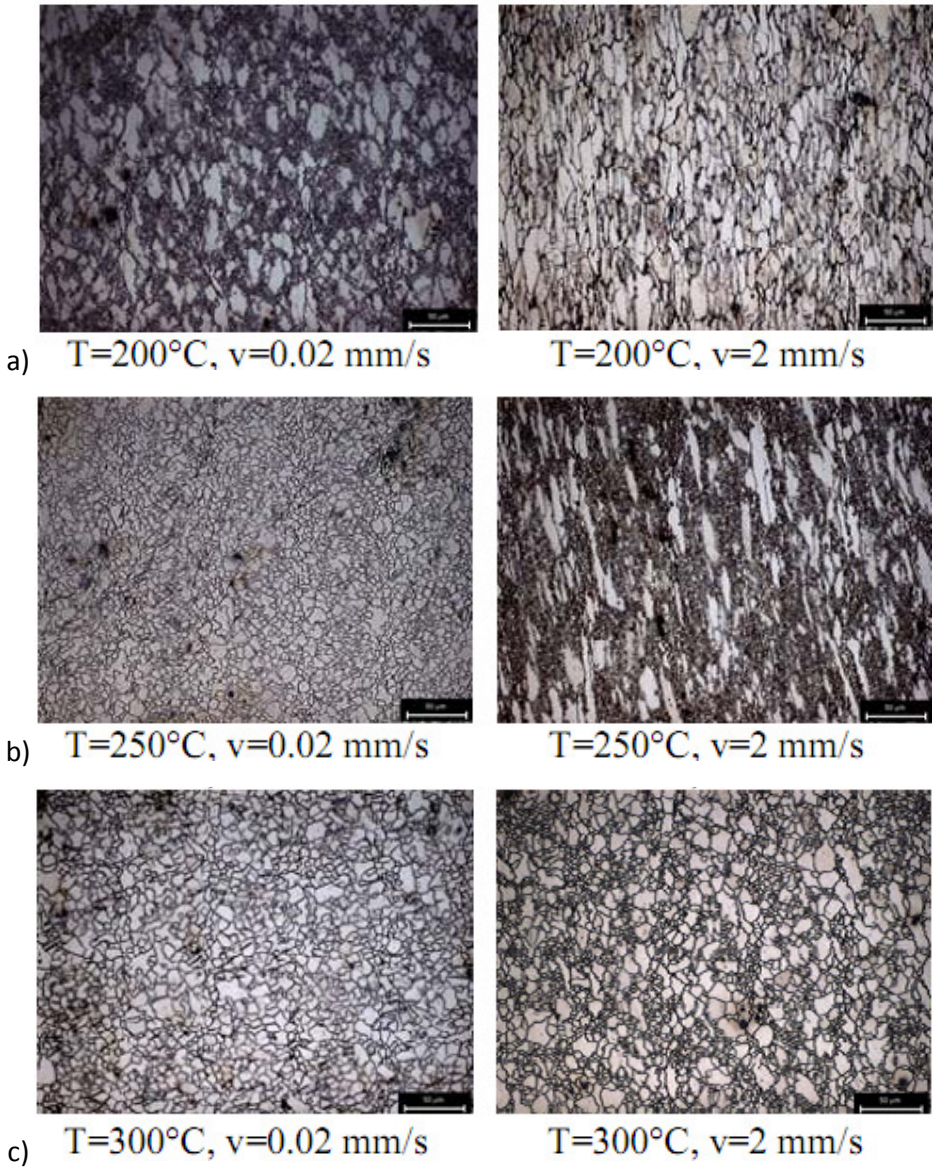

Fig. 5.6 Microstructure of specimens in direction of 45^0

The specimens for tensile testing provided in sheets with the annealed condition. The initial microstructure was fully recrystallized with an average grain size of 12µm. After the finished tensile test, segments of specimens at fracture zone were prepared for investigation of their microstructures. The aim of this investigation is to identify those process conditions that assure the best micro-structural quality. The results of observation under an optical microscope are presented in Fig. 5.6. For brevity, the

results of specimens in the direction of 45° with respect to rolling direction are shown in this section. The results of other directions are similar to these.

The Fig. 5.6 is arranged in an order of increasing the temperature from the top to the down and increasing the deformation speed from left to right side. They showed that it is clear to observe the dynamic recrystallization (DRX) at the low deformation speed while this phenomenon is absent from high deformation speed. Particularly, a recrystallized fraction of about 35% is observed at 200°C with low speed (0.2mm/s) while the grains are elongated in the tensile direction at 2mm/s without any appearance of DRX.

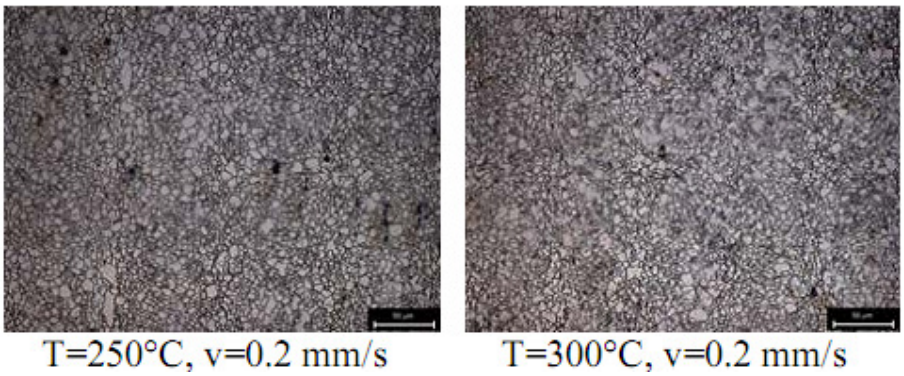

Fig. 5.7 Microstructure of specimens at v=0.2mm/s in different temperatures

At low deformation, v=0.02mm/s, increasing in the temperature driving to the microstructure of AZ31 becomes fully recrystallized with homogeneously recrystallized grains. However, at the high deformation speed, the grains are still elongated in the tensile direction with partial DRX although the temperate is increased to 250°C. At 300°C, the grains are recrystallized but the distribution of the grains is not uniform as in case of the lower speed. This phenomenon can be concluded that forming works of AZ31 at high strain rate cannot assure a homogeneous, fully recrystallized microstructure. Additionally, at a relative low temperature (T=200°C or lower than) the dynamic recrystallization is only partial even at low strain rate. It is not also feasible for forming workings. Fig. 5.7 shows the microstructures of AZ31 with deformation speed v=0.2mm/s at T=250°C and 300°C. These microstructures are fully recrystallized with a very fine grain size of the order of 5µm. Zhang et al. [74] also reported that the casted

slab-hot/cold rolled and cross-rolled AZ31 sheet with the grain size 5-15µm are not the remarkable anisotropy. It is very suitable to form AZ31 sheet with high formability.

5.1.3 Calibration of fracture models

In chapter 4, the criteria were presented in unique space of stress triaxiality and equivalent plastic strain. It is convenient to implement into the fracture criteria that are available in ABAQUS FEM simulation code. Therefore, it is necessary to determine a fracture locus (e.g. equivalent plastic strain, stress triaxiality, and critical damage value) for damage criteria.

In order to determine the damage parameters of fracture locus, a procedure is adopted by the parallel combination of the finite element simulation and experimental testing. This section presents the procedure of calibration of uniaxial and biaxial tests on a standard specimen of AZ31 sheet. The uni-axial test is performed on the standard dog-bone specimen to illustrate for this approach.

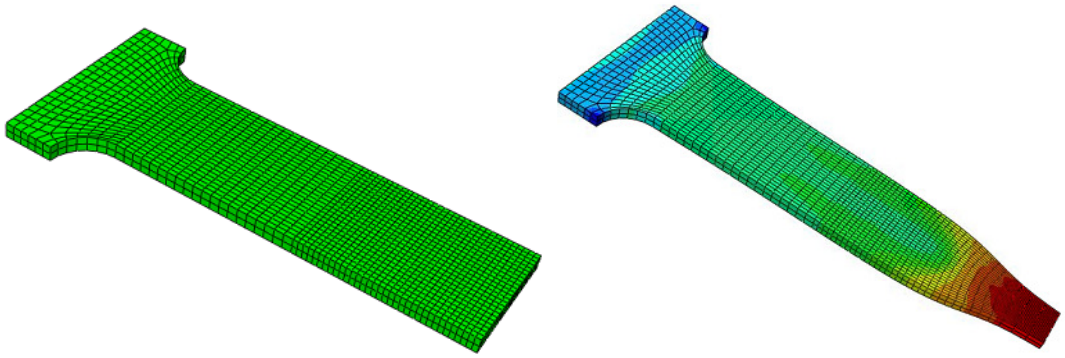

Fig. 5.8 FEM simulation of tensile specimen

The tensile testing is performed on a specimen cut from AZ31 magnesium sheet in 1.5mm thickness as presented on section 5.1.1. These experiments provided stress-strain relations, load-displacement of the cross-head. These data were then input to the finite element simulation. FEM simulation of specimens is run in parallel with each actual experiment. By using a trial-and-error method, the results from FEM simulation will be compared to experimental results to get the best fitting.

The explicit finite element code ABAQUS with fully couple thermal analysis was used. The eight-node solid elements (C3D8R) were employed to model the tensile specimen. A

preliminary simulation is performed to evaluate the effects of grid density, mass-scaled factor, and entirety of the model (e.g. full model of a part of the model). A half of a specimen was modeled with 9000 elements which not affected by modeling parameters as shown in Fig. 5.8. The nodes at the middle of specimen are assigned symmetric boundary conditions. The nodes of top part of a specimen are assigned a step displacement in which generated to constant velocity as the experimental test (2, 0.2, 0.02mm/s). To increase of calculation speed and to avoid the dynamic effect, the mass density of the model is reduced by the factor of 1000. The specimen is heated up to 200, 250, and 300^{o}C in gauge length.

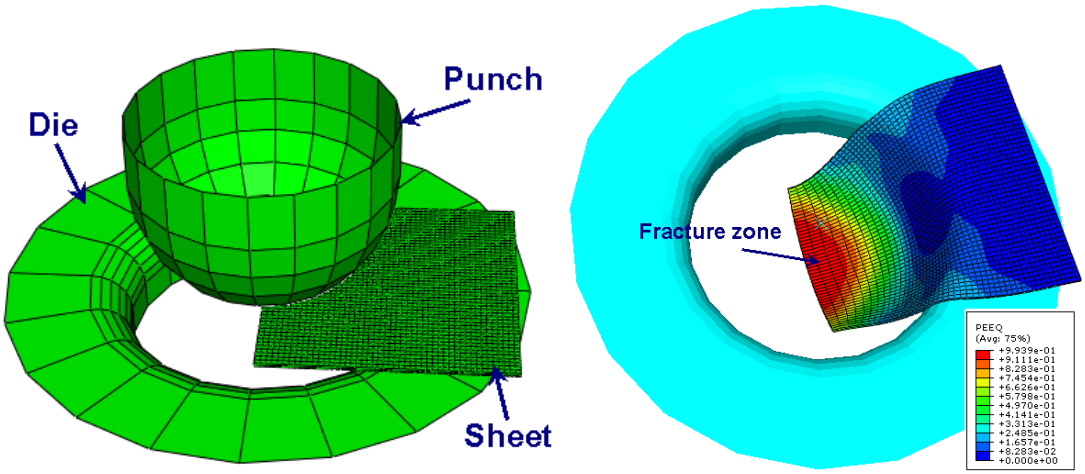

Fig. 5.9 FEM simulation of NAKAZIMA testing

The biaxial tests (Nakazima test) are also performed with the same procedure with uniaxial ones. The configuration for FEM simulation and results is presented on the Fig. 5.9. Two widths of a specimen (100mm and full width) were employed to get a range of stress triaxiality from $1/\sqrt{3}$ to 2/3. The velocities of punch and temperatures are set as the actual experiments. The sheet is only heated in a narrow zone at the center of sheet to assure temperature gradient to be similar to the actual experiments. The die and punch considered as isothermal rigid parts. Other parameters in this FEM simulation were similar to the FEM simulation of uniaxial test. The simulation is stopped when major strain is over the strain at fracture. These values got from the experiments of [97].

In order to get the stress triaxiality in a range (0, 0.33), a geometry of a specimen as showed in Fig. 5.10 is adopted in this study. The relationship between stress triaxiality

and equivalent strain in this test showed in Fig. 5.11. The value of stress triaxiality is close to zero as so-called pure shear.

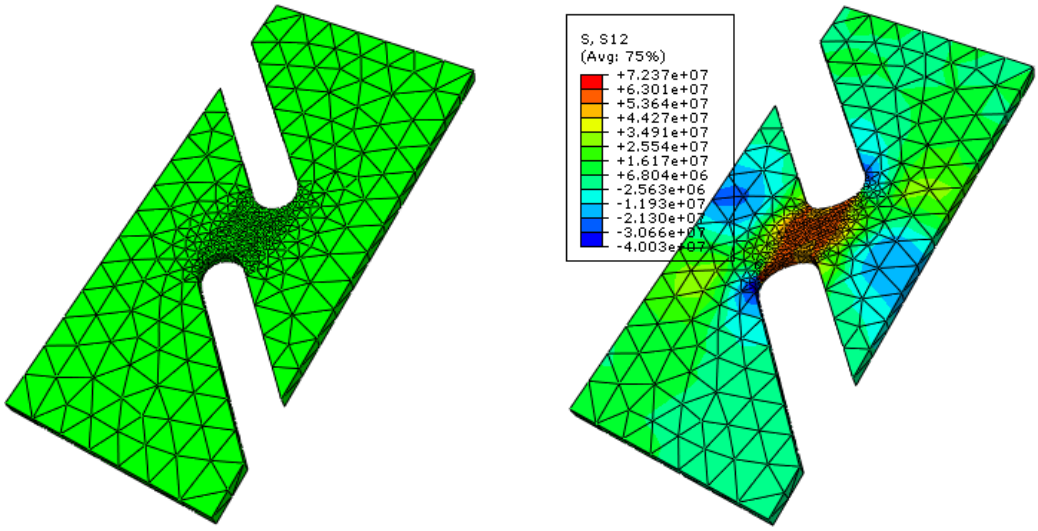

Fig. 5.10 FEM simulation for shear testing

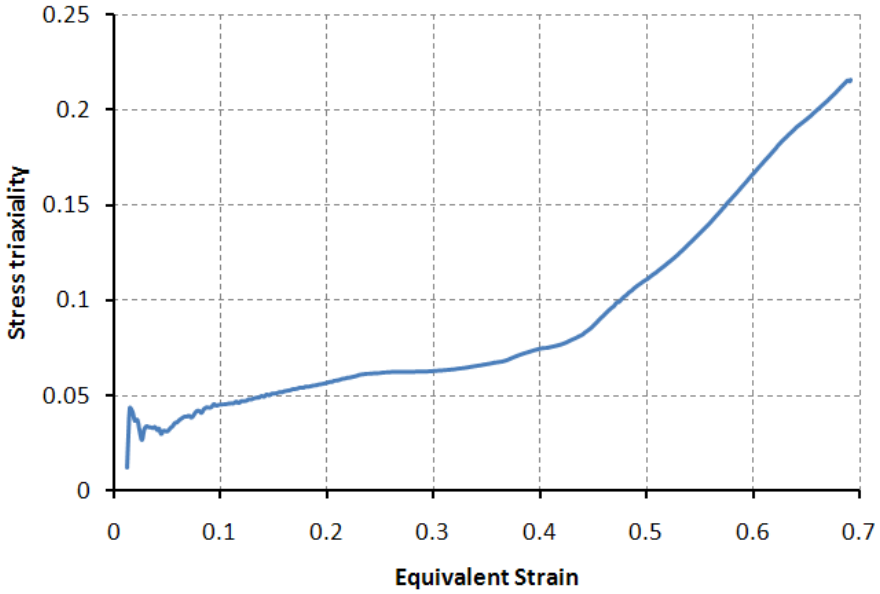

Fig. 5.11 Relationship between stress triaxiality and equivalent strain in shear testing

5.1.4 Validation of results

The stress-strain curve is fitted by Swift model rule as initial input to ABAQUS. The load-displacement response obtained from the FEM simulation is compared with the actual experience. The necking point started from the middle of specimen, the simulation is stopped when a fracture occurred. The dynamic effect on numerical simulation is

eliminated because the dynamic energy is too small to internal strain energy of the system, less than 4% (see Fig. 5.12). Therefore, this numerical simulation is performed in quasi-static condition.

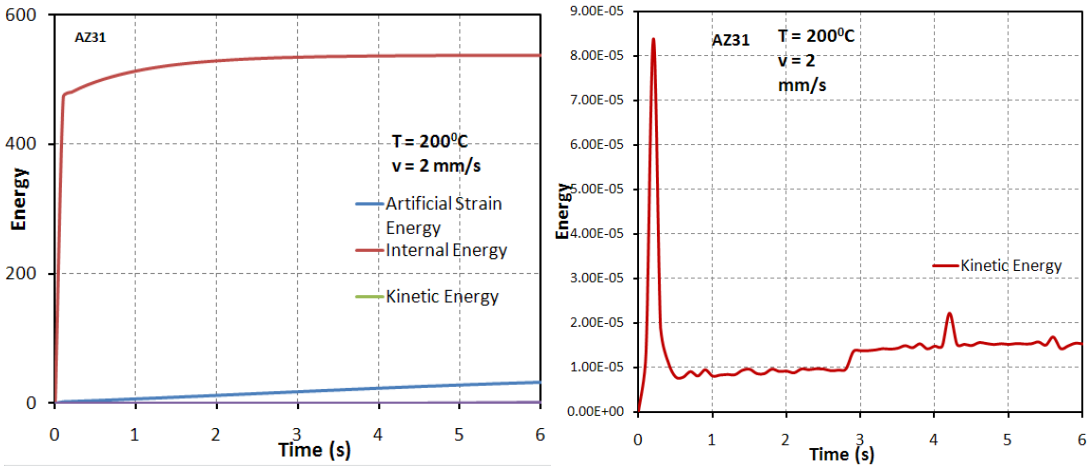

Fig. 5.12 Total energies and kinetic energy of model

After four times used trial-and-error method, the best fitting of load-displacement and stress-strain curves is shown in Fig. 5.13. The comparison of a true stress-strain curve in a last trial is presented on Fig. 5.14. These curves seem to be coinciding to give the best fitting between numerical simulation results and actual experiments.

The purpose of parallel combination of the numerical simulation and actual experiment is to obtain stress triaxiality and the accumulated equivalent plastic strain. The histories of stress triaxiality and the accumulated equivalent plastic strain during deformation until a fracture point at the middle of the specimen are extracted from FEM simulation as shown on Fig. 5.15. The stress triaxiality is not constant during deformation of a specimen. Therefore, an averaged value of stress triaxiality is taken as formula (5.1). The main reason of using the average stress triaxiality extracted from the simulated result is to include the loading history effect.

$$\bar{\eta} = \frac{1}{\bar{\varepsilon}_f} \int_0^{\bar{\varepsilon}_f} \eta(\bar{\varepsilon}) d\bar{\varepsilon} \tag{5.1}$$

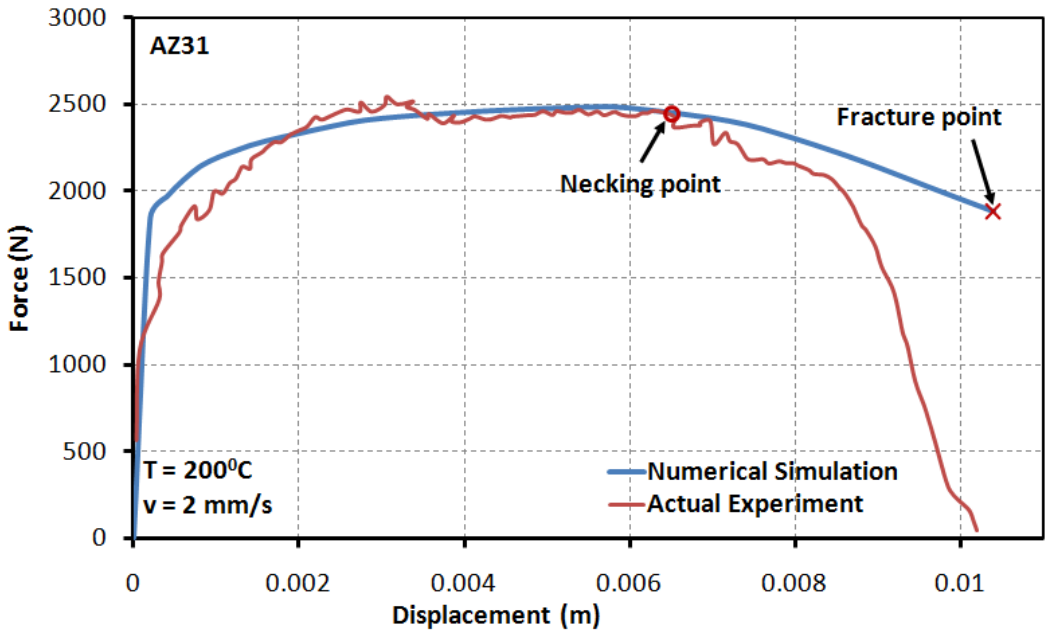

Fig. 5.13 Comparison between FEM simulation and experiment of load-displacement

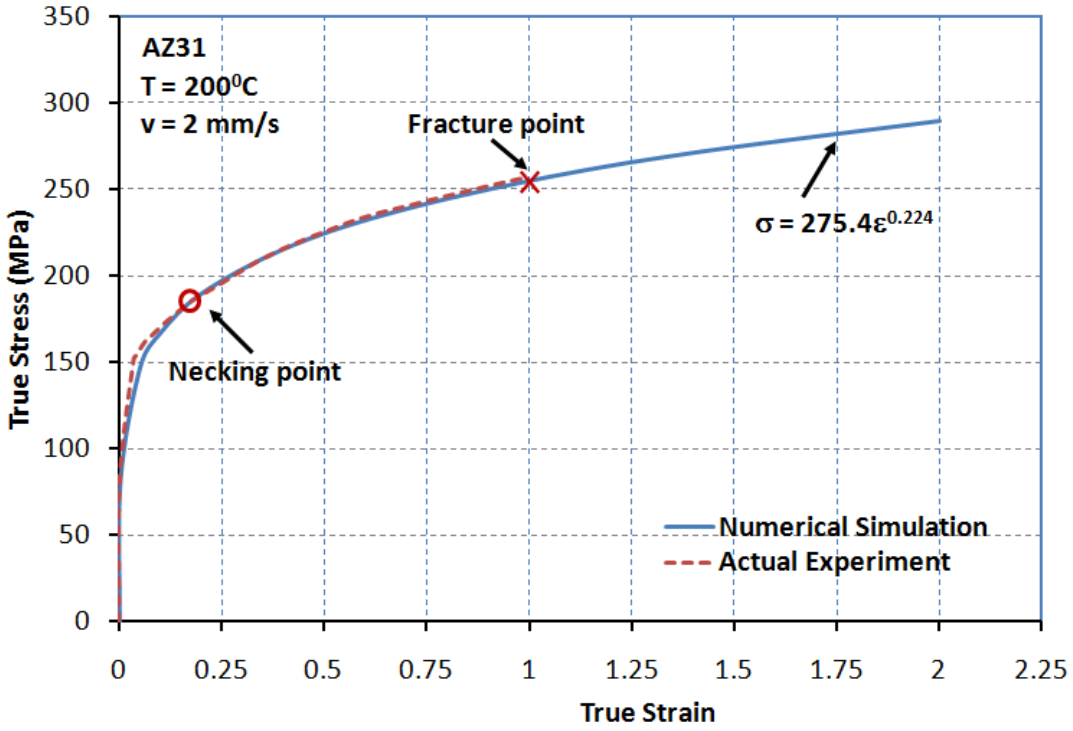

Fig. 5.14 Comparison between numerical simulation and experiment of stress-strain

The area under the curve (the range from zero of the maximum accumulated equivalent plastic strain to fracture) represents the magnitude of calibration constant for fracture

criteria (see Fig. 5.15). It is seen that the most failure in the center of the specimen is produced after formation of the localized neck.

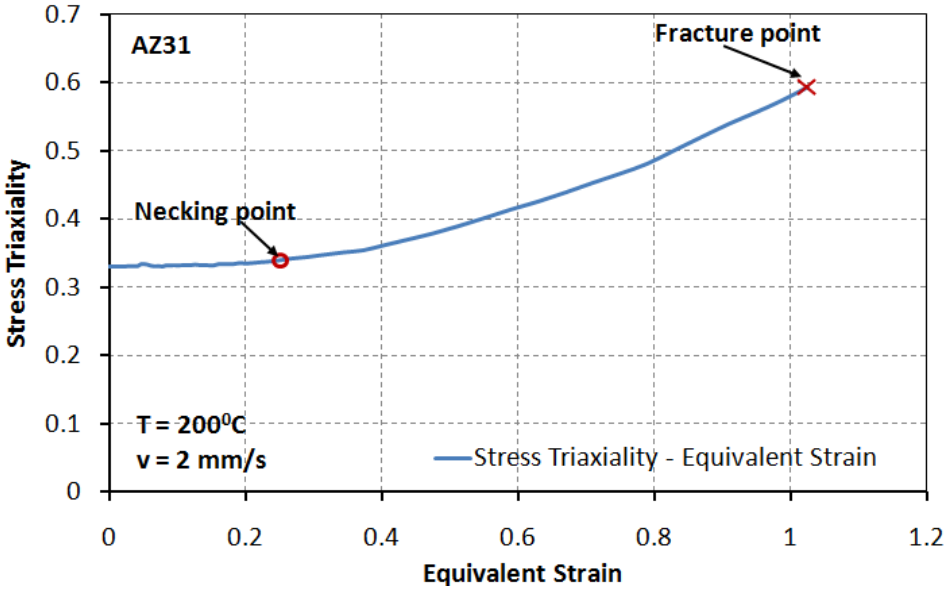

Fig. 5.15 History of stress triaxiality and equivalent strain at middle of specimen

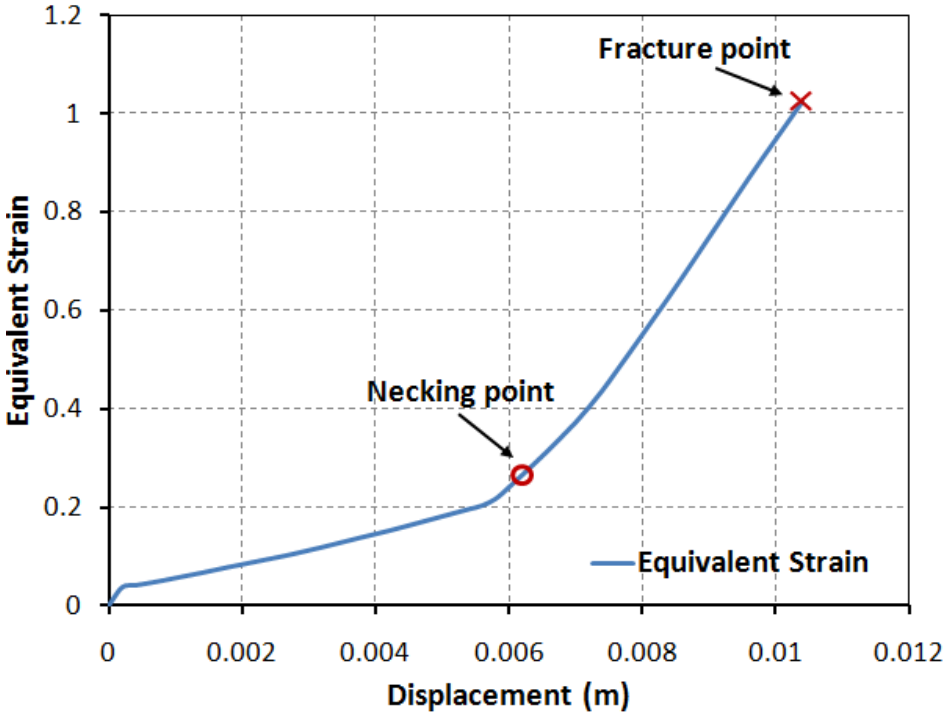

Fig. 5.16 History of equivalent strain and displacement of top nodes

The history of equivalent strain at the middle of a specimen and the displacement of top nodes is showed on Fig. 5.16. From this figure, the determinations of the magnitude of equivalent strain at necking and fracture point is relatively easy because the displacement to necking and fracture is known from actual experiment.

5.1.5 Calibrating CrachFEM criteria

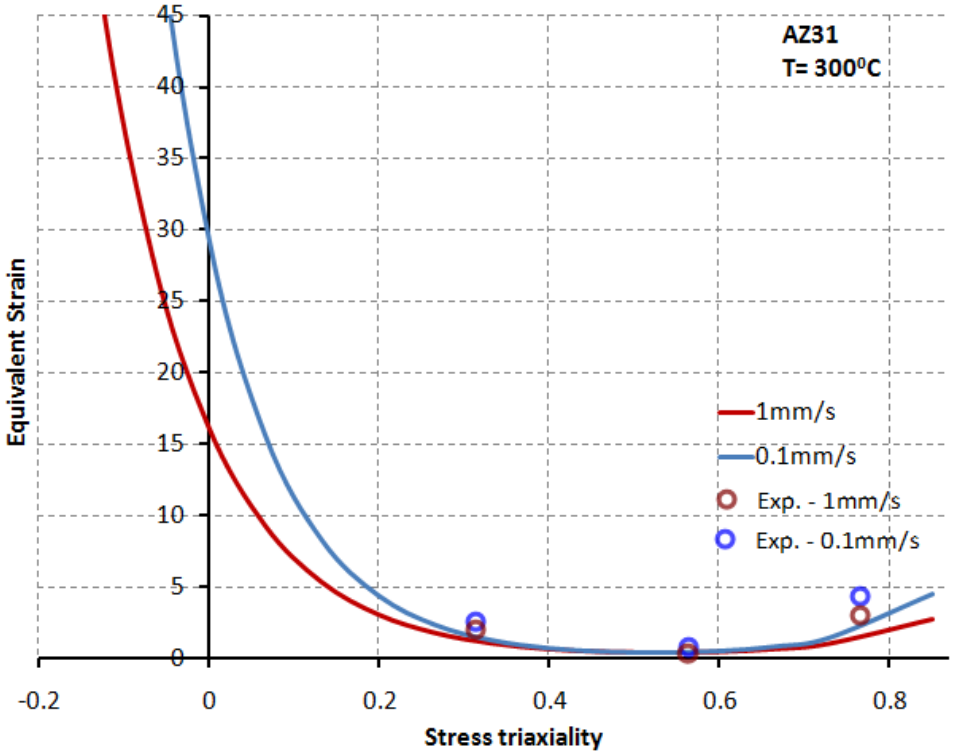

Fig. 5.17 The fracture locus for ductile criterion at strain rate 1mm/s and 0.1mm/s

Material Parameters	1mm/s	0.1mm/s
d_0	16.29855418	29.44593856
d_1	0.002138123	0.001319204
c	2.797756828	3.184863985

Table 5.4 Parameters of CrachFEM criteria for ductile damage

The data required for both criteria may be difficult to obtain through direct experimentation since it would require experiments spanning a range of stress triaxiality and shear stress ratio that may be difficult to achieve. The expression (4.25) has three parameters that must be determined by the hybrid approach (e.g. the combination between actual experiment and FEM simulation, see chapter 5). Two experiments are

performed to get a narrow range of triaxiality η (from tensile test), η (from biaxial test). Three points are taken from these range and is used to solve three linear equations. The solutions of this solving are shown in Table 5.4. The fracture locus for ductile criterion passed through three points is shown on Fig. 5.17.

Similar, in the initiation criterion of shear damage, the equivalent plastic strain at the onset of damage is given by the function of the shear stress ratio. The expressions (4.26) and (4.27) have four parameters that also are determined by the hybrid approach: k_s, ε_S^+, ε_S^- and f. As the ductile criterion, two kinds of above experiments is needed to solve linear equation systems. However, the biaxial test is performed with different sizes of the specimen in 100mm of width and full width. The predefined parameter, $k_s = 0.32$, is chosen as a suggestion of ABAQUS and evaluated again by the amount of simulations with different values. The material parameters of shear criterion presented in Table 5.5. The fracture locus for shear criterion passed through three points is shown on Fig. 5.18. The locus of shear criteria was presented in $(\bar{\varepsilon}, \eta)$ in comparison with the ductile criteria as shown on Fig. 5.19.

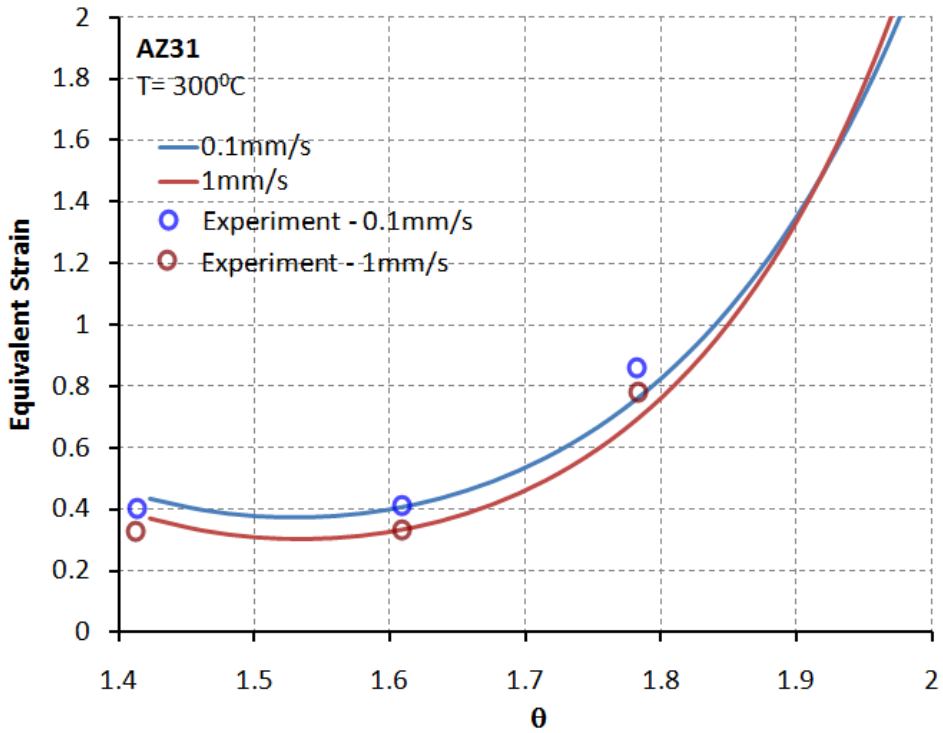

Fig. 5.18 The fracture locus for shear criterion

It is noted that the stress triaxiality is defined as a ratio of the equivalent mean stress to the Mises equivalent stress in ABAQUS. It is different with Hooputra's definition in all above formulas. Thus, the value of triaxiality used in this study to be scaled by a factor of 1/3.

Parameters	1mm/s	0.1mm/s
ε_S^+	0.338669252	0.405475758
ε_S^-	6.849356264	5.803718434
k_S	0.32	0.32
f	5.915141752	5.297619514

Table 5.5 Parameters of CrachFEM criteria for shear damage

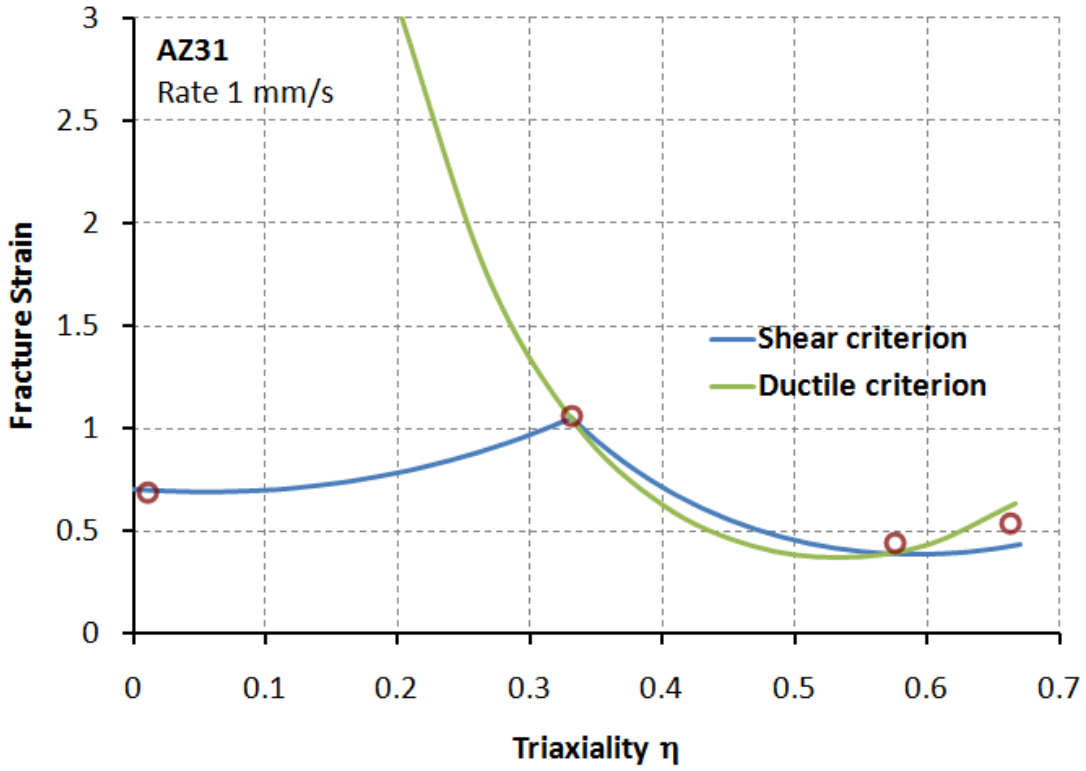

Fig. 5.19 Comparison between ductile and shear criterion

5.2 Constitutive model for thermoplastic material

In recent decades, a large number of constitutive equations have been developed to capture the complex behaviors in the polymeric materials. Most constitutive models of polymeric materials are proposed for a viscoelastic regime. They characterized well for the behaviors of the strain rate dependence, stress relaxation, and creep within a small

deformation. They have been aimed at different aspects of these observations, such as the yield phenomenon, creep, and rate dependency during monotonic loading. Frequently, one-model deals with only one of these behaviors and the other responses of the same polymer are not considered. Few models attempted to predict time dependence of various loading histories regarding finite deformation partially because of the absence of comprehensive experimental studies on any polymer, especially at high strain rates. For semi-crystalline polymers with a complex microstructure consisting of interweavement of amorphous phase and crystalline phase in their structure, multi-scale models were suggested to describe their behavior. The correspondences of crystalline phase are usually considered as elasto-plastic behavior. The complex correspondences of amorphous phase are assumed in a variety of mechanical behaviors.

Richeton et al. [98] presented a robust physically consistent constitutive model for the large inelastic deformation of amorphous polymers. This thermo-mechanical model is based on an elastic–viscoplastic rheological approach that is able to account for the effects of strain rate, temperature and hydrostatic pressure. It also can account for the possible change of the polymer from the glassy to the rubbery state due to adiabatic heating at very high strain rates. Dupaix [99], van Dommelen [100] also developed constitutive model following this direction.

Meyer et al. [101], Ghorbel [102], Lee et al. [103], Meddah et al. [104], Drozdov [105] assumed correspondences of amorphous phase as viscoplastic behavior. The viscoplastic flow is initiated in the amorphous phase before transitioning to the crystalline phase. Three deformation mechanisms of amorphous layers have been recognized: inter-lamellar shear that would lead to micro-cavities and then to lamellae separation at very large deformation and the rotation of stacks of lamellae. The viscoplastic deformation of crystalline phase is analogous to the viscoplastic deformation of crystallographic materials. Hence, at small strain, the dominant inelastic deformation mode is controlled by the amorphous phase.

Nikolov et al. [106], Lin et al. [107], Kichenin et al. [108], Kitagava [109], Ariyama [110] assumed as viscoelastic behavior at small deformations. However, the constitutive

modeling of polymeric materials is based on characteristics of microstructure of polymeric materials. The drawbacks of this method are: i) the developed models are complex; ii) it is very complicated and big time consuming to determine material parameters in such models [111,112].

In recent years, there are two constitutive laws that give a good agreement between the experimental results and the calculated ones on semi-crystalline polymer. Those are hyper-visco-hysteresis constitutive law (HVH) and viscoplasticity law based on overstress theory (VBO). The hyper-visco-hysteresis constitutive law is developed for PP by Zrida et al. [113], based on the superposition of stress contributions. To take into account with the different behavior and the evolution of the mechanical behavior of strain rate dependent materials, the authors suppose hyper-elastic, visco-elastic and pure hysteresis stress contributions Fig. 5.20. The superposition of stress states that the Cauchy stress tensor σ is expressed as sum of the hyper-elastic tensor of reversible stress contribution σ_e, the viscous tensor effect using Maxwell model σ_v and of the pure hysteresis contribution σ_h. The homemade software Sidolo is used for calibrating the modeling parameters. This model is introduced in the finite element computation software, called HEREZH++. The authors pointed out that the HVH model can be used to predict the results of simple monotonic loading, cyclic and relaxation tests if a relaxation time is coherent in all these tests. The constitutive model used two Maxwell units to present the linear viscoelastic behavior. This use exhibited some limitations. The identification procedure is less accurate in tensile and cyclic tests, although the identification can be improved by reducing the relaxation time. This model needs further studies to improve the modeling of nonlinear viscosity behavior by accounting both different loading time and strain rate.

Whereas hyper-visco-hysteresis constitutive law, the viscoplasticity based on overstress (VBO) theory without using yield surface. It is the endocrinal theory proposed by Krempl [114,115,116]. This theory is based on the overstress model which is applied successfully to metals. Kitagawa et al. [117,118,119] also used the overstress model explains the viscoplastic-plastic properties of PP. The author expressed an equation of a linear theory of viscoelasticity based on a three-element model. This model consists of a spring and

unit in series (i.e. the unit consists of a Newtonian dashpot and an element of the equilibrium stress-strain curve in parallel). This model is modified by Ho [115], Khan et al. [120], Colak [121], Dusunceli [122] to apply well for semi-crystalline polymer. The details are presented in next part.

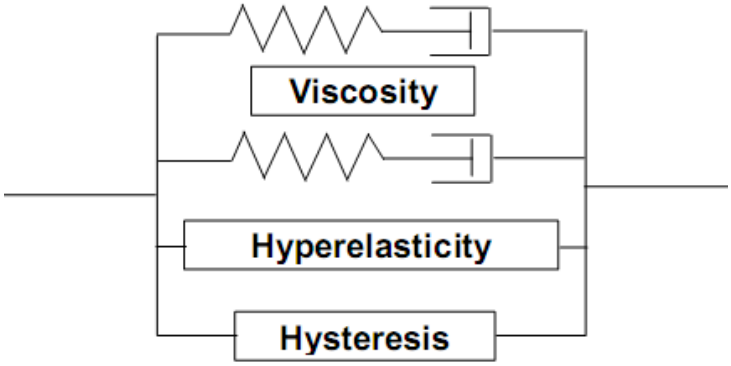

Fig. 5.20 Hyper-visco-hysteresis constitutive law (HVH)

Ariyama [110] also used a linear viscoelastic of a three-element model so-called as Standard Linear Solid model (SLS). It is a combination of a Maxwell model and linear spring in parallel, as shown in Fig. 5.27. The constitutive equation neglect temperature effect and hydrostatic dependence. However, the author showed the good agreement between numerical calculation and actual experiment. It indicated that the SLS model might be valid for the PP with comparatively large spherulites subjected to the cyclic preloading. The author concluded that the linear viscoelastic model explains well the viscoelastic behavior of isotactic PP.

5.2.1 Experiment with polypropylene

The experiments on PP exhibited important behaviors. One of the prominent behaviors of polymers is known as temperature and rate dependent and exhibited non-linear responses during loading and unloading state. Several experimental techniques may be used to measure and quantify this behavior even at very small deformation levels. There have been several experimental studies addressing different characteristics of polymer response, such as creep, relaxation, and strain rate sensitivity, but most of them have been restricted to small deformation levels and addressing to only one or two aspects of deformation such as creep and relaxation, or deformation at high strain rates.

Read [123,124] performed a mechanical relaxation test with different stress levels in the non-linear range and various durations of loading at 23^{o}C. The results are compared with predictions based on a pseudo-linear model. They have also been analyzed using a modified superposition procedure that allows for changes in mean retardation time due to both to physical ageing and to the application and removal of loads. This analysis has provided useful information on the variations of molecular mobility during the different loading histories.

Attalla et al. [125] reported that the relaxation behavior of isotactic polypropylene in the range of temperature between -20°C and 40°C was strongly influenced by both crystallinity and morphology. They also pointed out that an increase in size of crystalline aggregates increased the value of a relaxation module and changed both shape and location of the spectrum of relaxation times. In their discussions, the activation energy values of the shift factors were determined using the time-temperature superposition principle and the master curves were obtained for the various structures.

Ariyama et al. [110,117,126,127] performed the studies in various aspects of cyclic deformation, stress relaxation after cyclic preloading and effects of mean strain changes on deformation behavior of PP. The PP exhibited an excellent fatigue resistance during large strain cyclic deformation. The cyclic deformation tests were performed under various sets of strain rate, number of cycles, and strain amplitude in two different samples at room temperature. The stress relaxation tests were made after a cyclic preloading in both samples. The distinctive shape of the hysteresis loop, termed a propeller-like shape, is characteristic of the as-received PP with large spherulites, in marked contrast to the behavior of metals. There is a significant difference of stress drop in relaxation tests. This stress drop behavior reflects the difference of spherules structure. The stress relaxation behavior depends on the morphology, the predetermined strain amplitude, and the process of the tests.

Kitagawa et al. [118,119,128,109] investigated viscoelastic-plastic properties of PP at finite strains. The uniaxial compression tests were performed at different temperatures under conditions of constant strain rate, abrupt change of strain rate, stress relaxation,

creep loadings and their combination. Combined tension and torsion tests were also performed at various strain histories. The results show an elastic response immediately after the strain rate change and then gradually approach the stress-strain behavior expected at the new rate. The tensional strains were applied at three strain rates prior to the relaxation tests. In the relatively high strain region, it is seen that the magnitude of the stress relaxation drops is nearly independent of the strain and depends on the strain rate preceding the relaxation test. In a stress relaxation test at high strain, the amount of stress relaxation after a given time interval is independent of the test strain, and the initial rate of stress decrease is proportional to the strain rate preceding the relaxation test.

The most commercial PP is isotactic and has an intermediate level of crystallinity that characterized for semi-crystalline polymer. Depend on the degree of crystallinity, size and distribution of crystallites in polymer structure has a significant effect on the mechanical properties (e.g. elastic modulus, yield stress, stiffness … etc). Dusunceli et al. [122] investigated on modeling effects of the degree of crystallinity on mechanical behavior by modified vicoelasticity theory based on overstress (VBO). The modifications on VBO are done considering the polymeric materials as a composite material, since they consist of amorphous and crystalline phases. An amorphous and crystalline phase resistances a reconsidered acting in parallel and series. Various crystallinity ratios can be simulated by this modeling and is evaluated on Kurtz's experimental data [129]. Alberola et al. [130,131] investigated the influence of strain rate on yielding. Changes in the yield stress and strain driven by an increase in the rate of straining.

To investigate the behaviors of PP, a series of experiments is performed as following at room temperature:

- Tensile test with different strain-rates: 0.0001, 0.001, 0.01, 0.1, 1 ($1/s^{-1}$).
- Relaxation test at different predefined strain levels of 2%, 5%, 8% in 3600 second.
- Creep test at different predefined stress levels of 20, 25, 30 MPa.

All experiments were performed on the specimen cut from PP sheet following ASTM standard D638-03. The servo-hydraulic computer-controlled MTS 322 was used to perform displacement controlled zero to tension uniaxial tests at room temperature. Change in specimen strain can be measured using an extensometer (MTS 632.53F-11). This extensometer with 25mm gage length (maximum operating limit +/-10% strain) was used in the majority of the experiments. Although its capacity of 10% strain, experiments were strained up to 8% in maximum to insure the safe of extensometer and accuracy of the measured results. The displacement was used controlled-extensometer mode to insure a constant of strain rate. Each test is repeated at least twice to assure the probability of measuring.

5.2.1.1 Tensile test

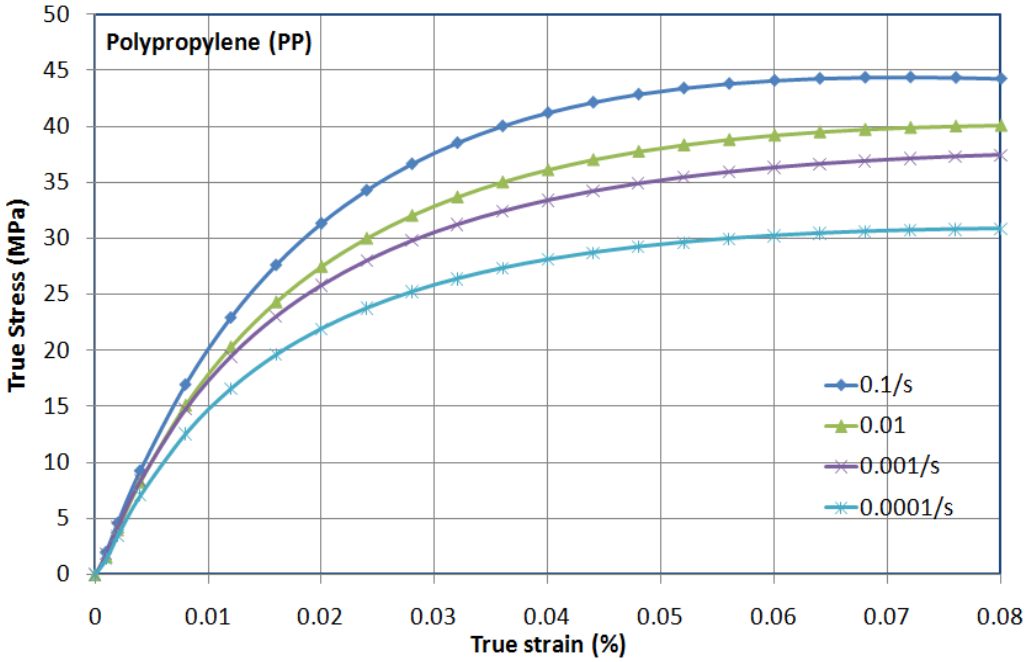

Fig. 5.21 Experimental results from tensile test

The first experiment is the tensile test with strain rates ranges from 1/s to 10^{-4} 1/s. The specimens were strained up to 8% strain with constant strain rate and then relaxation tests were performed in sixty minutes. It is found that the initial slope of the stress-strain curves is not so dependent on the strain rate. Those parts of curves are relative coincidence in a narrow range. The stress-strain curves at different strain rates are nearly parallel to each other when the stable state was reached which could justify an

additional viscous contribution to the total stress. When the strain rate increased, the difference among curves became increasingly significant. Clearly, PP is highly sensitive to the strain rate and that their viscous capacity increases with the strain rate. In high strain rate, the curve showed clearly negative slope in the end of the inelastic regime. However, the curves of low strain rate do not show the negative slope because specimens are only loaded up to 8%. It is clear to see this behavior when the specimens are loaded to high strain (without using the extensometer or using a special extensometer). It shows that material is softened with high strain.

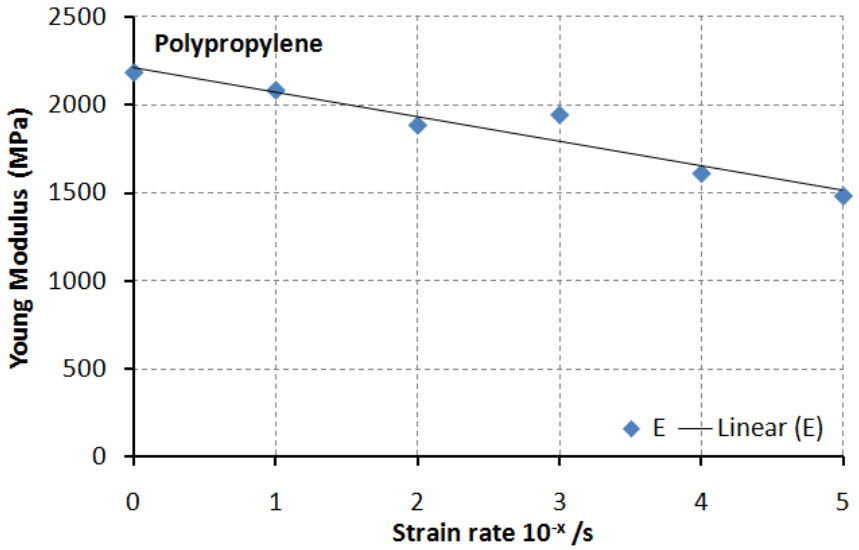

Fig. 5.22 The difference in Young Modulus with different strain rate

Young modulus is taken directly from the graph by the slope of stress-strain curves in a linear region. There are differences in the linear region of each stress-strain curve with respect to strain rates. It is obvious that higher the strain rate is tested, higher the Young modulus is found from the graph. This is described in graphic of Fig. 5.22.

However, it is difficult to determine precisely yield points by a manner. The transition from the elastic regime to plastic regime moves gradually. Therefore, the stress condition governed yielding also is a vagueness of the definition of yielding because of the viscosity presence. The Poisson's ratio is given as a ratio between the longitudinal deformation and the transversal deformation of the specimen. It is taken as an average value in the homogeneous deformation zone.

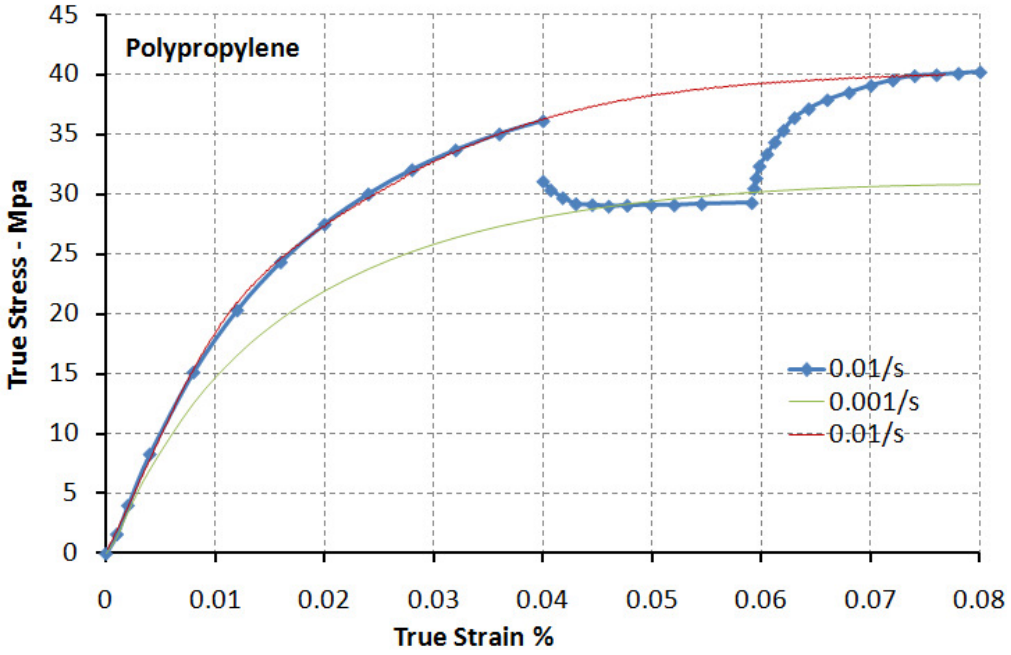

Fig. 5.23 Cycle loading/unloading test

An additional experiment also performed to consider the mechanical behavior in a cycle loading/unloading. The specimen is loaded up to 23MPa (about 4%) and switched off the load in 300 seconds. This specimen continues loading up to 39.5MPa (about 8%). The data of this experiment is plotted on same graphic with two tensile tests of different strain rate. There are surprisedly coincident among curves (Fig. 5.23).

5.2.1.2 Relaxation and creep test

Relaxation tests are also useful for determining the viscosity behavior of the material. Specimens are strained up to 8% (about 39.5 MPa) and relaxation test is started. The level of strain rate is the same tensile test ranged from 1 to 10^{-4} 1/s. The experimental results of relaxation test with different strain rates are shown on Fig. 5.24. It shows that the total stress drops in the sixty minutes relaxation tests are increasing with increasing prior strain rate. However, increasing level is not large in low strain rate. It will archive equivalent state with extremely low strain rate.

Another relaxation test also carried out with different strain levels and strain rates. The specimens are loaded up to 1%, 2%, 5% (level of 8% is done in above experiments) with very low strain rates (10^{-2}/s, 10^{-3}/s, 10^{-4}/s) then are relaxed in 3600 seconds. The points of the drop stress values reached after the relaxation tests are shown on Fig. 5.25.

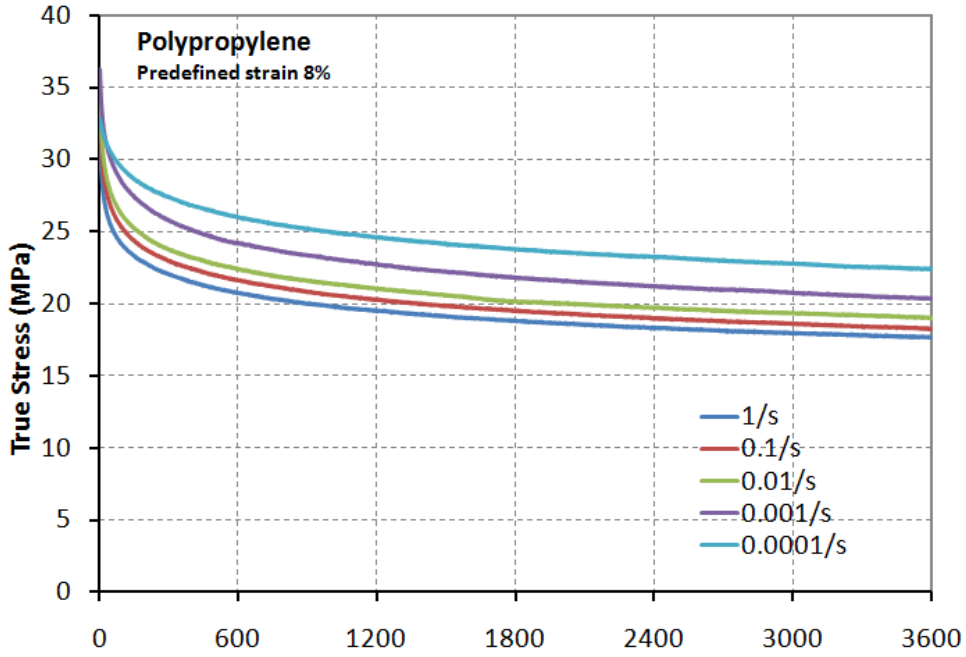

Fig. 5.24 Relaxation test at same predefined level of strain

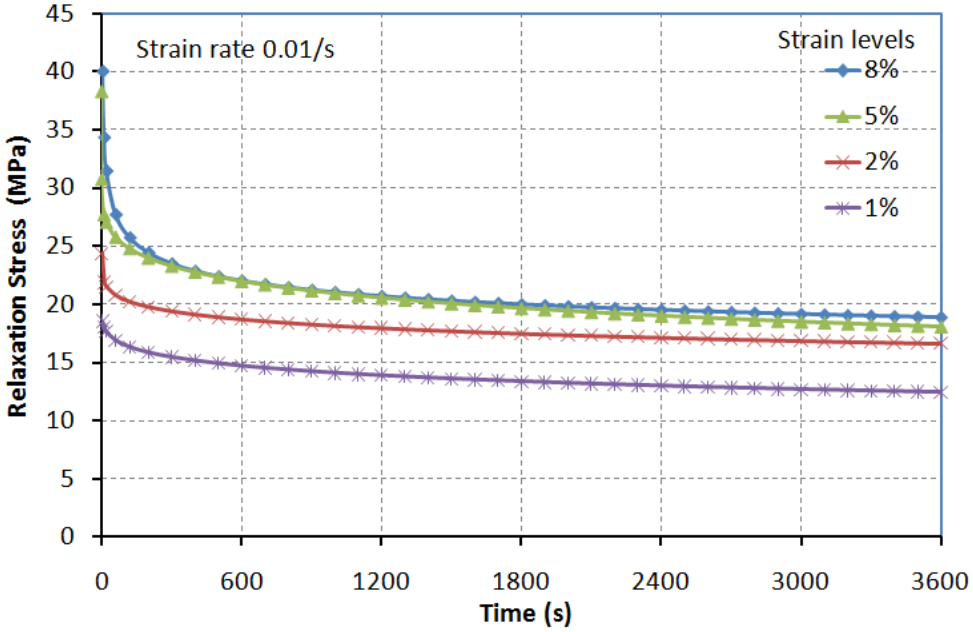

Fig. 5.25 Relaxation test at different predefined levels of strain

They showed that the rates of stress decrease were very small and the limits of relaxation would be reached. They construct a curve which is independent with the strain rate prior to the relaxation. The purpose of this series is to determine the parameters in the evolution equation of the equilibrium stress. Three points will be

extracted from these experiments. The equilibrium stress curve passed through the points. This curve is called an equilibrium stress-strain curve which is a limit of relaxation at a very slow strain rate. The equilibrium curve also seems to have the same negative slope of tensile stress-strain curves.

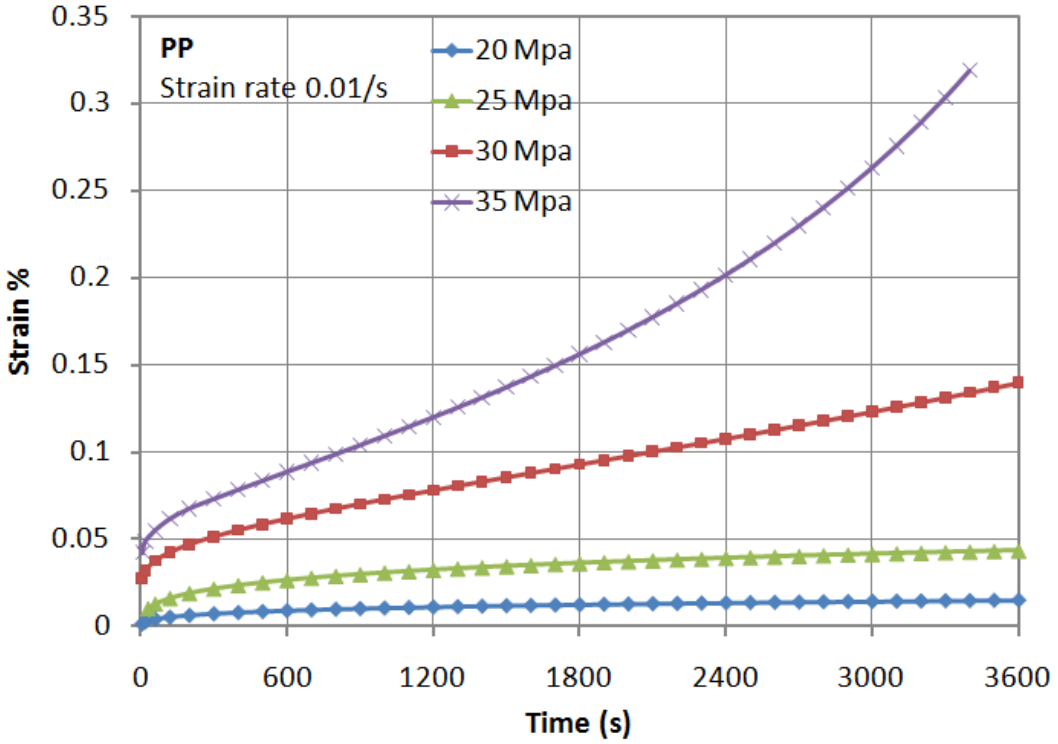

Fig. 5.26 Creep test with different predefined level of stress

The creep tests also were performed with the constant strain rate of 0.01/s. The specimens were loaded up to the predetermined values and kept at the constant stress levels of 20, 25, 35, and 39.5MPa. The results are shown on Fig. 5.26 with curves that have a very different shape. At low predetermined stress values, the strain is less difference up to stable state. However, the strain is increased rapidly to lead to a final fracture in high-predetermined stress.

5.2.2 Viscoplasticity based on overstress model

The viscoplasticity based on overstress theory (VBO) is proposed by Krempl which is not based on the assuming of yield surface [114]. Krempl and his co-worker develop it through the years. The basic form of the flow law in VBO can be developed through the consideration of a Kelvin-Voight element placed in series with a spring. The arrangement

is often referred to as the SLS model (Fig. 5.27) which is usually used to present mechanical response in both metallic and polymeric material. In overstress theory, the following modifications are made to the Kelvin elements:

- The spring is made non-linear and hysteretic, and
- The dashpot is made non-linear as well and dependent upon the overstress (the overstress is defined as the difference between the stress and the equilibrium stress).

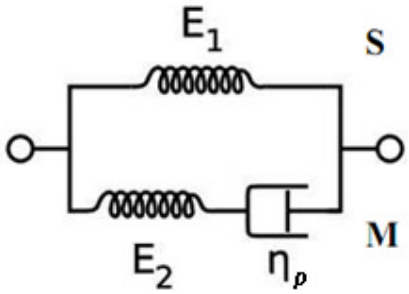

Fig. 5.27 Standard Linear Solid model

VBO is a unified theory with three state variables, namely, *g* the equilibrium, *f* the kinematic (rate dependent), and *A* the isotropic (rate independent) stress. The equilibrium stress is mathematically expressed in a differential formulation and forms a hysteretic path upon loading and unloading. Its prominence in the VBO formulation dictates that a qualifying remark on the nature of the equilibrium stress be supplied preemptively since skepticism on the judiciousness of using this state variable has, on few occasions, been voiced. The equilibrium stress is not a directly measurable (experimental) variable such as load. That it is a theoretical construct does not undermine the soundness of the model. Another point of interest in VBO is the absence of a purely elastic region and a yield surface. These characteristics make the model particularly amenable to modeling polymer deformation behavior since even for small strains a linear elastic region is absent. A continuously decreasing tangent modulus also erects an obstacle in the way of establishing a yield criterion for polymers.

The viscoelasticity theory is modified by Krempl and Ho to model nonlinear rate sensitivity and unloading, cyclic softening and recovery behaviour of Nylon 66 [116].

Then, it is implemented more to encompass well mechanical behaviour of polymeric material at room temperature [115,120,121,122]. The VBO theory used in this study is the modified form, a rate-dependent unified state variable theory without yield surface and loading/unloading conditions. The evolution equation of strain rate is sum of the elastic and inelastic strain rate in small strain, isotropy and incompressibility in three-dimension given by

$$\dot{\boldsymbol{\varepsilon}} = \dot{\boldsymbol{\varepsilon}}^{el} + \dot{\boldsymbol{\varepsilon}}^{in} \tag{5.2}$$

$$\dot{\boldsymbol{\varepsilon}}^{el} = \left(\frac{1+\nu_p}{E}\right)\dot{\boldsymbol{\sigma}} - \frac{\nu_p}{E}(tr(\dot{\boldsymbol{\sigma}}))\boldsymbol{I} \tag{5.3}$$

$$\dot{\boldsymbol{\varepsilon}}^{in} = \frac{1+\eta_d}{Ek[\Gamma]}(\boldsymbol{\sigma}-\boldsymbol{g}) - \frac{\eta_d}{Ek[\Gamma]}(tr(\boldsymbol{\sigma}-\boldsymbol{g}))\boldsymbol{I} \tag{5.4}$$

Where the symbol in bold denotes as Cauchy tensor, square bracket denotes "function of". A superposed dot denotes the time derivative. The σ, g and I are Cauchy tensor of the stress, equilibrium stress and identity, respectively. The $\dot{\boldsymbol{\varepsilon}}$ is a rate of deformation, strain rate tensor. The $E,\ \eta_p,\ \nu_p$ are Young modulus, inelastic Poison's rate, and elastic Poison's rate ($0 \le \eta_p \le 0.5$).

The quantities $\Gamma = |\boldsymbol{\sigma} - \boldsymbol{g}|$ are the scalar invariant of overstress with a dimension of stress. The concept of overstress is defined as the difference between the Cauchy and equilibrium stress tensor.

$k[\Gamma]$ is the positive, decreasing viscosity function which can be expressed as

$$k = k_1\left(1+\frac{\Gamma}{k_2}\right)^{-k_3} \tag{5.5}$$

where k_1, k_2, k_3 are material constants.

The evolution equation for the equilibrium stress tensor is presented in nonlinear rate-independent and hysteretic given by

$$\dot{\boldsymbol{g}} = \Psi\frac{\dot{\boldsymbol{\sigma}}}{E} + \Psi\left(\frac{\boldsymbol{\sigma}-\boldsymbol{g}}{Ek[\Gamma]} - \frac{\Gamma}{Ek[\Gamma]}\frac{\boldsymbol{g}-\boldsymbol{f}}{A}\right) + (1-\frac{\Psi}{E})\dot{\boldsymbol{f}} \tag{5.6}$$

where Ψ is the shape function which, as mentioned in the introduction to VBO, serves to control the transition between the initial quasi-elastic and region of plastic flow. The shape function can be explicitly defined as

$$\Psi = C_1 + \frac{C_2 - C_1}{\exp(C_3 \left| \dot{\varepsilon}^{in} \right|)} \tag{5.7}$$

where C_1, C_2 and C_3 are material constants. The rate independent isotropic stress, A, is a scalar quantity for which the growth law is defined as

$$\dot{A} = A_t (A_f - A) \left| \dot{\varepsilon}^{in} \right| \tag{5.8}$$

where A_0, A_c, A_f are material constants. The evolution of the isotropic stress allows the modeling of cyclic hardening or softening behavior. Another tensor valued state variable is kinematic stress f_k. It has the same form as the Prager kinematic hardening law in rate-dependent plasticity theory, which is why it has been called kinematic stress. The evolution equation of the kinematic stress is taken as

$$\dot{f}_k = E_t \left| \dot{\varepsilon}^{in} \right| \tag{5.9}$$

where E_t is the tangent modulus at the maximum strain of interest.

5.2.3 Calibration of VBO constitutive model

The calibration of material parameters in VBO constitutive equation is a complex work and long time consuming. The common way for calibration of material parameters introduced to Handbook of Materials Behavior Models [132], in which only needs experimental data from tensile test. The current study, another calibrating procedure is adopted which used experimental data from tensile, relaxation, and creep testing. It provided a better result. A 2D constitutive equation is used to calibrate the material parameters in VBO model. It presents as following:

$$\dot{\varepsilon} = \frac{\dot{\sigma}}{E} + \frac{\sigma - g}{Ek[\Gamma]} \tag{5.10}$$

$$\dot{g} = \Psi \frac{\dot{\sigma}}{E} + \Psi \left(\frac{\sigma - g}{Ek[\Gamma]} - \frac{\Gamma}{Ek[\Gamma]} \frac{g - f}{A} \right) + (1 - \frac{\Psi}{E}) \dot{f} \tag{5.11}$$

VBO model requires calibrating nine material constants in two above equations. The procedure for calibrating is as following:

Young modulus (E) and Tangent Modulus (E_t) takes directly from a graph of the experimental data in Fig. 5.21. Because Young Modulus in this experiment has a slight difference with various strain rates, average values used in this study.

The material constants in viscosity function can be identified from experimental data of relaxation test. In relaxation test ($\dot{\varepsilon} = 0$), the equation (5.10) is rewritten as below:

$$\dot{\sigma} = -\frac{\sigma - g}{k[\Gamma]} \tag{5.12}$$

Identifying three material constants k_1-k_3 of (5.12) can be done by trial-and error or use any curve fitting software. K-function is fitted by "NonlinearFit" package of MATHEMATICA following experimental data of tensile and relaxation testing.

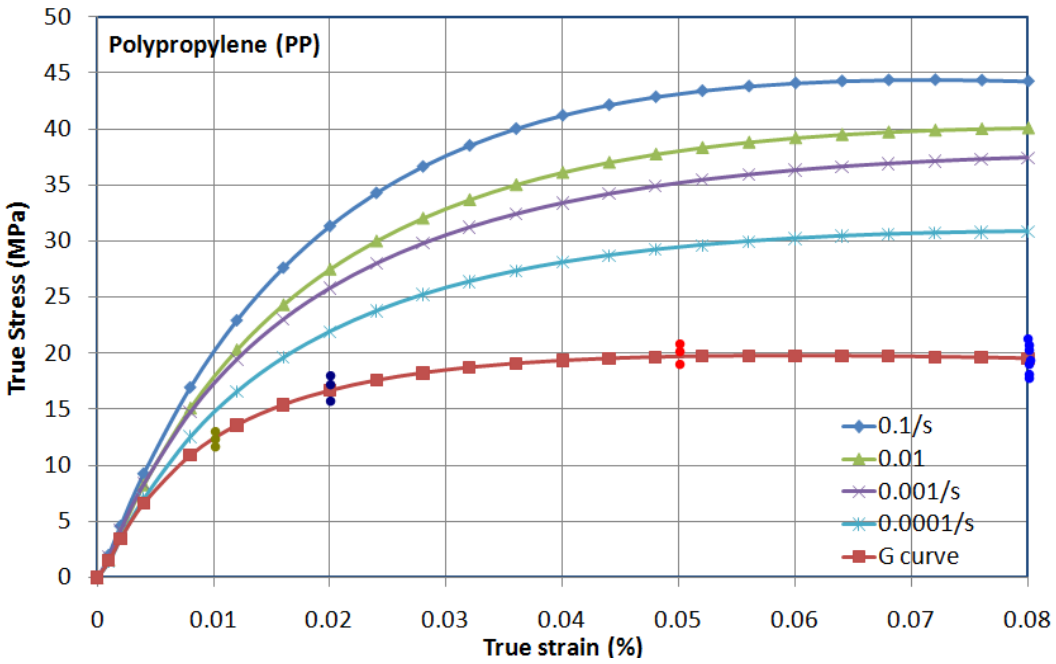

Fig. 5.28 Equivalent points from different strain rate and stress level

The equivalent function, g, is identified with experimental data of relaxation test with four different predefined values of stress level (1%, 2%, 5%, and 8%). The equivalent points of experiments with the different strain rate and stress level presented on Fig.

5.28. An equivalent curve of *g* will be passed through these points. The curve *g* is fitted through these points.

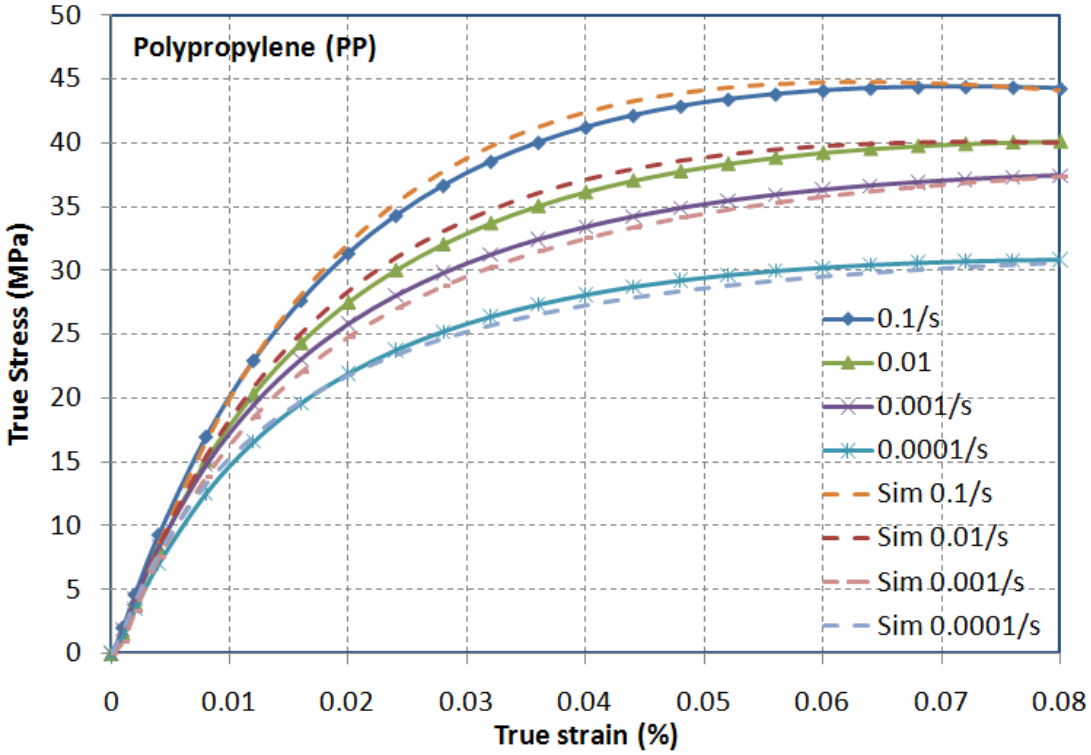

Fig. 5.29 A comparison between experimental result and fitted result in tensile

After identifying tangent modulus and *g*-curve, the value of isotropic stress, *A*, is easy to get. The value of the isotropic stress controls latitude in the positioning of the equilibrium stress curve g for the change in stress during relaxation.

Finally, shape function will be fitted by "NonlinearFit" package of MATHEMATICA or by a trial-and-error. All material constants are shown in Table 6.6. The comparison between the experimental results and calibrated results of tensile testing in VBO model presented on Fig. 5.29. It is shown a best fitting between experimental data and predicted data of VBO model. Two predefined strain levels of 2% and 8% in relaxation test are compared with predicted data. However, there is a little different (less than 6%) between experiment data and the predicted data.

The comparison of experimental data and predicted data in creep test showed on Fig. 5.31. There is a good agreement between experiment and prediction at a low

predefined stress level (25MPa). However, at a high level of predefined stress, predicted data is far from experiment data.

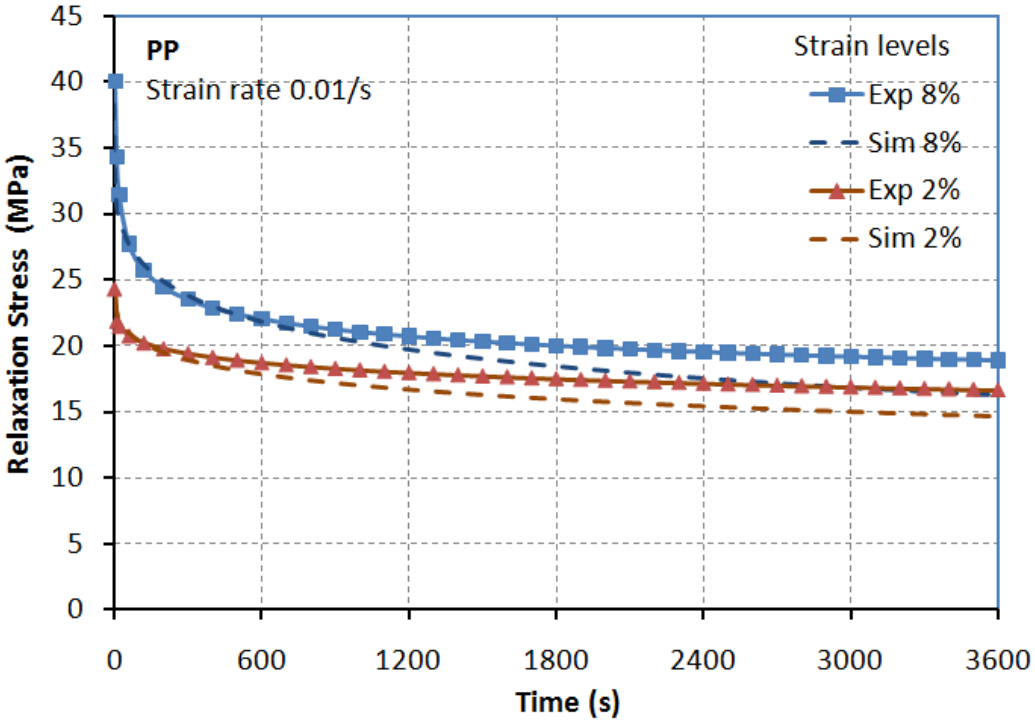

Fig. 5.30 A comparison between experimental result and fitted result in relaxation

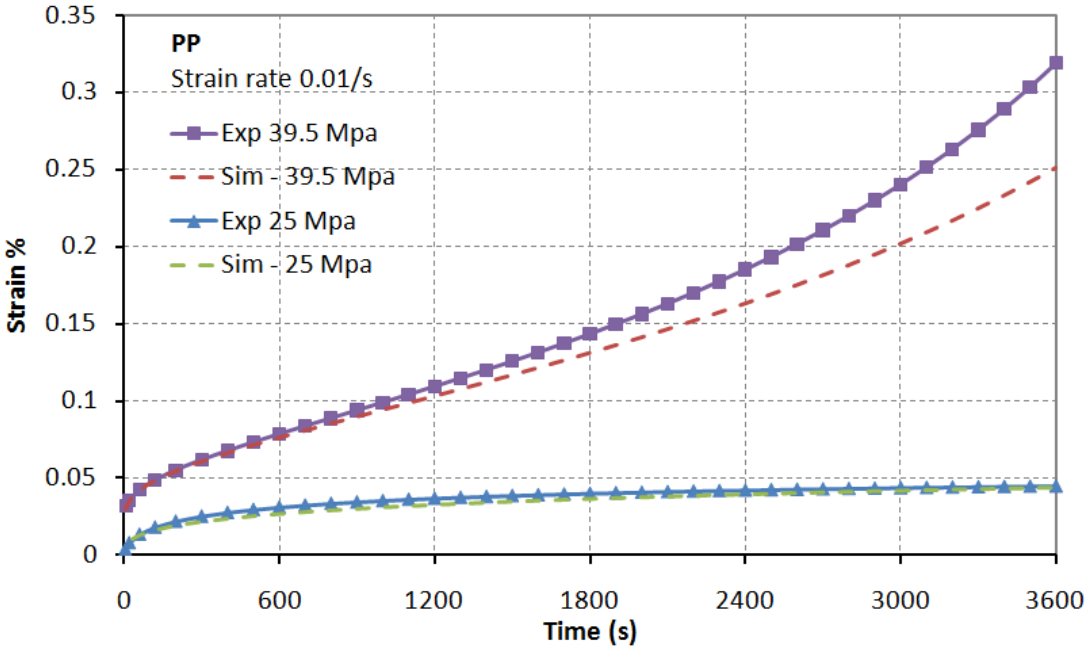

Fig. 5.31 A comparison between experimental result and fitted result in creep

5.3 Summarizing the chapter

This chapter described the mechanical testing of magnesium and polypropylene sheet. For magnesium sheet, anisotropy behaviour and high sensitivity of temperature and deformation speed is found. The observation of microstructure of specimens at fracture after the mechanical test is investigated to be able to explain the properties of deformation and fracture of magnesium sheet.

Parallel to each mechanical testing, FEM simulation is performed with same conditions of an actual experiment to calibrate the damage criteria for prediction of failure in SPIF process. Three kinds of testing are needed to able to get a large range of stress triaxiality from 0 to 0.67.

A summary of constitutive material models used commonly for thermoplastic material in recent years is presented. The viscoplasticity model based on overstress theory (VBO) is chosen to implement into FEM simulation. Tensile, relaxation, and creep tests is performed with the large range of strain rate (10^{-4} to 1/s) for polypropylene at room temperature. It exhibited high sensitivity of strain rate. The experimental results are used to calibrate the material parameters in VBO model. The calibrated model described well the mechanical properties of polypropylene such as tensile, relaxation, and creep.

Chapter 6

FEM Simulation for fracture prediction

6.1 FEM Simulation for sheet metal

FEM simulation of SPIF process is a very complicated task due to large and complex model and long movement of forming tool. A full model should be used for simulation of SPIF process because this process is not symmetrical even for producing symmetric parts. It also cannot be assumed in two-dimension space, therefore, the FEM simulation of SPIF process was always performed in 3D space. However, several studies in the past performed the simulation with great efforts to simplify the calculation by modeling only one sector of symmetric part [133,63]. Sequentially, considerable error occurs in an analysis.

The results of mechanical testing showed that magnesium alloy sheet AZ31 has a high sensitivity with temperature and strain rate. The linear thermal expansion of AZ31 is higher than aluminum and steel alloy at both room and elevated temperature. Thus, 3D-fully coupled thermal simulation is needed to take into account of thermal effects and strain rate. In additional, the heat conducted between surfaces of forming tool and sheet due to local deformation in SPIF process should be obtained simultaneously rather than sequentially.

In FEM simulation of SPIF process, the previous researchers claimed that implicit solver usually meet convergent problems and large computational time consuming. They are due to large model and many nonlinear problems contributed in this process. To overcome these, the explicit solver is a first choice for FEM simulation in which the mass-scale and time-scale approach are used to speed up the computational time.

The full model of cone shape with curvature generatrix should be used in FEM simulation to predict mechanical failure in SPIF process due to two reasons: i) the position of fracture that occurs on a deformed part cannot foreknow; ii) a partial model gives inaccuracy results because of incomplete boundary conditions.

Because of using full model and large deformation in SPIF process, the distortion of elements in simulation is difficult to avoid. To overcome this problem, meshing adaptive approach should be used in FEM simulation. It can trigger off a slight increase of computational time. However, reasonable setting of the parameters in meshing adaptive brings the computational efficiency in correspondence with the acceptable accuracy of the simulated results.

The positive explanations of the deformation mechanism in SPIF process have been proposed in recent years. They seem to be no definite answer to which one causes the very large formability occurring during SPIF. However, mechanical failure in SPIF process may fail due to one or a combination of the failure mechanisms:

- Ductile failure due to nucleation, growth, and coalescence of voids;
- Shear failure due to fracture within shear bands;
- Failure due to necking instabilities.

The failure due to necking instabilities can be skipped because the researches showed undoubtedly experimental evidence of fracture that occurred prior to necking state. Therefore, to predict the failures in SPIF process, ductile failure and shear failure mechanism should be focused.

ABAQUS offers phenomenological damage initiation criteria for both mechanisms. The damage initiation criterion for these mechanisms can be specified for a given material in which are treated independently. The ductile criterion is specified by providing the equivalent plastic strain at the onset of ductile damage as a function of stress triaxiality and strain rate. Similarly, the shear criterion is specified by providing the equivalent plastic strain at the onset of shear damage as a function of shear stress ratio and strain rate.

6.1.1 Modeling of parts

The configuration for FEM simulation of SPIF process presented in Fig. 6.1a. They were modeled as Fig. 6.1b with the following features:

- Forming tool and backing plate are modeled as isothermal rigid bodies.
- Sheet is modeled as a deformable body with a dimension of 200x200x1.5mm. It is meshed with an eight-node brick element (C3D8RT) with reduction integration used in the fully coupled thermal analysis for saving computational time.
- Sheet is meshed in three layers to take into account of bending stiffness.

The choice of element type has a significant influence on the simulated results of SPIF process. In previous research, it is reported that the best results can be achieved with the four-node shell element (S4R) which has assumed in a plane-stress state [63]. The computational time of this element type is lower than one of the brick element types because taking into account of bending effect with brick element type in analysis needs at least three layers in thickness of sheet.

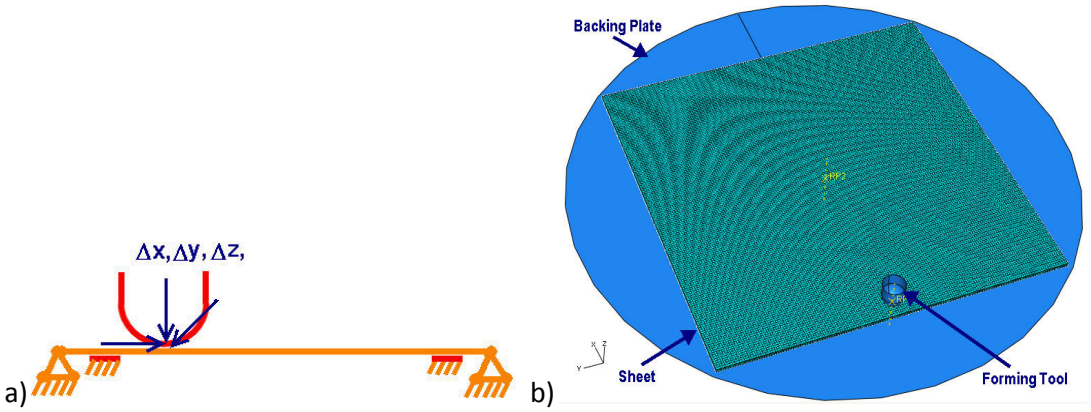

Fig. 6.1 Configuration of FEM simulation for SPIF process

However, 3D fully coupled thermal analysis only applies for brick element type. It describes more accurately the stress state occurring to cross the thickness of sheet. Additionally, it is also used to apply for 3D complex constitutive model that depends on strain rate and temperature. These are main reasons predisposed the use of brick element type in this study.

For evaluation of the accuracy of thickness and geometry, a model having the depth of 90mm (e.g. considering a model with wall angle from 28.25° to 88°) is used the FEM simulation. However, evaluation of mechanical fracture occurred in the deformed part does not need this large range of wall angle. Thus, the simulation started from the depth of 21.113mm until 90mm for saving computational time.

6.1.2 Full coupled thermal analysis

Fully coupled thermal-stress analysis is used with dynamic explicit solver. This analysis takes into account of thermal effects and strain rate sensitivity. In ABAQUS/Explicit, the heat transfer equations have the form as showed in (6.1). They are integrated using the explicit forward-difference time integration rule.

$$\theta_{i+1}^{N} = \theta_{i}^{N} + \Delta t_{i+1}\dot{\theta}_{i}^{N} \tag{6.1}$$

where θ_i^N is the temperature at node N with respect to i^{th} increment of the step. The current temperatures can be obtained by using known values of $\dot{\theta}_i^N$ from the previous increment. The values of $\dot{\theta}_i^N$ are computed at the beginning of the increment as following:

$$\dot{\theta}_{i}^{N} = (C^{NJ})^{-1}(P_i^J - F_i^J) \tag{6.2}$$

where C^{NJ} is the lumped capacitance matrix, P^J is the applied nodal source vector, and F^J is the internal flux vector (see more in section 6.5.4 of [86]).

6.1.3 The contacting and boundary condition

Surface to surface contacting condition is assigned between forming tool and upper surface of sheet; and between lower surface of sheet and inner surface of backing plate. The interactive properties for each contact are the Coulomb friction model and heat conduction coefficient. ABAQUS assumed that half of the heat dissipated because of friction is conducted into a sheet. The contact heat conductivity is defined as a ratio of the heat flux per unit area crossing the interfaces and the difference of temperature between those interfaces [86].

The sheet is heated by Joule effect in very short time that is considered uniform temperate in whole sheet.

6.1.4 Mass scaling

The previous researches claimed that FEM simulation of SPIF process took a huge computational time because of large model and non-linear conditions in the system. With ABAQUS/Explicit solver, there are two approaches can be applied to decrease the computational time such as mass scaling and time scaling. Depending on applications, a proper approach should be considered to have an accurate result. The analysis model of this study is taken into account of rate sensitivity. Therefore, mass scaling approach is the first choice for decreasing the computational time, but it still remains the kinetic energy of deforming material less than 4%-10% of total energy of the system (it should be noted that mass scaling does not influence on thermal solution).

The mass scale value is set to a value of 500 in the first simulation. It means that the mass of sheet is scaled to 500 times of actual mass. Unfortunately, dynamic energy exceeded 10% of the internal energy with this mass scaling. By using trial-and-error the proper value of mass scaling in 100 times is satisfactory for the dynamic energy to be less than 4% internal energy.

Additionally, an hourglass control is enhanced to avoid the zero-energy mode caused by the bending effects in deforming sheet.

6.1.5 Adaptive meshing

The final shape of the product in SPIF process is drastically different from the original shape of sheet. A mesh considered optimally in the original sheet geometry can become unsuitable in later stages of the SPIF process. A large material deformation in this process led to a severe element distortion and entanglement. These can lead to decrease in the size of the stable time increment and accuracy of simulated results. Therefore, the adaptive meshing tool should be used in the simulation of SPIF process to increase meshing quality at a reasonable CPU cost and avoid the distortion of elements.

ABAQUS has approaches to optimize a mesh which allow obtaining quality solutions while controlling the cost of the analysis. The adaptive meshing technique called

Arbitrary Lagrangian-Eulerian (ALE) is used in this study which is based on the combination of the features of pure Lagrangian analysis and pure Eulerian analysis.

By allowing the mesh to move independently of the material, ALE adaptive meshing is a tool that makes it possible to maintain a high-quality mesh throughout an analysis, even when large deformation or loss of material occurs. It does not alter the topology of the mesh, which implies some limitations on the ability of this method to maintain a high-quality mesh upon extreme deformation.

6.1.6 Movement of forming tool

The movement of forming tool in SPIF process is very complex path in long distance. To obtain the quasi-static simulation and to avoid an extreme accelerate condition, the forming tool is moved by using a smooth step definition method in ABAQUS. The smooth step definition method defines the amplitude, a, between two consecutive data points $\left(t_i, A_i^t\right)$ and $\left(t_{i+1}, A_{i+1}^t\right)$ as following:

$$a = A_i^t + \left(A_{i+1}^t - A_i^t\right)\xi^3\left(10 - 15\xi + 6\xi^2\right) \text{ for } t_i \le t \le t_{i+1} \tag{6.3}$$

$$\text{where } \xi = \frac{\left(t - t_i\right)}{\left(t_{i+1} - t_i\right)}. \tag{6.4}$$

The above function is such that $a = A_i^t$ at t_i, $a = A_{i+1}^t$ at t_{i+1}, and the first and second derivatives of a are zero at t_i and t_{i+1}. This definition is intended to ramp up or down smoothly from one amplitude value to another. The amplitude, a, is defined such that

$$\begin{aligned} a &= A_0^t \quad \text{for} \quad t \le t_0 \\ a &= A_f^t \quad \text{for} \quad t \ge t_f \end{aligned} \tag{6.5}$$

where $\left(t_0, A_0^t\right)$ and $\left(t_f, A_f^t\right)$ are the first and last data points, respectively.

6.1.7 Constitutive law

The Swift model is used to calibrate the evolution equation of metal material behavior in FEM simulation of SPIF process. The main reasons for this choice are due to its simplicity in calibration of material parameters and giving high accuracy of the prediction. This model is available in most commercial FEM simulation software. To using this material

model, the software requires the definition of two components: a shape of yield surface and a hardening evolution.

For definition of the yield surface, most of the previous researches used Von-Mises's or Hill's law. For definition of the hardening evolution, the researchers have a valuable comparison among types of the hardening evolution such as isotropic, kinematic, mixed-type isotropic-kinematic, Johnson-Cook, anisotropic law. They revealed that there are significant influences of each law on the accuracy of simulated results. Bambach et al. [3] concluded that the mixed-type isotropic-kinematic law gave more accurate deformation than the isotropic law. Bouffoux et al. [134] also have a same above conclusion. He et al. [133] used anisotropic hardening law to predict forming force in SPIF process. They concluded that the forming force in simulation is higher (about 20 to 30%) than one in experiment. Flores et al. [135] used a mixed-type hardening law to predict the forming force. They also concluded that the simulated result of forming force is consistent with the experimental result.

Rate	Temp.	R11	R22	R33	R12	R23	R13
0.1	300	1	1.032771	1.309909	0.968423	1	1
0.01	300	1	1.067037	1.182758	0.989567	1	1
0.001	300	1	1.046697	1.062514	0.996638	1	1
0.1	250	1	1.045278	1.440549	0.969314	1	1
0.01	250	1	1.099438	1.335401	1.011346	1	1
0.001	250	1	1.076096	1.138045	1.031356	1	1
0.1	200	1	1.022185	1.519581	0.972658	1	1
0.01	200	1	1.061493	1.465339	1.032522	1	1
0.001	200	1	0.995086	1.24682	0.971418	1	1

Table 6.1 Factors in potential function

The magnesium alloy sheet AZ31 showed slight anisotropic behavior at the elevated temperature. Particularly, the anisotropic behavior of AZ31 is very low at 300°C. However, to evaluate the simulating result, two hardening laws, mixed-type isotropic-kinematic and anisotropic law, were investigated in this study.

The results from tensile test in three directions are used to calculate the factor of anisotropic behavior in Hill's potential function as following and are shown in Table 6.1. They exhibited that their values are very close.

$R_{11}= R_{23} = R_{13} = 1,\ R_{22} = \sqrt{\frac{r_{90}(r_0+1)}{r_0(r_{90}+1)}},\ R_{33} = \sqrt{\frac{r_{90}(r_0+1)}{r_0+r_{90}}},\ R_{12} = \sqrt{\frac{3r_{90}(r_0+1)}{(2r_{45}+1)(r_0+r_{90})}}$ (6.6)

Finally, two options of temperature-dependent data and rate-dependent data in ABAQUS are used to present the sensitivity of temperature and strain rate in mechanical behavior of magnesium alloy AZ31.

6.1.8 Fracture modeling

It is well-known that mechanical failures of a part made of sheet metal may occur due to a number of mechanisms including: i) void nucleation and coalescence; ii) shear band formation; iii) necking instability. From previous results of different researchers and observation in the experiment of this study, the fracture occurred in deformed part of SPIF process is absent from necking phenomenon state. Therefore, to obtain reliable predictions of damage from SPIF simulations, it is essential to model damage initiation and progressive failure due to the first and second failure mechanism. Damage due to initiation, growth and coalescence of voids are considered as an agent leading to ductile failure in sheet metal. The formation of cracks within shear bands is considered as an agent leading to shear failure.

As presented in section 4.3.2.8 and advantages of CrachFEM presented on 4.4, CrachFEM criterion is proposed specially to predict damage due to one or combination of the mentioned mechanisms. However, the third failure criterion (e.g. instability due to the localized necking) is necessary only if a part is discretised with shell elements in FEM simulation. Thus, remaining damage criteria are implemented into ABAQUS to predict mechanical failure in SPIF process.

ABAQUS software is available to predict the phenomenological damage initiation criteria for these two mechanisms. The ductile criterion is specified by providing the equivalent plastic strain at the onset of ductile damage as a function of stress triaxiality and strain rate. The shear criterion is specified by providing the equivalent plastic strain at the onset of shear damage as a function of shear stress ratio and strain rate. Thus, it is convenient to apply CrachFEM criteria in ABQUS through its ductile criterion and shear criterion. The input values were calibrated from the chapter 5.

6.1.9 Numerical results

6.1.9.1 Influence of meshing density and mass scale

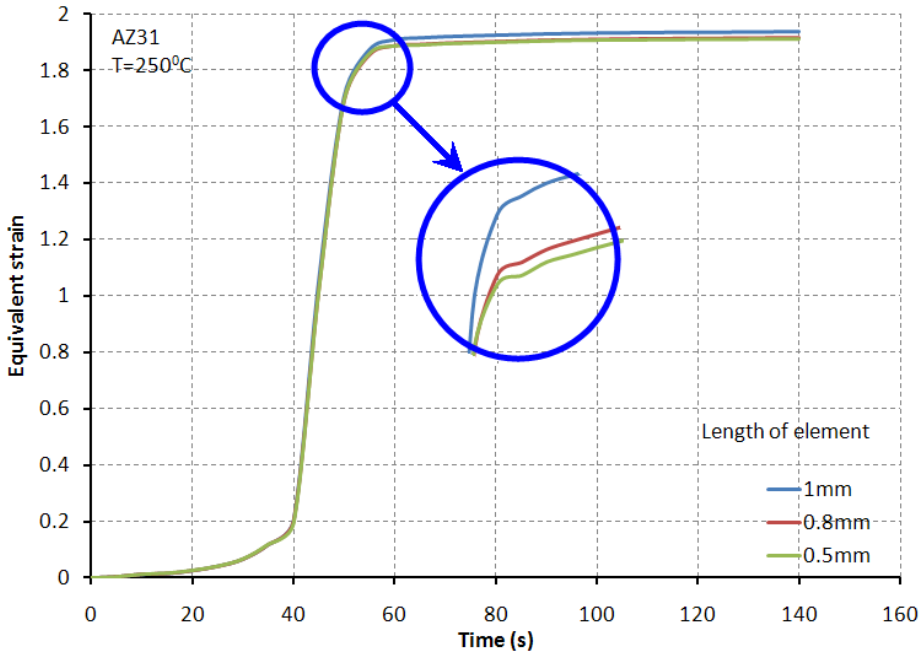

Fig. 6.2 Comparison of equivalent between meshing densities

It is known well that meshing density has a significant influence to predicting results of fracture in FEM simulation of conventional forming. The fracture criteria based on the nucleation of micro-voids and their growth (e.g Gurson type, Wikins model) is highly dependent on meshing density. Although CrachFEM criteria proposed as less dependent on meshing density, the consistent meshing density is also necessary to achieve a satisfying result. It is also not meshed too small because the computational time is decided by stable increment time that is strictly depended on the length of an element for an explicit integration scheme. It is usually suggested that the element length of 1mm gives a satisfactory result of crash simulation in automotive industry. However, there is a clear difference in using the element length of 1mm and 0.8mm for equivalent strain. By using trial-and-error, the element length of 0.8mm and 0.5mm is not much different. Nevertheless, the computational time increased significant as presented in Table 6.2 (without mass scaling).

In order to decrease the computation time, mass scale technique is used in this simulation, which is taken into account of the sensitivity of strain rate. The mass scaling of 500 times the actual mass is used in the first time with the element length of 0.8mm. The computational time is shown on Table 6.3.

Length of element	Total number of element	Number of CPUs	Computational time
1mm	73947	5	121h
0.8mm	115248	5	180h
0.5mm	295788	5	324h

Table 6.2 Comparison between the lengths of element

Ratio of mass scale	Total number of element	Number of CPUs	Computational time
500	115248	5	60h
100	115248	5	94h
50	115248	5	115h

Table 6.3 Comparison between the values of mass scale

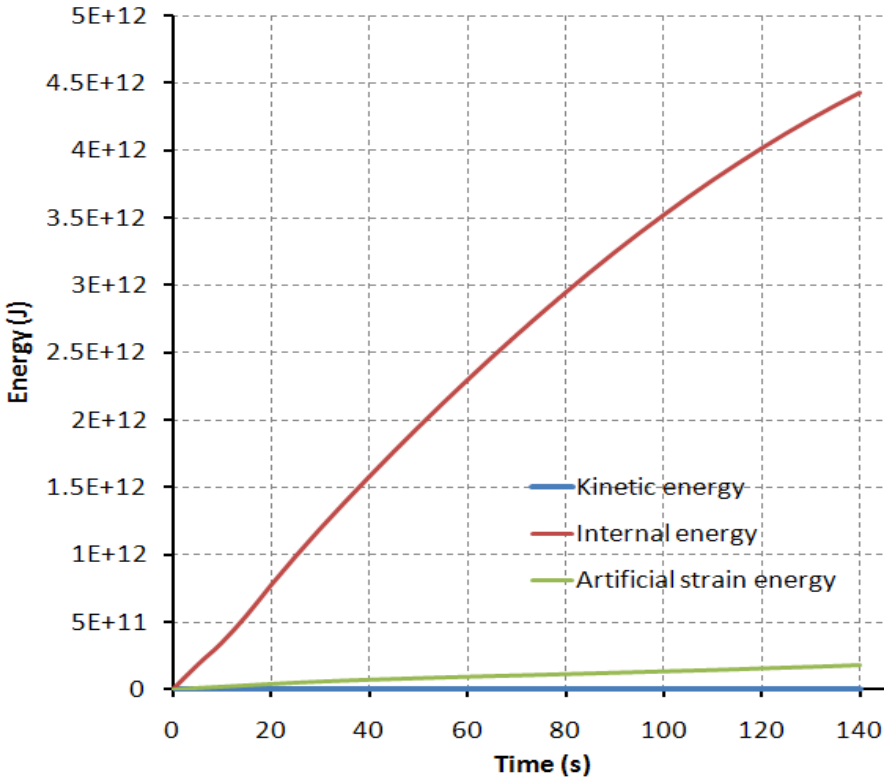

Fig. 6.3 The element of energy in system with mass scaling of 100

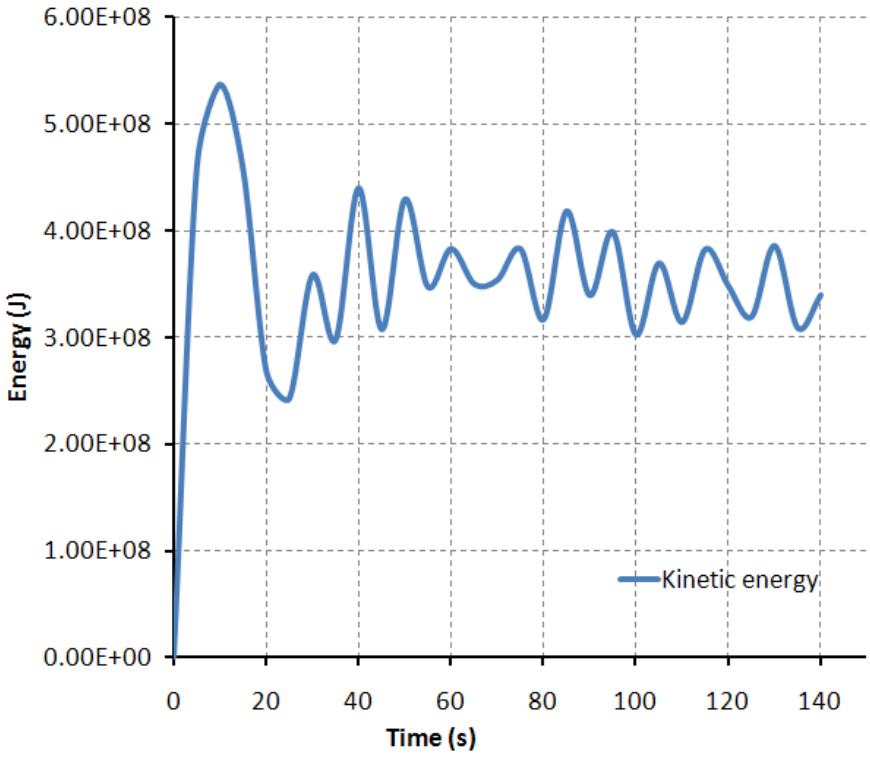

Fig. 6.4 Dynamic energy in system with mass scaling of 100

The dynamic energy in the mass scaling of 100 is less than 5%. Thus, it is a satisfactory to the condition of quasi-static simulation in forming operation. The history of dynamic energy with mass scaling of 100 is shown in Fig. 6.3 and Fig. 6.4. This value is used for all simulations of SPIF process in this thesis.

6.1.9.2 Isotropic and anisotropic material model

Pellegrini [96] presented the anisotropic behavior of magnesium AZ31 sheet through the values of average normal anisotropic ratio ($\bar{R}$) and planar anisotropy (ΔR) as a function of temperature and strain rate. The results showed that anisotropic behavior is depend significant on temperature and strain rate. However, at a high temperature (250°C and 300°C), the values of $\bar{R}$ and ΔR decrease significantly. Particularly, value of ΔR is close zero at the temperature of 300°C and strain rate of 2mm/s. This result is consistent with one of Zhang [74]. It can be explained that size of grains at 300°C is relatively small (less than 5μm) due to dynamic recrystallization. The formability is improved considerably at a temperature from 250°C to 300°C.

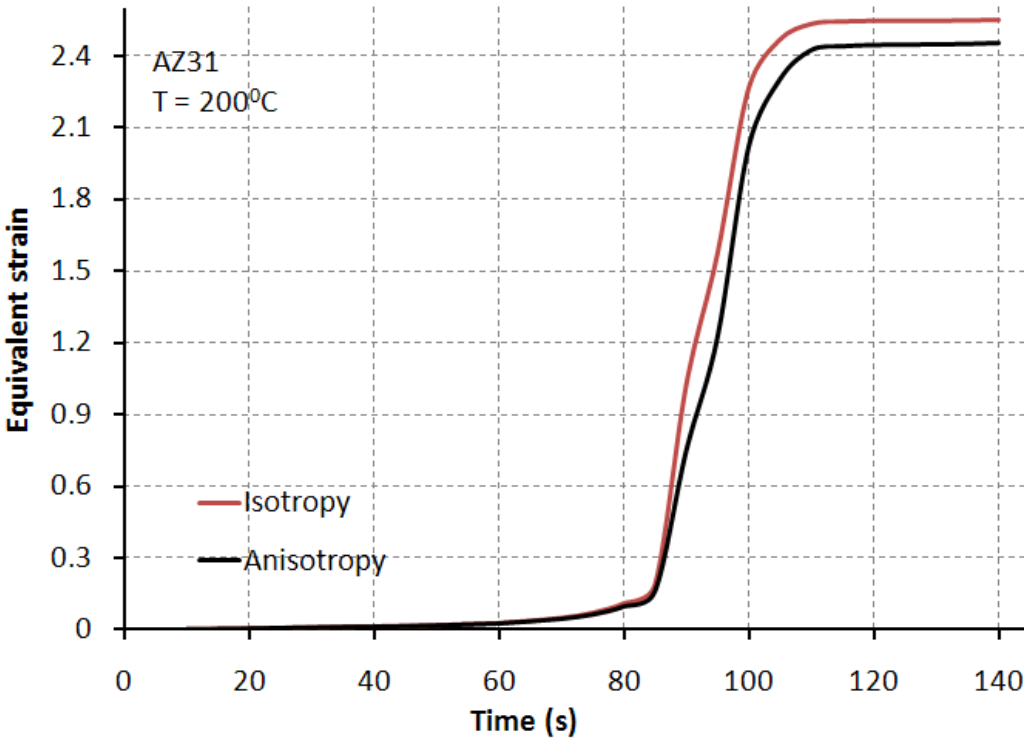

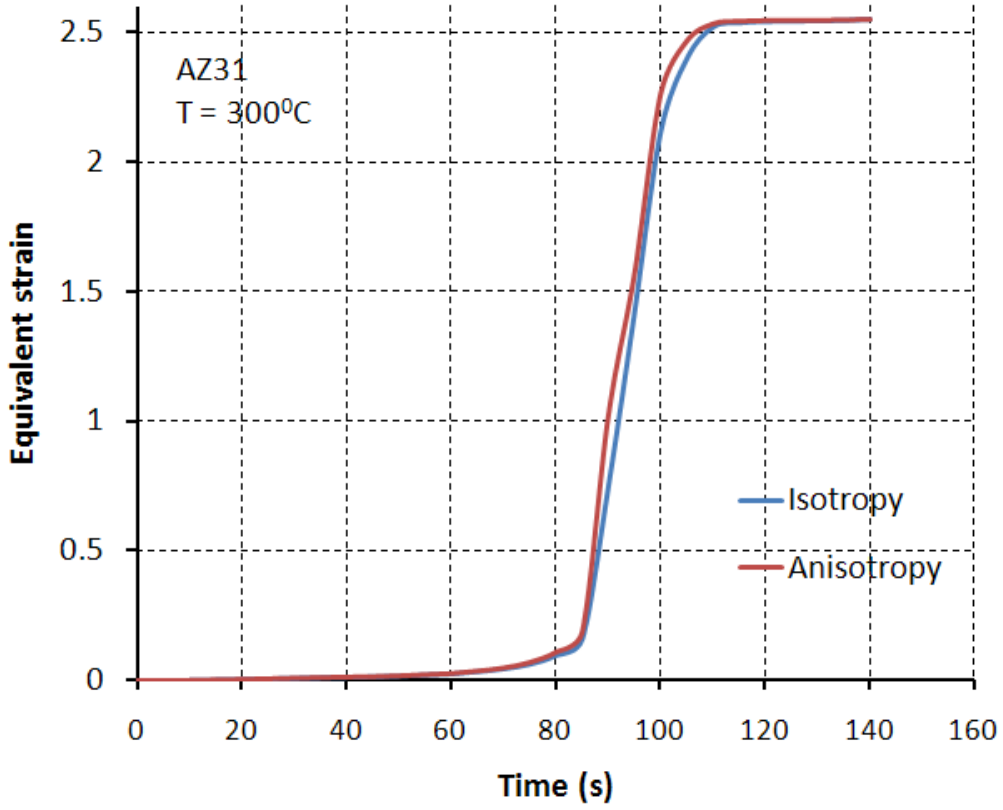

Fig. 6.5 Comparison of equi. strain between isotropy and anisotropy material model

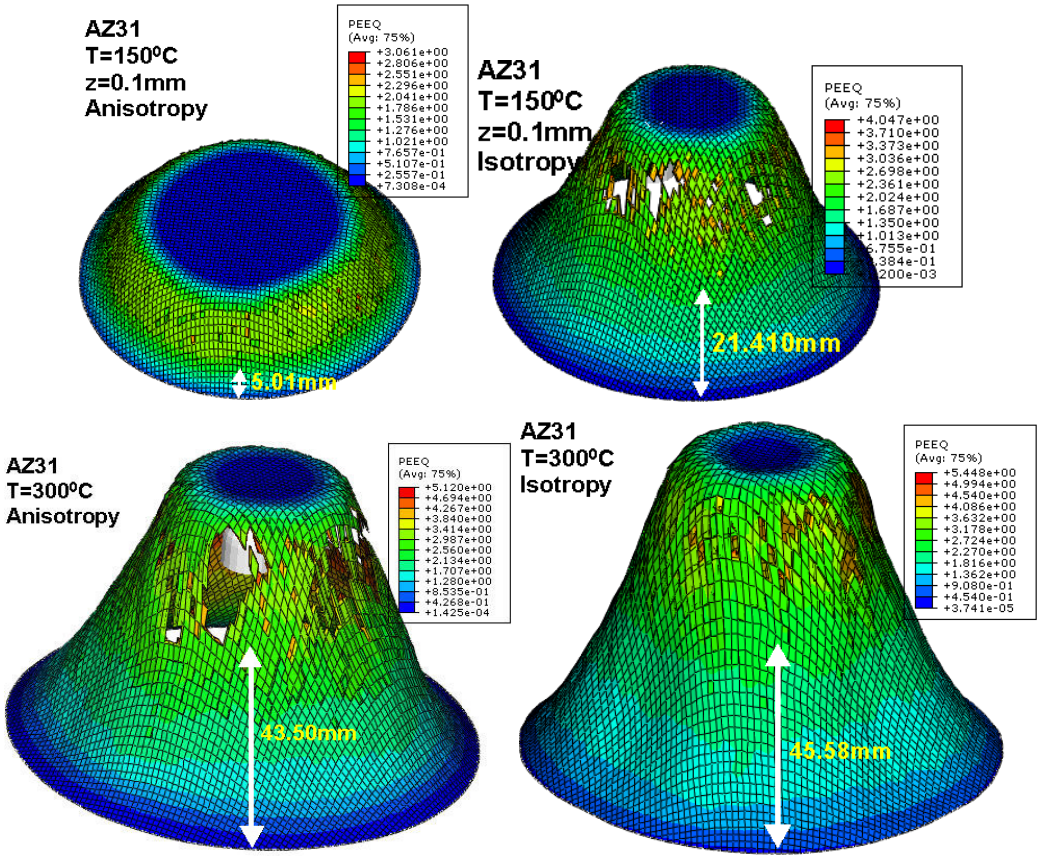

Fig. 6.6 Prediction of fracture in isotropy and anisotropy model at 300°C

For FEM simulation, two material models were considered in this thesis. The first material model is isotropy which used an isotropic plasticity model of ABAQUS library. The second material model is implemented an anisotropic behavior under a Hill potential function as presented on section of 6.1.7. FEM simulated results shown a large difference of the equivalent strain between two models (Fig. 6.5). These results are a good agreement with the evaluations of Pellegrini [96] in actual tensile experiment. The equivalent strain is taken from same node which is monitored during the simulation process in both material models with different temperature. The equivalent strain path has a step curve because forming tool is moving progressively along the length if an element in which contained this node. Strain increment is directly occurred in this element and a neighboring element. In turn, strain increments do not increase anymore when the forming tool moves far away from the node.

The prediction of fracture in two material models is presented in Fig. 6.6. The fracture of the anisotropy material model occurred prior to isotropy model. There is a difference of the time occurred the fracture in the formed part. In the anisotropic model with 150°C, the first element removed to FEM analysis started on frame 12 with respect to the achieved depth of 5.01mm[1]. The first element removed from FEM analysis started on frame of 40 with respect to the depth of 21.401mm for the isotropic model. However, there is a small difference (one frame) of fracture positions at the temperature of 300°C between models. From FEM results, it can be concluded that implementing the anisotropic behavior is necessary to obtain a better prediction for magnesium sheet AZ31.

6.1.9.3 Effect of friction at elevated temperature

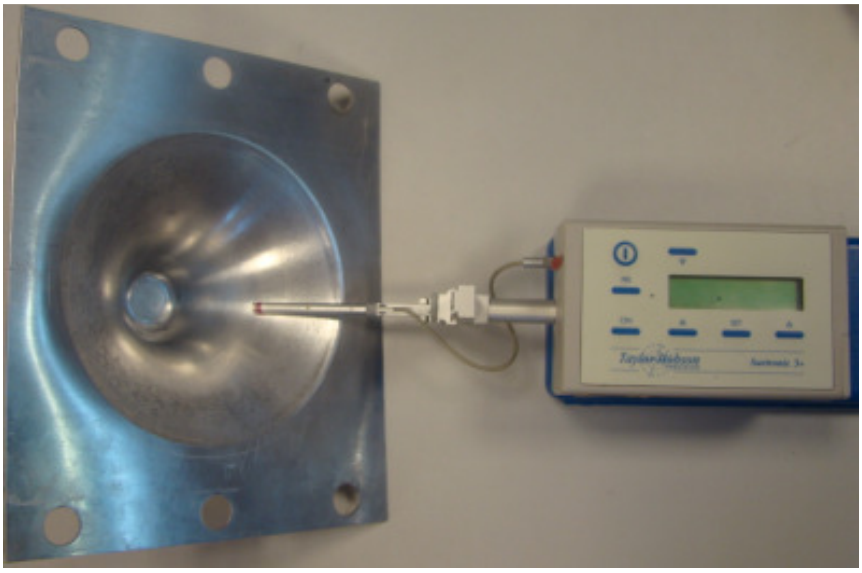

Fig. 6.7 Measurement of surface roughness by Surtronic 3+

The quality of deformed surface is influenced significant by lubricated condition. In this study, three different lubrications MoS_2, Tribostart, and solid graphite were used for deforming magnesium sheet at the elevated temperature. The results showed that MoS_2 gave a better surface in SPIF process at the elevated temperature. Using solid graphite powder has a problem with health and environment. Thus, MoS_2 is chosen for lubricating the contacting surface in all experiments of this study. The sheet surface is

[1] The simulation is started from the depth of 21.113mm, thus, the actual achieved depth is 26.123mm.

covered a layer of MoS_2 before deforming and it continues to be added during deformation.

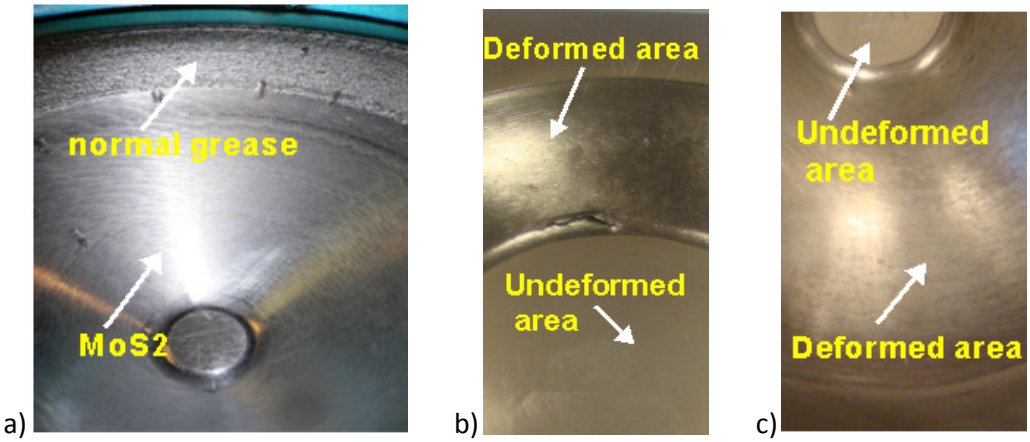

Fig. 6.8 Influence of lubrication conditions

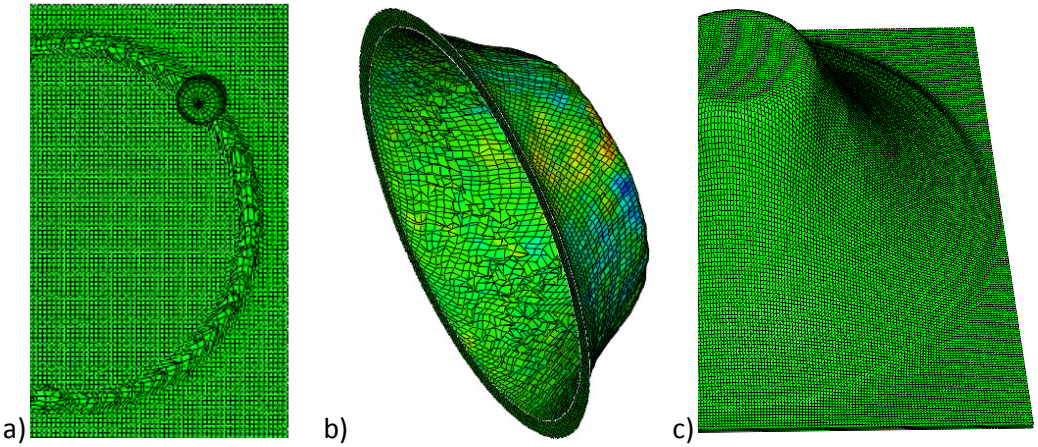

Fig. 6.9 Influence of friction coefficient on simulated results

Fig. 6.8 showed the difference of surface with different lubrication. In Fig. 6.8a, some first rounds are lubricated Tribostart which gave worse quality of surface (Ra = 5.4) with aluminum sheet at 200°C. However, the quality of surface became better with MoS2 (Ra =1.66). For magnesium sheet, the highest quality of surface achieved at the temperature of 250°C (Ra = 0.9, in Fig. 6.8c). At 150°C, the quality of surface (Ra=1.9) is less than one at 250°C (Fig. 6.8b).

Selecting a friction coefficient for FEM simulation is also an important problem. It influences significantly to simulated results. A large range of the friction coefficient (0.08

for sliding with grease and 1.2 for sliding with the dry condition) for magnesium sheet is suggested in engineer's handbook. This range of value is for contacting condition at ambient. However, the friction coefficient is different at an elevated temperature. There is no suggestion for choosing the friction coefficient at an elevated temperature in literature. By using trial-and-error the value of 0.09, 0.1, 0.2, 0.5, 1, and 1.2 is used in simulation. The simulated results are compared with actual experiment through an achievable wall angle. In Fig. 6.9a, it showed the result with the friction coefficient of 1.2. The mesh is distorted dramatically (over the limited ratio of meshing distortion) which caused the interruption of simulation after five rounds. For value of 0.5 as showed in Fig. 6.9, the distortion ratio is also over the limited ratio of meshing distortion. There are no changes with the value 0.09, 0.1, and 0.2 which gave a good agreement with actual experiments. The friction coefficient of 0.1 is chosen for FEM simulations as showed in Fig. 6.9b.

6.1.9.4 Accuracy of geometry and thickness

The geometric accuracy of deformed part is an important aspect in SPIF process. It is interested in this problem because the sheet is deformed without any die or partial die. Particularly, the sheet became softer when it is heated up to high temperature. The deformation of sheet occurs far from the contact area of backing plate that is twisted about symmetric axe of product following rotating direction of spindle. It can be difficult to predict in this case. In theoretical view, SPIF technique can deform a part with unlimited depth. However, a part with wall angle changing according to the obtaining depth can trigger off inaccuracy in geometric shape. Thus, the stability of geometric shape should be investigated carefully in this study.

A comparison between the bottom of simulated part and actual experimental part is shown in Fig. 6.10b. The profile of the bottom at maximum achieved depth is also shown in Fig. 6.10a. The bottom of part at depth of 61mm is a concave shape which top of concavity is outward of part. The maximum height of the concavity is 0.02mm that is very consistent with actual experiment. This result concluded that assuming a partial model for FEM simulation in SPIF process for saving computational time could trigger off the inaccuracy in simulated results of the previous results [26,3,48,63,28,65]. It should

be noted that the part used in FEM simulation is not assumed as symmetric part, although the geometry of product is symmetric. The result showed the difference in both stress-strain state and geometric accuracy.

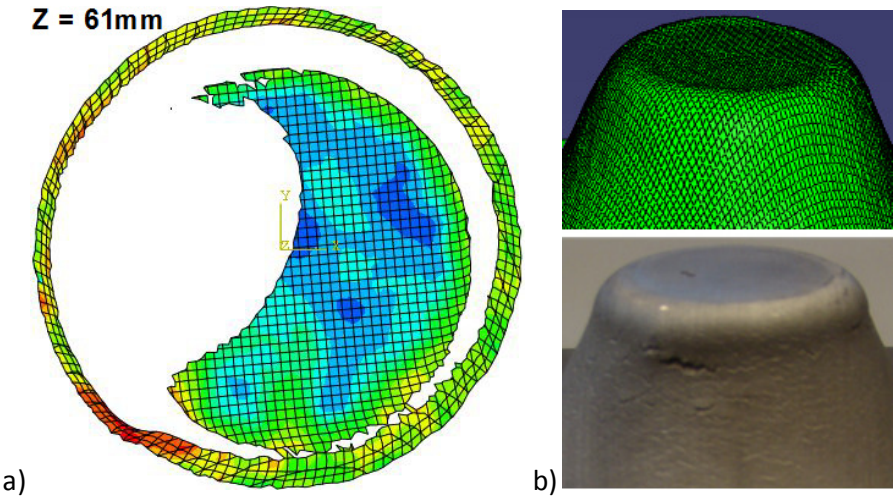

Fig. 6.10 Profile of deformed part cut at top of deformed part

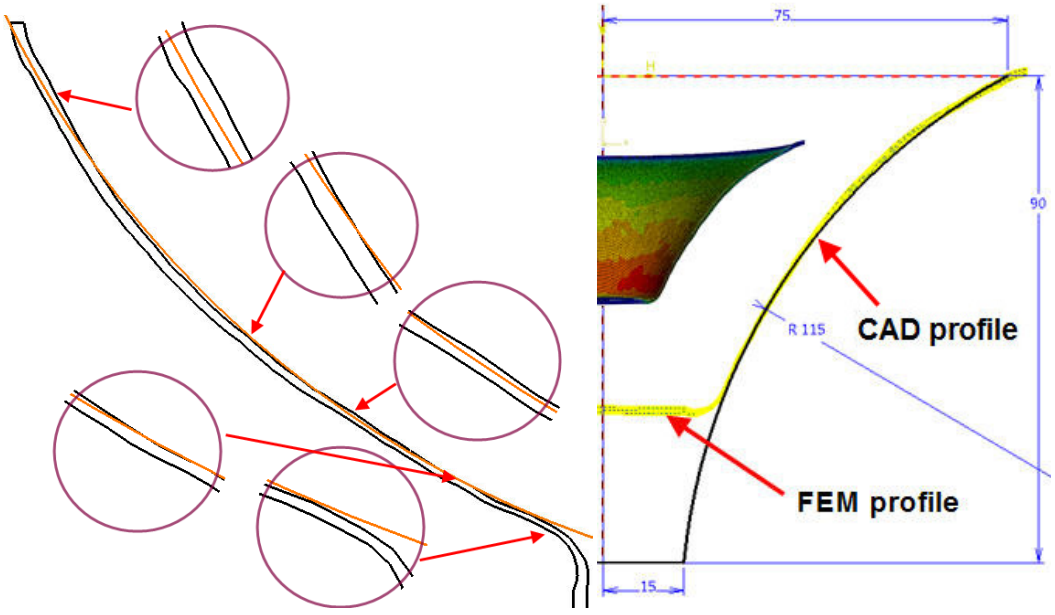

Fig. 6.11 Comparison between CAD profile and FEM profile

Fig. 6.11 presented a comparison between CAD profile and a profile extracted from FEM simulation. As shown in Fig. 6.10, the section at different heights is not concentric. Thus, the profile is cut along the z-direction at many positions and a profile which has the most inaccurate to be selected to compare with CAD profile as shown in Fig. 6.11. The

deviation between the center curve of FEM profile and CAD profile is presented in Fig. 6.12. The largest deviation at the depth of 28mm is 0.45mm.

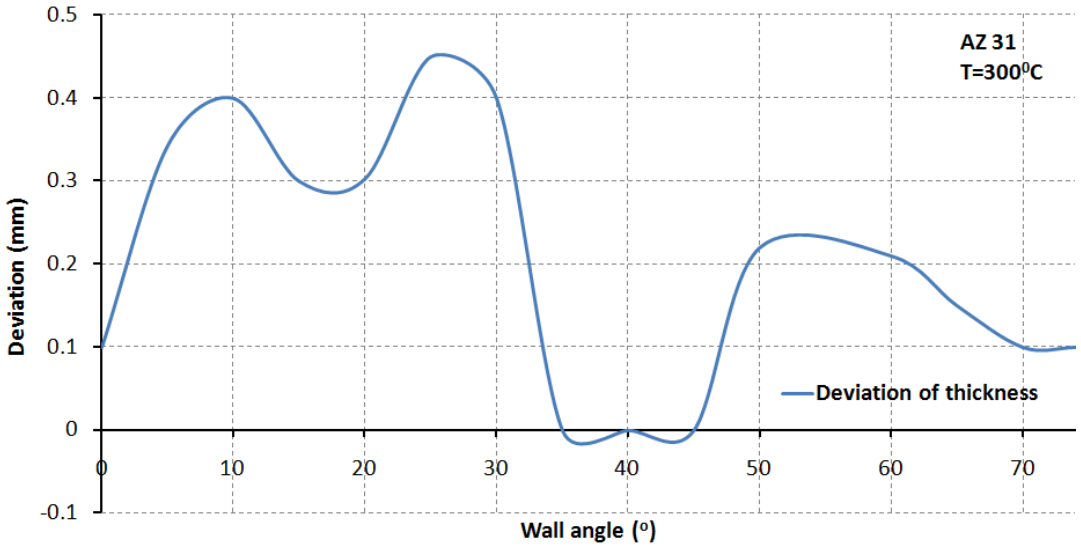

Fig. 6.12 Deviation between the center curves of FEM profile and CAD profile

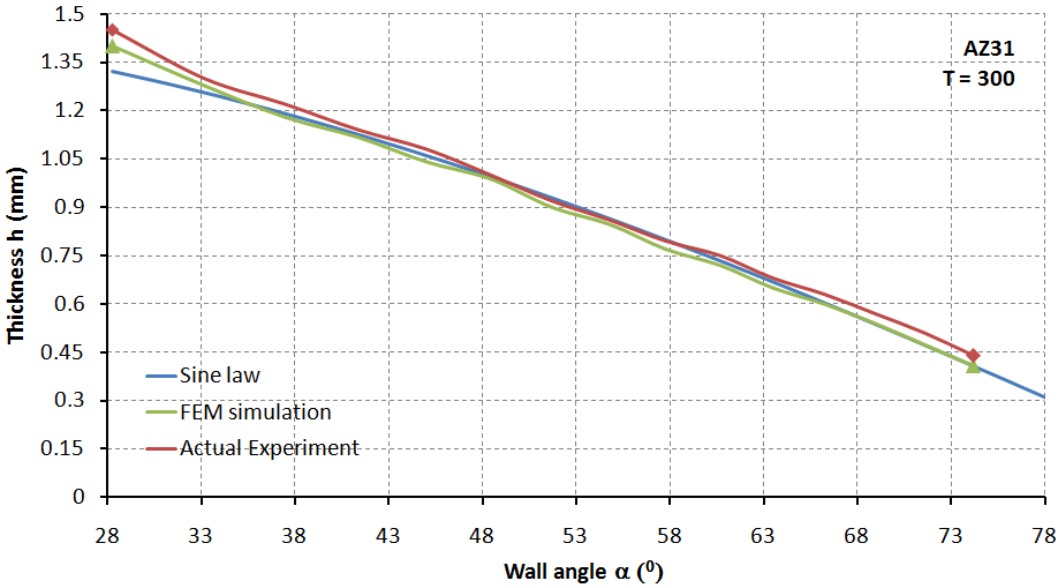

Fig. 6.13 Comparison of thickness between FEM simulation and actual experiment

The measuring results of deformed part from CMM machine are given two profiles of inner and outer surface. Each part is measured at three different positions along the achievable depth. The thickness of deformed part is calculated from measured results in Excel table. For FEM result, ABAQUS allows extracting two profiles of simulated part in wireframe. These profiles are then input into commercial CAD to measure the

perpendicular distance between the profiles along the depth of the simulated part. Fig. 6.13 presented the distribution of thickness of actual experiment and FEM simulation with respect to the achievable wall-angle in comparison with sine law. There is a good agreement between experimental result and FEM simulation.

6.1.9.5 Propagation of fracture path

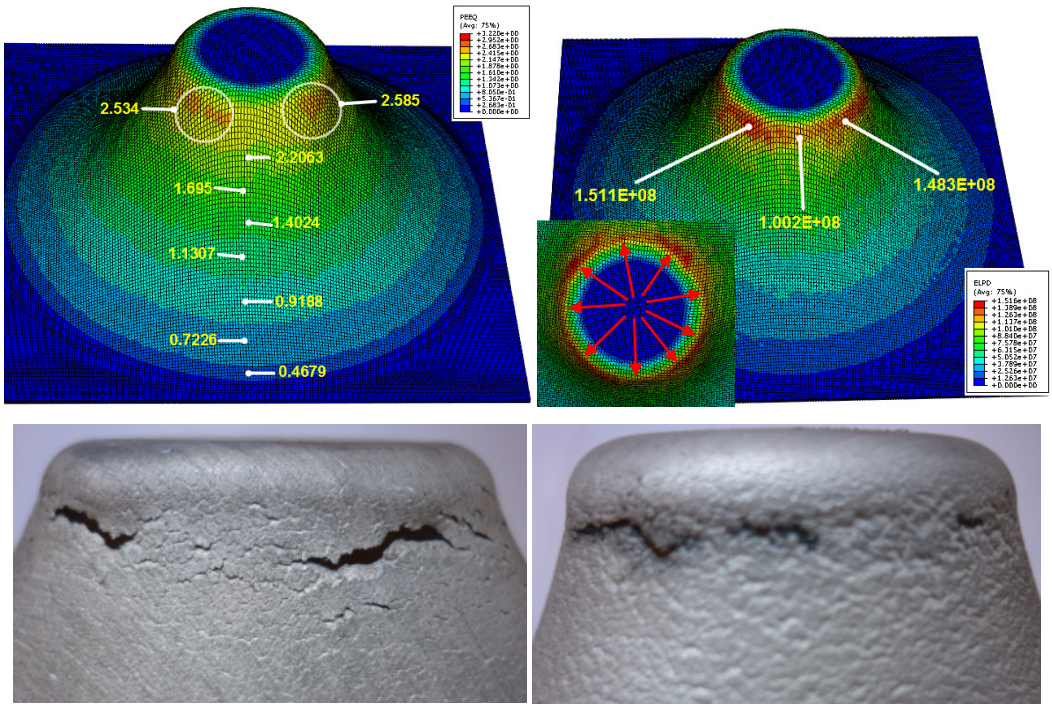

Fig. 6.14 Distribution of equivalent strain and strain dissipation energy at 300°C

To understand the fundament cause of mechanical failures in SPIF, it is necessary to explain the formative origin of the propagation fracture paths found in actual experiments. The propagation of mechanical fractures occurred in SPIF with sheet metal at an elevated temperature is found in two typical types: zigzag and the open fracture (see Fig. 3.16, Fig. 3.17, Fig. 3.18, Fig. 3.19, Fig. 3.20). The zigzag propagation of fracture at the elevated temperature is elongated more than one at room temperature. The open fracture usually occurs at a lower temperature. The FEM simulated results presented clearly the distribution of equivalent strain and minor and major strain at fracture zone in Fig. 6.14, Fig. 6.15.

Fig. 6.14 (in left side of upper row) showed the changes of the equivalent strain along the achievable depth of a deformed path. The equivalent strain distributed regularly into inconsecutive distances around a circumference at fracture zone. The value of equivalent strain seems to be equal and symmetric about revolution axe of part. Fig. 6.14 (in right side of upper row) showed a distribution of strain dissipation energy which is similar to the distribution of equivalent strain. The value of concentrated zones is equal and larger than the connected zone between ones. This distribution triggered off a zigzag propagation fracture in deformed parts as explained in section 3.3.

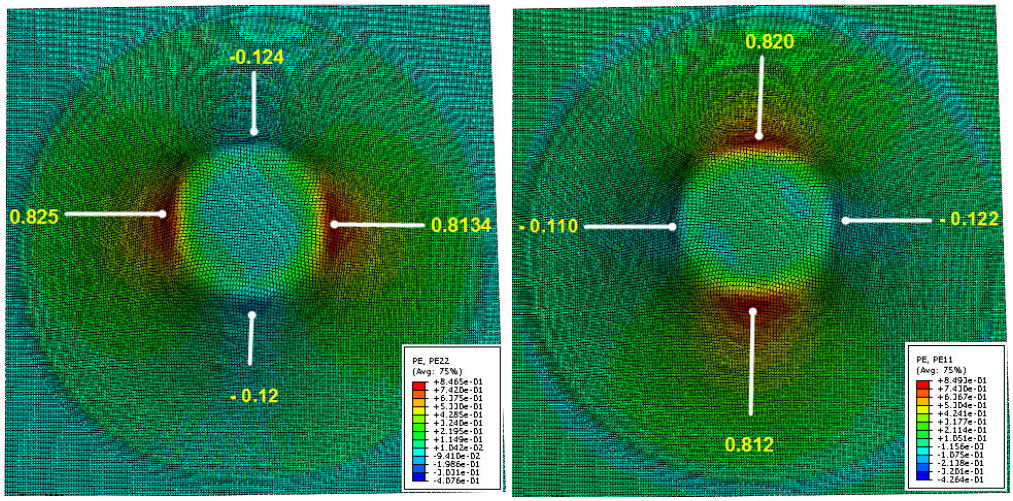

Fig. 6.15 Distribution of minor and major strain

The distribution of minor and major strain is shown on Fig. 6.15. It is clear to observe that tension and compression zone is symmetric about the revolution axe of the deformed part. The major strain is an opposite position with minor strain which seems to be caused by tensile stress in the axial direction of forming tool.

6.1.9.6 Prediction of mechanical failure

At the recent time, the deformation and fracture mechanism of SPIF has not well understood. There are many positive explanations for the deformation mechanism, but they are only valid in a certain situation. Thus, a definite answer may to be a combination of these explanations. Similarly, the mechanical failure in SPIF may happen due to one or a combination of the three failure mechanisms as mentioned in section 4.3.

Revelation of the failure mechanism caused the fracture in SPIF is very important in order to control processing parameters for obtaining the maximum achievable wall angle. FEM simulation for predicting the failures in SPIF showed a good agreement with observations from actual experiment.

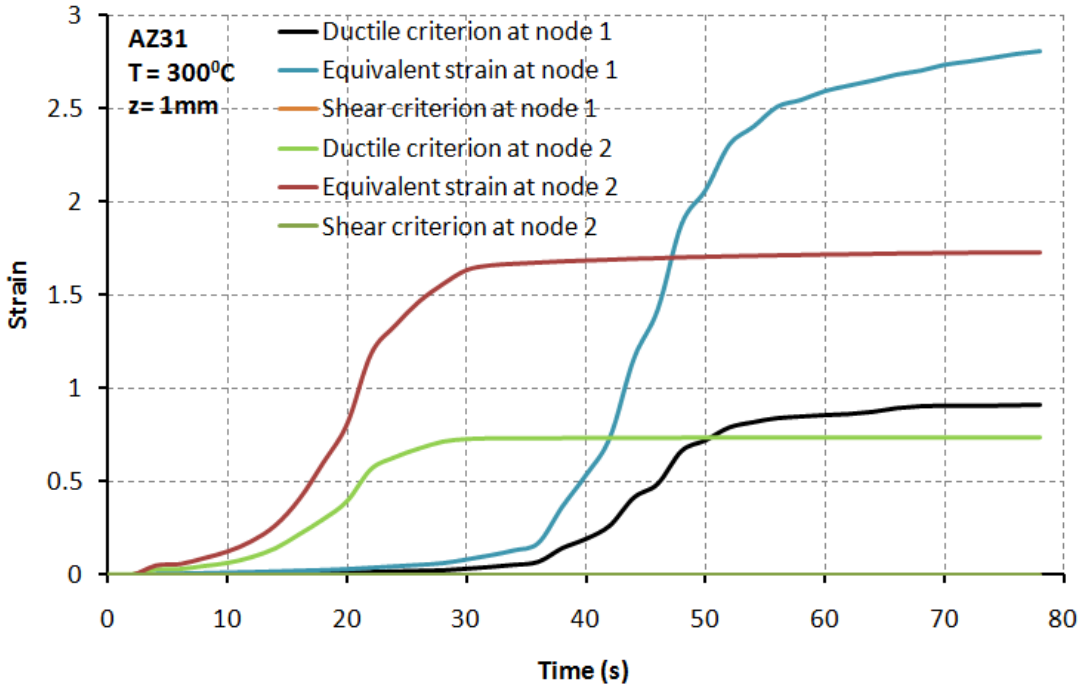

Fig. 6.16 Evolution of equivalent strain and damage criteria

The status of each element in FEM simulation is monitored during the simulation of SPIF process. It is very easy to reveal which criterion is active to remove the element obtained damage condition (D_c = 1). The SPIF process simulated at different conditions of temperature, depth step, friction, and material properties (e.g. anisotropy and isotropy) showed that most case of removing the fail element is because the ductile criterion obtained to damage condition. Fig. 6.16 presented the evolution of ductile damage criterion at two nodes. The first node is near a fail element that the evolution curve is asymptotic with a limited damage line. The second node located in a safe zone, thus, its evolution curve is far from the limited damage line. The evolution of shear criterion is extremely small. Therefore, the damage prediction in SPIF only needs to use the ductile criteria. It can conclude that ductile failure due to nucleation, growth, and coalescence of voids is a main reason caused the mechanical fracture in SPIF process.

The position of initiation of fracture is occurred at the smallest top of obtained bell-shaped curve as Fig. 6.17 and Fig. 3.17. The positions are usually symmetric about revolution axe which is parallel to rolling direction. These are caused by the anisotropic properties of magnesium sheet. For isotropic material model, initiation of damage happened randomly in a large zone as displayed on the pictures in the right side of Fig. 6.6. At the temperature of 300°C, the influence of anisotropy is low, thus, the position of neighbored fracture is near.

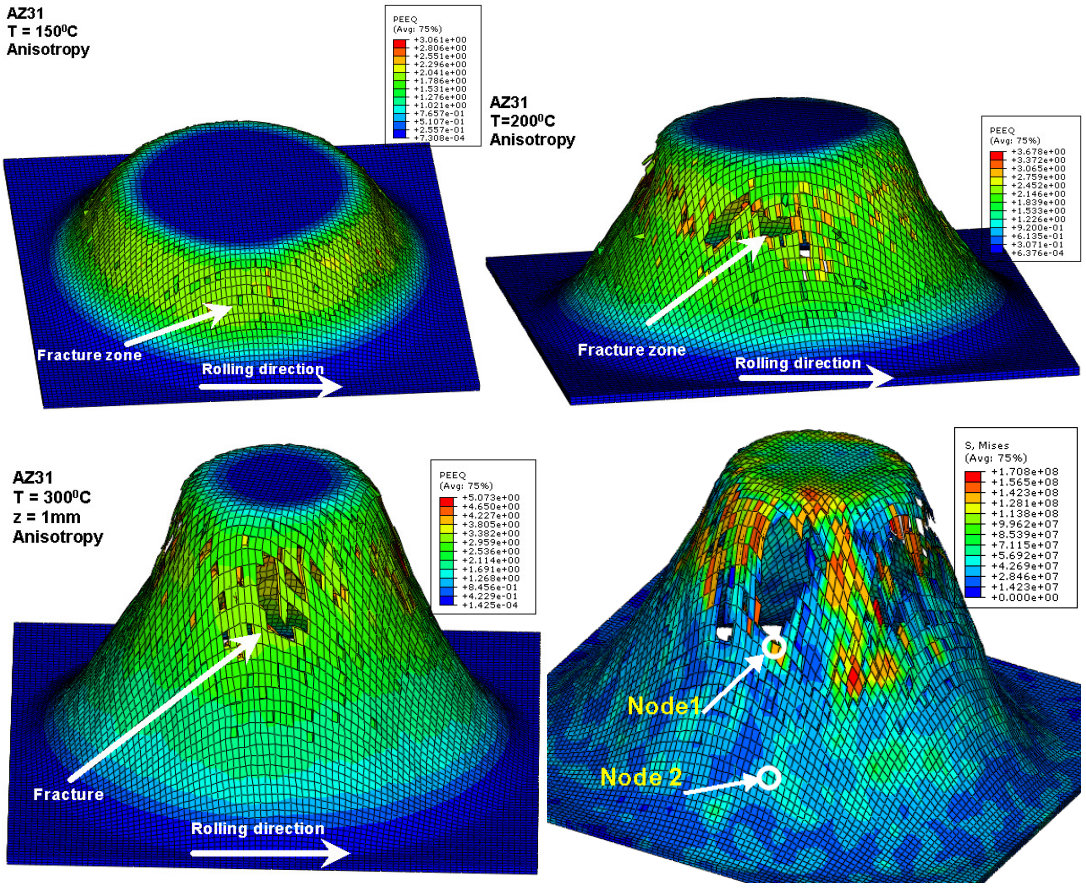

Fig. 6.17 The postion of initiation of fracture in SPIF

The distribution of shear stress component σ_{12} and frictional shear stress components presented on Fig. 6.18a and Fig. 6.18b, respectively. It is revealed that there are concentrated significantly of shear stress component before initiation of damage in deforming part. The frictional shear stress is given in two components. The first component is the frictional shear stress component in the down slip direction. The

second component is the frictional shear stress component in the moving slip direction of forming tool (Fig. 6.18b).

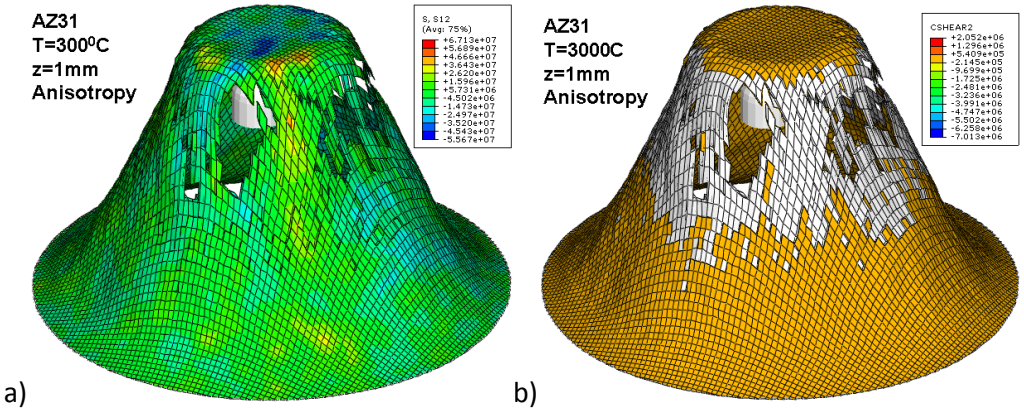

Fig. 6.18 Distribution of shear stress and frictional shear stress components

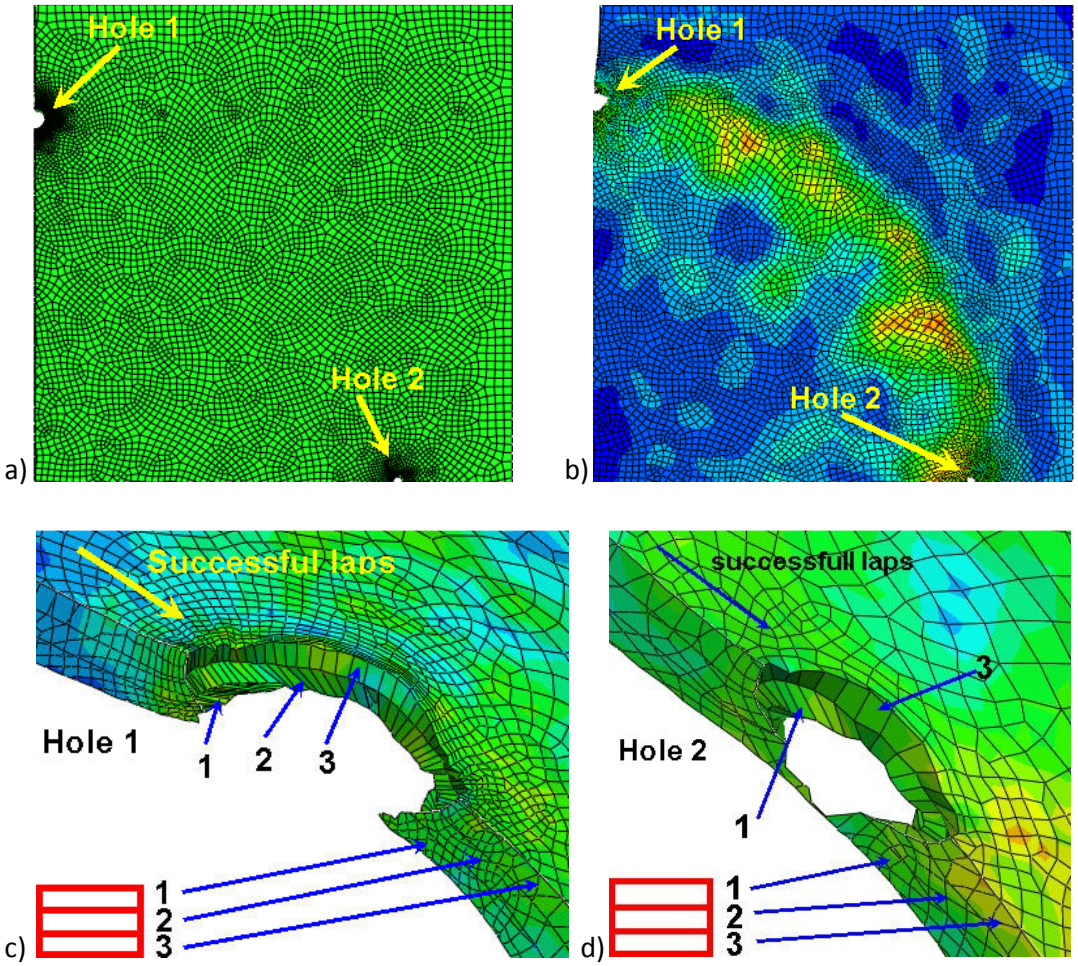

Fig. 6.19 Evident of shear through thickness in the deformation of SPIF

An additional simulation is performed to evaluate shear stress through thickness of the sheet. Two holes with different radius were made on the sheet before the deformation as displayed on Fig. 6.19a. The simulated result revealed that a large amount of shear stress occurred on upper layer of the sheet. The value of shear stress increased through the successful laps. The shear stress in the axial direction of forming tool is larger than one in rotational direction of forming tool. It can be concluded that shear stress contributed into the deformation of the sheet with SPIF process.

6.1.9.7 Validation of results

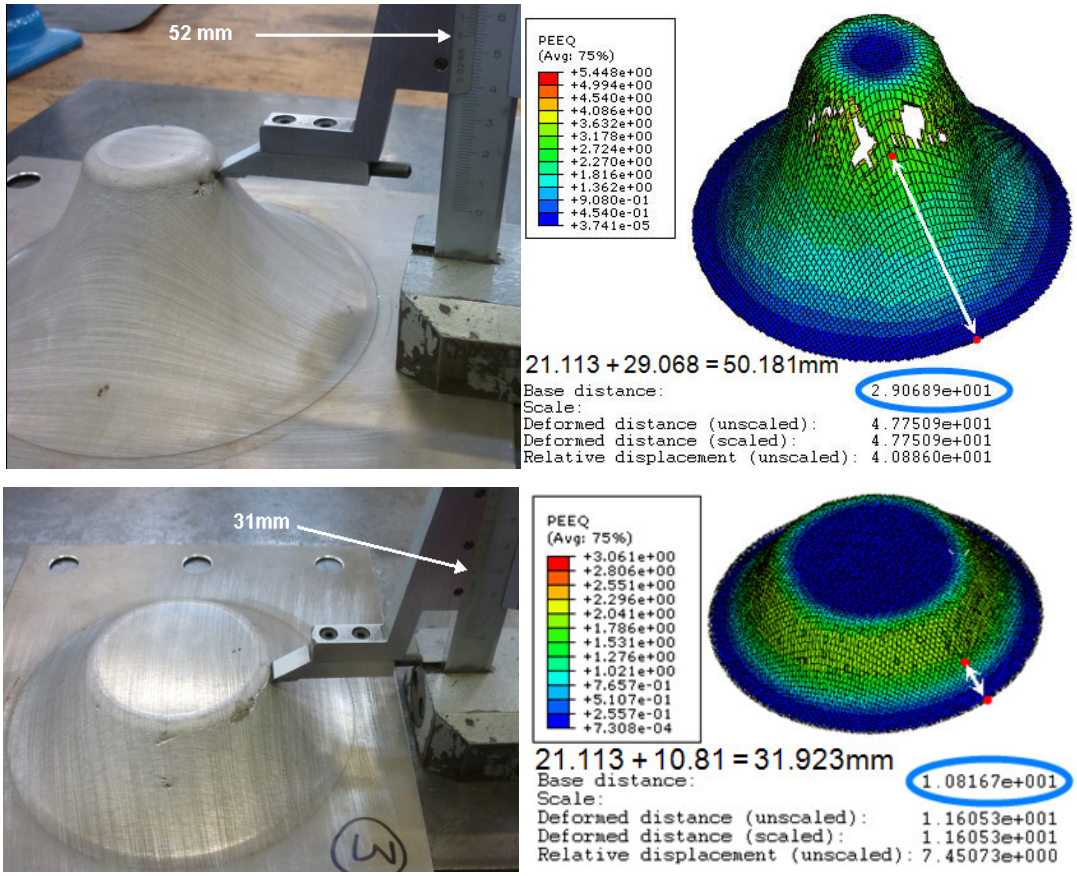

Fig. 6.20 Some simulated results in comparison with actual experiments

FEM simulation of SPIF is performed at different processing parameters similar to actual experiments. The simulated results shown a good consistent with one of the actual experiments about the position occurred fracture and the achieved depth. They also presented clearly the influences of processing parameters with respect to the

experiments. The comparison of obtained depth of SPIF between results of FEM simulation and experiment is shown in Table 6.4.

Parameters	FEM simulation	Actual experiment
T=300, F=6000, z=0.5	64.613	63
T=300, F=6000, z=1	58	Not yet
T = 250, F=6000, z=0.1	71.211	70
T=150, F=6000, z=0.1	26.123	28
T=150, F=6000, z=0.5	Occurred prior to simulated zone[2]	17
T=150, F=6000, z=1	Occurred prior to simulated zone	Not yet
T=200, F=6000, z=0.1	36.731	Not yet
T=200, F=6000, z=1	30.20	Not yet
T=25, F=6000, z=0.5	4.52	5

Table 6.4 Comparison of the results between simulation and experiment

6.2 FEM simulation for polymers

In this section, the finite computational procedure for constitutive material model is established to implement into a simulating environment under a user-material subroutine. The constitutive equation of VBO model is presented in details in chapter 5. This model is very complex in calculation and calibration of material parameters.

The constitutive model was implemented into ABAQUS under subroutine called UMAT. ABAQUS is the FEM simulation software which allows the user can implement into dedicated material models which are not available in its material library. The computational procedure for implementation of VBO model is presented in the form of implicit integration constitutive equation. It is important to note that all quantities are written at the end of the time increment in the implicit scheme. Because it enables significantly larger time increments to be used, the implicit scheme generally leads to much more rapid solutions. 3D simulation for SPIF process with the implemented constitutive models is performed. The simulated results of two models are compared with the actual experiments.

There are some researchers developed the finite computational procedure for VBO theory [136,137,138]. Nishiguchi et al. [138,136] developed a FE computation for VBO

[2] The simulation is started from the depth of 21.113mm

theory using the additive decomposition of the rate of deformation and a newly defined stress rate. A plastic spin and flow law with second order terms were postulated. Gomaa et al. [137] also developed a finite deformation, isotropic viscoplastic theory based on overstress (FVBO). They formulated VBO theory in the updated Lagrangian space (i.e. the current configuration is taken to be the reference configuration). The spatial rate of deformation tensor is considered to be the sum of elastic rate of deformation tensor and the inelastic rate of deformation tensor as displayed in equation (5.2).

There are two algorithms were developed for finite deformation of viscoplasticity theory based on overstress: i.) a one-step forward gradient approximation [139], ii.) An unconditionally stable implicit integration scheme based on the backward Euler [137,140]. The later algorithm was using in this study. An objective logarithmic co-rotational rate introduced by Xiao and Bruhns [141,142] proved that a co-rotational rate of the Eulerian logarithmic strain is identical with the rate of deformation tensor and all possible Eulerian strain measures. Only the logarithmic strain measure enjoys this property. These results were used to formulate in rate type constitutive models in Eulerian frame. The VBO theory does not require a separate stress or strain space formulation.

Xiao et al. [141,142] introduced the co-rotational, logarithmic derivative. The formula 61 of [142] in view of the striking properties of the log-spin $\boldsymbol{\Omega}^{\log}$, for the logarithmic rate of any symmetric Eulerian tensor $\boldsymbol{\tau}$ is defined as

$$\overline{\boldsymbol{\tau}}^{\log} = \dot{\boldsymbol{\tau}} + \boldsymbol{\tau}\boldsymbol{\Omega}^{\log} - \boldsymbol{\Omega}^{\log}\boldsymbol{\tau} \tag{6.7}$$

The calculation of $\boldsymbol{\Omega}^{\log}$ is presented explicitly algebraic expressions in detail of [143]. Thus, the deviator of Cauchy stress, equilibrium stress, kinematic stress will be transformed into the logarithmic rate form of $\overline{\sigma}^{\log}$, $\overline{\boldsymbol{g}}^{\log}$, $\overline{f}^{\log}$ and their deviatoric quantities as following.

The Cauchy stress can be taken as

$$\sigma^{\log} = \mathrm{E} : \varepsilon^{e} = \mathrm{E} : \left(\varepsilon - \varepsilon^{in}\right) = \mathrm{E} : \varepsilon - \sqrt{6}\mu\bar{\varepsilon}^{in}\mathbb{N} \tag{6.8}$$

where:

$\sigma^{\log} = \dot{\sigma} + \sigma\Omega^{\log} - \Omega^{\log}\sigma$ is the Eulerian logarithmic rate of Cauchy stress.

E is the fourth order tensor of elasticity.

$\mathbb{N} = \sqrt{\frac{3}{2}}\frac{o}{\Gamma}$ is normalization of the deviatoric overstress (6.9)

The deviator of Cauchy stress is defined as:

$$s = \sigma - \frac{1}{3}(\sigma : \mathrm{I})\mathrm{I} \tag{6.10}$$

On the other hand, it can be presented in others as:

$$s^{\log} = 2\mu\varepsilon^{e} = 2\mu d - \sqrt{6}\mu\bar{\varepsilon}^{in}\mathbb{N} \tag{6.11}$$

Where μ is elastic shear and $s^{\log} = \dot{s} + s\Omega^{\log} - \Omega^{\log}s$

The equilibrium stress deviator is written in Eulerian logarithmic rate as following:

$$\boldsymbol{g}^{\log} = \frac{\Psi}{CE}\left(s^{\log} + \frac{o}{k[\Gamma]} - \frac{\Gamma}{k[\Gamma]}\frac{(\boldsymbol{g}-\boldsymbol{f})}{A} + (1-\frac{\Psi}{E})\boldsymbol{f}^{\log} \right) \tag{6.12}$$

Where:

Eulerian logarithmic rate of $g^{\log} = \dot{g} + g\Omega^{\log} - \Omega^{\log}g$

$f^{\log}$ is Eulerian logarithmic rate of the kinematic stress, is taken as: $f^{\log} = \dot{f} + f\Omega^{\log} - \Omega^{\log}f$. The evolution equation of the kinematic stress is taken as $f^{\log} = \bar{E}_t\varepsilon^{in}$. (6.13)

$\dot{E}_t$ is an average tangent modulus that describes the slope of strain-stress curve at maximum strain of interested point. It is taken as $\bar{E}_t = \frac{2}{3}\frac{E_t}{\left(1-\frac{E_t}{E}\right)}$ (6.14)

The procedure of the integration of (6.16) is presented in formula (5.3.21) of [143]. Final results is summarized as

$$\boldsymbol{\sigma}_{n+1} = \boldsymbol{Q}_{n+1}\boldsymbol{\sigma}_n\boldsymbol{Q}_{n+1}^{T} + \Delta t\boldsymbol{Q}_{n+1}\boldsymbol{Q}_{n+\theta}^{T}\bar{\boldsymbol{\sigma}}_{n+\theta}^{\log}\boldsymbol{Q}_{n+\theta}\boldsymbol{Q}_{n+1}^{T} \tag{6.15}$$

where tensor function $\boldsymbol{Q}_{n+1} = \exp(\Delta t\boldsymbol{\Omega}^{\log}(t_{n+1/2}))$ has presentation in part 28.8 of [143].

Sham [140] introduced the integration algorithm based on the backward Euler method. This algorithm will be used in here to integrate the constitutive equations of VBO theory. The equations of Cauchy stress, equilibrium stress, the kinematic stress, and their deviator is written at the time t_{n+1} as following:

$$\begin{aligned}
&\sigma_{n+1} = \bar{\sigma} + \Delta t(\sigma^{\log})_{n+1} = \bar{\sigma} + \Delta t\left(\mathrm{E} : \varepsilon - \sqrt{6}\mu\bar{\varepsilon}^{in}\mathbb{N}\right)_{n+1} \\
&s_{n+1} = \bar{s} + \Delta t(s^{\log})_{n+1} = \bar{s}_n + \Delta t(2\mu d - \sqrt{6}\mu\bar{\varepsilon}^{in}\mathbb{N})_{n+1} \\
&f_{n+1} = \bar{f} + \Delta t(f^{\log})_{n+1} = \bar{f}_n + \Delta t(\sqrt{\frac{3}{2}}\bar{E}_t\bar{\varepsilon}^{in}\mathbb{N})_{n+1} \\
&g_{n+1} = \bar{g} + \Delta t(g^{\log})_{n+1}
\end{aligned} \quad \text{where} \quad \begin{aligned}
&\bar{\sigma} = Q_{n+1}\sigma_n Q_{n+1}^T \\
&\bar{s} = Q_{n+1}s_n Q_{n+1}^T \\
&\bar{f} = Q_{n+1}f_n Q_{n+1}^T \\
&\bar{g} = Q_{n+1}g_n Q_{n+1}^T
\end{aligned} \quad (6.16)$$

$$g_{n+1} = \bar{g}_n + \Delta t\left(\frac{\Psi}{CE}\left(2\mu d - \sqrt{6}\mu\bar{\varepsilon}^{in}\mathbb{N} + \frac{o}{k[\Gamma]} - \frac{\Gamma}{k[\Gamma]}\frac{(\boldsymbol{g}-\boldsymbol{f})}{A} + (1-\frac{\Psi}{E})\sqrt{\frac{3}{2}}\bar{E}_t\bar{\varepsilon}^{in}\mathbb{N}\right)\right)_{n+1} \quad (6.17)$$

Using relations among quantities in above equation, we can convert into nonlinear equation in the unknown overstress invariant Γ_{n+1} [137]. It can be solved for Γ_{n+1} by using the Newton method.

$$f(\Gamma_{n+1}) = \left(\sqrt{\frac{2}{3}}\Gamma_{n+1}C_1 + \sqrt{6}\mu\Delta t\bar{\varepsilon}^{in}_{n+1}C_1 + C_2\right)^2 - \left(C_1 s^* - g^*\right) : \left(C_1 s^* - g^*\right) = 0 \quad (6.18)$$

Where:

$$\begin{aligned}
&C_1 = 1 + \Delta t\Psi_{n+1}\frac{\bar{\varepsilon}^{in}_{n+1}}{A_{n+1}} \\
&C_2 = \Delta t\Psi_{n+1}\left(\left(-\sqrt{6}\frac{\mu}{E} + \sqrt{\frac{2}{3}}\right)\bar{\varepsilon}^{in}_{n+1} + \sqrt{\frac{2}{3}}\bar{E}_t\Delta t\frac{\left(\bar{\varepsilon}^{in}_{n+1}\right)^2}{A_{n+1}}\right) + \sqrt{\frac{2}{3}}\bar{E}_t\Delta t\left(1 - \frac{\Psi_{n+1}}{E}\right)\bar{\varepsilon}^{in}_{n+1} \\
&s^* = \bar{s}_n + 2\mu\Delta t\varepsilon \\
&g^* = \bar{g} + \Delta t\Psi_{n+1}\left(2\frac{\mu}{E}\varepsilon + \frac{\bar{\varepsilon}^{in}_{n+1}}{A_{n+1}}\bar{f}_n\right)
\end{aligned} \quad (6.19)$$

The final step is determination of the material JACOBIAN matrix $\frac{\partial\Delta\sigma}{\partial\Delta\varepsilon}$ for finite computational procedure. We have:

$\sigma_{n+1} = \bar{\sigma} + \Delta\sigma_{n+1}$ and $\sigma_{n+1} = \bar{\sigma} + \Delta t\left(\mathrm{E} : \varepsilon - \sqrt{6}\mu\bar{\varepsilon}^{in}\mathbb{N}\right)_{n+1}$, it can be extracted as following:

$$\Delta\sigma_{n+1} = \Delta t\left(\mathrm{E} : \varepsilon - \sqrt{6}\mu\bar{\varepsilon}^{in}\mathbb{N}\right)_{n+1} \quad (6.20)$$

The equation (6.20) show that $\Delta\sigma_{n+1}$ only depend on two variables ε and Γ_{n+1}. So, it can be written in a function of those variables $\Delta\sigma_{n+1} = F^*\left(\Gamma_{n+1}, \Delta\varepsilon\right)_{n+1}$, where $\Delta\varepsilon = \Delta t\varepsilon$.

Let take partial derivative of the function F^* with variable of $\Delta\varepsilon$ following the chain rule. We will extract the material JACOBIAN matrix

$$\frac{\partial\Delta\sigma}{\partial\Delta\varepsilon} = \left(\frac{\partial F^*}{\partial\Delta\varepsilon}\right)_{\Gamma} + \left(\frac{\partial F^*}{\partial\Gamma}\right)_{\Delta\varepsilon} \otimes \frac{\partial\Gamma}{\partial\Delta\varepsilon} \tag{6.21}$$

The finite computational procedure is described on diagram of Fig. 6.21**.**

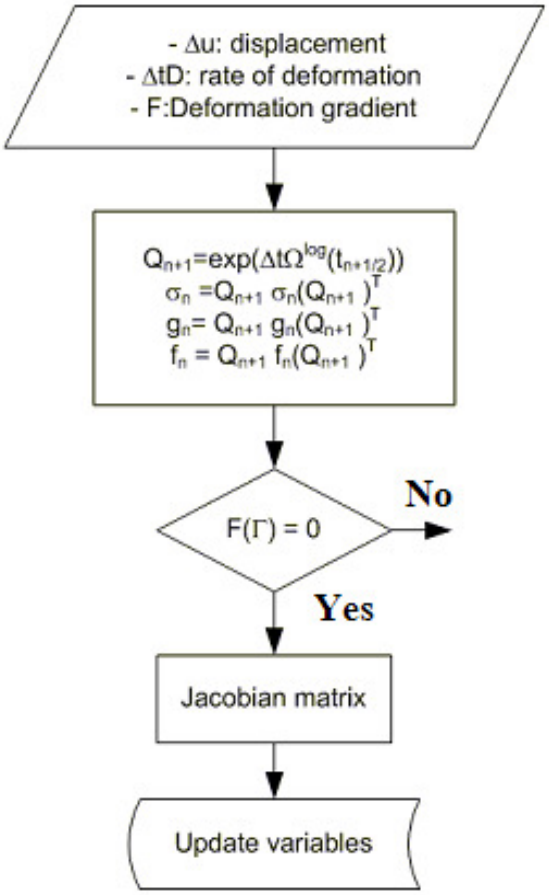

Fig. 6.21 Algorithmic of implementation into ABAQUS

6.2.1 Finite element modeling

A cone-shaped model with thickness in 3mm is modeled for FEM simulation purpose with sizes showed on Fig. 6.22. The simulation of the whole of a cone took very time consuming, even with the coarser mesh. Several nonlinearities (e.g. material, model,

contact conditions) are involved in this simulation which triggered off a huge computational time consuming with implicit solver. In addition, it is difficult to optimize the simulation of SPIF process with a full model. Therefore, a part of the model is necessary to get a relative result in the certain case. With a part of the model will reduce significantly the computation time. The simulation configuration of SPIF process is presented on Fig. 6.1a. with ABAQUS/Standard.

Some preliminary simulations were performed to evaluate the influences of the boundary condition, type of element, density of mesh, and number of element layer on the geometric accuracy. The result showed that the boundary conditions are assigned to the extend nodes along the radial edges in such a way that they are not allowed to move in the direction perpendicular to the edges. The edges derived by cutting the cone model in a pie of 45^{o} are assigned boundary condition that allows moving in a normal direction of blank.

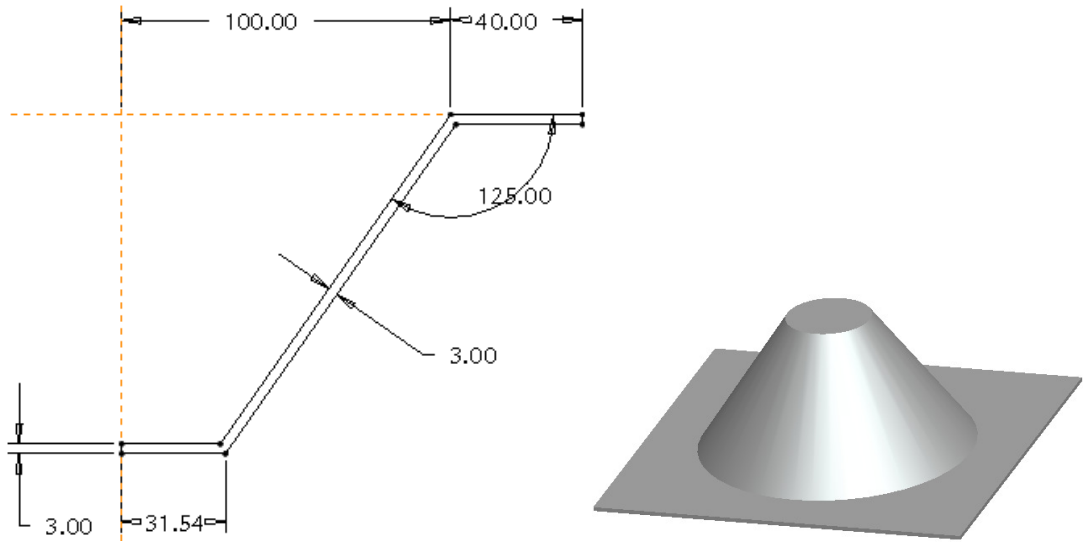

Fig. 6.22 The two dimension sketch and CAD model for simulation

The 8-node brick with a reduced number of integration points (C3D8R) are applied for blank. The tool, the backing plate and the support are considered as rigid parts, because, in reality, these parts are much stiffer than the work-piece, and this way it takes less time to simulate.

The effect of mesh density on thickness and geometry of the cone is relative large. By using trial and error method showed that number of seed on a radial edge is larger than

35 seeds, which have small change between two times of trial. The trials are performed with the first five helical rounds, and then check the thickness of the simulated cone between sequent trials.

The fifty seeds (number of grid on an edge) on a radial edge are assigned for this simulation. The three seeds on the vertical edge are assigned to take into account of the bending effects. To decrease computation time and to increase accuracy in deformed part of the cone, the bank is meshed in two different regions. The first region is a fine mesh; the second is a coarse mesh as Fig. 6.23. This model used 10202 nodes with 7200 elements of C3D8R for fine mesh and 665 elements of C3D4 for coarse mesh. The total computation time of CPU is spent in 192 hours.

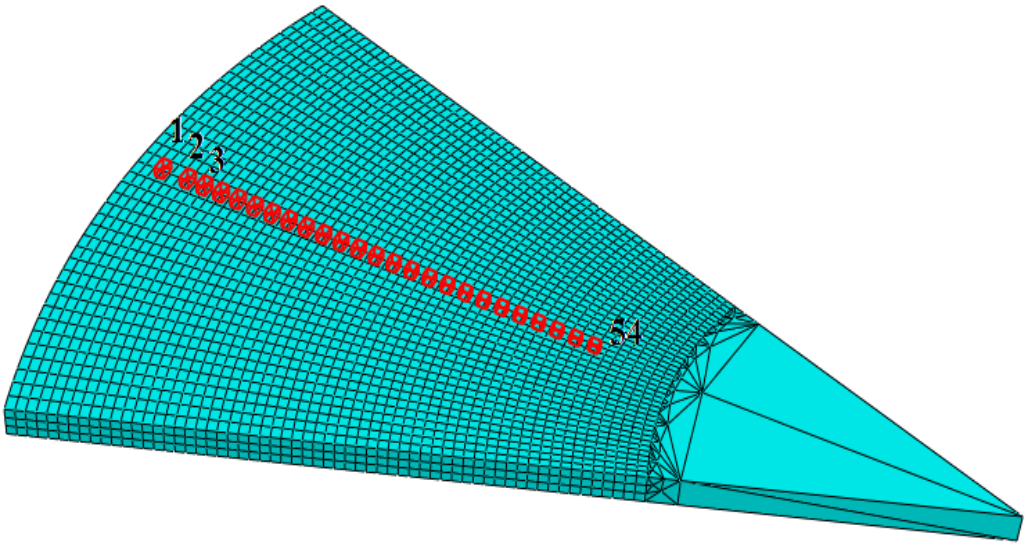

Fig. 6.23 The order of elements monitored during the simulation

The tool-path is exported from Pro Engineer and is converted into the helical tool-path [72]. Using this toolpath helps to decrease the influence at the beginning points which the tool goes down. Only first 40 arcs were simulated instead of 75 arcs to decrease computation time.

In order to find out how well the model is able to represent the reality, comparison with experimental study was made. The actually experimental model with similar parameters is also performed on a square PP sheet cut in dimension of 300x300mm, and 3mm thickness. The forming zone was a circle of 200mm diameter. When the part was

complete, its geometry was measured (using CMM) and compared with the simulation results.

Parameter	Value
Spindle Speed (rpm)	80
Depth of cut (mm)	1
Feed-rate (mm/min)	1000
Friction coefficient of tool-blank	0.02
Friction coefficient of spring-back plate	0.5
Lubrication (cooling water)	Blasocut™

Table 6.5 The parameters for simulation and experiment

The other parameters for this simulation are reported in Table 6.5. The material constants used in this simulation are reported in Table 6.6.

Material constant	Model values
Elastic modulus, E (MPa)	1863
Tangent modulus, E_t (MPa)	18
Elastic Poison's rate	0.33
Inelastic Poison's rate	0.3
A_0, A_c, A_f (MPa)	25.5, 10, 26.5
C_1, C_2 (MPa), C_3	12, 1100, 72
k_1 (s), k_2 (MPa), k_3	85.8, 5.4, 10
□, λ	0.4, 0.5

Table 6.6 Material constants used in simulation

6.2.2 Results and Discussions

Up to now, ISF technology in sheet metal can be considered as a mature technology. Since most aspects related to the process mechanics, industrial applications, and machine for ISF process were researched and achieved good results. However, many aspects in non-metallic materials need to be explained in most effective way due to their complex deformation behaviors. The polymeric materials exhibited the relaxation and creep behavior, and recovery at zero stress occurred at room temperature. Therefore, thickness distribution and geometric accuracy are main interest in applicability of ISF technique with polymeric materials. The section 3.5.2 pointed out the processing parameters which affected on the formability of the thermoplastic materials. Of course,

these effects can be reduced by using optimized process parameters or increasing some constraints to achieve better results. The increase in constraints of blank such as support, auxiliary die and other equipments to force to better accuracy will be stultified the flexibility and simplicity of ISF process. In recent years, many research efforts have been spent to mature this process for the different materials.

The deviations in other areas are most likely due to too approximate material model, inadequate boundary conditions and too large element size. It is possible to make results more accurate by modeling of a sheet fixture using contact calculation here also, but this procedure would increase the computation time considerably. The second option, to make a model more adequate, is by increasing element number (using smaller elements), but it will surely increase the computational time.

6.2.2.1 Full model vs. quarter model

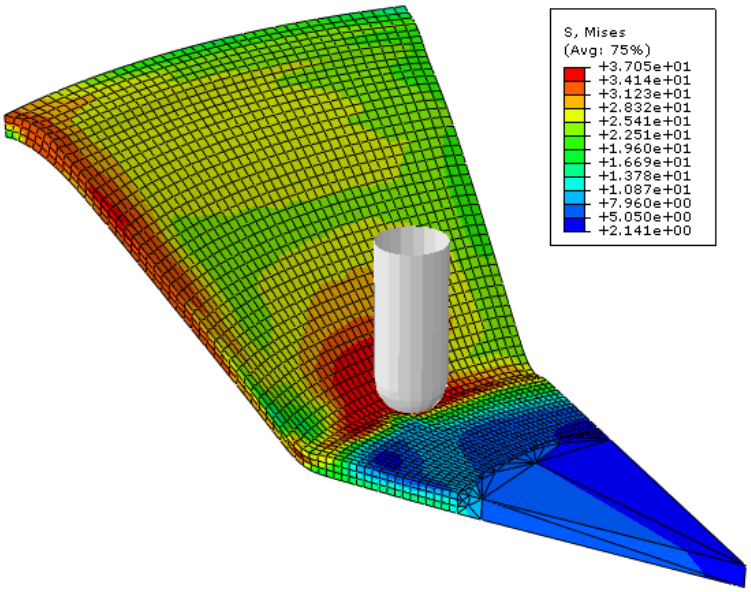

Fig. 6.24 Non-uniform stress in deformed part due to symmetric boundary

The deforming characterization of SPIF process is to occur locally at contacting point between the forming tool and the sheet. The stress distribution is local at a vicinity of this contacting point. This distribution of stress in SPIF process is not symmetric even for simulating a symmetric part. Assigning the symmetric boundary conditions for two side edges trigged off non-uniform stress in the vicinity of these edges (see Fig. 6.24). The

larger stress occurred on an edge which the forming tool passed through. This phenomenon does not happen in the case wall edge of a rectangle or pyramid model in simulation with full model of sheet metal.

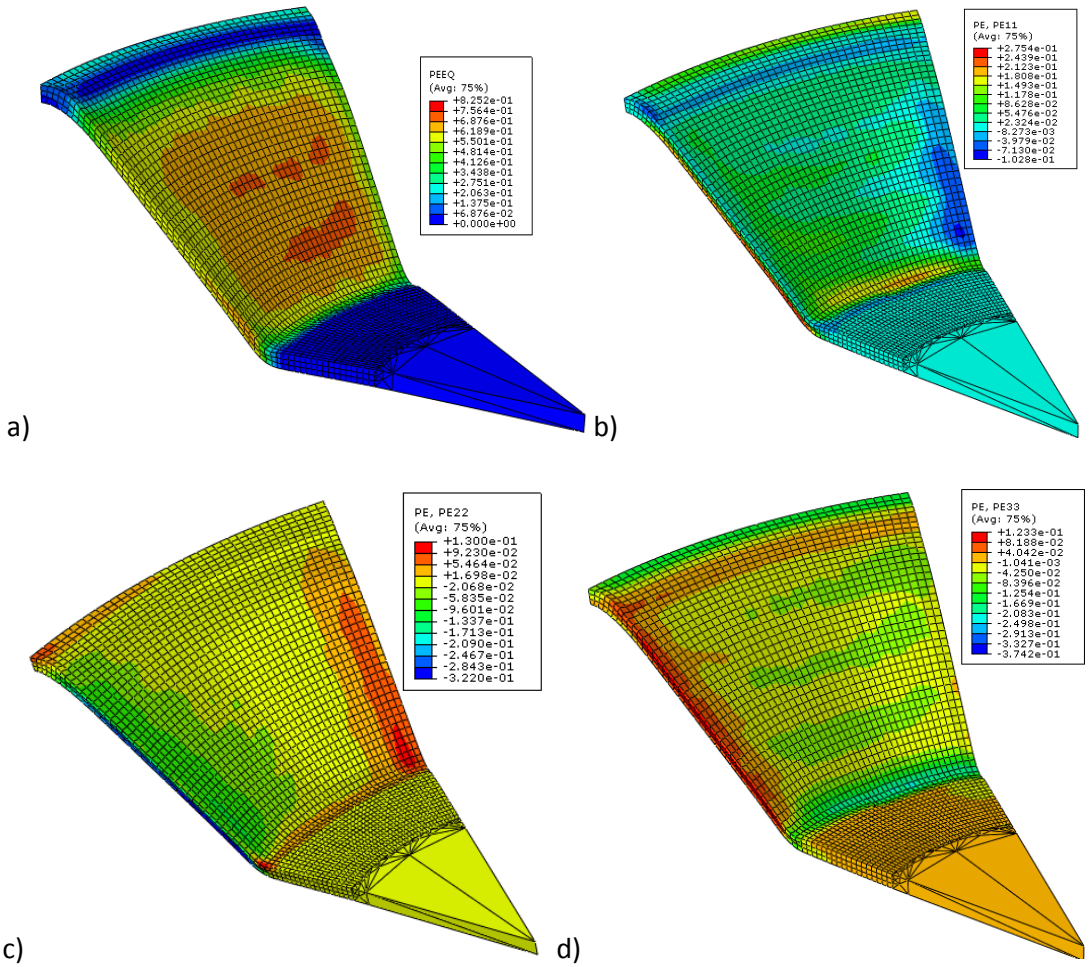

Fig. 6.25 Non-uniform stress in deformed part due to symmetric boundary

The Fig. 6.24 showed that the Von-Mises stress distributions are highest at forming region and contacting area between forming tool and sheet. The lowest stresses distributed at the central area of the part where the sheet is un-deformed. It is normally phenomenon in conventional forming process. However, there is a difference in this area in comparison between full model and quarter of the model. In a full model, this area seems to be flat. Otherwise, it is planoconcave or planoconvex part in considering the quarter of the model. This deviation may be emanated from assuming symmetric boundary conditions.

In Fig. 6.25b, it is clear to show non-uniform strain at two edges assigned the symmetric boundary conditions. The non-uniform strain in the third strain component contributes the deviation of thickness between two edges. The deviation is very large as presented on Fig. 6.25c and Fig. 6.25d. The non-uniform strain in the first and second strain components contributes the deviation of geometric accuracy. The evolution of equivalent strain of the elements marked in numerical order showed on Fig. 6.26.

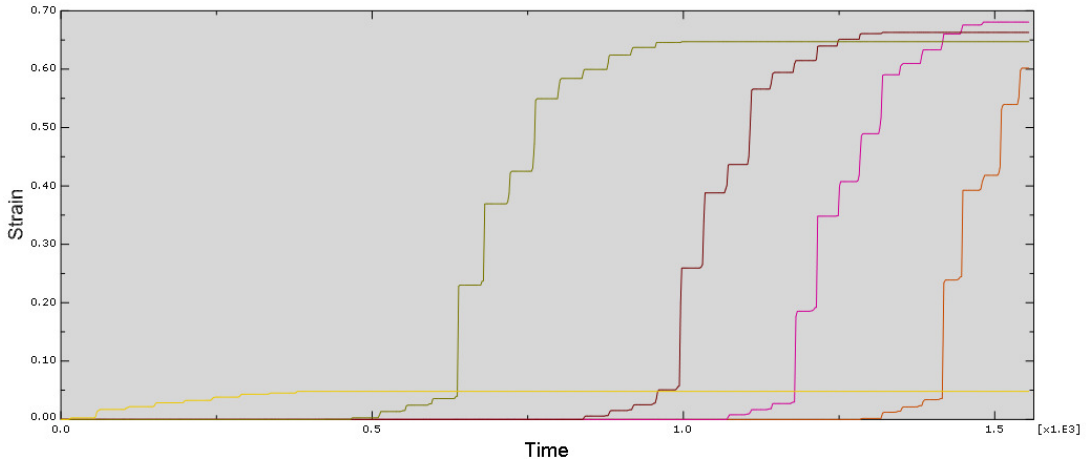

Fig. 6.26 Evolution of equivalent strain in the elements monitored during simulation

6.2.2.2 Geometric accuracy

The ISF process is performed without using dedicated die or support, sheet is deformed incrementally following to the designed path. Thus, the prediction of the geometric accuracy needs to be considered due to influence of the spring-back phenomenon. A comparison of profiles among CAD model, simulated model, and experiment is shown on Fig. 6.27 and Fig. 6.28. It showed that there is a difference between CAD profile and FEM profile. The largest deviation between the center curve of FEM profile and CAD profile is 1.66mm. However, the bottom edge of FEM profile is very flat which is different with observation in actual experiment. It can to be caused by insufficiency of boundary conditions as assuming a partial model for FEM simulation.

A coordination system is assigned into the simulated model to measure set of points on profile of third mesh layer (the model is meshed in three layers). The profile of the experiment model is measured by using Coordinate Measuring Machine (CMM). It gave two profiles as outer and inner profile in .VDA file extension. The simple procedure was

applied to process these file. They are converted into .STP file extension (STEP AP214 or STEP AP 203). The set of points that constructed to two profiles of the model can be extracted from these files (The STEP file can be opened by using any text editor). After removing keywords of STEP file, the set of points can be imported into Excel. The comparison among the profiles is shown on Fig. 6.27.

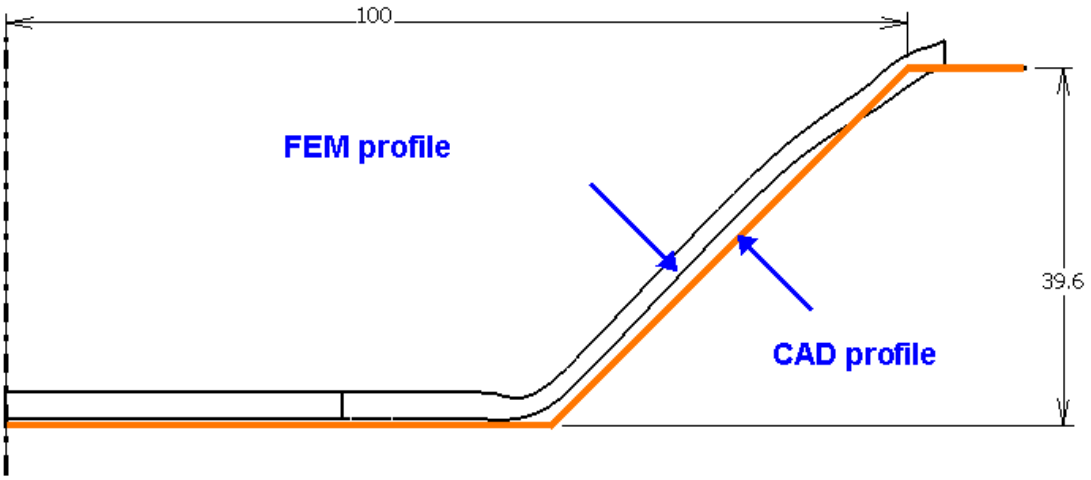

Fig. 6.27 A comparison between FEM profile and CAD profile

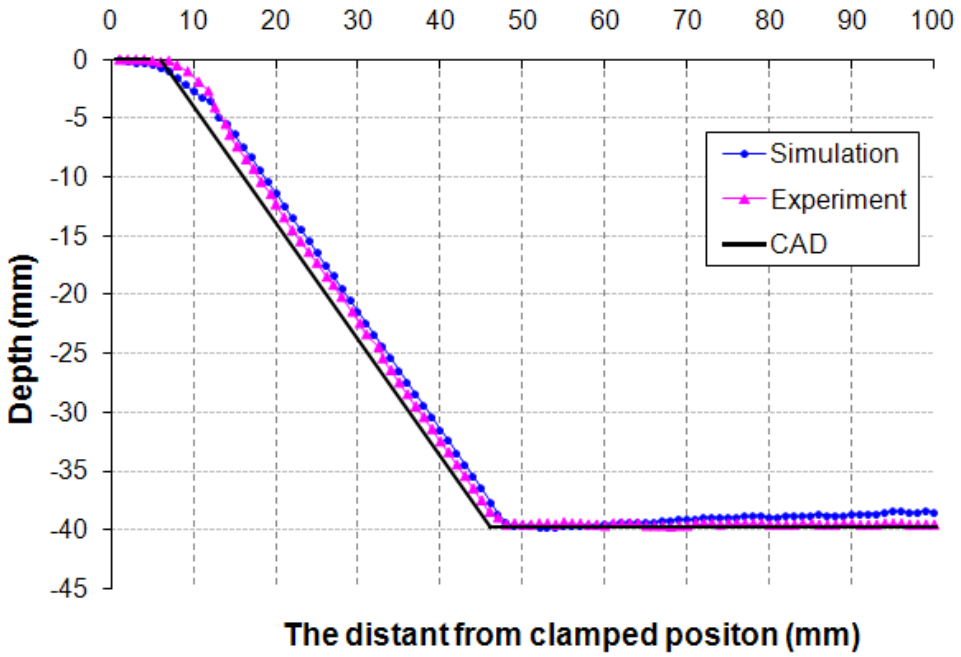

Fig. 6.28 A comparison among the profiles

Clearly, the good agreement between the simulated and experiment shape is in part of the cone wall. However, the cone bottom of the actual experimental model is higher

than simulated one about 1.63mm. This difference can be due to only cone pie used in this simulation, and it is constrained with the unsatisfied boundary conditions as above assuming.

For practical applications, in order to obtain high accuracy of geometric product, it is easy to modify the CNC machining program in the part of wall angle with a deviation of 1.66mm. This method is used to utilize in CNC technique to compensate an amount of a tool wearing. Thus, the deviation of geometric product can overcome by this method.

6.2.2.3 Thickness distribution

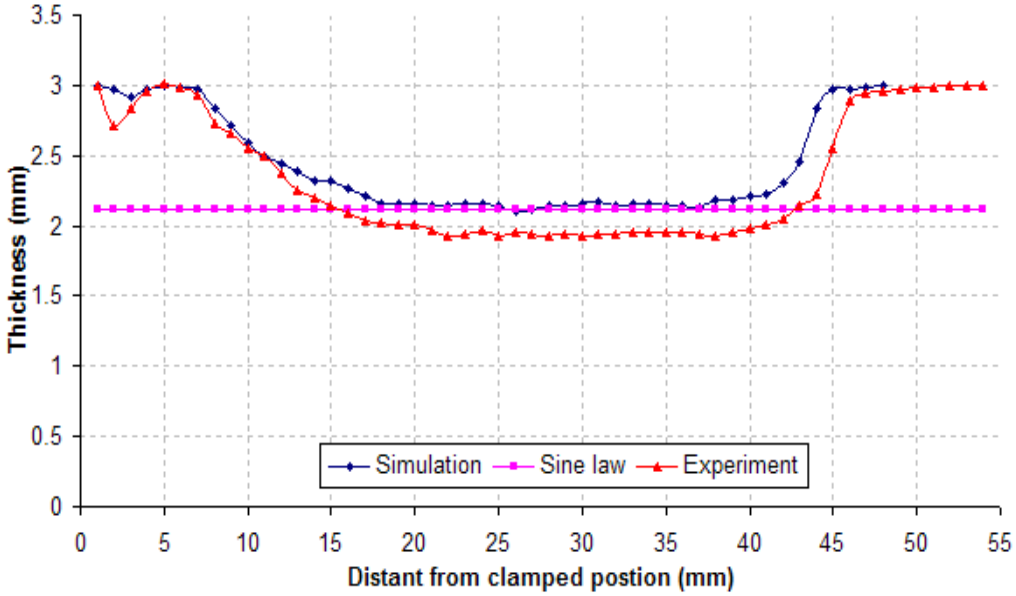

Fig. 6.29 Thickness distribution in different distant

An important factor in sheet metal forming, especially ISF, is the thickness after forming. Regarding to the calculation of deformed thickness, the formula (1.1) used for spin process is also applied for this process, called sine law. Actually, this formula only is used as a reference or average approximation to calculate a thickness of sheet because of complex distribution in thickness of the deformed sheet. The thickness distribution at different distant from the clamped position and measured in middle line from both edges of pie (see Fig. 6.23) is shown on Fig. 6.29.

It shows that thickness values are larger than the one calculated by the sine law at a region close to clamped part of a sheet and occurs in a region between undeformed and

deformed sheet. This phenomenon be due to the sheet is blended freely in the deformation process. In the previous study also observed that a complex distribution of thickness on adjoining edges of a pyramid or flower model occurred. As shown in Fig. 6.29, there are three distinguishable regions: i) close to clamped position, ii) wall region, iii) transition between deformed and undeformed part of the sheet. The first region is blended freely; the thickness is decreased drastically from 3mm to 2.15mm along a distance of 17.2mm from the clamped position (note that the diameter of a tool is 10mm). In the wall region, prediction of a thickness is a good agreement with the sine law. A maximum difference is less than 0.1mm between simulated one; maximum difference of simulated thickness and experiment is less than 0.35mm. There is a good agreement between simulation results and measured values. It is worth to mention that the thickness of real part varies slightly, because of small tool radius and large step size.

6.2.2.4 Colour variation

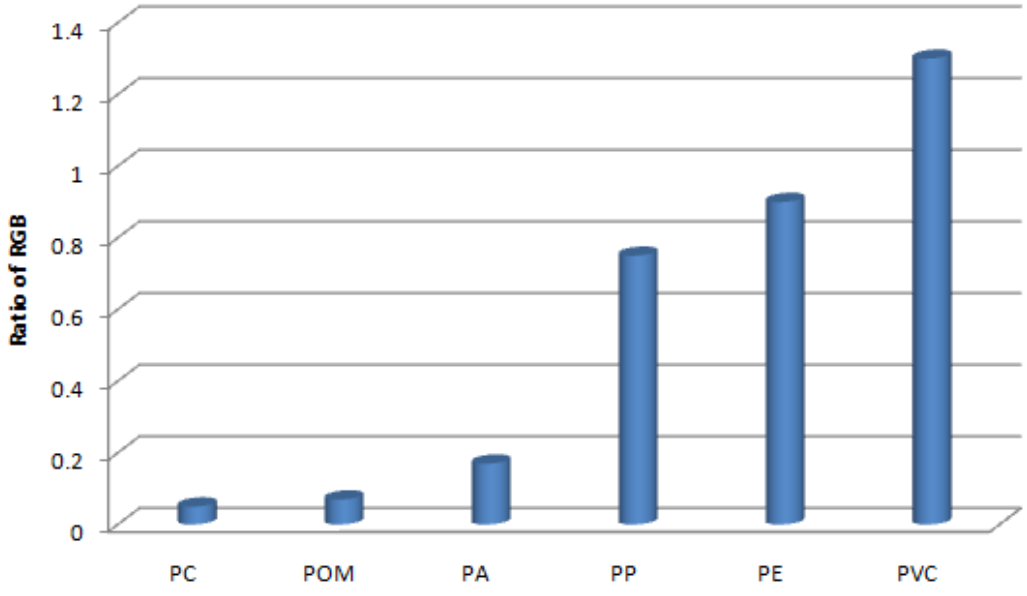

Fig 6.30 Comparison of the colour variation in deformed parts in SPIF process

The thermoplastic materials have various colors to enhance the aesthetic of product. They were remained well in a conventional process such as injection mould. However, both tensile tests and forming with the SPIF process show that deformed parts were changed slightly the color during forming. The slight filemot color of PP turns into opalescent color in a deformed zone. Franzen et al. [144] and Martin et al. [70] also

reported this phenomenon with PVC, PE, and PA. However, POM and PC still remain the transparency and an original color after deforming. To compare the changing level, the ratio of the RGB values before and after forming is used. The original sheet and deformed part is taken the pictures in same lighting condition. The RGB values got from these pictures is then compared together as showed on Fig 6.30.

6.3 Summarizing the chapter

This chapter is presented a procedure to identify the influence of processing parameters on the simulated results of SPIF with sheet metal. The simulation with optimal parameters is performed to predict the mechanical failures in SPIF. It revealed that the tensile stress is a main reason caused the fracture in deformed part. The contribution of shear stress is very small in causes of fracture. For prediction of damage in SPIF, the ductile criterion can respond to this task. The good agreement is found between the predicted results of damage and one of actual experiment for SPIF with magnesium sheet.

For polymer, a procedure for implementing VBO model into ABAQUS is presented in practice application of simulation of ISF process. The result shows that there is a good agreement between simulation and experiment for prediction of the thickness and geometric accuracy. However, there are some drawbacks relative to computation time and its consequence in geometric accuracy.

Chapter 7

Summary

7.1 SPIF with sheet metal

This thesis provided new aspects of SPIF with sheet metal at an elevated temperature. SPIF process is experimented with two metal materials: magnesium alloy sheet AZ31 and aluminum alloy sheet in series 1010. The main results can find in the current thesis as following:

- A heating system based on Joule effect was designed to serve the experiments of SPIF at an elevated temperature. It provided the uniform temperature on sheet in the shortest time to avoid the oxidation phenomenon of sheet surfaces.
- The experimental strategies were performed to investigate the influences of processing parameters on the responses of SPIF. There were two important responses of SPIF which were only studied through experimental approach such as a maximum wall angle and the quality of deformed surface. The three process parameters (temperature, feedrate and depth step) are considered in the DOE plans to be able to identify their influences on those responses. The regression models extracted from experimental results allowed estimating the influences of most important parameters in SPIF process. The temperature has most influence on the formability and the depth step has most influence on the quality of surface. The maximum wall angle obtained in the experiments is 89.3° and 74.2° for aluminum sheet and magnesium sheet, respectively. Performing SPIF process with sheet metal at the elevated temperature as a potential approach can obtain the highest formability.
- For aluminum sheet, the formability was influenced significantly temperature and feedrate. However, interaction between the feedrate and depth step on the

formability is small. Thus, selecting an optimal solution of these values brings a greatest efficient of formability and the quality of surface in a limited capacity of CNC machine at the recent time.

- For magnesium sheet, influences of feedrate, depth step and temperature on formability and surface roughness are very important. To understand well these influences, it is necessary to investigate mechanical test and observation of microstructure at fracture zone. The results showed that the texture of microstructure is highly depended on the temperature and deformation speed. These properties were reflected clearly in formability of SPIF process.
- FEM simulation of SPIF process used an explicit integrate scheme for the prediction of mechanical damage in SPIF process is performed on the full cone-shaped model. Fully coupled thermal analysis approach taking into account of anisotropic behavior and the sensitivity of temperature and strain rate was used in 3D-FEM simulation. This model removed the assuming of previous researchers such as using the partial model, unreal toolpath, material properties because of the complication and big time consuming in the FEM simulation of SPIF process. In this thesis, the processing parameters and other conditions were preserved as actual experiments. Thus, good correlation between the simulated results and experimental ones has been found.
- The influences of meshing density, mass scale, friction, anisotropic behavior on the simulated results were investigated in detail. The optimal FEM simulation model took from evaluating these influences was performed to predict the mechanical damage in SPIF process.
- Thanks to the simulated results with magnesium sheet in the damage prediction, it revealed that the tensile stress is a main reason caused the fracture in deformed part. The contribution of shear stress is very small in causes of fracture.
- The ductile criteria can respond well the task of the damage prediction in SPIF process. The good agreement was found between the predicted results of damage and one of the actual experiments with magnesium sheet.

- Thanks to the FEM simulation, formation of two types of the propagation path of fracture occurred in actual experiments is understood well. It can be concluded that axial tensile stress caused this path.

7.2 SPIF with sheet polymer

The incremental forming technique was applied successfully for sheet polymers at room temperature in the current thesis. It brought a potential approach to deform sheet polymers that can be substituted the conventional process (e.g. injection mold, thermoforming, etc) in low and medium production batches. The main results of SPIF process with polymers can find in this thesis as following:

- The cooling and lubrication system were designed to serve for successful deformation of sheet polymer at room temperature. The lubrication mixed cooling water was provided cyclically during SPIF process to assure no change of the temperature. The mixed lubrication is reused many times to avoid the effects on environment and saving the experimental cost.
- The experimental strategy was performed to investigate influences of processing parameters on formability of polypropylene. Four parameters of feedrate, depth step, tool size, and spindle speed is used in a DOE plan. The regression analysis showed that the influence of depth step and tool size has most influence on the formability of PP. The maximum wall angle obtained in PP with SPIF process was 75°.
- The procedure for implementing the material constitutive VBO model was presented. It was implemented under a user-material model (UMAT) into FEM simulation for predicting the accuracy of thickness and geometry.
- The tensile, relaxation and creep test were performed at a large range of strain rate. They exhibited that PP is highly depended on strain rate. The relaxation and creep phenomenon occurred at room temperature. The results of mechanical testing were used to calibrate VBO model for FEM simulation.
- The FEM simulation used implicit integration scheme was performed with a partial cone-shaped model. The simulated result showed a good correction of sheet thickness between the FEM simulation and experiment. The prediction of

geometric accuracy between the simulation and experiment result gave a very good result. However, the prediction of geometric accuracy has the deviation of 1.66mm between the simulated result and CAD model. This can overcome by using the compensative algorithm which is usually utilized in CNC programming technique.

Fig. 7.1 Some samples in aluminum alloy

Bibliography

[1] I. Drishtikona, "Sheet Metal Stamping in Automotive Industry," 2009.

[2] F. Micari, G. Hirt , A. Bramley, J. Duflou, J. Allwood J. Jeswiet, "Asymmetric Single Point Incremental Forming of Sheet Metal," *CIRP Annals - Manufacturing Technology*, vol. 54, no. 2, pp. 88-114 , 2005.

[3] G. Hirt, S. Junk M. Bambach, "Modelling and Experimental Evaluation of the Incremental CNC Sheet Metal Forming Process," in *7th International Conference on Computational Plasticity*, Barcelona, 2003.

[4] C. Powell N. and Andrew, "Incremental forming of flanged sheet metal components without dedicated dies," *Journal of engineering manufacture*, vol. IMECHE part B, no. 206, pp. 41-47, 1992.

[5] S Matsubara, "Incremental backward bulge forming of a sheet metal with a hemispherical head tool—a study of a numerically controlled forming system," *Journal of the Japan Society for Technology of Plasticity*, vol. 35, no. 1, pp. 1311-1316, 1994.

[6] T. J., Yang, D. Y. Kim, "Improvement of formability for the incremental sheet forming process," *International Journal of Mechanical Sciences*, vol. 42, no. 1, pp. 1271-1286, 2000.

[7] L. Kwiatkowski, G. Sebastiani, R. Shankar, A. E. Tekkaya, M. Kleiner V. Franzen, "Dyna-Die: Towards Full Kinematic Incremental Forming," in *Esaform 08*, Lyon, France, 2008, pp. 1163-1166.

[8] Leszak E., "Apparatus and Process for Incremental Dieless Forming," 3342051, Sep. 19, 1967.

[9] H., Kato, K., Sakamoto, S. Iseki, "Flexible and Incremental Sheet Metal Bulging Using a Path-Controlled Spherical Roller," *Transactions of the Japan Society of Mechanical Engineers*, vol. 58, no. 554, p. 3147–3155, 1992.

[10] K. Kitazawa, "Incremental Sheet Metal Stretch-Expanding with CNC Machine Tools," in *Proceedings of the Fourth ICTP*, vol. Proc. of the 4th ICTP, Beijing, 1993, p. 1899–1904.

[11] MACDOR Machine Industry And Trade. (2009) MACDOR Machine Industry And Trade. [Online]. http://www.firearmsid.com

[12] E., Jeswiet, J. Hagan, "A review of conventional and modern single point sheet metal forming methods," *Proceedings of the Institution of Mechanical Engineers. Part B. Journal of engineering manufacture* , vol. 217, no. Part B, p. 213–225, 2003.

[13] FRANJO METAL SPINNING. (2009) FRANJO METAL SPINNING. [Online]. http://www.franjometal.com

[14] X.C. Gao, X.F. Meng, Z.H. Wang D.C. Kang, "Study on the deformation mode of conventional spinning of plates," *Journal of Materials Processing Technology*, vol. 226–230, no. 91, pp. 226-230, 1999.

[15] L. -N Yang, H. Kudo K. Kawai, "Flexible shear spinning of truncated conical sheels with general-purpose mandrel," *Journal of Materials Processing Technology*, vol. 113, no. 1-3, pp. 28-33, 2001.

[16] R.Q. Hsu, K.H. Fuh M.D. Chen, "Analysis of internal dieless spinning of cones," in *Fourth International Conference of Rotary Forming*, 1989, p. 114–119.

[17] L.-N. Yang, H. Kudo K. Kawai, "Dieless shear spinning of truncated conical shells," in *6th ICTP*, vol. 2, Springer-Verlag, 1999, pp. 1089-1094.

[18] T.A. Dean, J. Lin C.C. Wong, "A review of spinning, shear forming and flow forming processes," *International Journal of Machine Tools and Manufacture*, vol. 43, no. 14, pp. 1419-1435 , 2003.

[19] Hagan, E. J. Jeswiet, "Rapid Proto-typing of a Headlight with Sheet Metal," in *Transactions of North American Manufacturing Research Institute*, 2001, pp. 33 - 38.

[20] D., Green, A. J., Bramley, A. N. Leach, "A new incremental sheet forming process for small batchand prototype parts," in *Verlag Meisenbach Bamberg*, Germany, 2001, pp. 95-102.

[21] L., Fantini, L., Micari, F. Filice, "Analysis of Material Formability in Incremental Forming," *CIRP Annals - Manufacturing Technology*, vol. 51, no. 1, pp. 199-202 , 2002.

[22] L. W.and Gahlert, C., Hahn, F. Meyer, "Influence of an incremental deformation on

material behaviour and forming limit of Aluminium Al99,5 and QT-steel 42CrMo4," in *International Research Conference TMT 2005*, Switzerland, 2005.

[23] Jeswiet, J. D. Young, "Forming Limit Diagrams for Single-Point Incremental Forming of Aluminium Sheet," *Journal of engineering manufacture*, vol. IMechE, Part B, no. 219/4, pp. 359-364, 2005.

[24] Young, D., Ham, M. J. Jeswiet, "Non-traditional Forming Limit Diagrams for Incremental Forming," *Journal Advanced Materials Research*, vol. 6, no. 8, pp. 409-416, 2005.

[25] I. Costantino, L. De Napoli, L. Filice, L. Fratinir and M. Muzzupappa G. Ambrogio, "Influence of some relevant process parameters on the dimensional accuracy in incremental forming a numerical and experimental investigation," *Journal of Materials Processing Technology*, vol. 153-154, no. 10, pp. 501-507, 2004.

[26] L. Filice, F. Gagliardi and F. Micari G. Ambrogio, "Sheet thinning prediction in single point incremental forming," in *SheMeet*, Erlangen, Germany, 2005, pp. 471-478.

[27] J. Jeswiet D. Young, "Wall thickness variations in single-point incremental forming," *Journal of engineering manufacture*, vol. 218, no. 11, pp. 1453-1459, 2004.

[28] N. Bay, B. Endelt, G. Ingarao M. Skjoedt, "Multi Stage Strategies for Single Point Incremental Forming of a Cup," in *Esaform 08*, vol. 1, Lyon, France, 2008, pp. 1199-1202.

[29] "The Magnesium Sheet Casting Process – The Process, Properties, Economics, Advantages and Capabilities," *Materials World*, vol. 11, no. 06, 2003.

[30] Fadi K. Abu-Farha and Marwan K. Khraisheh, "Mechanical Characteristics of Superplastic Deformation of AZ31Magnesium Alloy," *Journal of Materials Engineering and Performance*, vol. 16, no. 02, pp. 192-199, 2007.

[31] M., Geiger, M., Klaus, A. Kleiner, "Manufacturing of Lightweight Components by Metal forming," *CIRP Annals - Manufacturing Technology*, vol. 52, no. 2, pp. 521-542, 2003.

[32] Michaeli W. Rettemeier G., "Thixomoulding injection moulding of semi-solid magnesium alloys," *Journal of polymer engineering*, vol. 24, no. 1-3, pp. 49-64,

2004.

[33] K. Mori and H. Tsuji, "Cold Deep Drawing of Commercial Magnesium Alloy Sheets," *CIRP Annals - Manufacturing Technology*, vol. 56, no. 1, pp. 285-288, 2007.

[34] T. Yoshii, N. Hatta H. Takuda, "Finite-element analysis of the formability of a magnesium-based alloy AZ31 sheet," *Journal of Materials Processing Technology*, vol. 89–90, no. 135–140, pp. 1258-1262 , 1999.

[35] R., Altan, T., Geiger, M., Kleiner, M., Sterzing, A. Neugebauer, "Sheet Metal Forming at Elevated Temperatures," *CIRP annals*, vol. 52, no. 5, pp. 793-816, 2006.

[36] H.Tashiro, H.Okamoto, K.Shimizu K.Iwanaga, "Improvement of formability from room temperature to warm temperature in AZ-31 magnesium alloy," *Journal of Materials Processing Technology*, vol. 155–156, no. 30, pp. 1313-1316 , 2004.

[37] K.Manabe, H.Nishimura S.Yoshihara, "Effect of blank holder force controlin deep-drawing process of magnesium alloy," *Journal of Materials Processing Technology*, no. 3, pp. 579-585 170, 2000.

[38] H.Yamamoto, K.Manabe, H.Nishimura S.Yoshihara, "Formability enhancement in magnesium alloy deep drawing by local heating and cooling technique," *Journal of Materials Processing Technology*, vol. 140-144, no. 20, pp. 612-615 , 2003.

[39] B.J.MacDonald, H.Nishimura, H.Yamamoto, K.Manabe S.Yoshihara, "Optimisation of magnesium alloy stamping with local heating and cooling using the finite element method," *Journal of Materials Processing Technology*, vol. 153–154, no. 10, pp. 319-322, 2004.

[40] K. Droder E. Doege, "Sheet metal formability of magnesium wrought alloys—formability and process technology," *Journal of Materials Processing Technology*, vol. 115, no. 14-19, pp. 14-19, 2001.

[41] G. Ngaile,T. Altan H. Palaniswamy, "Finite element simulation of magnesium alloy sheet forming at elevated temperature," *Journal of Materials Processing Technology*, vol. 146, no. 56-60, pp. 52-60 , 2004.

[42] L. Filice, G. L. Manco G. Ambrogio, "Warm incremental forming of magnesium alloy AZ31," *CIRP Annals - Manufacturing Technology*, vol. 57, no. 257–260, pp. 257-260 , 2008.

[43] J.J.Park Y.H.Ji, "Formability of magnesium AZ31 sheet in the incremental forming at warm temperature," *Journal of Materials Processing Technology*, vol. 210, no. 354–358, pp. 354-358, 2008.

[44] H. Guo, F. Xiao, L. Gao, A.B. Bondarev, W. Han Q. Zhang, "Influence of anisotropy of the magnesium alloy AZ31 sheets on warm negative incremental forming," *Journal of Materials Processing Technology*, vol. 209, no. 15-16, pp. 5514-5520, 2009.

[45] J. Jeswiet M. Ham, "Forming Limit Curves in Single Point Incremental Forming," *CIRP Annals - Manufacturing Technology*, vol. 56, no. 1, pp. 277-280, 2007.

[46] L. Filice, F. Micari G. Ambrogio, "A force measuring based strategy for failure prevention in incremental forming," *Journal of Materials Processing Technology*, vol. 177, no. 1-3, pp. 413-416, 2006.

[47] G. Ambrogio, F. Micari Filice, "On-Line Control of Single Point Incremental Forming Operations through Punch Force Monitoring," *CIRP Annals - Manufacturing Technology*, vol. 55, no. 1, pp. 245-248 , 2006.

[48] V. Cozza, L. Filice, F. Micari G. Ambrogio, "An analytical model for improving precision in single point incremental forming," *Journal of Materials Processing Technology*, vol. 191, no. 1-3, pp. 92-95, 2007.

[49] Y. Tunckol, R. Aerens J. R. Duflou, "Force Analysis for Single Point Incremental Forming," in *Sheet Metal 07*, 2007, pp. 543-550.

[50] G. Hirt, "Tools and Equipment used in Incremental Forming," in *1st Incremental Forming Workshop*, University of Saarbrucken, 2004.

[51] F. Micari, "Some remarks on material formability in single point incremental forming of sheet metal," in *8th International Conference on Technology of Plasticity*, Verona, 2005.

[52] S.He, A.Van Bael, P.Van Houtte, and J.Duflou P. Eyckens, "Forming Limit Predictions for the Serrated Strain Paths in Single Point Incrementa lSheet Forming," in *9th International Conference on Numerical Methods in Industrial Forming Processes*, AIP Conference Proceedings, 2007, pp. 141-146.

[53] A.H. van den Boogaard W.C. Emmens, "An overview of stabilizing deformation

mechanisms in incremental sheet forming," *Journal of Materials Processing Technology*, vol. 209, no. 8, pp. 3688-3695, 2009.

[54] A.H. van den Boogaard W.C. Emmens, "Incremental forming by continuous bending under tension—An experimental investigation," *Journal of Materials Processing Technology*, vol. 209, no. 14, pp. 5456-5463, 2009.

[55] M. Skjoedt, P.A.F. Martins, N. Bay M.B. Silva, "Revisiting the fundamentals of single point incremental forming by means of membrane analysis," *International Journal of Machine Tools and Manufacture, Volume 48, Issue 1, January 2008, Pages 73-83*, vol. 48, no. 1, pp. 73-83, 2008.

[56] N. Bay, M. Skjoedt and M.B. Silva P.A.F. Martins, "Theory of single point incremental forming," *CIRP Annals - Manufacturing Technology*, vol. 57, no. 1, pp. 247-252, 2008.

[57] K. Jackson Allwood J., "The mechanics of incremental sheet forming," *Journal of Materials Processing Technology*, vol. 209, no. 3, pp. 1158-1174 , 2009.

[58] D.R. Shouler and A.E. Tekkaya Allwood J.M., "The increased forming limits of incremental sheet forming processes," in *International Conference on Sheet Metal. SheMet '07*, Palermo, Italy, 2007.

[59] H. Iseki, "An approximate deformation analysis and FEM analysis for the incremental bulging of sheet metal using a spherical roller," *Journal of Materials Processing Technology*, vol. 111, no. 1-3, pp. 150-154 , 2001.

[60] H. Iseki, "Vertical wall surface forming of rectangular shell using multistage incremental forming with spherical and cylindrical rollers," *Journal of Materials Processing Technology*, vol. 130-131, no. 20, pp. 675-679 , 2002.

[61] Meelis Pohlak, Jüri Majak, and Rein Küttner, "Incremental Sheet Forming Process Modelling - Limitation Analysis," in *Mechanics and Materials in Design*, Porto, 24-26 July, 2006.

[62] P. Eyckens, A. Van Bael, and J. R. Duflou R. Aerens, "Force prediction for single point incremental forming deduced from experimental and FEM observations," in *10.1007/s00170-009-2160-2*, Springer London, 2009, pp. 1433-3015.

[63] A. M. Habraken, A. Szekeres, J. Duflou, S. He, A.V. Bael, P.V. Houtte Henrard C.,

"Comparison of FEM Simulations for the Incremental Forming Process," in *Trans Tech Publications*, vol. 6, Switzerland, 2005, pp. 533-542.

[64] P. Dal Santo, A. Delamézière, A. Potiron, J.-L. Batoz Robert, "On some computational aspects for incremental sheet metal forming simulations," in *Esaform 08*, vol. 1, Lyon, France, 2008, pp. 1195-1198.

[65] A. Van Bae, R. Aerens, J. Duflou and P. Van Houtte P. Eyckens, "Small-scale Finite Element Modelling of the Plastic Deformation Zone in the Incremental Forming Process," in *Esaform 08*, vol. 1, Lyon, France, 2008, pp. 1159-1162.

[66] M. Gotoh and S. Atsumia M. Yamashita, "Numerical simulation of incremental forming of sheet metal," *Journal of Materials Processing Technology*, vol. 199, no. 1-3, pp. 163-172, 2008.

[67] E.S. Masuku, A.N. Bramley, A.R. Mileham, G.W. Owen Q. QIN, "Incremental sheet forming simulation and accuracy," in *Proceedings of 8th ICTP*, Verona, 2005.

[68] S. Thibaud and J. C. Gelin S. Dejardin, "Finite element analysis and experimental investigations for improving precision in single point incremental sheet forming process," in *Esaform 08*, vol. 1, Lyon, France, 2008, pp. 121-124.

[69] L. Kwiatkowski, P.A.F. Martins, and A.E. Tekkaya V. Franzen, "Single point incremental forming of PVC," vol. 209, no. 1.

[70] L. Kwiatkowski, V. Franzen, A.E. Tekkaya, and M. Kleiner P.A.F. Martins, "Single point incremental forming of polymers," *CIRP Annals - Manufacturing Technology*, vol. 58, no. 1, pp. 229-232, 2009.

[71] J.M. Allwood, M. Landert K.P. Jackson, "Incremental forming of sandwich panels," in *SheMet'07*, vol. 204, Palermo, Sicily, 2007.

[72] M. H. Hancock, and N. Bay M. Skjoedt, "Creating Helical Tool Paths for Single Point Incremental Forming," in *12th International Conference on Sheet Metal Forming*, Palermo, 2007, pp. 583-590.

[73] J. R. Duflou and A. Szekeres J. Jeswiet, "Forces in Single Point and Two Point Incremental Forming," in *Sheet Metal 05*, vol. 6-8, Switzerland, 2005, pp. 449-456.

[74] K.F., Yin, D.L., Wu, D.Z. Zhang, "Formability of AZ31 magnesium alloy sheets at warm working conditions," *International Journal of Machine Tools and*

Manufacture, vol. 46, no. 11, pp. 1276-1280, 2006.

[75] J. Jeswiet M. Ham, "Single Point Incremental Forming and the Forming Criteria for AA3003," *CIRP Annals - Manufacturing Technology*, vol. 55, no. 1, pp. 241-244, 2006.

[76] Fugui Xiao, Hailing Guo, Changsheng Li, Lin Gao, Xingwu Guo, Weidong Han, A.B. Bondarev Qinglai Zhang, "Warm Negative Incremental Forming of Magnesium Alloy AZ31 Sheet: New Lubricating Method," *Journal of Materials Processing Technology*, vol. 210, no. 2, pp. 323-329, 2010.

[77] J., Houghton, N. E., Jackson, K. P. Allwood, "The Design of an Incremental Sheet Forming Machine," in *Advanced Materials Research, Sheet Metal 2005*, vol. 6–8, Switzerland, 2005, pp. 471-478.

[78] Douglas C. Montgomery Raymond H. Myers, *Response Surface Methodology*, 3rd ed. Canada: Jonh Wiley & Sons , 2002.

[79] S. Matsubara, M. Sakamoto and G. Fukuhara, T. Sawada, "3D FE deformation analysis for stretch forming of sheet metal with CNC machine tools," in *Advanced Technology of Plasticity*, Bejing, China, 1999, pp. 123-124.

[80] A.V. Bael, and Paul Van Houtte P. Eyckens, "Marciniak–Kuczynski type modelling of the effect of Through-Thickness Shear on the forming limits of sheet metal," *International Journal of Plasticity*, vol. 25, no. 12, pp. 2249-2268, 2009.

[81] H. Gese, H. Dell and H. Werner H. Hooputra, "A comprehensive failure model for crashworthiness simulation of aluminum extrusions," *International Journal of Crashworthiness*, vol. 9, no. 5, pp. 449 - 464 , 2004.

[82] V. Needleman, A. Tvergaard, "Analysis of the cup-cone fracture in a round tensile bar," *Acta Metallic*, vol. 32, no. 1, pp. 157-169, 1984.

[83] A. Tvergaard, V. Needleman, "An analysis of ductile rupture in notched bars," *Journal of the Mechanics and Physics of Solids*, vol. 32, no. 6, pp. 461-490, 1984.

[84] Tomasz Wierzbicki Yingbin Bao, "On the cut-off value of negative triaxiality for fracture," *Engineering Fracture Mechanics*, vol. 72, no. 7, pp. 1049-1069, 2005.

[85] Tomasz Wierzbicki Yingbin Bao, "On fracture locus in the equivalent strain and stress triaxiality space," *International Journal of Mechanical Sciences*, vol. 46, no. 1,

pp. 81-98, 2004.

[86] Simulia, *Abaqus Analysis User's Manual*.: Simulia, 2006.

[87] Wierzbicki T. Lee Y.W., "Relationship between the Forming and Fracture Limit Diagrams with calibration and applications," in *AmeriPAM03 ESI Group*, Troy, 2003.

[88] Tomasz Wierzbicki Lee Y.W., "Fracture prediction of thin plates under localized impulsive loading. Part I: dishing," *International journal of impact engineering*, vol. 31, no. 10, pp. 1253-1276, 2005.

[89] Tomasz Wierzbicki Lee Y.W., "Fracture prediction of thin plates under localized impulsive loading. Part II: discing and petalling," *International journal of impact engineering*, vol. 31, no. 10, pp. 1253-1276, 2005.

[90] Jeffrey C. Woertz, Tomasz Wierzbicki Lee Y.W., "Fracture prediction of thin plates under hemi-spherical punch with calibration and experimental verification," *International journal of mechanical sciences*, vol. 46, no. 5, pp. 751-781, 2004.

[91] B. Deluca, R. Rendina P. Brozzo, "A new method for the prediction of formability in metal sheets," in *Seventh Biennial Conference of the International Deep Drawing Research Group*, Amsterdam, 1972.

[92] P. Hartley, C.E.N. Sturgess and G.W. Rowe S.E. Clift, "Fracture prediction in plastic deformation processes," *International Journal of Mechanical Sciences*, vol. 31, no. 1, pp. 1-17, 1990.

[93] T. Sato, K. Okimoto and S. Shima M. Oyane, "Criteria for ductile fracture and their applications," *Journal of Mechanical Working Technology*, vol. 4, no. 1, pp. 65-81, 1980.

[94] Yingbin Bao, Young-Woong Lee, Yuanli Bai Tomasz Wierzbicki, "Calibration and evaluation of seven fracture models," *International Journal of Mechanical Sciences*, vol. 45, no. 4-5, pp. 719-743, 2005.

[95] A. Turetta, *PhD Thesis*. Padova: DIMEG, University of Padua, 2008.

[96] A. Ghiotti, S. Bruschi D. Pellegrini, "Microstructure Phenomena and Mechanical Properties of AZ31B under Warm Forming Conditions," in *Esaform 09*, The Netherlands, 2009.

[97] C. Bruni, S. Bruschi, L. Filice, A. Ghiotti, M. Simoncini G. Ambrogio, "Characterisation of AZ31B magnesium alloy formability in warm forming conditions," *International Journal of Material Forming*, vol. 1, no. 1, pp. 205-208, 2008.

[98] S. Ahzi, K.S. Vecchio, F.C. Jiang and A. Makradi J. Richeton, "Modeling and validation of the large deformation inelastic response of amorphous polymers over a wide range of temperatures and strain rates," *International journal of solids and structures*, vol. 44, no. 24, pp. 7938-7954, 2007.

[99] Mary C. Boyce Rebecca B.Dupaix, "Constitutive modeling of the finite strain behavior of amorphous polymers in and above the glass transition," *Mechanics of Materials*, vol. 39, no. 52, pp. 39-52, 2007.

[100] D.M.Parks, M.C.Boyce, W.A.M.Brekelmans, F.P.T.Baaijens J.A.W.V.Dommelen, "Micromechanical modeling of intraspherulitic deformation of semicrystalline polymers," *Polymers*, vol. 44, no. 19, pp. 6089-6101 , 2003.

[101] R.W. Meyer and L.A. Pruitt, "The effect of cyclic true strain on the morphology, structure, and relaxation behavior of ultra high molecular weight polyethylene," *Polymer*, vol. 42, no. 12, pp. 5293-5306, 2001.

[102] E. Ghorbel, "A viscoplastic constitutive model for polymeric materials," *International Journal of Plasticity*, vol. 24, no. 11, pp. 2032-2058 , 2008.

[103] A.S.Argon, D.M.Parks, S.Ahzi, Z.Bartczak B.J.Lee, "Simulation of large strain plastic deformation and texture evolution in high density polyethylene," *Polymer*, vol. 34, no. 17, pp. 3555-3575, 1993.

[104] N. Selini, M. Benguediab, M. Bouziane Mohamed and M. Belhamiani H.M.Meddah, "Analysis of the polypropylenenext term mechanical behaviour response: Experiments and numerical modeling," *Materials & Design*, vol. 30, no. 4192–4199, pp. 4192-4199, 2009.

[105] Christiansen J. Dec and A. D. Drozdov, "Constitutive Equations for the Viscoplastic Response of Isotactic Polypropylene in Cyclic Tests: The Effect of Strain Rate," *Polymer engineering and science*, vol. 44, no. 3, pp. 548-556, 2004.

[106] S. Nikolov and I. Doghri, "A micro/macro constitutive model for the small-

deformation behavior of polyethylene," *Polymers*, vol. 41, no. 5, pp. 1883-1891 , 2000.

[107] L. Lin and A. S. Argon, "Structure and plastic deformation of polyethylene," *Journal of Materials Science*, vol. 29, no. 2, pp. 294-323, 1994.

[108] Kichenin J., "PhD Thesis," 1992.

[109] M. and D.Zhou Kitagava, "Stress-Strain Curves for Solid Polymers," *Polymer Engineering and Science*, vol. 35, no. 22, 1995.

[110] T. Ariyama, "Stress Relaxation Behavior After Cyclic Preloading in Polypropylene," *Polymer engineering and science*, vol. 33, no. 22, pp. 1494-1501, 1993.

[111] M. C., A. Hasan Boyce, "A Constitutive Model for the NonlinearViscoelastic Viscoplastic Behavior of Glassy Polymers," *Polymer Engineering and Science*, vol. 35, no. 4, 1995.

[112] M. C., David M. P., Ali S. Argon Boyce, "Large inelastic deformation of glassy polymers. Part I: rate dependent constitutive model," *Mechanics of Materials*, vol. 7, no. 15-33, pp. 641-659, 1988.

[113] H. Laurent, G. Rio, S. Pimbert, V. Grolleau, N. Masmoudi, C. Bradai M. Zrida, "Experimental and numerical study of polypropylene behavior using an hyper-visco-hysteresis constitutive law," *Computational Materials Science*, vol. 45, no. 2, pp. 516-527, 2009.

[114] E. Krempl, "From the standard linear solid to the viscoelasticity theory based on overstress," *Journal of Rheology*, vol. 42, no. 4, pp. 713-725, 1995.

[115] K. Ho Kremp E.l, "Extension of the viscoplasticity theory based on overstress (VBO) to capture non-standard rate dependence in solids," *International Journal of Plasticity*, vol. 18, no. 7, pp. 851-872, 2002.

[116] E. and Ho, K. Krempl, "An overstress model for solid polymer deformation behaviour applied to Nylon 66," 2000.

[117] T., Y. Mori, and K. Kaneko Ariyama, "Tensile Properties and Stress Relaxation of Polypropylene at Elevated Temperatures," *Polymer engineering and science*, vol. 33, no. 1, pp. 81-90, 1997.

[118] T. Matsutani Kitagawa M., "Effect of time and temperature on nonlinear constitutive equation in polypropylene," *Journal of Materials Science*, vol. 23, no. 11, pp. 4085-4090, 1988.

[119] K., H. Takagi Kitazawa, "Nonlinear constitutive equation of polypropylene under combined tension and torsion," *Journal of Materials Science*, vol. 25, no. 6, pp. 2869-2872, 1990.

[120] Erhard Krempl and Fazeel Khan, "Rate (time)-dependent deformation behavior: an overview of some properties of metals and solid polymers," *International Journal of Plasticity*, vol. 19, no. 7, pp. 1069-1095, 2003.

[121] Ozgen U. Colak, "Modeling deformation behavior of polymers with viscoplasticity theory based on overstress," *International Journal of Plasticity*, vol. 21, no. 1, pp. 145-160 , 2005.

[122] Ozgen U. Colak N. Dusunceli, "Modelling effects of degree of crystallinity on mechanical behavior of semicrystalline polymers," *International Journal of Plasticity*, vol. 24, no. 7, pp. 1224-1242, 2008.

[123] B. E. Read and P. E. Tomlins, "Time-dependent deformation of polypropylene in response to different stress histories," *Polymer*, vol. 38, no. 18, pp. 4617-4628, 1997.

[124] B.E. Read, "Mechanical relaxation in isotactic polypropylene," *Polymer*, vol. 30, no. 8, p. 1439–1445, 1989.

[125] I. B. Guanella, R. E. Cohen G. Attalla, "Effect of morphology on stress relaxation of polypropylene," *Polymer engineering and science*, vol. 23, no. 16, pp. 883-887, 1983.

[126] T. Ariyama, "Viscoelastic-plastic behaviour with mean strain changes in polypropylene," *Journal of Materials Science*, vol. 31, no. 15, pp. 4127-4131, 1996.

[127] T. Ariyama, "Cyclic Deformation and Relaxation Characteristics in Polypropylene," *Polymer engineering and science*, vol. 33, no. 1, pp. 18-25, 1993.

[128] M. T. Mori, and Tomohiko Kitagawa, "Rate-dependent Nonlinear Constitutive Equation of Polypropylene," *Journal of Polymer Science Part B: Polymer Physics*, vol. 27, no. 85-95, pp. 85 - 95, 1989.

[129] M.L. Villarragaa, M.P. Herra, J.S. Bergström, C.M. Rimnacc and A.A. Edidin S.M. Kurtz, "Thermomechanical behavior of virgin and highly crosslinked ultra-high molecular weight polyethylene used in total joint replacements," *Biomaterials*, vol. 23, no. 17, pp. 3681-3697 , 2002.

[130] M. Fugier, D. Petit, B. Fillon N. Alberola, "Tensile mechanical behaviour of quenched and annealed isotactic polypropylene films over a wide range of strain rate," *Journal of Materials Science*, vol. 30, no. 4, pp. 860-868, 1995.

[131] M. Fugier, D. Petit, B. Fillon N. Alberola, "Microstructure of quenched and annealed films of isotactic polypropylene," *Journal of Materials Science*, vol. 30, no. 5, pp. 1187-1195, 1995.

[132] Jean Lemaître, *Handbook of Materials Behavior Models*.: ACADEMIC PRESS, 2001.

[133] S., Van Bael, A., Van Houtte, P., Szekeres, A., Duflou, J., Henrard, Christophe He, "Finite element modeling of incremental forming of aluminium sheets," *Trans Tech Publications*, vol. 6, no. 8, pp. 525-532, 2005.

[134] C.Henrard, P.Eyckens, R.Aerens, A.Van Bael, H.Sol, J.R.Duflou, and A.M.Habraken C. Bouffioux, "Comparison of the Tests Chosen for Material Parameters Identification to Predict Single Point Incremental Forming Forces," in *Esaform 08*, Lyon, France, 2008, pp. 1147-1150.

[135] P. Flores, T. Lelotte, C. Bouffioux, F. El Houdaigui, and A.M.A. Van Bael, S. He, J. Duflou, and A. M. Habraken Habraken, "Model Identification and FE Simulations: Effect of Different Yield Loci and Hardening Laws in Sheet Forming," *International journal of plasticity*, vol. 23, no. 3, pp. 420-449, 2005.

[136] T.-L. Sham and E. Krempl, I. Nishiguchi, "A finite deformation theory of viscoplasticity based on overstress. Part 1.," *Journal of Applied Mechanics*, vol. 57, no. 3, p. 553, 1990.

[137] T. L. Sham, E. Krempl S.Gomaa, "Finite element formulation for finite deformation,isotropic viscoplasticity theory based on overstress," *International Journal of Solids and Structures*, vol. 41, no. 13, pp. 3607-3624 , 2004.

[138] T.-L. Sham and E. Krempl, I. Nishiguchi, "A finite deformation theory of viscoplasticity based on overstress. Part II. Finite element implementation and,"

Journal of Applied Mechanics, vol. 57, no. 3, p. 548, 1990.

[139] D., Shih, C. F., Needlman, A Peirce, "A tangent modulus method for rate dependent solids," *Computers & Structures*, vol. 18, no. 875-887, pp. 875-887, 1884.

[140] T., L. Sham, "Implicit (backward Euler) integration method for a version of TVBO with constant isotropic stress and without static recovers.," 1994-S2,.

[141] Xiao, O. T. Bruhns and A. Meyers H., "Logarithmic strain, logarithmic spin and logarithmic rate," *Acta mechanica*, vol. 124, no. 1-4, pp. 89-105, 1997.

[142] H., Xiao, and A. Meyers O. T. Bruhns, "New results for the spin of the Eulerian triad and the logarithmic spin and rate," *Acta mechanica*, vol. 115, no. 1-2, pp. 95-109, 2002.

[143] Hans. Schwerdtfeger, *Introduction to Linear Algebra and the Theory of Matrices* , 2nd ed.: P. Noordhoff (Groningen), 1961.

[144] L.Kwiatkowski, P.A.F.Martins, A.E.Tekkaya V.Franzen, "Single point incremental forming of PVC," *Journal of Materials Processing Technology*, vol. 209, no. 1, pp. 462-469, 2009.

[145] S., Amino, H., Lu, Y., Matsubara, S. Aoyama, "Apparatus for dieless forming plate materials," EP0970764, 2000.

[146] Y.W. Lee, "Fracture prediction in metal sheets," 2004.

[147] H., Lu, Y., Maki, T., Osawa, S., Fukuda, K. Amino, "Dieless NC Forming, Prototype of Automotive Service Parts," in *7th ITCP*, Beijing, 2002, pp. 1015-1020.

Information

Author's coordinates:

Mr. Van-Sy. Le (Lê Văn Sỹ)

- Nationality: Vietnamese
- BME, Ho Chi Minh City University of Technology, Vietnam, 2003
- Msc, University of Ulsan, South Korea, 2006
- PhD student, University of Padua, Department of Innovation in Mechanics and Management – DIMEG - Floor 7th, Via Venezia, 1, 35131, PD, Padova, Italy.
  Tel. +39 049 827 6819 Fax +39 049 827 6816
  Email: vansy.le@unipd.it or vansyle@yahoo.com
  Website: http://www.dimeg.unipd.it/

Supervisor's coordinates:

Full Prof. Paolo F. Bariani

Director of Doctoral School in Industrial Engineering

Department of Innovation in Mechanics and Management, University of Padua, Italy.

Tel. +39 049 827 6815 Fax +39 049 827 6816

Email: paolo.bariani@unipd.it

Website: http://www.dimeg.unipd.it/